Measurements of Bottom Hadron Lifetimes and the Λ^0 Production Rate in $Z^0 \to b\bar{b}$ Events using Data from the OPAL Experiment

Mark Pearce

Thesis submitted for the degree of
Doctor of Philosophy

March 1996

School of Physics and Space Research
Faculty of Science
The University of Birmingham

Synopsis

The OPAL detector has been used to collect data from decays of the Z^0 boson, produced with e^+e^- collisions at the LEP collider. Approximately 3.5 million events, recorded between 1991 and 1994 with the silicon microvertex detector operational, were considered for measurements of the average bottom hadron lifetime, τ_b, and the bottom baryon lifetime, $\tau_{\Lambda_b^0}$. The Λ^0 baryon production rate in $Z^0 \to b\bar{b}$ events was studied using approximately one million multihadronic events, recorded between 1991 and 1992. A neural network algorithm was used to enhance $Z^0 \to b\bar{b}$ events relative to other hadronic decay modes of the Z^0 boson.

The average bottom hadron lifetime was evaluated using a binned maximum likelihood fit to the reconstructed decay time distribution formed using estimates of the bottom hadron decay length and momentum. The lifetime measurement :

$$\tau_b = (1.637 \pm 0.008\,(\text{stat}) \pm 0.034\,(\text{syst}))\,\text{ps},$$

has a systematic error dominated by uncertainties on the bottom quark fragmentation modelling in the Monte Carlo and the resolution function that describes the distribution of reconstructed decay times for a given true decay time.

A study of Λ^0 baryon production in $Z^0 \to b\bar{b}$ events was used to measure :

$$\text{Br}(\text{b hadron} \to \Lambda^0 X) = (5.9 \pm 0.6\,(\text{stat})^{+0.5}_{-0.4}\,(\text{syst}))\,\%.$$

The systematic error is dominated by uncertainties on the momentum spectrum of Λ^0's from bottom quark fragmentation. The bottom baryon production rate was subsequently estimated as :

$$f(b \to \Lambda_b^0)\,\text{Br}(\Lambda_b^0 \to \Lambda^0 X) = (2.3^{+0.9}_{-0.8})\,\%.$$

The bottom baryon lifetime was measured with the same overall technique as used for the measurement of τ_b. The additional requirement of a high momentum Λ^0, associated with the jet in which the decay length measurement is made, enhanced the bottom baryon component in the reconstructed decay time distribution. This bottom baryon enhanced lifetime was measured as :

$$\tau_{b\Lambda^0} = (1.38 \pm 0.09\,(\text{stat}) \pm 0.06\,(\text{syst}))\,\text{ps},$$

where, the dominant contribution to the systematic error comes from uncertainties in the signal resolution function. An estimate of the proportion of the $\tau_{b\Lambda^0}$ sample due to a bottom baryon component was used to derive :

$$\tau_{\Lambda_b^0} = (1.10 \pm 0.19\,(\text{stat}) \pm 0.13\,(\text{syst}) \pm 0.05\,(\text{syst}))\,\text{ps}.$$

The first error is due to the statistical uncertainty on $\tau_{b\Lambda^0}$ and the second error is due to the systematic error on $\tau_{b\Lambda^0}$ and τ_b. The final error is due to the uncertainty on the contribution of bottom baryons to the $\tau_{b\Lambda^0}$ sample.

This method of measuring the bottom baryon lifetime is systematically different to other techniques that use baryon-lepton correlations ($\Lambda_c^+\ell$, $\Lambda^0\ell$ or $p\mu$).

"Before I came here I was confused about this subject. Having listened to your lecture I am still confused. But on a higher level."

Enrico Fermi

The research presented in this thesis was financed, for the most part, from funds administered on behalf of the British tax-payer by PPARC, the Particle Physics and Astronomy Research Council (formerly the Science and Engineering Research Council). Additional funding was very generously provided by the OPAL Collaboration. Attendance at various meetings, summer schools and conferences was made possible thanks to generous funding received from : The School of Physics and Space Research, The University of Birmingham; PPARC; The Scientific Affairs Division of the North Atlantic Treaty Organisation and The Euroconference Programme of the European Union.

This thesis was typeset on a Hewlett Packard workstation using LaTeX2$_\varepsilon$ and some of the functionality of the $\mathcal{AMS}$-LaTeX package. Most of the figures were produced using PAW, others came from scans and the OPAL event display software. Typeset text and figures were converted into a single PostScript file using dvips. The final document was previewed using Ghostview and subsequently printed on a Hewlett Packard LaserJet 5 Si printer. The entire PostScript file can be retrieved, in a format suitable for double-sided printing, from `http://www.ep.ph.bham.ac.uk/publications/`.

Acknowledgements

The work described in this thesis is the culmination of many years of education and training. Many people have guided me through these formative years and I owe you all a huge debt of thanks. Most of all, I want to thank my Mum and Dad for their continual love and unfailing support. It was (is !) always appreciated and I'll be eternally grateful. Thanks are also due to my brothers, Matthew and Andrew, even though I'm still not convinced they know what exactly I do !

A couple of people had a significant influence on my pre-PhD years. From my time at sixth form college I'd like to thank Simon Fitzjohn for introducing me to the way a physicist should think, even though he was supposed to be teaching me electronics. Peter Clarke nourished my interest in particle physics whilst at Brunel University, and his infectious enthusiasm was well appreciated.

My first 'thesis-type' thank-you goes to my supervisor, Pete Watkins. He has endured many (often foolish) questions from me over the years and always provided answers that gave valuable insight and motivation. His clear explanations of concepts that, at first look had left me puzzled, were always admired greatly.

I've also benefited significantly from the considerable expertise (not to mention patience) of my 'surrogate' supervisor, Martin Jimack. He has put up with a myriad of questions by e-mail, phone and fax, and always managed to provide valuable guidance and comments. This was particularly appreciated as he was (often) busy with his own top research.

I also thank Pete, Martin and John Wilson for their many incisive comments while proof reading draft versions of this thesis. Needless to say, I take total responsibility for any remaining errors.

I spent the majority of my funded research time based in Geneva. I thoroughly enjoyed the stimulating atmosphere of CERN and, in particular, the OPAL collaboration. The members of the best (!) LEP collaboration are listed in appendix B. Things in bât28 would have been far less organised if it wasn't for the OPAL secretariat, ably headed by Mette Stuwe. My move to Geneva was made considerably easier thanks to the help I received from Mary-Elizabeth Shewry and Sue Cannon. Frances Hall made my life at CERN easier by dealing efficiently with all the bureaucracy back in Birmingham.

Whilst at CERN, many people proved to be invaluable fountains of knowledge which they had no hesitation in generously sharing with me. In particular, I'd like to thank Bob Kowalewski, for many useful discussions and suggestions about my work; Nige Watson, for solving my computing problems while I peered over his shoulder trying to keep up; and Dave Charlton and Terry Wyatt, who were always available to discuss problems, despite being busy chaps themselves.

A non-negligible proportion of my time at CERN was spent dealing with the various gas, high-voltage and data-acquisition quirks of the muon endcap subdetector. Despite the omnipresent 'beep', I actually enjoyed every moment of it and appreciated the chance to go and get my hands dirty, rather than sitting in front of a computer all day. My task was made considerably easier thanks to the in-depth knowledge of Jim Homer, Pedja Jovanovic, Alain Renoux, Alasdair Smith, Pete Watkins, Alan Watson and John Wilson.

Although not described in this thesis, I spent about seven months with the OPAL silicon tungsten group, working on cross-talk phenomena in Amplex chips and minimum ionising particle tracking. Despite being an incredibly busy time, just after the detector had been installed, I benefited from Marcello Mannelli's expert guidance and David Wagner's patience in answering my endless stream of software enquiries.

Of course, life in Geneva was not all work - *mais non !* Thanks to Paul Bright-Thomas for 'teaching' me to ski and introducing me to the delights of the Hermance *au-pair* scene. John Holt tried to persuade me that *I* was really doing applied physics and that *he* could ski – failing on both counts. The Barker MC's 'Dr-sized' apartment was put to good use many times, which is more than can be said for his home-brew. Well removed from CERN, I have many *sympa et génial* memories of times spent with Amy Burkard, Patrick Ebbers, Linda Gréfjord, Caroline Olsson, Suzie Scales, Malin Thelander and the irrepressible 'butter-girls' - Anna Dahlén and Valerie Morgan. Cheers to Paul Phillips, Christine Beeston and Jason Ward for some excellent trips into (and up) the Alps - the latter two also provided amusing thesis-type encouragement via the soon to be extinct chat-machine (`CERNVM`). Dave Rigby was a mine of dubious information (and driving) and kept me admirably informed of the many goings-on in R-015 when I returned to Birmingham. Kwasi Ametewee,

Andrew Bell, James Bloomer, Jim Clayton, Ollie Cooke (thanks for the NN help), Jim Edwards, Clive Lewis and Warren Matthews could always be counted on for a coffee-break or a lift to the shops, errr ... pit.

On my return to Birmingham, the particle physics group seemed a rather alien environment, devoid of croissants and the other Swiss-type things I'd become accustomed to. However, I'd like to thank the members of the group for, in fact, making it an ideal environment to write-up in. In particular, I'd like to thank the head of group, John Dowell for the generous manner with which he ensured that resources were available. In the early days, all those years ago, I benefited greatly from the talents of Alan Watson, from whom I learnt much about the OPAL computing environment. Lawrie Lowe proved to be an invaluable system manager, who dealt efficiently with my (many) 'How do I ... ?' questions. I also thank John Wilson for many useful discussions and his general interest in my work. Late-night thesis sessions were made less spooky by Paul Newman's smoky ethereal presence. Lunch-times were quite literally *Spartabulous* thanks to the presence of Jean-Paul Davies, Brian Earl, Dave Evans, Steve Hillier, Keith Norman, Steve Oglesby, Dave Rees, Mark Venables and Ian Brawn, who also had the dubious pleasure of sharing an office with my frequent out-bursts of frustration whilst trying to get LaTeX to put the text there and not *there*.

On the home-front, I'm especially grateful to Jo Cook and Paul Eddington for letting me share their luxurious abode, even though they often stared with incredulity at my 'culinary' concoctions. The addition of Bill Calthorpe was most welcome, as he had a similar disregard for housework as myself (allegedly).

Last, but by no means least ... vill jag säga ett speciellt tack till Jenny Jansson för hennes kärlek och förståelse under de senaste två och lite till åren. Nu när min 'upptagenhet' med den här avhandlingen är över, hoppas jag att vi snart kommer att vara (geografiskt) mindre avlägsna från varandra.

25th March 1996,
Birmingham.

Contents

List of Figures

List of Tables

Chapter 1

The Standard Model of Particle Physics

The Standard Model is a remarkably successful set of theories that describe current understanding of the fundamental particles (quarks and leptons) and forces (gauge bosons) that make up the known Universe. The LEP accelerator (described in the next chapter) creates Z^0 gauge bosons from e^+e^- interactions. This process is described by the electroweak theory, the main features of which are summarised. One of the e^+e^- interaction points is instrumented with a large general purpose detector, called OPAL (also described in the next chapter). In this thesis, aspects of Z^0 decays to bottom quarks are studied with the OPAL detector. This reaction is observed as 'jets' of particles within the detector. The production of jets is described by quantum chromodynamics, the relevant features of which are discussed. The chapter ends with a brief review of the short-comings of the Standard Model and alternate theories that will be tested in future experiments.

1.1 Introduction

One of mankind's[a] greatest and most successful endeavours has been the continual desire to understand phenomena of the physical world. Science has evolved to encompass man's best theories explaining observations of such physical phenomena.

[a] This word is not gender specific !

The philosophy of science is straight-forward. A model proposed to describe some class of physical phenomena must describe accurately the phenomena as they occur and predict new phenomena or relationships not experienced previously. A model is retained as long as it fulfils these criteria but must be replaced or revised as soon as experimental observations disagree with the predictions of the model.

The material presented in this thesis concerns a branch of science that began approximately 50 years ago called particle physics. The aim of particle physics is to provide a description of the interactions of particles that are thought to be the smallest building blocks of Nature.

The first recorded suggestion that matter may consist of separate particles was made in the 5^{th} century, probably by Leucippus of Miletus. His pupil, Democritus, adopted the now commonly used word atom from the Greek *atomos* meaning indivisible. Dalton revived the word at the start of the 19^{th} century and provided a scientific basis for this simple Greek idea. Dalton suggested that the atom was the invisible particle that takes part in chemical reactions. This view was overturned in 1897 by Thomson's discovery that atoms could 'emit' smaller negatively charged particles, which are now called electrons. This discovery indicated that the atom had some internal structure, which was duly confirmed by Rutherford in 1911 with an alpha particle scattering experiment performed by Geiger and Marsden. With the structure of the atom unravelled, physicists turned their attention to investigating the properties of the zoo of particles that were being discovered experimentally in cosmic-ray and accelerator based experiments, and theoretically predicted by the rapidly developing quantum theory.

There are now more particles recorded than elements in the periodic table. Our understanding of the micro-world has improved by many orders of magnitude. In the 1920's energies of a few electron-volts probed distances of some 10^{-10} m; to date, energies of $\sim 100 \times 10^9$ electron-volts have been used to probe distances as small as 10^{-18} m.

All of the particle properties are predicted with very impressive accuracy by a collection of theories known as the Standard Model. The theories that form the Standard Model are tested in a number of laboratories around the world. The data presented in this thesis comes from the OPAL experiment which is based at the LEP

collider at CERN, the European Particle Physics Laboratory, situated near Geneva, in Switzerland.

To date, the Standard Model has withstood detailed probing from experiments at CERN and elsewhere. However, there are questions about fundamental processes in Nature that are not answered by the current set of experiments. Further experiments are planned to address such questions.

1.2 The Particle Spectrum

The Standard Model seeks to describe the interaction of matter-like fermions and force-like bosons which are believed to be the constituents of all matter in the Universe. Although four interactions have been identified in Nature (electromagnetic, weak, strong and gravitational), the Standard Model cannot yet provide a theoretical description of the gravitational interaction on the same footing as the other interactions due to problems with incorporating the quantum nature of space-time. However, the dimensions covered in particle physics experiments are so small that the effects of the gravitational interaction are insignificant compared to the other three interactions.

In the following sections the constituent fermionic and bosonic particles of the Standard Model will be discussed along with the gauge-invariant renormalisable field theories that describe the interactions between them.

1.2.1 Elementary Fermions

It is believed that the material world consists of point-like spin $\frac{1}{2}$ particles called fermions. The fermions are divided into two classes : the quarks (q) which experience the strong force and the leptons (ℓ) which do not[b].

There are six types (flavours) of quark divided into three 'up-type' quarks (up, charm and top[c] – u, c and t) and three 'down–type' quarks (down, strange and bottom – d, s and b). The 'up' and 'down' type quarks carry electrical charge $+\frac{2}{3}$ and $-\frac{1}{3}$ respectively. The six leptons comprise of three that are electrically charged

[b] Each fermion also has an anti-particle partner with opposite quantum numbers (except spin) but the same mass. The antiparticle is represented as $q \Rightarrow \bar{q}$ for quarks and $\ell^{\pm} \Rightarrow \ell^{\mp}$ for leptons.

[c] The top quark was discovered recently by the CDF and D0 collaborations at Fermilab [1]

(e, μ, τ) and three electrically neutral neutrinos (ν_e, ν_μ and ν_τ). The leptons can exist as free particles but free quarks have never been observed and they are predicted to form bound combinations called baryons (qqq) and mesons ($q\bar{q}$).

The fermions can be classified into sets of three generations thus :

$$\begin{pmatrix} e \\ \nu_e \end{pmatrix}_L \begin{pmatrix} \mu \\ \nu_\mu \end{pmatrix}_L \begin{pmatrix} \tau \\ \nu_\tau \end{pmatrix}_L , \tag{1.1}$$

$$\begin{pmatrix} u \\ d' \end{pmatrix}_L \begin{pmatrix} c \\ s' \end{pmatrix}_L \begin{pmatrix} t \\ b' \end{pmatrix}_L , \tag{1.2}$$

$$e_R \quad \mu_R \quad \tau_R , \tag{1.3}$$

$$\begin{pmatrix} u \\ d' \end{pmatrix}_R \begin{pmatrix} c \\ s' \end{pmatrix}_R \begin{pmatrix} t \\ b' \end{pmatrix}_R . \tag{1.4}$$

The subscripts R and L refer to right- and left-handed particles[d]. There are no right-handed neutrinos in the Standard Model. The lower members of the quark doublets are linear combinations of weak mass eigenstates. The combinations are described by the Kobayashi-Maskawa mixing matrix, which is discussed in more detail in section 1.6.

Each successive generation is simply a heavier version of the previous one[e], with the same basic quantum numbers, as shown in table 1.1 for the quantum numbers associated with the electromagnetic (electrical charge, Q) and weak (third component of weak isospin, I_3) interactions. Also shown is a quantity called weak hypercharge (Y) that will be discussed in more detail in section 1.4. Only matter consisting of the first (lightest) generation has been observed. The hierarchical structure formed by the generations is not explained in the Standard Model.

[d] A right- (left-) handed particle has its spin vector aligned parallel (anti-parallel) to its momentum vector.

[e] To date, there is insufficient experimental evidence to either confirm or reject the Standard Model prediction that neutrinos are massless.

Fermion	Q	I_3	Y
e_L	-1	$-\frac{1}{2}$	-1
ν_L	0	$+\frac{1}{2}$	-1
u_L	$+\frac{2}{3}$	$+\frac{1}{2}$	$+\frac{1}{3}$
d'_L	$-\frac{1}{3}$	$-\frac{1}{2}$	$-\frac{1}{3}$
e_R	-1	0	-2
u_R	$+\frac{2}{3}$	0	$+\frac{4}{3}$
d'_R	$-\frac{1}{3}$	0	$-\frac{2}{3}$

Table 1.1: The quantum numbers : Q (electric charge, in units of e), I_3 (the third component of weak isospin) and Y (weak hypercharge), for the first generation of fermions.

1.2.2 Gauge Bosons

The interactions between fermions are postulated to be mediated by the exchange of virtual[f] spin 1 gauge bosons. The electromagnetic force is mediated by the massless photon (γ), the weak interaction by the massive $W^{\pm}$ and Z^0 bosons and the strong interaction by an octet of massless gluons (g).

The electromagnetic interaction has an infinite range whereas the mass of the $W^{\pm}$ ($\sim$80 GeV/c^2) and the Z^0 ($\sim$90 GeV/c^2) bosons give the weak interaction an effective range of 10^{-18}m. The strong interaction has a typical range of $\leq 10^{-15}$m for reasons described in section 1.5.

The interaction of the gauge bosons with the fundamental fermions and the self-interaction of gauge bosons is described within the framework of the Standard Model using a set of relativistically invariant theories known as gauge field theories.

1.3 Gauge Field Theories

Field theories describe particles as quantised perturbations of physical fields. The propagation and interaction of these fields are described in terms of a Lagrangian density. A Lagrangian density can be used to describe any physical system and such

[f] The exchange process must take place over a time limited by the uncertainty principle in order to satisfy conservation laws.

methods have been exploited for many years in the field of classical physics [2]. The basic methodology of a gauge theory is to ensure that the Lagrangian[g] describing the interactions of particle wave functions remains invariant under certain symmetry transformations which reflect conservation laws in Nature.

In quantum field theory fermions are introduced as complex fields used to construct the Lagrangian, the quantum mechanical phase of these fields being unobservable and therefore arbitrary. Changes in phase (known historically as gauge transformations) should therefore leave the physical nature of the system unchanged. If the phase change is the same for all space-time points (a global transformation) then charge conservation is predicted. A local gauge transformation (where the phase changes are arbitrarily different for all space-time points) is even more fruitful. As one might expect, such a transformation does not leave the system invariant as desired. Invariance is recovered by introducing a further set of fields called gauge fields, which turn out to describe the gauge bosons [3], [4], [5].

Hence, by demanding invariance under local gauge transformations we have produced terms in the Lagrangian that correspond to the dynamics of the fermion interaction. No *a priori* reason has been discovered to explain why this should be so. The entire theory of interacting particles is determined by the way in which the fermion fields transform under the operations of a particular symmetry group.

The choice of symmetry group depends on the interaction to be described. The electromagnetic interaction (quantum electrodynamics or QED) uses the Lie group U(1) to provide the generators of the gauge transformations. To describe the weak interaction the non-Abelian SU(2) gauge group is used. The members of a non-Abelian gauge group (in this case 2×2 matrices) do not commute. The strong interaction is based on the non-Abelian SU(3) gauge group. The electromagnetic and weak gauge field theories have been unified into a single 'electroweak' model which is described in section 1.4. In order to construct successful field theories, that yield calculable results which can therefore be compared to experimental observations, a procedure called 'renormalisation' must be performed.

[g] 'Lagrangian density' is often shortened to 'Lagrangian'.

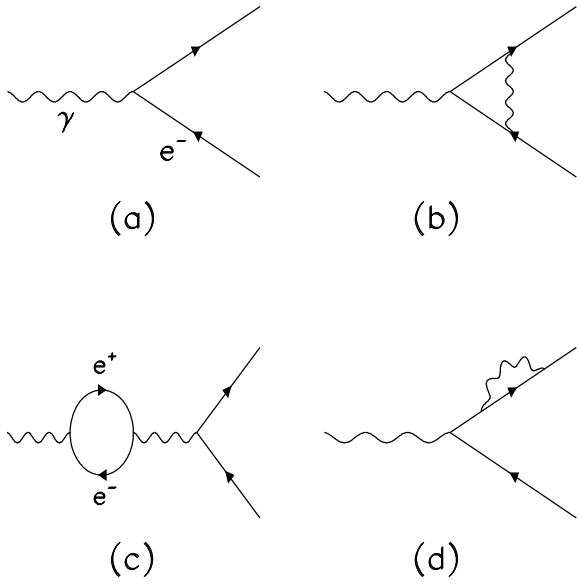

Figure 1.1: Feynman diagrams for the γ–e^- scattering process. Diagram (a) shows the basic zeroth order process and diagram (b) is a first order correction. Diagrams (c) and (d) show processes which cause the probability amplitude calculations for the scattering process to become divergent.

1.3.1 Renormalisation

Feynman developed the tools which allow the probability for a given process (say, γ–e^- scattering) to be calculated from a pictorial representation. A unique Feynman diagram is used to represent each term in the perturbation expansion for the scattering process and the total probability is the sum of all the possible Feynman diagrams that have incoming and outgoing lines representing the interacting particles.

For example, figure 1.1a shows the basic zeroth order vertex in a simple QED γ–e^- scattering process, and figure 1.1b shows a first order correction. The probabilities for both these processes can be calculated through well behaved convergent expressions and compared to results from precise scattering experiments. Figures 1.1c and 1.1d show cases where the production of an e^+e^- pair from a γ or the bremsstrahlung of a γ from an electron are totally internal to one line of the Feynman diagram. If such diagrams are included with the lowest order diagrams, the calculations become divergent and the net result becomes unphysical because the momenta of the internal lines are free and therefore must be integrated over an infinite range.

Renormalisation gets around these infinities by absorbing the troublesome dia-

grams into the original definition of the electron or photon lines. The charge of the electron associated with the lowest order QED interaction (figure 1.1a) is not the familiar charge measured in the laboratory (1.6×10^{-19}C), but rather, the bare charge. The measured charge is this bare charge including the higher order corrections. The theory is therefore renormalised by inputting an experimentally measured quantity. In the case of QED, this is the charge of the electron. One consequence of this is that the higher the energy of the probe used to investigate the structure of the electron, the larger the electron charge appears to be, since the outer layers of higher order 'shielding' are penetrated.

A quantity called α is used to denote the strength of the electromagnetic interaction[h]. This is not a constant but is said to 'run' (vary) with the measurement energy. For example, α ~0.0073 when evaluated in low energy experiments, whereas, α ~0.0078 when measured by experiments operating around the Z^0 resonance. The coupling constant for the strong interaction also 'runs' (but in an opposite sense), as described in section 1.5.

It has been shown that only locally gauge invariant non-Abelian theories are renormalisable. Therefore, all gauge theories in the Standard Model can be renormalised, making them useful theories. A more complete overview and rigorous mathematical proofs are given in [6].

1.4 The Electroweak Theory

1.4.1 Overview

The electroweak theory is one of the most remarkable parts of the Standard Model of particle physics. It is worth taking a brief historical view of the theory and its subsequent confirmation by experiment.

The physical theory behind electromagnetic forces were put into a classical framework by Maxwell over one hundred years ago. In the 1940's Tomonaga, Feynman and Schwinger perfected the *quantum* theory of electrodynamics (QED) [7]. Quantum electrodynamics is the most successful theory in physics, having been

[h] $\alpha=\frac{e^2}{4\pi}$, where e is the unit electric charge.

tested to the limit of experimental uncertainty [8].

The first theory of weak interactions was devised by Fermi in 1933 to explain β decay. He hypothesised that the reaction, $n \rightarrow p^+ + e^- + \bar{\nu}_e$, involved a direct four-particle coupling of magnitude G_F. This theory predicted low energy[i] phenomena well, but had unacceptable high energy behaviour which predicted that the cross-sections for neutrino–electron scattering would rise linearly with the energy of the incoming neutrino; this cannot, of course, be true for arbitrarily high energies.

To get around this problem the weak interaction was described in terms of massive charged W-bosons mediating the weak force. This heralded the first steps towards electroweak unification, as both the electromagnetic and weak forces now involved particle-exchange processes.

Neutral current interactions were first hypothesised by Bludman in 1958 [9]. During the 1950's and 1960's a great deal of work was carried out to try and identify neutral currents by searching for the decay $K^0 \rightarrow \mu^+\mu^-$. No events were found in the $\sim$100 million kaon decays that were investigated. It was not known at the time that the process was strongly suppressed due to an exact cancellation in the cross-section due to the presence of charm quarks. There was no direct experimental evidence for charm quarks until the 'November Revolution' of 1974 [10].

Both charged and neutral current interactions were predicted by the unification of the weak and electromagnetic interactions, published by Glashow in 1961. In 1967 Weinberg and Salam independently formulated Glashow's model in terms of a spontaneously broken gauge theory, which invoked the Higgs mechanism to endow the gauge bosons with mass. The theory gained respectability in 1971 when t'Hooft demonstrated that the theory was renormalisable and therefore could be used to calculate physical quantities.

Charged current interactions had been experimentally identified for many years (for instance in β, μ-decay), but there was no indication of neutral current interactions until 1973 when the reactions $\bar{\nu}_\mu + e^- \rightarrow \bar{\nu}_\mu + e^-$ and $\bar{\nu}_\mu$+nucleus $\rightarrow \bar{\nu}_\mu$+hadrons were detected in the Gargamelle bubble chamber [11]. The final outstanding confirmation of the theory came in 1983 at CERN when the $W^\pm$ and Z^0 bosons were

[i] Low energy in this context means that the experimental energy is much smaller than $\mathcal{O}(100)\mathrm{GeV}/c^2$ – the mass of the $W^\pm, Z^0$ bosons.

produced in proton-proton collisions, with the masses predicted by the theory [12].

1.4.2 Formalism

The electroweak theory of Glashow, Salam and Weinberg (the GSW theory) [13] unifies the description of the electromagnetic and weak interactions by imposing the principle of local gauge invariance on the group $SU(2)_L \times U(1)_Y$. Only left-handed fermions participate in the charged current weak interaction, as denoted by the subscript 'L' on $SU(2)_L$[j]. This automatically incorporates the maximally parity violating nature of the weak interaction [14]. The subscript 'Y' on $U(1)_Y$ denotes weak hypercharge, which is needed because the members of the $SU(2)_L$ weak doublet must take the same quantum number under the U(1) symmetry. Electric charge cannot be used as the electron and its neutrino obviously cannot be assigned the same electric charge quantum number, so weak hypercharge is used. Weak hypercharge (Y) is defined in terms of the electric charge (Q) and the third component of weak isospin (I_3) in the Gell-Mann–Nishijima formula, as :

$$Y = 2\,(Q - I_3). \tag{1.5}$$

Since Y and I_3 are conserved quantities in the $SU(2)_L \times U(1)_Y$ scheme, charge conservation is implicit.

To ensure that the fermionic Lagrangian remains invariant under $SU(2)_L \times U(1)_Y$, four new fields are required : a triplet of fields W_i^μ coupling to weak isospin and a neutral field B^μ, coupling to weak hypercharge. The physical $W^\pm$ gauge bosons, which mediate the charged current interaction within weak doublets, emerge if linear orthogonal combinations of W_1^μ and W_2^μ are taken :

$$W^{\pm\mu} = \frac{1}{\sqrt{2}}\,(W_1^\mu \mp W_2^\mu)\,. \tag{1.6}$$

The gauge fields of the electromagnetic (A^μ) and weak neutral current (Z^μ) interactions still need to be identified from this formalism. The unused W_3^μ field only couples to left-handed particles and since the Z^0 couples to both left- and

[j]The $SU(2)_L$ group is non-Abelian and therefore allows gauge bosons to interact directly with each-other. This will be tested by looking for triple boson vertices during the forthcoming LEP programme, when the beam energies will be appropriately increased so that W^+W^- pairs can be produced directly.

right-handed particles, a further step is needed[k]. If the following linear orthogonal combinations of the W_3^μ and B^μ fields are taken :

$$Z = W_3^\mu \cos\theta_w - B^\mu \sin\theta_w, \tag{1.7}$$

$$A = W_3^\mu \sin\theta_w + B^\mu \cos\theta_w, \tag{1.8}$$

then the physical fields describing the photon (A) and the Z^0 boson are manifest. The weak mixing angle (θ_w) gives the relative strength between the weak and electromagnetic interactions. The weak mixing angle is not predicted by the Standard Model and must be determined experimentally.

1.4.3 Spontaneous Symmetry Breaking

The GSW theory is formulated in terms of massless bosons in clear contradiction with theoretical predictions (at first) and experimental observations (later) that the weak bosons are extremely massive – $\mathcal{O}(100)$ GeV/c^2. Adding explicit bosonic mass terms to the electroweak Lagrangian destroys the gauge invariance and the theory as a whole loses its predictive power.

The proposed solution is to introduce a complex scalar Higgs field of non-zero vacuum expectation value (VEV) with which the gauge fields of the GSW theory can interact. This mechanism is called spontaneous symmetry breaking [15]. The Higgs field must be constructed respecting the symmetries of the gauge theory to allow renormalisation and produce terms in the electroweak Lagrangian that are quadratic in nature and therefore interpreted as mass terms. The magnitude of the mass depends on the VEV of the Higgs field.

An isospin doublet of four complex scalar Higgs fields is needed to provide Lagrangian mass terms for the bosons of $SU(2)_L$. Combining three of the Higgs fields with the weak bosons results in the $W^\pm$ and Z^0 particles acquiring mass leaving one scalar Higgs field remaining. This field is thought to manifest itself as a massive scalar Higgs boson (H^0). Although the Higgs model provides a mechanism to endow the gauge bosons with mass it does not explicitly predict these masses or the mass of the Higgs boson itself. However, the masses of the electroweak gauge bosons

[k] Equation 1.5 also indicates that the electromagnetic field is related to both W_3^μ and B^μ.

can be predicted with knowledge of the weak mixing angle, using the following relationships :

$$m_{W^{\pm}} = (38.5/\sin\theta_W)\,\mathrm{GeV}/c^2, \quad m_{Z^0} = (m_{W^{\pm}}/\cos\theta_W)\,\mathrm{GeV}/c^2. \tag{1.9}$$

The existence of the Higgs boson has not yet been verified experimentally, and so it remains an untested part of the Standard Model. The current experimental mass limit from the LEP experiments is $m_{H^0} > 65.2$ GeV/c^2 at 95% confidence level [16]. One of the main goals of the next generation of particle physics experiments like ATLAS [17] and CMS [18] operating in the multi-TeV energy region will be to test the Higgs hypothesis. The Higgs boson is expected to be found at such energies, if it exists. Corrections[l] to the lowest order calculations describing electroweak observables computed within the Standard Model are logarithmically sensitive to the Higgs boson mass. Recent fits to all available electroweak data [19] combined with the top quark mass from the CDF and D0 experiments and the direct upper bound from the LEP experiments yield a χ^2 minimum for $m_{H^0} \sim 90$ GeV/c^2, but the minimum is shallow and the upper limit constraint is not very stringent at ≤ 500 GeV/c^2 for a 95% confidence level.

1.5 Quantum Chromodynamics

Quantum chromodynamics (QCD) is a gauge invariant field theory based on the $SU(3)_c$ 'colour' group structure, proposed by Fritzsch, Leutwyler and Gell-Mann in 1973 [20]. It describes the strong interaction that binds quarks (q) into composite particles called baryons (qqq) and mesons $(q\bar{q})^m$. The strong force is mediated by gluons (g). A rich spectrum of states not exclusively containing quarks is also predicted by QCD. These states are known generically as glueballs if they are composed purely of gluons (ggg) and hybrids if they contain gluons and quarks ($q\bar{q}g$). There is experimental evidence for such states [21] but the quark–gluon composition is not fully understood.

Gluons couple to the colour charge of quarks and other gluons. Colour charge

[l] Figure 1.1 shows examples of QED corrections.
[m] The top quark is thought to decay too rapidly to produce bound states.

can be thought of as analogous to the electrical charge in quantum electrodynamics. Three types of colour are postulated: red ($\overline{\text{red}}$), green ($\overline{\text{green}}$) and blue ($\overline{\text{blue}}$). The number of colours has been measured at electron-positron colliders where the cross-section for $e^+e^- \rightarrow q\bar{q}$ is three times greater than expected from calculations which contain no colour. There are eight physical gluons needed to maintain local gauge invariance under $SU(3)_c$, each of the gluons carries a colour-anticolour combination, while quarks carry a single colour.

It is postulated that only colourless particles can be directly observed and so single quarks cannot exist alone. This is called colour confinement and arises as a direct consequence of the asymptotic freedom associated with the strength of the strong force increasing with quark separation. Isolated quarks or composite quark states of non-zero net colour have never been observed.

The predictive power of electroweak calculations is very impressive. Such a strong claim cannot be made of QCD calculations due to the magnitude of the strong coupling constant, $\alpha_s(90\text{ GeV})\sim0.12$, compared to the magnitude of the electromagnetic coupling constant $\alpha(90\text{ GeV})\sim0.008$. The coupling constant enters into probability amplitude calculations for a given process to the power of the number of boson-fermion vertices. The magnitude of the strong coupling constant increases with decreasing energy ($\alpha_s(10\text{ GeV})\sim0.19$). Workable perturbative calculations in QCD are therefore restricted to applications involving small distances (or large momentum transfers), where α_s is relatively small and the quarks can be considered as essentially non-interacting states[n].

For example, in figure 1.2 the e^+e^- pair annihilates into an excited photon or Z^0 which subsequently decays into a primary $q\bar{q}$ pair. Electroweak theory predicts the probability of such decays with a relative accuracy of $\sim2\%$. These primary quarks radiate gluons which can convert into $q\bar{q}$ pairs or radiate further gluons causing a $q\bar{q}$ shower. In principle, perturbative QCD should be able to provide a fully quantitative description of this process, although to date most calculations are only carried out to second order in α_s. The quarks dress themselves as hadrons by exciting the vacuum to provide further $q\bar{q}$ pairs and are observed as physical jets of baryons and mesons.

[n] A free parameter in QCD, Λ_{QCD}, sets the scale at which α_s becomes 'strong'. This denotes the boundary between quasi-free quarks and gluons and bound hadronic states. It is determined by experiment to lie in the range $0.1 \rightarrow 0.5\text{ GeV}/c^2$ [3].

Various empirical models [22] exist to describe this process, since at energy scales typical of hadronic processes α_s becomes large enough ($\alpha_s \sim 1$) that perturbation theory can no longer be applied, and calculations become impractical. The models used in this thesis are described in section 3.3.3.

1.6 The Kobayashi–Maskawa Mixing Matrix

In 1963, Cabibbo postulated that d and s quarks could mix, in order to explain experimental observations of strangeness changing currents [23]. Seven years later, the GIM (Glashow, Iliopoulus and Maiani) mechanism was introduced and predicted an extra quark, charm, to be the isospin partner of the strange quark. The GIM mechanism allowed the lack of flavour changing neutral currents in kaon decays to be explained [24]. In 1973 Kobayashi and Maskawa realised that adding a third quark generation would allow CP violation to be accommodated in the Standard Model [25]. The violation of a combined charge conjugation (C) and parity (P) symmetry was observed for the weak interaction in 1964, in the decay of neutral kaons [26].

Kobayashi and Maskawa (KM) proposed that a set of weak eigenstates (d', s', b') should be invoked as a linear mix of the flavour eigenstates (d, s, b) :

$$\begin{pmatrix} d' \\ s' \\ b' \end{pmatrix} = V_{KM} \begin{pmatrix} d \\ s \\ b \end{pmatrix}, \tag{1.10}$$

where the unitary rotation matrix is given by :

$$V_{KM} = \begin{pmatrix} |V_{ud}| & |V_{us}| & |V_{ub}| \\ |V_{cd}| & |V_{cs}| & |V_{cb}| \\ |V_{td}| & |V_{ts}| & |V_{tb}| \end{pmatrix}. \tag{1.11}$$

It is only by convention that quarks with electric charge $+\frac{2}{3}$ are unmixed. Mixing between lepton doublets has not been observed. All of this was postulated by Kobayashi and Maskawa when only three quarks had been discovered ! The KM matrix can be parameterised in terms of three real angles and one complex phase that cannot be removed by redefining the matrix elements; this phase generates

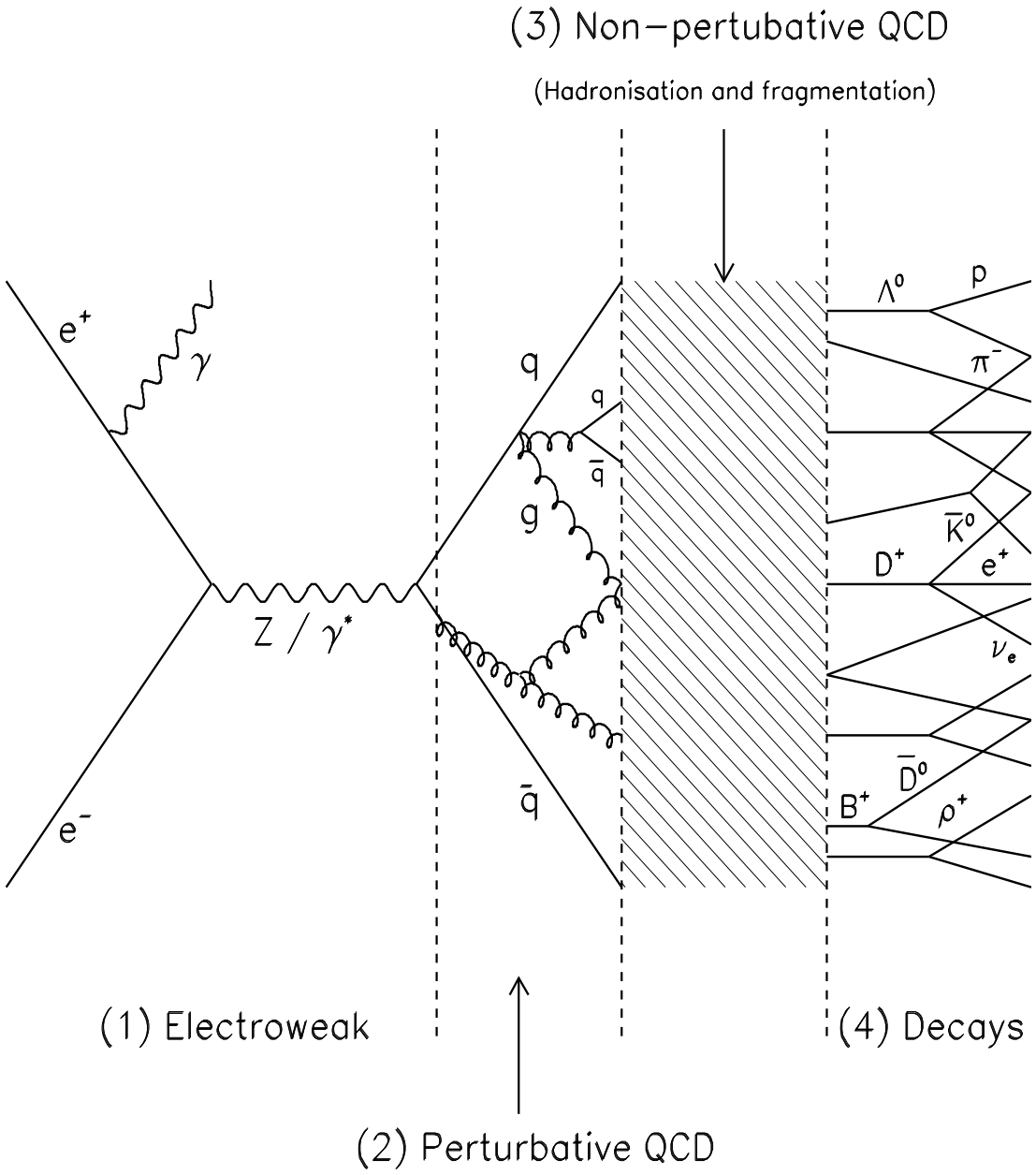

Figure 1.2: A schematic representation of the creation of a multihadronic final state from an e^+e^- interaction at a centre of mass energy around the mass of the Z^0 gauge boson. Details of models used to describe the fragmentation stage are discussed in section 3.3.3.

CP violation. The matrix elements are not predicted by the Standard Model but they can be measured and constrained experimentally. All the matrix elements can, in principle, be determined from the weak decays of the relevant quarks or from deep inelastic neutrino scattering [28]. The matrix elements $|V_{tq}|$ can be determined from unitarity bounds. The measured magnitudes of the matrix elements are currently [28] :

$$\begin{pmatrix} |V_{ud}| & |V_{us}| & |V_{ub}| \\ |V_{cd}| & |V_{cs}| & |V_{cb}| \\ |V_{td}| & |V_{ts}| & |V_{tb}| \end{pmatrix} = \begin{pmatrix} 0.9747 \rightarrow 0.9759 & 0.218 \rightarrow 0.224 & 0.002 \rightarrow 0.005 \\ 0.218 \rightarrow 0.224 & 0.9738 \rightarrow 0.9752 & 0.032 \rightarrow 0.048 \\ 0.004 \rightarrow 0.015 & 0.030 \rightarrow 0.048 & 0.9988 \rightarrow 0.9995 \end{pmatrix},$$

where the range quoted is for the 90% confidence level. These values show the dominant quark decay scheme is $t \rightarrow b \rightarrow c \rightarrow s$.

The striking parameterisation of Wolfenstein [29] (ignoring CP violation) is :

$$V_{KM} = \begin{pmatrix} 1 & \lambda & \lambda^3 \\ -\lambda & 1 & \lambda^2 \\ -\lambda^3 & -\lambda^2 & 1 \end{pmatrix}, \tag{1.12}$$

where, $\lambda \sim \sin\theta_c \sim 0.22$ and θ_c is the Cabibbo angle describing the mixing between d and s quarks :

$$d' = d\cos\theta_c + s\sin\theta_c. \tag{1.13}$$

The striking pattern of these KM amplitudes discovered by Wolfenstein is perhaps indicative of a hierarchy of inter-generational quark couplings and could signal symmetries beyond the Standard Model.

1.7 Beyond the Standard Model

Ignoring the effects of the gravitational interaction, particle physics has been reduced to two sets of particles (quarks and leptons) and two forces (electroweak and strong). To date, the Standard Model that describes the electroweak and QCD theories has withstood detailed probing from a wealth of experimental studies. The most recent results are reviewed in [30] and [31]. An intrinsic shortcoming of the Standard Model is that there are 19 fundamental free parameters that must be determined by experiment. These 19 parameters are shown in table 1.2.

Free Parameter	Description
α	Fine structure constant
G_F	Fermi constant
m_{Z^0}	Mass of the Z^0 boson
α_s	Strong coupling constant
Λ_{QCD}	QCD mass scale
m_q	Six quark masses
m_ℓ	Three lepton masses
m_H	Higgs boson mass
V_{KM}	Quark mixing matrix, 3 angles and a complex phase

Table 1.2: The fundamental parameters of the Standard Model.

It is postulated that the Standard Model $SU(3)_c \times SU(2)_L \times U(1)_Y$ group structure may be a subset of a larger gauge group that predicts the values of these free parameters naturally. The forces we observe are then simply just the low energy manifestation of a single grand unified force. Many schemes to produce a grand unified theory of Nature have been proposed.

The smallest candidate gauge group is SU(5) [32], but this puts quarks and leptons into the same multiplets and thus suggests the existence of quark-lepton currents and therefore the possibility of proton decay. The predicted proton lifetime is $\sim 10^{30}$ years, but this disagrees with the current experimental value of $> 10^{32}$ years [28].

Another fashionable proposal to predict physics beyond the Standard Model is supersymmetry, which relates particles of different spin (fermions and bosons) and predicts a supersymmetric partner for every Standard Model particle. Supersymmetry is particularly attractive as it naturally incorporates the general theory of relativity and provides an explanation for the huge difference between the electroweak ($\sim 10^2$ GeV/c^2) and grand unification ($\sim 10^{15}$ GeV/c^2) mass scales, where the strong, electroweak and gravitational interactions are unified. The Higgs boson mass is also controlled without fine tuning parameters, which is a problem with the Higgs extension to the Standard Model.

Chapter 2

The OPAL Detector at LEP

The LEP accelerator collides electrons and positrons at a centre of mass energy suitable to create Z^0 bosons. The analyses presented in this thesis use candidate $e^+e^- \rightarrow Z^0 \rightarrow b\bar{b}$ events recorded by the OPAL detector. Firstly, the LEP accelerator and techniques to measure the e^+e^- beam energies are described. Next, the component parts of the OPAL detector are examined. The central tracking detectors and (to a lesser extent) the electromagnetic calorimeter are particularly important for the analyses described in later chapters. Finally, the mechanism used to convert the raw subdetector signals into data suitable for analysis is described.

2.1 The LEP Collider

In 1983 the UA1 and UA2 collaborations at CERN announced the discovery of the $W^{\pm}$ and Z^0 bosons [12]. Although predicted by theory the discovery of these particles caused great excitement amongst the particle physics community. It was subsequently proposed that an e^+e^- storage ring should be built at CERN to allow the properties of the Z^0 to be investigated, leading eventually to a study of the $W^{\pm}$. This machine (the largest in the world) is called LEP (Large Electron Positron collider) [33]. Construction started in 1983 and took 5 years to complete. The first Z^0 event was seen on 13^{th} August 1989 by the OPAL collaboration.

LEP provides an ideal environment for the study of the Z^0. Electron–positron collisions take place at accurately measured centre of mass energies close to the

mass of the Z^0 and provide clean final states. The LEP machine energy can also be scanned across the Z^0 resonance to allow the mass, decay widths and fermionic couplings to be measured. Towards the end of 1995 LEP entered a new phase. The beam energies were increased and eventually the centre of mass energy will be sufficient to study $Z^0 \rightarrow W^+W^-$ and $\gamma \rightarrow W^+W^-$ vertices [34].

The location of the LEP accelerator complex is shown in figure 2.1.

2.1.1 Pre-LEP Acceleration

The LEP Injector Linac (LIL) forms the first part of the accelerator complex shown in figure 2.2. It consists of two LINAC's (LINear ACcelerator) about 100 m long in total. A thermionic source (thermal emission from a heated filament followed by electrostatic extraction) provides electrons that are accelerated by the first LINAC to 200 MeV and directed towards a tungsten target, where (through pair production from bremsstrahlung photons) positrons are produced. The positrons are separated using a magnet and the resulting positrons and electrons are further accelerated to 600 MeV in the second LINAC from where they are directed into the Electron Positron Accumulator (EPA). This machine is 126 m in circumference and stores the particles until there are sufficient to be injected into the 200 m circumference Proton Synchrotron (PS), where they are accelerated to 3.5 GeV.

The final acceleration to 22 GeV prior to injection into LEP is provided by the 2.2 km circumference Super Proton Synchrotron (SPS). Beams are extracted from the SPS and injected into LEP. This use of the SPS complex takes advantage of the inherent dead-time in the pulsed proton cycle and does not interfere with the fixed target program also fed by the SPS.

2.1.2 The LEP Accelerator

The LEP accelerator is 26.7 km in circumference and lies beneath the Pays de Gex at a depth ranging from 51 m to 143 m[a], giving it an overall tilt with respect to the horizontal of 0.8°. Electrons and positrons traverse the ring in opposite directions and collide at eight points, four of which are instrumented with large general purpose

[a] To ensure the accelerator tunnel lies within stable rock strata.

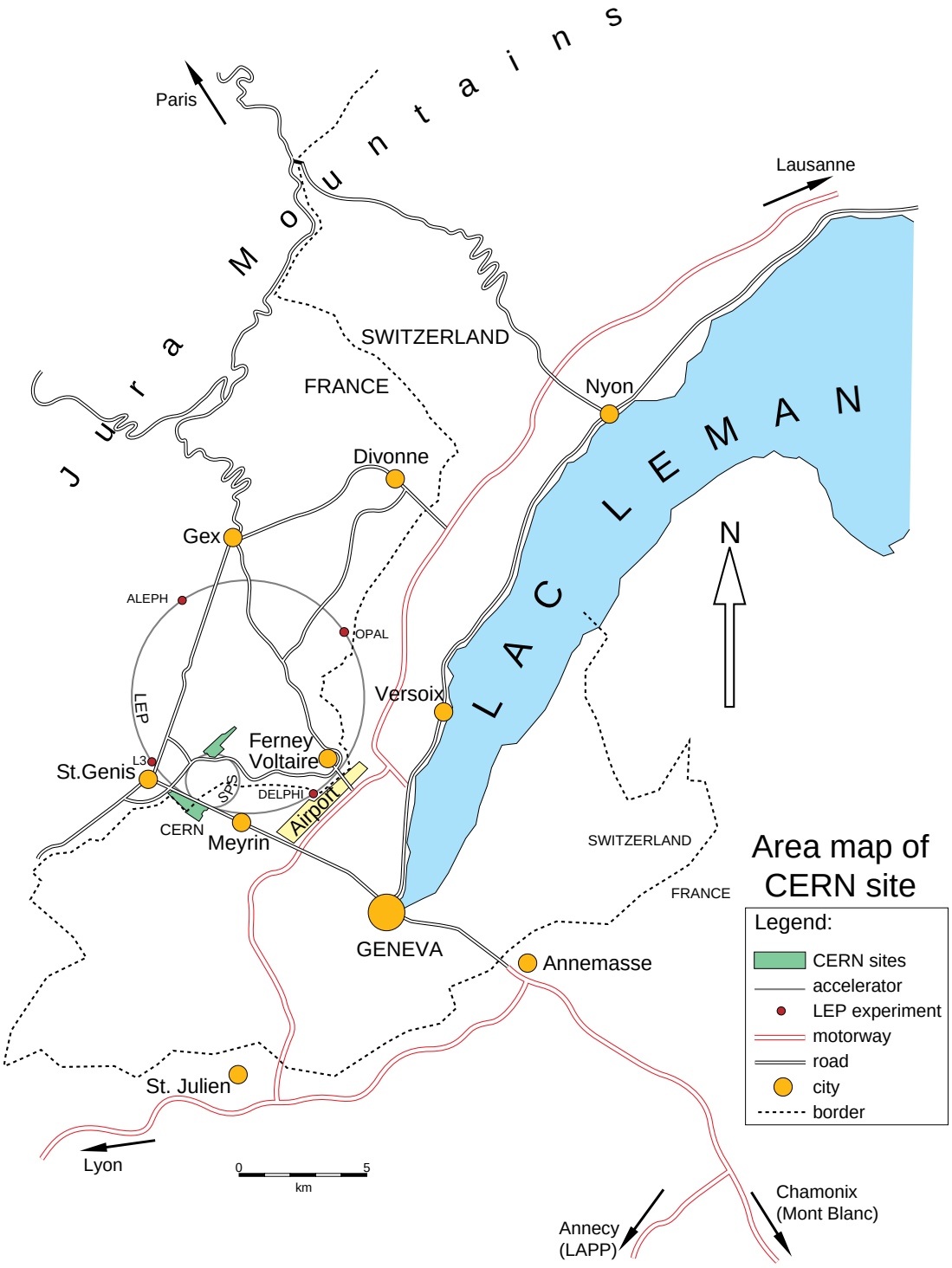

Figure 2.1: A map showing the position of the Large Electron Positron Collider (LEP) within the Pays de Gex. The four LEP experiments : ALEPH, DELPHI, L3 and OPAL are shown along with the Super Proton Synchrotron (SPS) that pre-accelerates electrons and positrons prior to injection into LEP.

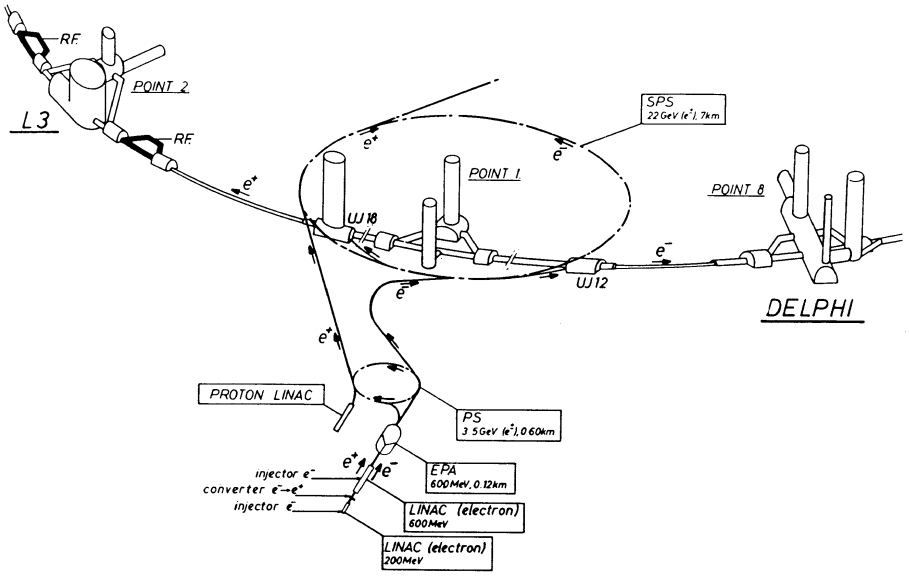

Figure 2.2: A schematic representation of the LEP injector complex. A linear accelerator (LINAC) accelerates electrons to an energy of 200 MeV and a tungsten target is used to produce positrons and electrons (through a bremsstrahlung and pair-production process) which are accelerated to 600 MeV by a second LINAC. The Electron Positron Accumulator (EPA) stores the beams prior to further acceleration by the Proton Synchrotron (PS) and Super Proton Synchrotron (SPS) and subsequent injection, at 20 GeV per beam, into LEP.

detectors. These detectors are called ALEPH [36], DELPHI [37], OPAL [35] and L3 [38]. Two of the other points used to be instrumented with very much smaller experiments called MODAL (a search for highly ionising particles) and BREMS (a luminosity monitor using bremsstrahlung photons) [39], but these experiments are now completed.

The electron and positron beams travel in a pipe pumped out to maintain a vacuum of better than 10^{-11} torr. The vacuum is maintained using getter strip pumping and is needed to reduce the probability of the beams colliding with gas molecules. The LEP ring is octagonal with rounded corners, to reduce beam energy losses due to synchrotron radiation[b]. The straight sections flank each side of the detectors for a distance of $\sim$150 m. This ensures protection from synchrotron radiation and provides a station for the acceleration cavities.

Synchrotron radiation losses total around 128 MeV per beam per turn of LEP. Therefore, even when the beams have been 'ramped' up to full energy their energy

[b]Synchrotron radiation losses scale as the fourth power of the beam energy and scale inversely with the accelerator radius.

must be continuously boosted. This boost is provided by 128 copper radio-frequency (RF) cavities powered by 16 MW klystrons. Thirty-two of these cavities are located on either side of the OPAL and L3 experiments in the straight tunnel sections. In order to reduce losses, the copper cavities are coupled to low loss spherical storage cavities into which the RF power is directed when it is not needed for acceleration purposes. For the future operation of LEP at up to 100 GeV per beam, niobium coated superconducting cavities have been installed which have much smaller losses than their copper counterparts. This is essential because synchrotron losses will increase by a factor of over twenty at this new energy.

To keep the beams on a curved trajectory around the machine over three thousand steel laminate/concrete-core dipole bending magnets are used, each with a field strength of approximately 0.1 T. Over two thousand focusing magnets (quad-, sex- and octopoles) ensure the beam profile is optimised for high luminosity. About 75% of LEP's circumference is filled with magnets. The precision with which all these components must be aligned is enormous; a short range relative precision of less than 0.1 mm on the scale of many kilometres [40].

LEP operations began using counter–rotating beams of 4 bunches of electrons and positrons. Since 1992 each beam has contained 8 bunches. Each bunch[c] is $(150 \times 10 \times 10\,000)$ μm and contains $\sim 2 \times 10^{11}$ particles. A bunch traverses LEP approximately every 89 μs giving an approximate luminous volume of $(300 \times 60 \times 2000)$ μm at the interaction point every 11 μs. The relative energy spread in a bunch is $\sim$0.1%. The bunches are kept apart outside the instrumented interaction points by electrostatic separators. Typically, it takes 30 minutes to 'fill' LEP, 30 minutes to 'ramp' the beams up to full energy and 'squeeze' to produce good luminosity and 15 minutes to correct orbits, cure backgrounds and produce stable colliding beams. Once set-up with high current beams the luminosity is dominated by beam-beam effects; so careful tuning of the machine parameters can result in $\sim$15 hours of data taking by the experiments at luminosities of $\sim 1.8 \times 10^{31}$ cm^{-2} s^{-1}. At the Z^0 pole the hadronic and visible leptonic cross-sections are 30 nb and 4.5 nb respectively, giving $\sim$15 000 hadronic and $\sim$2250 visible leptonic events a day.

[c]Measured (σ_x, σ_y, σ_y), where : σ_x is measured along the bending radius, σ_y is measured perpendicular to the bending plane and σ_z is measured along the beam direction.

2.1.3 Measuring the Energy of the LEP Beams

To extract exact parameters of the Z^0, the energy of the LEP beams must be precisely known. Until 1991, the beam energy (E_b) was measured using the integrated flux in one octant of LEP calibrated with 20 GeV protons [41]. This method was not compatible with normal physics running and, moreover, the inherent error ($\Delta E_b/E_b \sim 10^{-4}$) proved to be the dominant error ($\pm$ 5.2 MeV/c^2) on the extraction of m_{Z^0}.

After 1991 resonant spin depolarisation was used to determine the beam energy. When an electron (positron) circulates in the vertical dipole bending field of LEP it becomes spin polarised ($10 \rightarrow 20\%$, transversely) due to the emission of synchrotron radiation. This is called the Sokolov-Ternov effect [42]. In the classical picture the spin vector can be considered to precess about the bending field lines at a frequency ν_p. At a point on the LEP ring an oscillating magnetic field of frequency ν_a is applied in the horizontal direction, perpendicular to the beam direction. When $\nu_p = \nu_a$ resonant depolarisation occurs and the electron spin is flipped [43]. Since the spin depolarisation frequency is proportional to the beam energy and can be measured very accurately, the error on the beam energy can be reduced to around 1 MeV (corresponding to an error of $\sim$2 MeV/c^2 on m_{Z^0}).

A beautiful example of the power and accuracy of this technique is the 'LEP Tide Experiment' [44]. Small changes in the beam energy due to the movement of the Earth's crust (and therefore of LEP too) resulting from the tidal action of the moon and sun can be observed. The beam orbits are defined in space by the RF timing. The action of the moon–Earth interaction causes the LEP magnets to move relative to the beams. The movement of the dipolar bending magnets has no effect on the beams as the magnetic field across the magnet aperture is uniform. The focusing quad- and sextupoles, however, have a non-uniform field across the magnet aperture and so an electron (positron) bunch will experience a different average magnetic field during one cycle around LEP, thus changing the beam energy[d].

A 1 mm change in the length of LEP over the 27 km circumference will give rise to a beam energy change of $\sim$4 MeV. A periodic variation in the beam energy consistent with tidal action can be seen in fig. 2.3. The minima are of different

[d] This is shown in equation 2.1, where the radius, r, is fixed.

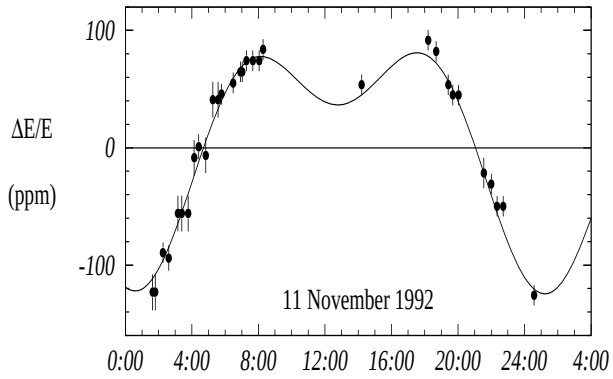

Figure 2.3: The points show the relative change in the LEP beam energy, measured using a resonant depolarisation technique, over approximately 24 hours. There is good agreement with the calculated effects from the Earth's tides, as shown by the curve.

depths due to the inclination of the Earth's axis relative to the orbital plane.

2.2 The OPAL Detector

The OPAL detector [35] is a multi-purpose apparatus with efficient detection and accurate momentum and calorimetric measurements for final states produced from Z^0 decay. Almost the entire solid angle is covered by a series of concentric cylindrical ('barrel') and endcap subdetectors enclosing the e^+e^- interaction point. The design is based mainly on technology that had proven itself with existing detectors, particularly the JADE detector at PETRA. Figure 2.4 shows the overall layout of the OPAL detector.

The trajectories of charged particles are measured by the central tracking detector which comprises of the vertex chambers, the jet chamber and the z-chambers. A solenoid produces an axial magnetic field within the central tracking detector and charge and momentum determination are therefore possible through the relationship

$$p_\perp = 0.3\,B\,r, \tag{2.1}$$

where, $p_\perp$ is the momentum component in the plane perpendicular to the magnetic field lines, B is the magnetic field strength in Tesla and r is the radius of track curvature in metres. Particle identification is achieved by measuring the ionisation loss of charged particles passing through the gaseous volume of the jet chamber. Tracks can be reconstructed with sufficient accuracy to allow secondary vertices

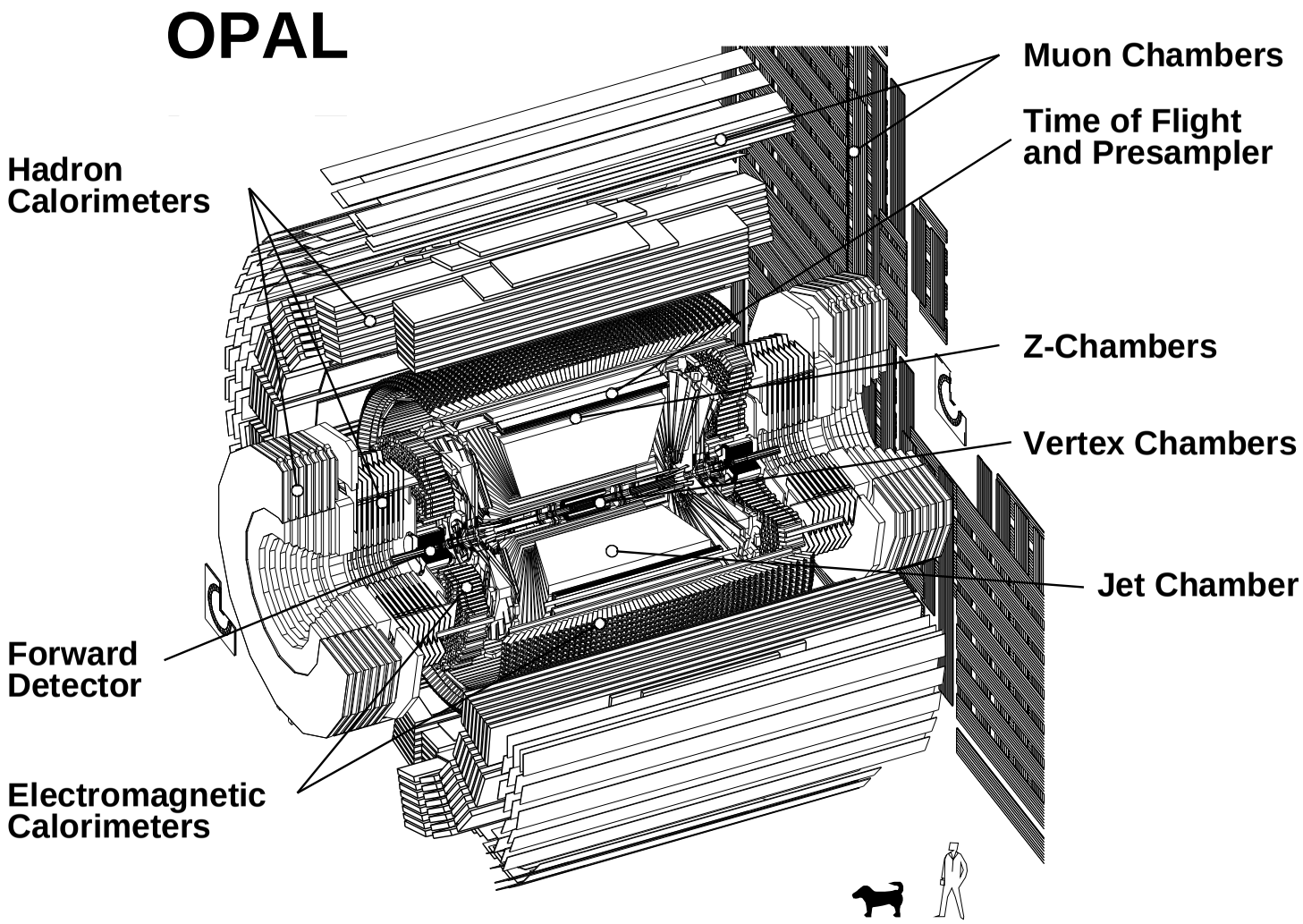

Figure 2.4: The OPAL detector, with the major subdetectors labelled.

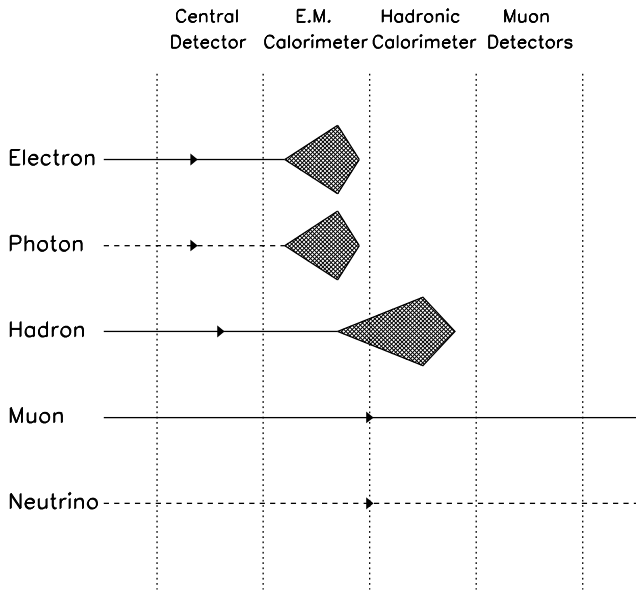

Figure 2.5: A schematic diagram to illustrate particle identification within the OPAL detector. The solid lines indicate reconstructed tracks and dashed lines show the path of a particle. The shaded areas indicate energy deposits. Note that muons leave small energy deposits in the electromagnetic and hadronic calorimeters, but these are not shown.

from short lived particles to be resolved. The addition of the silicon microvertex detector in 1991 greatly enhanced this capability.

The time-of-flight system surrounds the solenoid and helps in the rejection of cosmic rays and other backgrounds. Electron and photon energies are measured by the electromagnetic calorimeter – an array of lead-glass blocks divided into a barrel and two endcap sections. The magnet return yolk surrounds the electromagnetic calorimeter and is instrumented to form a sampling hadron calorimeter. Four layers of muon chambers form the final layer of the OPAL detector and allow particles not absorbed by the previous layers of the detector to be detected.

The luminosity of the LEP beams is measured by counting Bhabha scattering events ($e^+e^- \rightarrow e^+e^-$) in the forward region using a lead-scintillator calorimeter, and more recently, a silicon tungsten calorimeter.

Figure 2.5 shows how the different subdetectors are used together to identify particles produced from Z^0 decays. More detailed descriptions of each of the subdetectors that make up the OPAL detector are given in the following sections.

2.2.1 The OPAL Co-ordinate System

The OPAL detector is situated approximately 100 metres underground at point 6 on the LEP ring. The LEP beams and the axis of the OPAL solenoid are inclined at an angle of ∼13.9 mrad relative to the horizontal plane. In order to describe the spatial positioning of OPAL subdetectors and event geometries a Cartesian co-ordinate system is used.

The positive x-axis is horizontal and points towards the centre of the LEP ring, the y-axis is approximately vertical and the z-axis points along the electron beam direction. The nominal interaction point for the LEP beams is at x=y=z=0. A polar angle, θ, is defined relative to the z-axis and an azimuthal angle, ϕ, is measured from the x-axis in the x-y plane.

2.2.2 The Beam Pipe

The LEP beams pass through the OPAL detector in a beam pipe that must withstand the large forces produced by the central detector gas pressure on one side and the high vacuum within the beam pipe on the other. The original beam pipe installed in 1989 consists of three sections about 1150 mm long, with an inner radius of 78 mm. The sections consist of an aluminium pipe of thickness 0.1 mm. This must ensure continuity for the wake fields of the LEP beams, reduce RF losses, provide electromagnetic shielding and a vacuum seal. The pipe is layered with a carbon fibre composite of thickness ∼2 mm to provide strength. The total structure represents 0.66% of a radiation length (X_0[e]). In 1991 an additional beryllium beam pipe was added at a radius of 53 mm, presenting 0.3% X_0 to normally incident particles. The carbon fibre/aluminium pipe remains to preserve the vacuum seal. The space between the two pipes is used for the silicon microvertex detector.

2.2.3 The Central Tracking Detector

The central tracking detector is composed of a vertex drift chamber and a pictorial jet chamber surrounded by an outer layer of z-chambers. A silicon microvertex

[e] A radiation length (X_0) denotes the distance over which the initial energy of an electron is reduced by a factor 1/e due to radiation losses.

detector was added close to the beam pipe in 1991. The central detector is housed within a cylindrical pressure vessel which contains a gas mixture[f] at a pressure of 4 bar.

2.2.3.1 The Silicon Microvertex Detector

The silicon microvertex detector (SI) [45] has been active since the middle of the 1991 physics run. It sits against the beryllium beam pipe and consists of two barrels of single-sided silicon microstrip detectors at radii 6.1 and 7.5 mm. The inner and outer layers comprise 11 and 14 ladders respectively, each ladder consisting of 3 daisy-chained detectors of total (active) length 180 (160) mm and width 33 mm. Each detector is made from an array of 300 μm thick single-sided FOXFET silicon wafers with 629 strips at a 25 μm pitch. Every second strip is read out with overlaid aluminium strips parallel to the z-axis. A two layer angular coverage of $|\cos\theta| < 0.76$ is obtained. The intrinsic r-ϕ co-ordinate resolution including alignment uncertainties is $\leq 8\mu$m for single hits. The separation between the concentric detector layers allows the two-dimensional reconstruction of secondary decay vertices. This enables short lived particle (τ, hadrons containing b,c quarks) lifetimes to be measured and heavy quark (b, c) events to be tagged using an impact parameter or decay length technique. Figure 2.6 and figure 2.7 show the overall layout of the microvertex detector and a view along the beam direction showing the orientation of the silicon detectors, respectively. For the 1993 physics run a new microvertex detector was installed which is capable of three-dimensional co-ordinate reconstruction [46]. Two 250 μm thick silicon wafers were glued back-to-back to replace the 300 μm thick detectors described above. The wafer responsible for the z co-ordinate measurement has a 100 μm read-out pitch orthogonal to the r-ϕ side. The z co-ordinate is not used in the analyses presented in this thesis.

2.2.3.2 The Vertex Detector

The vertex detector (CV) [47] is a 1 m long cylindrical drift chamber of diameter 470 mm that surrounds the carbon fibre/aluminium beam pipe. The gas-tight chamber which houses the detector is mechanically independent of both the central

[f] 88.2% argon, 9.8% methane, 2.0% isobutane.

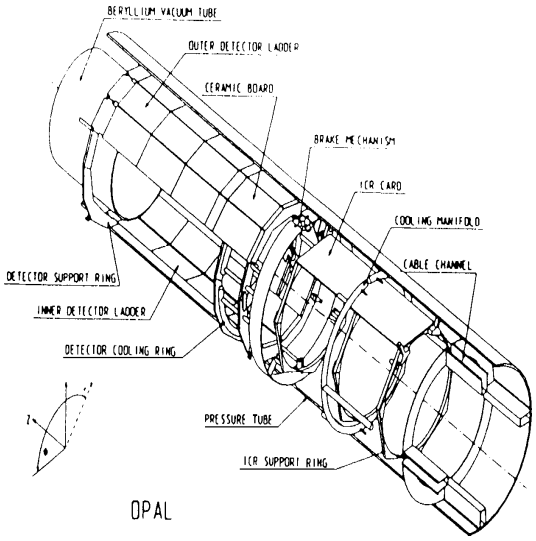

Figure 2.6: A cut-away view of the silicon microvertex detector *in situ* around the beryllium beam pipe. The silicon wafers are visible toward the top of the picture, and the read-out electronics are towards the bottom.

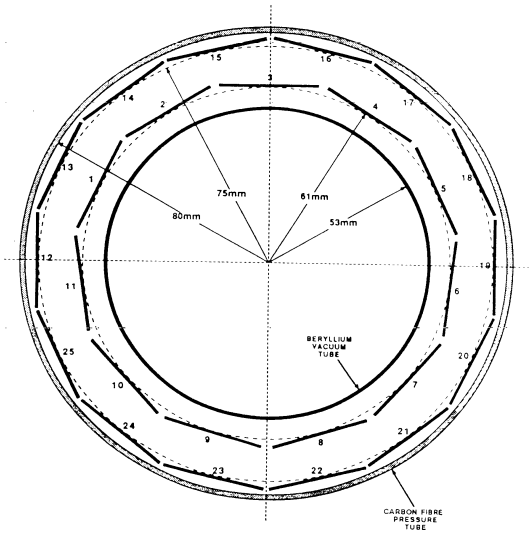

Figure 2.7: A view along the beam direction of the orientation of the silicon wafers in the microvertex detector. The beryllium beam pipe and the carbon fibre pressure tube are shown.

detector volume and the beam pipe.

Internally, the detector consists of 36 inner cells with axial wires and 36 outer cells with stereo wires at a 4° twist to the z-axis. Each cell is defined by planes of cathode wires with a 1 mm radial spacing. The ionisation electrons are detected by an anode wire plane at the centre of each cell. The anode wires are alternated with potential wires which shape the electric field, producing a drift field of 2.5 kV cm^{-1} within a cell. Inner (outer) cells have 12 (6) anode wires that are staggered to resolve left-right ambiguities.

Axial and stereo wire coverage is provided for the polar range $|\cos\theta| \leq 0.92$ and axial wire only coverage is provided for $|\cos\theta| \leq 0.95$. In the r-ϕ plane space-points can be measured with a precision of 55 μm and the two track separation is 2 mm. An approximate z co-ordinate can be derived from the time difference in arrival times for signals at each end of the anode wires; this is used for triggering. The resolution of the z measurement is 700 μm with the addition of stereo wire information.

2.2.3.3 The Jet Chamber

The jet chamber (CJ) [48] is heavily based on a previous design tested at the JADE experiment. It provides good space-point/double track resolution and particle identification, over nearly all the solid angle. This is essential for physics with jets of

particles from multihadronic events.

The detector is a 4 m long cylinder with conical end plates. It has an inner and outer diameter of 0.5 m and 3.7 m respectively. The gas-filled volume is divided in ϕ into 24 sectors each containing a plane of 159 staggered (to resolve left-right ambiguities) anode wires with a radial spacing of 10 mm, alternated with potential wires. Cathode wires form the the boundary between sectors. All wires are parallel to the beam axis and each plane of wires runs radially like bicycle spokes. The drift field within a sector is maintained at 890 V cm^{-1} using a resistor network to degrade the cathode wire potentials. The maximum drift time in a cell is 5 μs and the Lorentz angle is 20°.

All 159 space-points are measured over the range $|\cos\theta| < 0.73$ and at least 8 points are measured over 98% of the entire solid angle. Each space-point can be described as (r, ϕ, z), derived from the wire position, drift time and charge division respectively. Charge division is calculated from the ratio of integrated charge at each end of the wire.

The spatial resolution in the r-ϕ plane is 135 μm and 60 mm in the z direction. An impact parameter resolution of 113 μm is achieved using CJ alone[g], this is improved to ~40 μm using information from the vertex chambers.

The momentum resolution for tracks of all momenta, including a term due to multiple scattering, is given by :

$$\sigma(\mathrm{p_t})/\mathrm{p_t} = \sqrt{(0.02)^2 + (0.0015\,\mathrm{p_t})^2}, \tag{2.2}$$

where, $\mathrm{p_t}$ is the momentum component of a track in the plane transverse to the beam axis, in GeV/c.

Particle identification is performed through a dE/dx measurement derived from the measured charge collected at each space-point. Tracks with at least 130 measured points yield dE/dx resolutions of ±3.8% for minimum ionising pions in multihadronic events. This resolution allows the separation of electrons and pions in the momentum range (~2.5 → 13) GeV/c and the separation of pions and kaons/protons in the momentum range (~2.5 → 20) GeV/c, at a 95% confidence level.

In figure 2.8 the dE/dx value is plotted as a function of the charged particle

[g]This is measured using di-muon events where there is very little multiple scattering.

momentum for a variety of particle types. An extensive on-line calibration system, using di-muon and multihadronic events, ensures that the performance of CJ remains stable.

2.2.3.4 The Z-chambers

The z-chambers (CZ) [49] form a barrel geometry around the jet chamber. Their purpose is to provide a precise measurement of the z co-ordinate of particles leaving the jet chamber. This improves the polar angle and invariant mass resolutions.

The detector consists of 24 drift chambers of length 4 m and width 50 cm divided into 8 bi-directional cells. A polar angle range of $|\cos\theta| \leq 0.72$ is covered along with 94% of the azimuthal angle. Each cell contains 6 staggered anode wires with a preamplifier at each end to allow ϕ to be determined by charge division. Each cell has 6 anode wires perpendicular to the beam axis and the drift field within a cell is 800 V cm^{-1}, giving a maximum drift time of 5 μs. The z resolution of the chambers is around 300 μm after survey errors are accounted for and the r-ϕ resolution is 1.5 cm.

2.2.4 The Magnet

The magnet consists of a water cooled aluminium/epoxy solenoid coil ($\sim$1.7 X$_0$) and an iron yoke constructed from soft steel plates. The pressure vessel containing the central detector provides mechanical support for the coil assembly.

A current of 7000 A is used to produce a field of 0.435 T which is measured to be uniform to $\pm$0.5% over the volume of the central tracking detector. Less than 5 MW of power is consumed. The coil was wound as one unit to ensure a residual field of only a few tens of Gauss outside the solenoid to protect sensitive electronics in this area.

2.2.5 The Time-of-Flight System

The barrel time-of-flight system (TB) produces signals by measuring the time-of-flight of particles from the interaction point. This allows charged particle identification (0.6$\rightarrow$2.5 GeV/c) and is important in the rejection of cosmic rays.

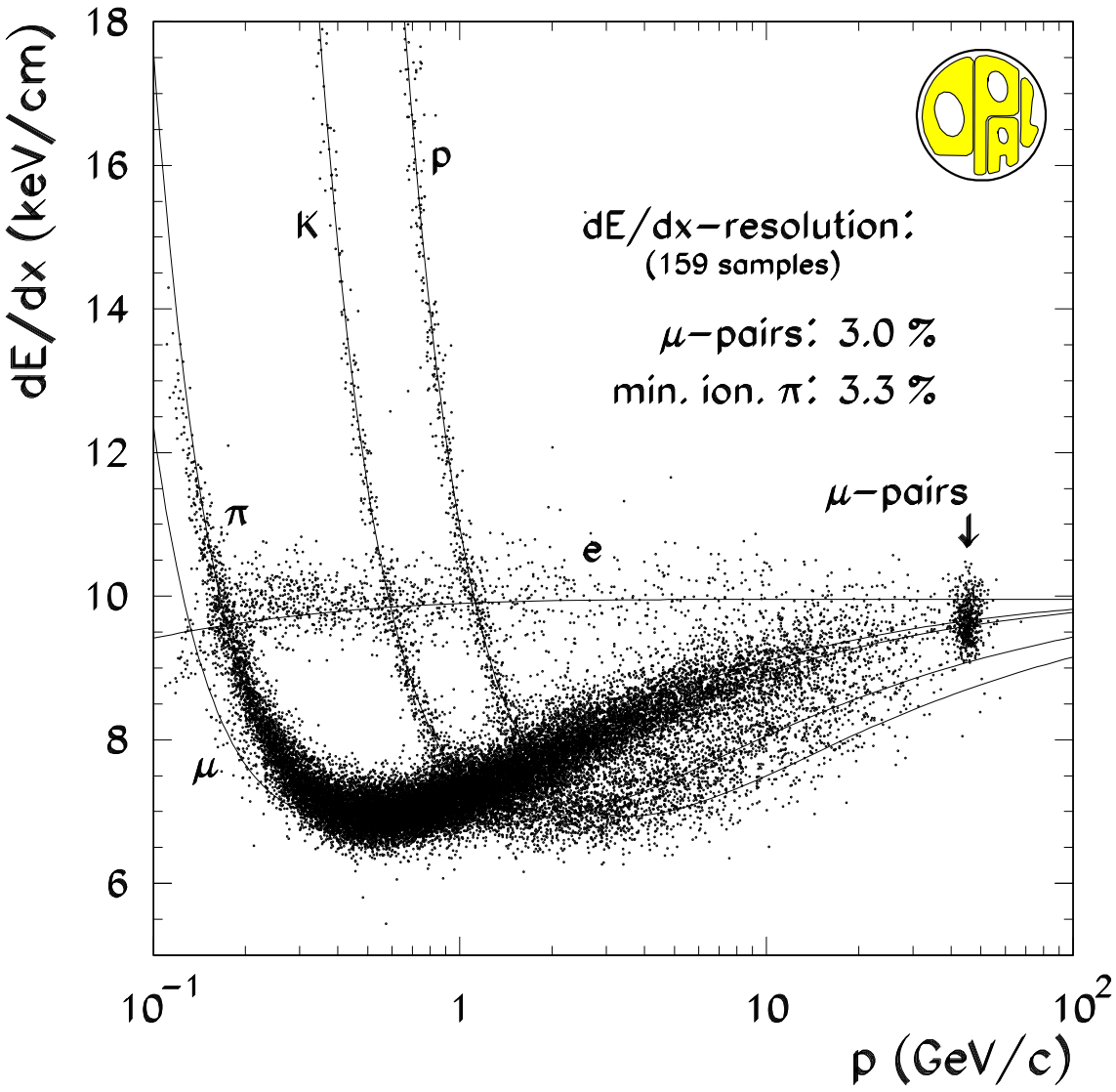

Figure 2.8: The measured and expected dE/dx for multihadronic tracks and muon-pairs as a function of particle momentum. The dE/dx resolution for minimum ionising pions (0.4→0.8 GeV/c) within a multihadronic event and muon-pairs (with 159 dE/dx hits) is indicated.

It consists of 160 scintillation bars, of length 6.84 m, outside and co-axial with the coil covering the entire azimuthal angle and $|\cos\theta| \leq 0.82$. Each scintillator is wrapped in aluminium foil and black PVC with the scintillation light collected at both ends by photomultiplier tubes attached to Perspex lightguides. Soft iron and μ-metal provide magnetic shielding.

A z co-ordinate is derived from the difference in arrival times of the light pulse at either end of the scintillator bar. The best z resolution, utilising z information from other sub-detectors, is around 5 cm. The time resolution of the detector, using di-muon events, has been determined as 460 ps.

2.2.6 The Electromagnetic Calorimeter

The aim of the electromagnetic calorimeter is to measure the energy and position of electrons and photons with energies in the range 100 MeV$\rightarrow$100 GeV. It also allows π^0–γ discrimination and, along with the central tracking system, electron–hadron discrimination. The total absorption lead-glass calorimeter is mounted between the coil and the iron magnet yoke. Utilising a barrel section and two endcaps 98% of the entire solid angle is covered. Lead-glass is used as an absorber due to its excellent energy resolution. Particles entering the lead-glass give rise to bremsstrahlung photons, which undergo pair production to produce a 'shower' of e^+e^- pairs. These particles are travelling faster than the speed of light in the lead-glass and therefore emit Čerenkov light which is collected by photomultiplier tubes. Since there are $\sim 2\,X_0$ in front of the lead-glass, mainly from the pressure vessel and magnet coil, most electromagnetic showers will start prior to the calorimeter. Gaseous presamplers are mounted immediately before the lead-glass and measure the energy and position of such showers, allowing the amount of energy deposited in the material in front of the lead-glass to be estimated.

The energy resolution of the barrel and endcap calorimeters is $\sigma(E)/E \sim 15\%/\sqrt{E}$ and $\sigma(E)/E \sim 20\%/\sqrt{E}$ respectively [50]. Using additional information from the presampler, an electron identification efficiency of $\sim$90% is achieved[h] and the hadron misidentification probability is 0.5% per hadron. The 40 mrad granularity of the lead-glass array is the limiting factor for separating π^0 decays from single photons.

[h] For an electron momenta above 2 GeV/c.

However, the shape of the electromagnetic cluster can provide a statistical separation.

Figure 2.9 shows an example of the power of the electromagnetic calorimeter, the components of which are now described in more detail.

2.2.6.1 The Barrel Electromagnetic Presampler

The presampler barrel (PB) [51] consists of a cylinder of 16 chambers containing two layers of limited mode streamer tubes mounted between the time-of-flight barrel and the lead-glass calorimeter, covering a polar angle of $|\cos\theta| \leq 0.81$. Each layer consists of 4 PVC extrusions containing 24 cells. Between layers the cells are offset by half a cell to eliminate dead-spots. The extrusion walls are coated in graphite and anode wires run axially in the centre. Streamers initiated by charged particles are detected by the charge induced onto 1 cm wide cathode strips on both sides of each layer of tubes at 45° to the anode wires. Positions obtained through charge division yield 10 cm and $\sim$2 mm resolutions in z and r–ϕ respectively. The chambers use a gas mixture of 32% n-pentane and 68% CO_2.

2.2.6.2 The Barrel Lead Glass Calorimeter

The barrel lead-glass calorimeter (EB) consists of 9440 lead-glass blocks. Each comprises 24.6 X_0 and is suspended at a radius of 2455 mm outside the magnet coil. The full azimuthal angle is covered and $|\cos\theta| <0.82$. Each block subtends a solid angle of about 40 mrad^2. The calorimeter is segmented into 59 blocks in the z direction and 160 blocks in the ϕ direction. The blocks are arranged in a non-perfect pointing geometry towards the interaction region. This reduces the probability of a particle traversing more than one block and a particle escaping through gaps between blocks. The blocks are instrumented with magnetically shielded[i] photomultipliers to collect the Čerenkov light and are individually wrapped in aluminium foil and black PVC to ensure optical isolation.

[i]The residual field outside the magnet coil is about 0.002 T.

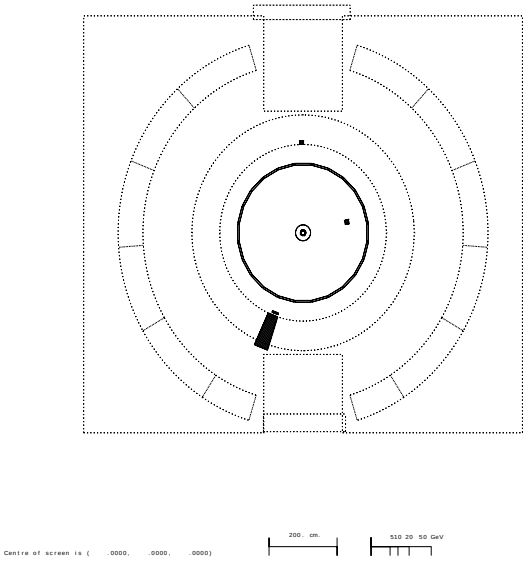

Figure 2.9: A view of a candidate $Z^0 \rightarrow \nu\bar{\nu}$ event, looking along the beam direction. The energy deposit in the electromagnetic calorimeter is the consequence of initial state radiation from the initial e^+e^- pair that interact to produce a Z^0. There is no other activity in the detector, since neutrinos are very weakly interacting.

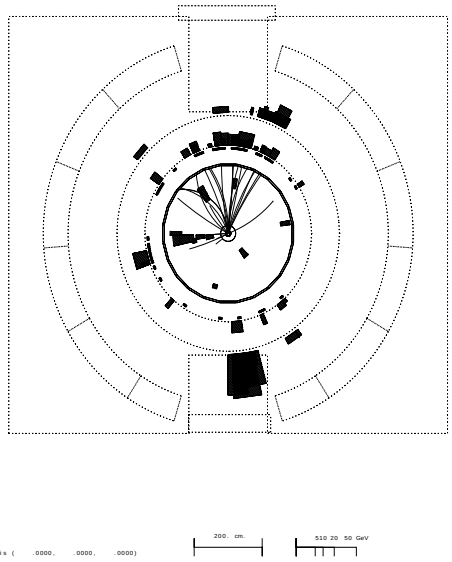

Figure 2.10: An example of neutral energy in a multihadronic event. Energy has been deposited in the hadron calorimeter (denoted by the outer layer of blocks) which balances the momentum of the charged tracks recorded by the central tracking detectors. The information from the hadron calorimeter allows discrimination against the event faking the process $e^+e^- \rightarrow Z^0 \rightarrow Z^*\ H^0$, where the Higgs boson decays to two bottom quarks, giving the jets of particles and the Z^0 decays to $\nu\bar{\nu}$ leaving no signal in the detector.

2.2.6.3 The Endcap Electromagnetic Presampler

The presampler endcap (PE) [52] consists of 32 umbrella shaped multi-wire chambers using a 45% n-pentane/55% CO_2 gas mix. The chambers are divided into 16 sectors mounted behind the central detector pressure bell. A full azimuthal coverage is provided and $0.83 < |\cos\theta| < 0.95$. The multi-wire chambers are operated in high gain mode, which gives good energy and position resolution in the small space available. The design follows closely that of the hadron poletip calorimeter. Space co-ordinates for showers and minimum ionising particles are produced by the simultaneous read-out of groups of 4 wires and 10 mm cathode strips on both surfaces of each layer, at an angle of 45° to the sense wires. An energy measurement is provided by square cathode pads on the opposite surface of the chamber.

2.2.6.4 The Endcap Electromagnetic Calorimeter

The electromagnetic endcap calorimeter (EE) [53] is made up of two dome shaped arrays of 1132 lead-glass blocks. These are mounted in front of the pole-tip hadron calorimeter, covering the full azimuthal angle and $0.81 < |\cos\theta| < 0.98$. The axes of the blocks are co-axial to the beam-line. Each block is read out with a single-stage vacuum photo-triode as the blocks are mounted in the full axial field of the magnet. Each block provides at least 20.5 X_0 of material (more typically 22 X_0).

2.2.7 The Hadron Calorimeter

The hadron calorimeter measures the energy of hadrons that exit the electromagnetic calorimeter and helps with muon identification. The magnet return yolk iron is used as an absorber providing 4 interaction lengths[j] over 97% of the entire acceptance. Detectors are placed between the layers of the iron, to produce a sampling calorimeter. The hadron calorimeter is divided into a cylindrical barrel, two endcaps and two pole-tips. Since most hadronic showers start in the electromagnetic calorimeter, the hadronic energy resolution is improved by including signals from the electromagnetic calorimeters.

The performance of the hadron calorimeter is illustrated in figure 2.10 and the constituent parts are described below.

2.2.7.1 The Barrel and Endcap Hadron Calorimeters

The barrel (HB) and endcap (HE) hadron calorimeters are based on the same design [54] with the return yolk iron segmented such that the spacing between the iron slabs is $\mathcal{O}(30)$ mm in both cases. The detectors are limited streamer tubes made from PVC extrusion divided into 8 cells and using a 75% isobutane/25% argon gas mixture. The inner walls are coated in graphite and an anode wire runs through the centre of the extrusion. In the barrel there are 8 layers of absorber and 9 layers of detector over the region $|\cos\theta| \leq 0.81$. In the endcaps there are 7 layers of absorber and 8 layers of detectors over the region $0.81 < |\cos\theta| \leq 0.91$. Read-out is achieved through large area pads that divide the solid angle into 976 elements and can be

[j] The interaction length is the distance travelled by a beam of monoenergetic particles resulting in a factor of e reduction in the beam intensity.

used to provide an approximate measurement of the hadronic shower energy. There are 2400 m^2 of detector in total.

The typical energy resolution for a 10 GeV hadron is $\sigma(E)/E = 120\%/\sqrt{E}$. The positional resolution of muon tracks is limited to 10 mm by the anode wire spacing. The efficiency for muon identification varies from 60→90% depending on the number of detector layers used.

2.2.7.2 The Pole Tip Hadron Calorimeter

The poletip calorimeter (HP) [55] extends the hadron calorimetry to $|\cos\theta| < 0.99$. The iron yoke is once more instrumented but this time with thinner high gain multi-wire proportional chambers. The energy resolution in the forward region is improved by reducing the sampling interval and increasing the number of sampling layers to compensate for the poorer central detector momentum resolution in this region. Read-out is achieved through large cathode pads and aluminium strips. Each chamber has strips that fan out radially and perpendicular to the anode wires, 12% of each layer is dead due to gas lines and support. However, these areas are covered by the overlap with other layers. A 45% n-pentane/55% CO_2 gas mixture is used.

For energies less than 15 GeV the energy resolution is $\sigma(E)/E = 100\% /\sqrt{E}$; otherwise shower leakage reduces it to $\sigma(E)/E = 140\% /\sqrt{E}$.

2.2.8 The Muon Detector

Muon detection is divided into barrel and endcap regions and takes place over 93% of the entire solid angle by at least one layer of detector. Over nearly the whole solid angle a muon has to traverse 1.3 m of iron (equivalent) from the interaction point, which is greater than 7 interaction lengths for a pion. The probability for a pion not to interact is less than 0.1%. Only muons with an energy above ∼3 GeV will reach the muon detectors, although some of the stopping muons may be identified in the hadron calorimeter. The efficiency for identifying a muon with an energy above 3 GeV is ∼100%. The probability of misidentifying an isolated pion, with an energy of 5 GeV, as a muon, is less than 1%.

2.2.8.1 The Barrel Muon Detector

Four layers of barrel detector (MB) [56] cover the range $|\cos\theta| < 0.68$ and at least one layer covers the range $|\cos\theta| < 0.72$. The detectors consist of 110 large area drift chambers, using a 10% ethane/90% argon gas mixture. Each layer of detector is mounted off the previous inner neighbour. Chambers in the four layers are staggered by 50 mm in ϕ to resolve any left-right ambiguities. The ϕ co-ordinate is determined by drift time with a resolution of $\sim$1.5 mm. The z co-ordinate is determined by diamond shaped cathode pads with a resolution of $\sim$2 mm.

2.2.8.2 The Endcap Muon Detector

The angular range $0.67 < |\cos\theta| < \sim 0.985$ is covered by muon endcaps (ME) [57] of area $\sim$150 m^2 at each end of the OPAL detector perpendicular to the beam pipe. The endcaps consist of 4 layers of limited mode streamer tubes perpendicular to the beam axis, which are divided up into eight 6×6 m quadrants. Four 3×2.5 m patches fill in the regions above and below the beam-line not covered by the quadrants. Each detector plane consists of 2 layers of orthogonal streamer tubes. The distance between these planes is about 670 mm. Each chamber has one layer of tubes running horizontally and another with tubes running vertically, enabling the reconstruction of pointing track segments. The streamer tubes are made from plastic extrusion with the walls covered in graphite and a central anode wire running the full length of the extrusion. The anode wire pitch is 10 mm. Read-out is through charge induced onto orthogonal aluminium strips at a 10 mm pitch on either side of the gas jacket that encloses the extrusion. A 75% isobutane/25% argon gas mixture is used. Using a weighted average technique, spatial resolutions of $\sim$3 mm (parallel) and $\sim$1 mm (perpendicular) can be achieved, with a directional resolution of about 5 mrad.

2.2.9 The Luminometers

All the LEP experiments measure the luminosity of the LEP beams by counting Bhabha scattered electrons ($e^+e^- \rightarrow e^+e^-$) into a precisely known detector acceptance. The Bhabha process has a cross-section dominated by QED which varies as $\sim 1/\theta^3$ (θ is the angle between the scattered and incident electron). The cross-section can be calculated to a high degree of precision. Detectors with a large accep-

tance in the far forward region therefore obtain large samples of Bhabha scattering events. The dominant systematic error on a luminosity measurement is dependent on knowledge of the inner acceptance of the detector.

Luminosity was originally measured with a relative accuracy of 0.5% using the forward detector. In 1993 a silicon tungsten calorimeter was installed with the aim of measuring the luminosity to a relative accuracy of 0.1%. Such accuracy was needed due to the event sample sizes used for Z^0 lineshape measurements and has been achieved.

The luminometers are also used to tag $\gamma\gamma$ interactions[k] and extend the acceptance for multihadronic events.

2.2.9.1 The Forward Detectors

Two forward detectors (FD) are located at ~2.6 m on either side of the nominal interaction point and cover the polar range between 47 and 120 mrad. In this range the acceptance is clean with only 2 mm of carbon fibre and 2 mm of aluminium in the path of particles, thus minimising preshowering. The cross-section within this acceptance for Bhabha scattered electrons is ~1.7 times the multihadronic acceptance measured over the entire OPAL detector.

The forward detector can be separated into six parts. The three main parts are described below and three smaller parts (the fine luminosity monitor, the gamma catcher and the far forward monitor) are not described, but are well documented in [35].

The Calorimeter The calorimeter is divided into 16 azimuthal segments and consists of 35 layers (24 X_0) of lead-scintillator sandwich. The first 4 X_0 make up a presampler. The radial shower position can be determined to ± 2 mm, the azimuthal resolution is $< \pm 1.5^\circ$ and the energy resolution for well contained showers is $\sigma(E)/E = 17\%/\sqrt{E}$.

The Tube Chambers The tube chambers are mounted between the presampler and main parts of the calorimeter. They consist of brass walled proportional

[k] The electron and positron beams radiate photons which interact to produce a hadronic final state.

tubes, surveyed to ± 1 mm. Their purpose is to provide a more accurate back-up measurement of the calorimeter shower positions.

The Drift Chambers The drift chambers [58] are used to survey the position of the tube chambers. Positional information is obtained through charge division and diamond shaped pads close to the anode wires. A resolution of ±300 μm in the drift direction (approximately radial) is obtained.

2.2.9.2 The Silicon Tungsten Calorimeter

Two silicon tungsten calorimeters (SW) [59] are positioned at ∼2.4 m on either side of the nominal interaction point. The calorimeters totally encircle the beam pipe and therefore cover the entire azimuthal angle range. The polar angle is covered over the range 25 → 60 mrad. This gives an acceptance of ∼80 nb, approximately 2.5 times the multihadronic cross-section, measured over the entire OPAL detector.

Each calorimeter comprises of 19 layers of silicon detector interleaved with 18 layers of tungsten. The 19 layers of silicon constitute a total of 22 X_0 and less than one interaction length. The first 14 layers of tungsten constitute a total of 14 X_0 and the last four a total of 8 X_0. Tungsten was chosen due to its high density which therefore limits the lateral spread of electromagnetic showers (leading to a precise co-ordinate reconstruction) and results in a small calorimeter size. A bare layer of silicon is placed before the first tungsten plate of the calorimeter. This allows showers that start before the calorimeter to be studied in detail.

An angular acceptance of 25.7 → 55.7 mrad is covered by the sensitive area of each detector. In each layer the sensitive area is made up from 16 silicon 'wedges', about 311 μm thick. The active side of the wafer (the side facing the interaction point) comprises of 64 p^+ diodes, in a pattern of 2×32 radial pads which are 2.5 mm wide and separated by 11.25°. In order to fit the wedges together in a layer so that there are no gaps between adjacent detectors, alternate detectors are staggered by 800 μm in the z direction. Even and odd detector layers are offset by half a wedge in ϕ so the gaps between wedges in one layer line up with the centres of the wedges in the next. This helps to control systematic effects due to shower leakage. In total the luminometer (both ends) contains 608 silicon wedge detectors or 38 912 read-out channels.

An extremely high standard of metrology is needed during the construction of the entire detector. Results [60] show that the internal (pad–pad) alignment precision achieved is $\sim 7\mu$m and the inner radius is known to better than 10 μm. The energy resolution of the calorimeter is $\sigma(\mathrm{E})/\mathrm{E}\ \sim 24\%/\sqrt{\mathrm{E}}$ and the positional resolution is ~ 220 μm. The luminosity is measured with a relative accuracy of 0.07% [60].

2.3 The OPAL Data Chain

2.3.1 The Trigger

The purpose of the trigger system [61] is to select LEP bunch crossings that produced interesting physics events and initiate the operations that take the raw data from such events and store it in a form suitable for future analysis. In the 4×4 LEP running mode the beam bunches collide every 22 μs. It is impossible to read-out the whole detector for each bunch crossing as the inherent data acquisition dead-time is around 20 ms. The philosophy of the trigger system therefore is to reduce the recorded data volume by rejecting background triggers (due to cosmic rays, beam-gas interactions, beam-wall interactions and subdetector noise) whilst retaining an extremely high efficiency for recording Z^0 decays[l]. Once a trigger is received the OPAL data acquisition system reads out each participating subdetector.

The solid angle covered by the OPAL detector is divided into a matrix of 6 overlapping θ bins and 24 overlapping ϕ bins. Subdetectors[m] provide inputs to this matrix and the OPAL central trigger logic decides if the event should be processed further. Subdetectors can also make stand-alone decisions giving a high degree of flexibility and redundancy, allowing efficiencies to be calculated for each subdetector.

The various parts of the trigger can be split into 5 parts and these are discussed briefly below :

Track Trigger Information from CV and CJ is processed with the aim of finding tracks. For each hit in either subdetector a quantity z/r is determined and fed into the $\theta - \phi$ matrix discussed above. Charged tracks can be thought of as straight in the r-z projection. If originating from the vertex, the hits along

[l] The event rate on the Z^0 peak is ~ 0.7 Hz.
[m] CV, CJ, TB, EB, EE, MB, ME, FD and SW.

the track will have the same z/r value. If not, then z/r will have a radial dependence. For speed only 4 annular groups of 12 adjacent wires are used. One annulus is totally within CV and the other 3 are in CJ at various radii. The efficiency of this trigger is estimated to be >98%.

Time-of-Flight Trigger The primary purpose of this trigger is to reject cosmic rays. A coincidence on each end of a scintillator bar is demanded within 50 ns of a LEP bunch crossing. A trigger is generated if more than a quarter of the scintillator bars satisfy the coincidence condition. The efficiency of this trigger is measured to be >90%.

Electromagnetic Trigger The barrel and endcap electromagnetic calorimeters are divided into groups of 48 lead-glass blocks to form a binned $\theta - \phi$ array. Energy in these bins is discriminated at 4 GeV to produce stand-alone triggers. Discrimination at 1 GeV allows the signals to be combined with other trigger signals and entered into the main $\theta - \phi$ matrix.

Muon Trigger The barrel and endcap are treated separately. In the barrel, 3 out of 4 layers must fire over a ϕ bin of around 15°. This trigger is never used stand-alone as it suffers from the cosmic ray background. A trigger signal is generated in the endcaps if charge deposited in half the layers is above a lower threshold and the muon track segment can be associated with a central detector track. The x-y co-ordinates of the track are transposed into $\theta - \phi$ and entered into the main trigger matrix. The endcap trigger is only used with a left-right coincidence in the stand-alone mode to reduce the cosmic ray background rate. The overall efficiency of the muon trigger is measured as >95%.

Luminometer Trigger The FD trigger signal is made up from energy sums in the presampler, calorimeter and fine luminosity scintillators. Left-right coincidences of these signals are used to produce stand-alone triggers. The trigger signals are also combined with other detectors for $\gamma\gamma$ event detection. The efficiency of this trigger is measured to be > 98.5%. The silicon tungsten calorimeter provides a trigger by requiring the energy from either end to exceed a low threshold. This is checked against an independent FD trigger formed

from energy sums at both ends of the detector and is measured to be ∼100% efficient.

With the advent of the LEP 8×8 running mode the time between beam crossings was halved. A pretrigger [62] was introduced to reduce the potential deadtime involved in trigger decisions to <1.5% without altering the acceptance to genuine physics events. Each of the triggering subdetectors form a pretrigger based on 60° ϕ segments using essentially the same scheme as described above. The efficiency for single particles is almost 100%.

2.3.2 The Data Acquisition System

The OPAL detector has about 200×10^3 analogue data channels, producing approximately 45 Kbytes of raw data per multihadronic event (considerably less for a di-lepton event !). The OPAL data acquisition system [63] buffers the data from each subdetector before routing it to a central node, where it is merged and stored. Each event is fully reconstructed on an on-line computer cluster.

The component parts of the data acquisition system are outlined below.

2.3.2.1 Front End Processing

The VME-based local system crates associated with each subdetector perform basic functions such as pedestal subtraction and pulse height analysis in order to reduce data volume. Some partial event reconstruction and data compression is also performed.

2.3.2.2 The Event Builder and Filter

The event builder takes data from each local system crate and merges it for further processing by the filter. The filter software performs a fast analysis on each event and classifies it (multihadronic, leptonic etc.) for future physics analysis [64]. The filter can accept an event rate of up to 10 Hz and since the filter disk can hold up to 12 hours of data this processing stage is essentially independent of the data processing and storage stages. This is useful if there is a problem with these procedures. Some additional background events are also rejected in the filter reducing

the data-flow by 30%. Checks have shown that there is no loss of physics events and a sample of the events rejected as background are stored for inspection. The filter is also connected to a colour event display that provides a very useful diagnostic tool which can also be used to impress visitors[n].

2.3.2.3 Data Storage

The filter is an integral part[o] of a high-speed network that links workstations which form a powerful data processing farm used for event reconstruction. Data from the filter are stored on optical disk. Once calibration constants (such as the drift velocity in the central detector gas, which is measured online) are available from the subdetectors the raw data are passed through the `ROPE` event reconstruction program discussed below. The reconstructed data is written to a buffer disk and copied over a network to the main CERN site and the SHIFT [65] analysis farm. This consists of a powerful UNIX based system which accesses data or Monte Carlo files from disks over a high speed network. Data are usually available for quality checks and preliminary analyses within an hour of the end of a physics run.

2.3.3 Event Reconstruction

A computer program called `ROPE` (Reconstruction of OPal Events) [66] is used along with a calibration database, `OPCAL` [67], to convert the raw detector[p] digits into quantities that are useful for physics analyses, such as track momenta and angles. These quantities are stored on the Data Summary Tape. `ROPE` is a suite of routines structured with `PATCHY` [68], using the `ZEBRA` [68] dynamic memory management system to transfer the subdetector raw digits into the user's analysis code. A graphical interface to `ROPE` (`GROPE` [69]) allows the reconstruction of any event to be viewed in three-dimensions[q].

The main quantities of interest produced by `ROPE` and used in this thesis are charged tracks in the central tracking detector and electromagnetic clusters in the

[n] Figure 2.11 shows an early version of the event display.

[o] The filter is located 100 m underground and is connected to the rest of the network via an optical link.

[p] or Monte Carlo.

[q] Figure 4.1 was produced using `GROPE`.

lead-glass calorimeter. A thorough overview of track and cluster finding can be found in [70] and [71] respectively. To aid understanding in later chapters a brief overview of track and cluster finding is given below.

2.3.3.1 Track Finding

Charged tracks in the central detector region are bent into a helical form by the magnetic field. The helices can be transformed via a suitable conformal mapping into a straight line that is used for track fitting. Track segments are formed within sectors of CJ and extrapolated to try and include hits that are near by. This process is repeated with the extended track segments until all the track segments have been found. At this point, track segments from adjoining sectors are merged to form single track segments. A similar approach is used in CV and CZ. An attempt is made to merge track segments from all three central detectors by extending CJ track segments into CV and CZ and trying to merge with CV axial, CZ or CV stereo track segments or hits (in that order). The resulting final tracks are defined using a Billoir fit [72] and the resulting helix is described using five track parameters and their errors :

- κ, the track curvature is defined as $|\kappa| = 1/2\,\rho$, where ρ is the radius of curvature of the track and κ is signed such that $\kappa > 0$ corresponds to a negatively charged particle.
- ϕ_0, the azimuthal angle of the track at the point of closest approach to the origin in the r-ϕ plane.
- d_0, the transverse distance from the origin to the point of closest approach.
- $\tan\lambda$, the polar angle of the track ($\tan\lambda = \cot\theta$).
- z_0, the z co-ordinate at the point of closest approach.

2.3.3.2 Cluster Finding

Electromagnetic clusters in the lead-glass calorimeters are found from groups of contiguous blocks around a seed block, all with an energy above threshold. The coarse clusters are searched for local maxima of energy and if found are split into finer

clusters. A raw energy is calculated from the energies of the blocks in the cluster. A more useful corrected energy is calculated by allowing for the material before the calorimeter [71]. The cluster position is determined from an energy weighted sum over the constituent blocks of a cluster.

Tracks in the central detector are extrapolated from the last measured space-point to the electromagnetic calorimeter with multiple scattering in the intermediate material accounted for. If the track is within 150 (50) mrad in θ and 80 (50) mrad in ϕ for the barrel (endcaps) then the track is said to be associated to the cluster.

2.3.4 The Slow Controls System

The OPAL slow controls system [73] ensures that the entire detector operates safely in the presence of many potentially dangerous elements, such as high voltages and explosive gas mixtures. The system is divided into two parts. The first part monitors the common OPAL environment and the second is dedicated to each subdetector. Seven VME-based stations distributed amongst the electronics huts are used to monitor about 5000 channels including voltages, gas parameters and temperatures. An interface to the LEP-wide security systems ensures a homogeneous safety system. Each subdetector usually runs the slow controls software in the local systems crate and a link is provided to the central data acquisition system to enable slow controls data to be included in the event record.

All warnings and alarms generated by the slow controls system are permanently on display in the control room (which unlike the other LEP experiments is situated 100 m underground, next to the detector). A human interface to the status of the whole detector is provided by a computer workstation.

2.4 The Data Recorded with the OPAL Detector

The OPAL detector was completed in July 1989. The first Z^0 event seen at LEP was recorded with the OPAL detector at 23:16 on August 13^{th} 1989. The event is shown, as recorded on the event display, in figure 2.11. The Z^0 decay is revealed as two back to back deposits, of total energy near 90 GeV, in the barrel lead-glass calorimeter. Figure 2.12 shows the number of multihadronic events recorded with

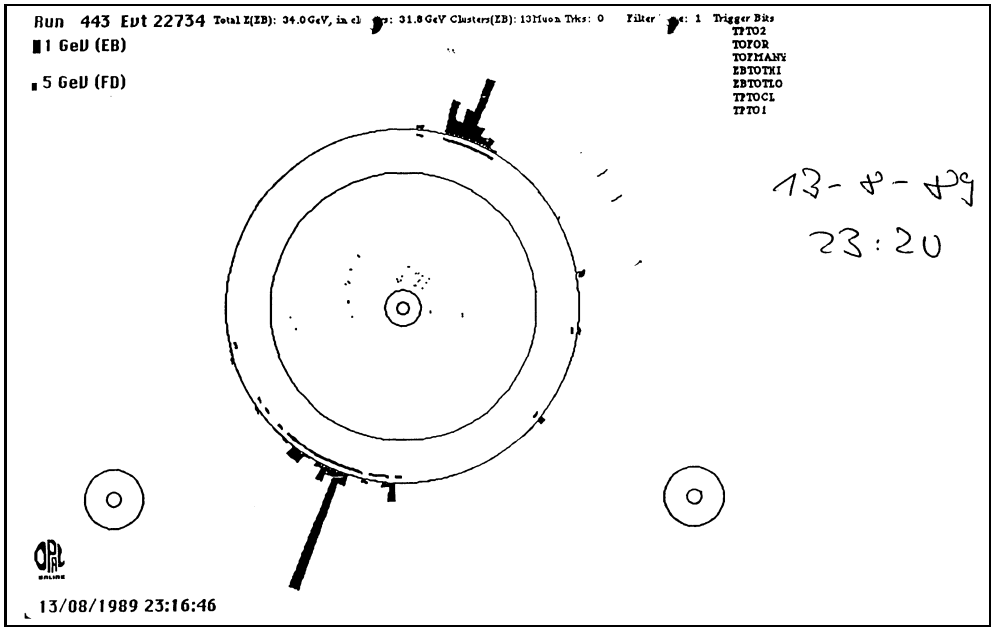

Figure 2.11: A view of the first decay of the Z^0 boson recorded by the OPAL experiment on 13^{th} August 1989. The event display comes from the filter and shows the OPAL detector viewed in the plane perpendicular to the beam line. This was the first Z^0 decay to be seen by any of the LEP experiments after the LEP accelerator was commissioned. The Z^0 is clearly identified by two back-to-back energy deposits in the electromagnetic calorimeter which have a combined energy totalling the Z^0 mass. The central tracking chambers were not operational at this time, although the spatial extent of the electromagnetic showers are indicative of a multihadronic event.

the OPAL detector and retained by the filter in the period 1991 to 1995 as a function of the week number during data taking. The number of multihadronic events used to produce the results shown in this thesis will be slightly different due to selection criteria that are applied to ensure only well understood event samples are used. The OPAL detector has a data-taking efficiency of $\sim$90%. Some data are unavoidably lost due to detector deadtime, background triggers and detector or operational problems. Data from 1992 and 1994 was recorded on the Z^0 peak, other data was recorded in energy scans with centre of mass energies within $\pm$ 3 GeV of the Z^0 peak.

2.5 The OPAL Detector Simulation

It is essential to be able to simulate LEP physics events and the detector's response to them, in order to understand detector performance and optimise physics analysis. Monte Carlo events are used to do this. The OPAL detector is simulated using the `GOPAL` [74] program, which is based on the widely used `GEANT` [75] package. The

kinematic properties of the particles in a physics event are provided by generator programs. The generated particles are tracked through the comprehensive model of the OPAL detector geometry and material composition. The simulated subdetector raw data output is in the same format as that produced from a real physics event and is reconstructed by the ROPE program. Monte Carlo modelling of the detector and particle generation is periodically updated in light of comparisons to real data events.

Many types of generator programs are available depending on the physics process under consideration. In this thesis, Monte Carlo samples are produced using the JETSET [76] generator. More details can be found in section 4.8.2.

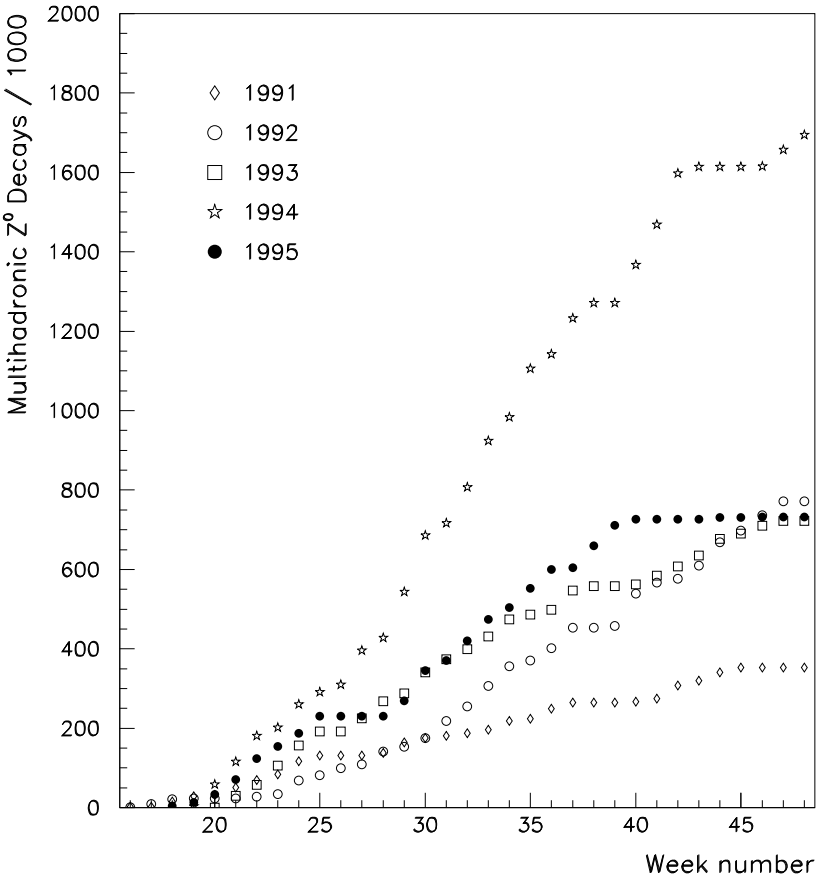

Figure 2.12: The development of the number of multihadronic decays logged by the filter as a function of time, for each year of LEP running from 1991 to 1995. Approximately 4 million multihadronic events have been recorded to date from an integrated luminosity of $\sim$140 pb^{-1}. The LEP beam energies were tuned to the mass of the Z^0 in 1992 and 1994. In 1991, 1993 and 1995 the beam energies were scanned around the Z^0 mass to allow lineshape measurements to be carried out. Only data recorded between 1991 and 1994 with the silicon microvertex detector operational is used for the analyses described in this thesis.

Chapter 3

Bottom Quark Physics

This chapter presents an overview of bottom quark physics pertinent to the analyses described in chapters 5, 6 and 7. Firstly, the discovery of the bottom quark is outlined and the differences in bottom quark production from $\Upsilon(4s)$ and Z^0 decays is discussed. Results from $\Upsilon(4s)$ experiments provide valuable information on bottom meson decays which are used to complement the measurements made in this thesis. The majority of the chapter deals with bottom quark production from Z^0 decays at LEP. The formation of bottom hadrons is described, and particular attention is paid to bottom hadron decays to Λ^0 baryons. A measurement of the branching ratio, Br(b hadron$\rightarrow \Lambda^0$X), is presented in chapter 5. The final part of the chapter starts with a description of the spectator model of bottom hadron lifetimes, which assumes the bottom hadron decay is dominated by the bottom quark. A more realistic theory, based on quantum chromodynamics, is also described. The average bottom hadron lifetime and the bottom baryon lifetime are measured in this thesis. The chapter concludes with a review of the contemporary techniques used to measure these lifetimes.

3.1 The Discovery of the Bottom Quark

In 1973 Kobayashi and Maskawa proposed a third quark generation to accommodate CP violation in the Standard Model [25]. Adding an extra quark generation ensured that a phase term was present in the quark mixing matrix, as needed to account for

CP violating effects in the neutral kaon system [26]. Also, in 1975 the third charged lepton, τ, was discovered [27]. In order to preserve the symmetry between the lepton and quark generations, the discovery of a third quark family was 'mandatory'.

The b quark was experimentally observed at Fermilab by the CFS collaboration [77] in 1977. It was discovered through a narrow di-muon resonance in the process p + Be $\rightarrow \mu^+\mu^-$ + X, produced at a fixed target experiment. The Drell-Yan background process produces a monotonically falling invariant di-muon mass distribution which is well understood. Data yielded evidence for a narrow resonance, called Υ, at $\sim$9.5 GeV [77] and further resonances Υ' [78] and Υ'' [79] at $\sim$10 GeV and $\sim$10.4 GeV respectively. The width of the Υ resonance was measured to be 7.8$\pm$0.9 MeV which implies a relatively long state lifetime, giving the first indication of a bound $b\bar{b}$ state. Experiments using e^+e^- annihilation at DORIS [80] and later at CESR [81] confirmed these results and firmly established the $b\bar{b}$ nature of the Υ family of resonances. Such e^+e^- facilities are ideally suited for the clean production of b quark resonances.

These bound $b\bar{b}$ resonances are today known as the Υ(1s), Υ(2s) and Υ(3s) states. In 1980 a further Υ state (Υ(4s)) was discovered at CESR [82] at a centre of mass energy of 10.58 GeV. This resonance was much broader than the previous three resonances indicating that the B meson (B^0, B^+) production threshold had been crossed, as predicted by theory [83]. The entire Υ spectrum can be seen in figure 3.1. The light quark background can be investigated using data taken at centre of mass energies just below the Υ(4s) production threshold.

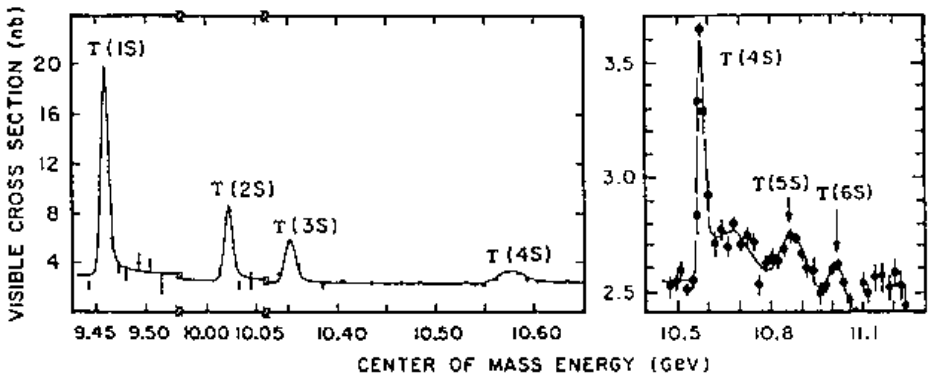

Figure 3.1: The e^+e^- total cross-section measured by the CLEO collaboration in 1984. The energy region Υ(1s) through Υ(4s) is shown on the left and the energy region Υ(4s) through Υ(6s) is shown on the right. The majority of data recorded by the CLEO experiment is from the Υ(4s).

The CESR and DORIS-II e^+e^- machines, running at the $\Upsilon(4s)$ threshold provided the main data on B meson decays until the LEP and SLC e^+e^- machines started running on the Z^0 resonance. The bottom quark production rate at hadron machines such as the Tevatron are much larger[a] than at e^+e^- machines, but the backgrounds are very high.

3.2 Bottom Quark Production from $\Upsilon(4s)$ and Z^0 Decays

There are several differences between studies of the bottom quark possible at the $\Upsilon(4s)$ and Z^0 machines. At the $\Upsilon(4s)$ the B^0 ($b\bar{u}$) and B^+ ($\bar{b}u$) mesons are produced at rest[b]. Results from the CLEO collaboration (at CESR) and the ARGUS collaboration (at DORIS-II) dominate studies of B meson physics from the $\Upsilon(4s)$. At LEP a mixture of B^0, $B^{\pm}$, B_s^0 ($b\bar{s}$), excited states of these B mesons, b baryons and their excited states are produced in Z^0 decays. The CLEO experiment has recorded approximately ten times more B meson decays than a typical LEP experiment to date.

At $\Upsilon(4s)$ experiments, decay channels without open beauty are heavily suppressed by the OZI (Zweig) rule. However, there is a background from the $q\bar{q}$ continuum. Events from the continuum tend to produce back-to-back jet-like events, whereas $b\bar{b}$ events are rather spherical due to the low ($\sim$300 MeV/c) momentum of the B mesons. Simple topological and kinematical cuts can therefore be employed to select $b\bar{b}$ events. The excellent energy resolution of the detectors at CESR are used to exclusively reconstruct specific final states. The reconstruction of final states can be constrained with an accurate measurement of the beam energy to improve the overall invariant mass resolution. Other more specialised $b\bar{b}$ selection methods are detailed in [84]. Bottom meson species form a coherent state ($B^0\overline{B^0}$ or B^+B^-) due to the small amount of energy that remains after a B meson has been formed, preventing multiple $q\bar{q}$ pairs being formed from the vacuum.

At the Z^0 experiments, the b hadrons are produced in jet-like events and have

[a] At LEP $\sigma_{b\bar{b}} \sim \mathcal{O}(\text{nb})$. At the Tevatron $\sigma_{b\bar{b}} \sim \mathcal{O}(\mu\text{b})$!
[b] At least for current experiments where the e^+e^- beams have equal energies.

a large Lorentz boost ($\gamma\beta \sim 6$) which makes it possible to measure the decay length (ℓ_d) between the nominal interaction point (the primary vertex) and the point of b hadron decay (the secondary vertex). Typically, $\langle \ell_d \rangle \sim 2700$ μm which allows events from b hadron decays to be cleanly tagged. The advent of silicon microvertex detectors has greatly improved the accuracy with which decay lengths can be measured. Other tagging methods [85], [86] include : the large average impact parameter (distance of closest approach between a track and the primary vertex) of charged tracks from b hadron decays, high transverse momentum (with respect to the jet axis) leptons coming from semileptonic b quark decay and geometrical tags based on event sphericity.

3.3 Bottom Quark Physics at LEP

3.3.1 Bottom Quark Production

Figure 3.2 shows the production cross-section for fermion pairs from e^+e^- annihilation for a range of centre of mass collision energies ($\sqrt{s}$). Experiments operating well below the Z^0 peak show the expected 1/s dependence which is characteristic of photon exchange. Around the Z^0 peak, real Z^0 exchange dominates the interaction.

Bottom quark production at LEP is an electroweak process that is described by QCD in the final state as the quarks dress themselves as hadrons. The $q\bar{q}$ production cross-section at $s = m^2_{Z^0}$ is given by [87] :

$$\sigma(q\bar{q}) \sim \frac{12\pi\alpha^2}{3s} \frac{1}{256 \sin^4\theta_w \cos^4\theta_w} \left(\frac{m^2_{Z^0}}{\Gamma^2_{Z^0}}\right) \left(\nu_e^2 + a_e^2\right) \left(\nu_q^2 + a_q^2\right), \qquad (3.1)$$

where, α is the QED coupling constant, θ_w is the weak mixing angle, m_{Z^0} is the Z^0 mass, Γ_{Z^0} is the Z^0 width, $\nu_{e,q}$ is the vector coupling for electrons (e) or quarks (q) and $a_{e,q}$ is the axial-vector coupling. The vector and axial-vector couplings can be expressed as $\nu_{e,q} = I_3(e,q) - 2\,Q(e,q)\,\sin^2\theta_w$ and $a_{e,q} = I_3(e,q)$. The nomenclature is defined in section 1.2.1.

The $q\bar{q}$ cross-section is proportional to $(\nu_q^2 + a_q^2)$ which gives a larger cross-section for $b\bar{b}$ production ($\nu_b \sim -0.7$, $a_b = -1.0$) than for $c\bar{c}$ production ($\nu_c \sim 0.4$, $a_c = +1.0$). The hadronic partial width for bottom quarks derived from a formalism similar to

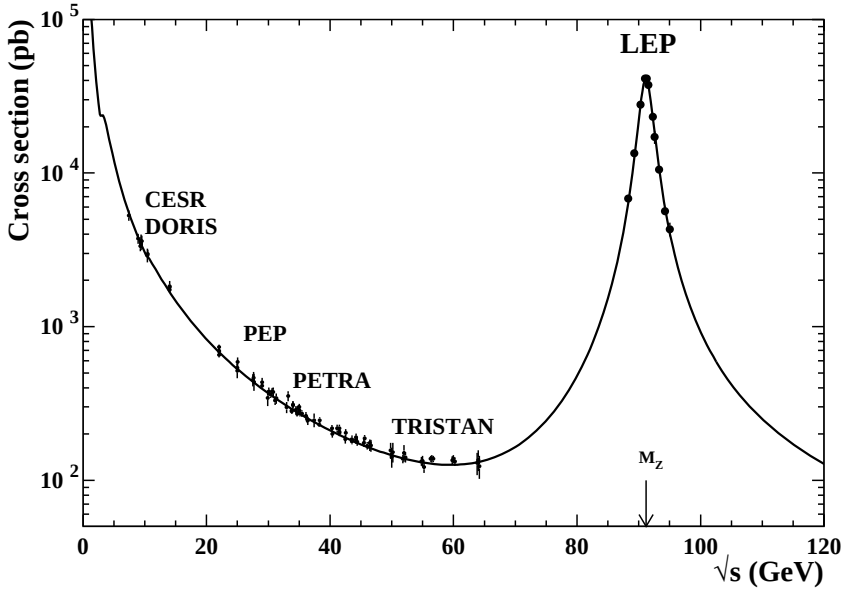

Figure 3.2: Measurements of the cross-section for $e^+e^- \rightarrow$ fermion pairs for a range of centre of mass energies. The Z^0 resonance is clearly visible.

equation 3.1 is given by [19] :

$$R_{b\bar{b}} = \frac{\Gamma\left(Z^0 \rightarrow b\bar{b}\right)}{\Gamma\left(Z^0 \rightarrow q\bar{q}\right)} = 0.2155 \pm 0.0005. \tag{3.2}$$

Experimentally, a value of :

$$R_{b\bar{b}} = \frac{\Gamma\left(Z^0 \rightarrow b\bar{b}\right)}{\Gamma\left(Z^0 \rightarrow q\bar{q}\right)} = 0.2219 \pm 0.0017 \tag{3.3}$$

is measured [19] from a global fit to electroweak data. The experimental measurement differs from the Standard Model prediction by $\sim$3.6 standard deviations. Much work is currently in progress to understand this discrepancy, which could, in principle, be the first sign that the Standard Model is not a complete description of particle dynamics at LEP energies. Measurements of $R_{b\bar{b}}$ are a sensitive probe for physics outside the Standard Model because of the weak dependence of $R_{b\bar{b}}$ on the top quark mass and total independence on the Higgs boson mass and the strong coupling constant [88]. The electroweak vertex corrections shown in figure 3.3 are specific to the process $Z^0 \rightarrow b\bar{b}$ and give $R_{b\bar{b}}$ the weak dependence on the top quark mass.

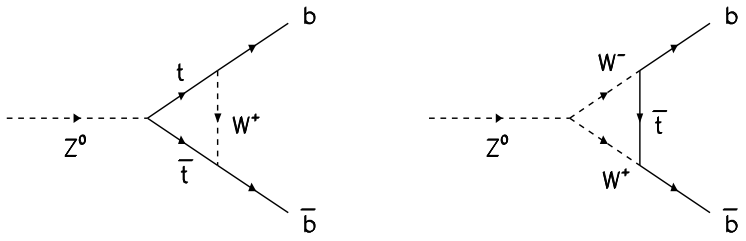

Figure 3.3: Electroweak vertex corrections, specific to the $Z^0 \rightarrow b\bar{b}$ process, from the top quark.

3.3.2 Bottom Quark Polarisation

If the scattering angle between the incoming electron direction and the outgoing quark direction is θ then the differential $q\bar{q}$ cross-section takes the form :

$$\frac{d\,\sigma(q\bar{q})}{d\cos\theta} \propto (1 + \cos^2\theta + \frac{8}{3}A_{fb}\cos\theta), \tag{3.4}$$

where :

$$A_{fb} = \frac{3}{4}\frac{2\nu_e a_e}{(\nu_e^2 + {a_e}^2)}\frac{2\nu_q a_q}{(\nu_q^2 + {a_q}^2)}. \tag{3.5}$$

A forward-backward asymmetry is observed in the $q\bar{q}$ differential cross-section due the term linear in $\cos\theta$. The magnitude of the asymmetry is quantified by A_{fb} and is dependent on the vector and axial vector coupling strengths for the incoming electrons and outgoing quarks.

A quark polarisation variable ($\mathcal{P}_q$) can be constructed if the left and right handed quark states in the differential cross-section ($D = d\,\sigma(q\bar{q})/d\cos\theta$) are separated :

$$\mathcal{P}_q = \frac{D(R) - D(L)}{D(R) + D(L)}. \tag{3.6}$$

It can be shown [87] that the mean b quark polarisation can be expressed as :

$$\langle\mathcal{P}_b\rangle = \frac{24\sin^2\theta_w - 18}{9 + (4\sin^2\theta_w - 3)^2} = -0.936. \tag{3.7}$$

This polarisation is destroyed during the hadronisation of the b quarks to spin 0 and spin 1 B mesons but is predicted to be partially retained in spin $\frac{1}{2}$ b baryons since the light quarks in the baryon are arranged in a singlet of spin. Theory [89] predicts the mean b baryon polarisation ($\langle\mathcal{P}_{\Lambda_b^0}\rangle$) to lie in the range –47→–94%, while the ALEPH collaboration have made a preliminary measurement [90] of :

$$\langle\mathcal{P}_{\Lambda_b^0}\rangle = -0.26^{+0.23}_{-0.20}\,(\text{stat})\,^{+0.13}_{-0.12}\,(\text{syst}). \tag{3.8}$$

3.3.3 Bottom Quark Hadronisation and Fragmentation

The primary b quarks in the reaction $Z^0 \rightarrow b\bar{b}$ have never been observed directly. This is also true for any quark flavour in any reaction. The process in which the bare primary quarks dress themselves as observable hadrons is called hadronisation. Hadronisation is described in the framework of QCD as the degradation of quark energies by gluon emission and the associated production of $q\bar{q}$ pairs from the vacuum. Eventually, the momentum transfer in this process becomes too small to be modelled using perturbative techniques (when $\alpha_s \sim 1$). At this point phenomenological fragmentation models are used to predict subsequent $q\bar{q}$ production and hadron formation. Understanding fragmentation is important as it affects many experimentally measured quantities.

Various models have been proposed to describe the fragmentation process. One such model pertinent to the studies described in this thesis is the Lund model [91], based on the string model of Artu et al. [92]. As the primary quark and anti-quark fly apart, a string of colour flux lines is stretched between them. The colour string has fixed energy per unit length (k$\sim$1 GeV fm^{-1} $\sim$0.2 GeV^2) and therefore the potential energy between the quarks rises linearly with separation. As the potential energy stored in the string increases, the string may break into a (di)quark–anti-(di)quark pair, with the quark masses coming from the potential energy of the string. Di-quark pairs are needed to allow baryons to be produced. Alternately, a popcorn mechanism [93] forms baryons from the successive production of $q\bar{q}$ pairs.

A tunnelling process is thought to be responsible for the creation of a $q\bar{q}$ pair from the vacuum. If μ is the quark mass then the probability ($\mathbb{P}$) of exciting a $q\bar{q}$ pair can be expressed as :

$$\mathbb{P} \propto \exp\left(-\pi\mu^2/k\right). \tag{3.9}$$

The creation of a $c\bar{c}$ pair[c] suppressed by a factor of $\sim 10^{-11}$ with respect to the creation of a $u\bar{u}$ pair and even more so for a $b\bar{b}$ pair. Therefore, the presence of a b hadron (bqq, $b\bar{q}$) in a multihadronic final state is a signature for a primary branching into a $b\bar{b}$ pair, but the presence of a c hadron (cqq, $c\bar{q}$) could be a

[c]The process $g \rightarrow q\bar{q}$ is ignored. The OPAL collaboration have measured the average number of gluons splitting into a $c\bar{c}$ pair per hadronic event to be $\bar{n}_{g\rightarrow c\bar{c}} = (2.27 \pm 0.28 \pm 0.41) \times 10^{-2}$ and estimate $\bar{n}_{g\rightarrow b\bar{b}} = (3.0 \pm 1.2) \times 10^{-3}$ [94].

signature for primary branching into a $c\bar{c}$ pair or b hadron decay into a c hadron.

In higher order QCD, where a gluon can radiate another gluon, the radiated gluon is treated as a kink in the string carrying energy and momentum. A hadron is created when the string breaks either side of the kink. Since gluons carry more colour than quarks it was predicted that there should be a depletion in particle production between two quark jets[d] compared to between quark and gluon jets. This is called the 'string effect' and was first observed by the JADE collaboration [95] at a centre of mass energy of 35 GeV. This effect has also been observed by the LEP collaborations [96] at a centre of mass energy of 90 GeV.

The exact form of the fragmentation process is poorly known. The fraction of longitudinal momentum carried by the colour singlets formed when the string is broken are described by phenomenological distributions called fragmentation functions. The function is parameterised by a fragmentation variable that is usually defined as :

$$z = \frac{E_{hadron}}{E_q}, \tag{3.10}$$

where, E_q and E_{hadron} are the energy carried by the fragmenting quark and the resulting hadron respectively. Since E_q is not an experimental observable, another (measurable) quantity :

$$x_E = \frac{E_{hadron}}{E_{beam}}, \tag{3.11}$$

is often used as the fragmentation variable instead.

The LUND symmetric fragmentation function [91] is used to describe the fragmentation function for light quark (u, d, s) hadron production :

$$f(z) \propto \frac{(1-z)^a}{z} \exp\left(\frac{-bm_T^2}{z}\right), \tag{3.12}$$

where, m_T is the transverse mass[e] of the light quark hadron and a and b are constants. The Peterson function [97] is a popular fragmentation function for heavy quarks based on kinematics. The function is defined as :

$$f(z) \propto \frac{1}{z\left(1-\frac{1}{z}-\frac{\varepsilon_Q}{1-z}\right)^2}, \tag{3.13}$$

[d] Usually the two most energetic jets in a multi-jet event.

[e] Transverse mass is defined as : $m_T^2 = p_T^2 + m^2$, where p_T is the hadron transverse momentum with respect to the string and m is the hadron mass.

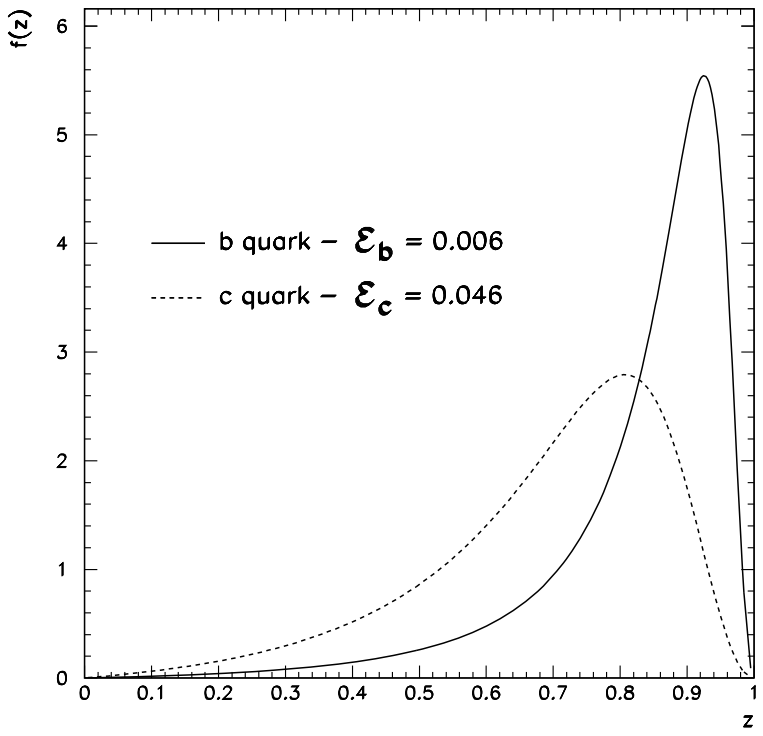

Figure 3.4: The form of the Peterson function used to model the fragmentation for bottom (solid line) and charm (dashed line) quarks.

and the functional shape is determined by the parameter :

$$\varepsilon_Q = \frac{m_q^2}{m_Q^2}, \tag{3.14}$$

where, m_Q is the heavy quark mass and m_q is an effective mass for the light quark produced as a fragmentation remnant. The Peterson function is used to describe the fragmentation of b and c quarks in the Monte Carlo generators used in this thesis. Figure 3.4 shows the form of the Peterson function using values of ε_b=0.006 and ε_c=0.046. The Peterson function has a maximum at high z, where the heavy quark production momentum is retained by the resultant hadron. The Peterson form has been verified as a reasonable description of heavy quark fragmentation by experimental measurements [98]. Recent measurements [99] of the fraction of beam energy taken by bottom mesons ($\langle x_E \rangle_B$) during fragmentation indicate that :

$$\langle x_E \rangle_B = 0.701 \pm 0.008. \tag{3.15}$$

The Peterson form for bottom quarks shown in figure 3.4 generates $\langle x_E \rangle_B = 0.680$[f].

[f] The values of ε_b and ε_c shown here are used by the default Monte Carlo samples described in

3.3.4 Bottom Meson Production

Bottom mesons dominate b hadron production at LEP. A high energy b ($\bar{b}$) quark produced from Z^0 decay will join with a single quark from the vacuum about 90% of the time to produce a B meson. The other 10% of the time, a di-quark from the vacuum allows the formation of a b baryon. The production ratio for the common b hadrons is approximately[g] :

$$B^0 \ : B^+ \ : B_s^0 \ : \Lambda_b^0 \ = 0.4 \ : 0.4 \ : 0.1 \ : 0.1, \tag{3.16}$$

where, Λ_b^0 denotes a generic b baryon and the production rate of B_c mesons are thought to be negligible, due to the large charm quark mass that must be popped from the vacuum[h].

At LEP approximately 30% of all B mesons produced are in an orbitally excited (L=1) state denoted B^{**}, and decay via the strong interaction into ground state B mesons [100, 102]. The ground state pseudoscalar and vector B mesons are denoted B (25%[i]) and B^* (75%[i]) respectively [101]. The factor of three in the primary B/B^* production ratio is as expected from the naive spin counting picture of 2J+1 equally populated helicity states. The B^* can only decay electromagnetically, via photon emission, as the B–B^* mass difference is only 46 MeV/c^2. During the fragmentation process when a B_s^0 meson is formed, the production of strange quarks from the vacuum is suppressed, as already shown in equation 3.9. There is also another factor that reduces B_s^0 production due to suppression of B_s^{**} decay modes. The decay $B_s^{**} \rightarrow B_{u,d}^{(*)} K$ is seen to dominate over the decay $B_s^{**} \rightarrow B_s^0 \pi$ which is forbidden due to isospin conservation [102].

In the following section the production of Λ^0 baryons in B meson decays is discussed in some detail, as this plays a prominent role in the measurements presented in later chapters.

---

section 4.8.2. Another Monte Carlo sample with optimised bottom fragmentation parameters is also described which gives values of $\langle x_E \rangle_B$ that are compatible with experimental measurements.

[g] The masses of the common b hadrons are : $m(B^{\pm}) = (5278.7 \pm 2.0)$ MeV/c^2, $m(B^0) = (5278.9 \pm 2.0)$ MeV/c^2, $m(B_s^0) = (5375 \pm 5)$ MeV/c^2 and $m(\Lambda_b^0) = (5641 \pm 30)$ MeV/c^2 [28].

[h] See equation 3.9.

[i] For primary B mesons.

3.3.4.1 The Production of Λ^0's in Bottom Meson Decays

Experiments running on the $\Upsilon(4s)$ have provided the wealth of information on B meson decays to baryons. In particular, results from the CLEO and ARGUS collaborations have provided valuable information on the decay of B mesons to Λ^0's. Since these experiments run on the $\Upsilon(4s)$ B_s^0 mesons are not produced.

When a B meson decays to a Λ^0 it must also produce another anti-baryon in the final state. In order to produce a baryon-pair, two di-quark pairs must be popped from the vacuum, which results in the baryonic decay mode of the B meson being highly suppressed compared to the mesonic decay modes, as shown by the branching ratio Br(B meson $\rightarrow$ baryons) = (6.8$\pm$0.6)% [28]. The CLEO collaboration have identified two dominant baryonic decay modes of the B meson [103] :

$$\text{B meson} \rightarrow \mathrm{Y_c}\,\overline{\mathrm{N}}\,\mathrm{X}, \tag{3.17}$$

$$\text{B meson} \rightarrow \mathrm{D\,N}\,\overline{\mathrm{N}}\,\mathrm{X}, \tag{3.18}$$

where, table 3.1 explains the nomenclature.

By measuring :

$$\frac{\mathrm{Br(B} \rightarrow \Lambda^0\overline{\Lambda^0}\mathrm{X)}}{\mathrm{Br(B} \rightarrow \Lambda^0\mathrm{X)}} < 0.5\%, \tag{3.19}$$

at 90% confidence level, the CLEO collaboration concludes that the other two baryonic decay modes, B$\rightarrow \Xi_c\overline{\mathrm{Y}}$X and DY$\overline{\mathrm{Y}}$X are heavily suppressed since these are the only two which can result in a $\Lambda^0\overline{\Lambda^0}$ in the final state.

A search for B meson decays to DN$\overline{\mathrm{N}}$X was made by searching for $\mathrm{D}^{*+}\mathrm{p\bar{p}X}$ final states. No such states were found and so the dominant baryonic decay mode was

Generic Name	Baryons
N	p, n, $\Delta^{(*)}$
$\mathrm{Y_c}$	Λ_c^+, Σ_c^0, $\Sigma_c^{\pm}$
Y	Λ^0, Σ^0, $\Sigma^{\pm}$
D	$\mathrm{D}^{0(*)}$, $\mathrm{D}^{\pm(*)}$
X	Any charmless meson

Table 3.1: The nomenclature used by the CLEO collaboration to categorise bottom meson decays.

determined to be $Y_c\overline{N}X$. The dominant production mechanism for a Λ^0 in a B meson decay is therefore through the decay $B\rightarrow \Lambda_c^+X$, followed by $\Lambda_c^+ \rightarrow \Lambda^0X$. The CLEO collaboration measures :

$$\mathrm{Br}(B \rightarrow \Lambda_c^+X) = (6.4 \pm 1.1)\%. \tag{3.20}$$

The ARGUS [104] and CLEO collaborations measure $\mathrm{Br}(B \rightarrow \Lambda^0X)$ to be (4.2±0.8)% and (3.8±0.7)% respectively. These measurements are averaged [28] to give :

$$\mathrm{Br}(B \rightarrow \Lambda^0X) = (4.0 \pm 0.5)\%. \tag{3.21}$$

3.3.5 Bottom Baryon Production

3.3.5.1 Overview

The Λ_b^0 is the lightest b baryon, consisting of a ud di-quark system in a spin zero state together with a single b quark. The other $J^P = \frac{1}{2}^+$ b baryons with a single b quark are : Σ_b^+ (uub), Σ_b^0 (udb), Σ_b^- (ddb), Ξ_b^- (dsb), Ξ_b^0 (usb) and Ω_b^- (ssb). The Σ_b^*, Ξ_b^* and Ω_b^* have $J^P = \frac{3}{2}^+$.

The Λ_b^0 is assumed to be the dominant weakly decaying b baryon produced at LEP energies. Two further weakly decaying b baryons, the Ξ_b and the Ω_b, are also kinematically allowed but require strange di-quark pairs to be popped from the vacuum, which suppresses their production rate. The Σ_b^0 baryon has the same quark make-up as the Λ_b^0 and decays via the electromagnetic interaction, $\Sigma_b^0 \rightarrow \Lambda_b^0\ \gamma$. The charged $\Sigma_b^\pm$ can decay via the strong ($\Sigma_b^\pm \rightarrow \Lambda_b^0\ \pi^\pm$) or weak ($\Sigma_b^\pm \rightarrow \Sigma_c^\mp$ X) interactions depending on the mass difference between the Λ_b^0 and the $\Sigma_b^\pm$. It is thought that the strong decay dominates since quark model calculations [105] and non-relativistic potential models [106] predict that the $\Sigma_b^\pm$ has a mass approximately 180–210 MeV/c^2 above the Λ_b^0.

The first claim for the observation of a beauty baryon came in 1981 from the R415 group based at the ISR accelerator at CERN using the SFM facility [107]. The group used a positron trigger to select semileptonic decays of the b quark and time-of-flight particle identification to select $K^-\pi^+$ combinations in the D^0 mass range. This preferentially selected the decay $\Lambda_b^0 \rightarrow pD^0\pi^-$. They measured a Λ_b^0 mass of 5425^{+175}_{-75} MeV/c^2 with a signal of 30±5 events over background. A second group

using the same SFM facility with similar operating conditions failed to see the same effect [108], [109]. Furthermore, when the first group repeated their study with much improved machine luminosity before the ISR was shut down they failed to show a more significant signal in their original discovery channel [110]; these results were not published until 1991 !

The next reported Λ_b^0 sighting came from the 1988–89 data of the UA1 experiment, taken at the SPS $p\bar{p}$ accelerator, again at CERN [111]. At a centre of mass energy of 630 GeV an integrated luminosity of 4.7 pb^{-1} was collected. Signals were reported for the decay $\Lambda_b^0 \rightarrow J/\psi\,\Lambda^0$, where $J/\psi \rightarrow \mu^+\mu^-$ and $\Lambda^0 \rightarrow p\pi^-$. The group claimed to see a 5 standard deviation effect in the $J/\psi\,\Lambda^0$ mass spectrum at a Λ_b^0 mass of 5640$\pm$58 MeV/c^2. They also quoted a product branching ratio of :

$$f(b \rightarrow \Lambda_b^0)\,Br(\Lambda_b^0 \rightarrow J/\psi\,\Lambda^0) = (0.18 \pm 0.11)\%. \tag{3.22}$$

This claim from the UA1 collaboration has not been confirmed by the LEP collaborations or the CDF collaboration at Fermilab. The CDF collaboration [112] collected 2.6 pb^{-1} of $p\bar{p}$ data at a centre of mass energy of 1.8 TeV and amassed similar statistics to UA1 for $J/\psi\,\Lambda^0$ decays. No peak was seen in the $J/\psi\,\Lambda^0$ mass spectrum and an upper limit of :

$$f(b \rightarrow \Lambda_b^0)\,Br(\Lambda_b^0 \rightarrow J/\psi\,\Lambda^0) < 0.05\%, \tag{3.23}$$

was set with a 90% confidence level. The OPAL collaboration [113] has also searched for the $J/\psi\,\Lambda^0$ decay mode using 1990–93 data and also observe no signal. They set an upper limit at 90% confidence level of :

$$f(b \rightarrow \Lambda_b^0)\,Br(\Lambda_b^0 \rightarrow J/\psi\,\Lambda^0) < 0.034\%, \tag{3.24}$$

which is tighter than the limit set by the CDF collaboration. The OPAL collaboration have also looked at the decay channel $\Lambda_b^0 \rightarrow \Lambda_c^+\pi^+$ [113], where the Λ_c^+ decays to a $pK^-\pi^+$ final state. Once again, they see no signal and set a 90% confidence level limit of :

$$f(b \rightarrow \Lambda_b^0)\,Br(\Lambda_b^0 \rightarrow \Lambda_c^+\pi^+) < 0.2\%. \tag{3.25}$$

The ALEPH collaboration have produced a preliminary result [114], from 1991–94 data, for the $\Lambda_b^0 \rightarrow \Lambda_c^+\pi^+$ decay mode. They look for a Λ_c^+ decaying to $pK^-\,\pi^+$, $p\,\overline{K^0}$

or $\Lambda^0\ \pi^+\ \pi^-\ \pi^+$. They observe a signal of 4 events over approximately 1 background event, and assign the signal a significance of 2→3 standard deviations. Assuming the signal is due exclusively to Λ_b^0 decays they quote a Λ_b^0 mass of 5621±23 MeV/c^2 and a rate of[j] :

$$f(b \to \Lambda_b^0)\, Br(\Lambda_b^0 \to \Lambda_c^+ \pi^+) = (1.0 \pm 0.5)\%. \tag{3.26}$$

Fully exclusive hadronic decay modes of the b baryon are predicted to be very small ($\mathcal{O}(1\%)$) from calculations [115] based around the Heavy Quark Effective Theory bottom baryon form factors of Isgur and Wise [117]. Evidence for inclusive b baryon production is therefore more forthcoming from the study of $\Lambda^0\ell$ and $\Lambda_c^+\ell$ correlations. The b baryon decays semileptonically, producing a high momentum lepton which can be charge correlated to a high momentum Λ^0 ($\Lambda^0\ell^-$) or Λ_c^+ ($\Lambda_c^+\ell^-$).

Using data from the 1990 LEP run the ALEPH collaboration reported the first evidence for b baryon production through $\Lambda^0\ell^-$ correlations using 160 $\times 10^3$ hadronic Z^0 decays [118]. The background is subtracted using 'wrong-sign' $\Lambda^0\ell^+$ combinations. The current combined results of studies of $\Lambda^0\ell^-$ correlations from the ALEPH [119], DELPHI [120] and OPAL [121] collaborations yields :

$$f(b \to \Lambda_b^0)\, Br(\Lambda_b^0 \to \Lambda^0 \ell^- \bar{\nu} X) = (0.29 \pm 0.03)\%. \tag{3.27}$$

Using $\Lambda^0\ell$ correlations can only provide evidence for generic b baryon production, since Λ_b^0 and Ξ_b decays give the same $\Lambda^0\ell^-$ final state. The ALEPH [119] and DELPHI [122] collaborations use a similar technique with $\Lambda_c^+\ell^-$ correlations, where the Λ_c^+ is reconstructed through the decay $\Lambda_c^+ \to pK^-\pi^+$ and wrong sign combinations are again used to subtract background. The combined result is :

$$f(b \to \Lambda_b^0)\, Br(\Lambda_b^0 \to \Lambda_c^+ \ell^- \bar{\nu} X) = (1.35^{+0.54}_{-0.50})\%. \tag{3.28}$$

The $\Lambda_c^+\ell^-$ correlations are dominated by Λ_b^0 decays but the event samples are small compared to the $\Lambda^0\ell$ samples, as the Λ_c^+ must be exclusively reconstructed.

[j] The DELPHI collaboration [116] have recently measured a bottom baryon mass of (5668±18) MeV/c^2. They use three events in the $\Lambda_c^+\pi^-$ channel and one in the $\Lambda_c^+ a_1^-$ channel. They fail to find any events in the $J/\psi\Lambda^0$ channel.

3.3.5.2 The Bottom Baryon Production Rate

All of the bottom baryon branching ratios quoted so far have included the unknown parameter f(b$\rightarrow \Lambda_b^0$), which represents the number of b baryons produced per bottom quark in $Z^0 \rightarrow b\bar{b}$ events at LEP energies. Two ways to evaluate this quantity are :

1. The branching ratio shown in equation 3.27 can be expressed as :

$$f(b \rightarrow \Lambda_b^0)\,Br(\Lambda_b^0 \rightarrow \Lambda^0 \ell^- \bar{\nu} X) = \mathbf{f(b \rightarrow \Lambda_b^0)}\,Br(\Lambda_b^0 \rightarrow \Lambda_c^+ \ell^- \bar{\nu} X)\,Br(\Lambda_c^+ \rightarrow \Lambda^0 X). \tag{3.29}$$

The $\Lambda_c^+ \rightarrow \Lambda^0 X$ branching ratio has been measured as [28] :

$$Br(\Lambda_c^+ \rightarrow \Lambda^0 X) = (35 \pm 11)\%. \tag{3.30}$$

An estimation of $Br(\Lambda_b^0 \rightarrow \Lambda_c^+ \ell^- \bar{\nu} X)$ can be obtained by scaling the semileptonic B meson branching ratio[k] [28] :

$$Br(B \rightarrow D\,\ell\,\nu\,X) = (10.43 \pm 0.24)\%, \tag{3.31}$$

by the lifetime ratio [99]:

$$\tau(\Lambda_b^0)/\tau(B) = 0.75 \pm 0.05, \tag{3.32}$$

to account for the expected enhancement of the hadronic decay modes of the bottom baryon, to yield :

$$Br(\Lambda_b^0 \rightarrow \Lambda_c^+\,\ell^-\,\bar{\nu}\,X) = (7.8 \pm 0.6)\%. \tag{3.33}$$

Combining these results predicts :

$$\underline{f(b \rightarrow \Lambda_b^0) = 0.11 \pm 0.04.} \tag{3.34}$$

2. Individual B meson production rates at LEP energies can also be used to predict the bottom baryon production rate. Current results indicate that :

$$f(b \rightarrow B^+) + f(b \rightarrow B^0) = 0.81 \pm 0.11 \ \ [123], \tag{3.35}$$

$$f(b \rightarrow B_s^0) = 0.12 \pm 0.03 \ \ [124]. \tag{3.36}$$

If the remainder of b hadron production is assumed to be from b baryons :

$$\underline{f(b \rightarrow \Lambda_b^0) = 0.08 \pm 0.04.} \tag{3.37}$$

[k] The result comes from the $\Upsilon(4s)$ experiments, where B represents either a B^0 or $B^\pm$ meson and D represents a charmed (non-strange) meson.

The error has been assigned to cover all reasonable variations, as adopted in [125].

The error weighted average of these results yields :

$$\boxed{\mathrm{f}(\mathrm{b} \to \Lambda_\mathrm{b}^0) = 0.09 \pm 0.03.} \tag{3.38}$$

3.3.5.3 The Production of Λ^0's in Bottom Baryon Decays

To date, the only published measurement of the Λ^0 production rate in bottom baryon decays comes from the DELPHI collaboration [126], who estimate :

$$\underline{\mathrm{f}(\mathrm{b} \to \Lambda_\mathrm{b}^0)\mathrm{Br}(\Lambda_\mathrm{b}^0 \to \Lambda^0 \mathrm{X}) = (2.2 \pm 1.5)\%.} \tag{3.39}$$

Their estimate is derived from a measurement of Br(b hadron $\to \Lambda^0$X), where a lifetime tag based on impact parameter significance is used to produce an enhanced sample of $\mathrm{Z}^0 \to \mathrm{b\bar{b}}$ events. A technique based on rapidity is used to select Λ^0's originating from bottom hadron decays rather than bottom fragmentation.

An independent estimate of $\mathrm{f}(\mathrm{b} \to \Lambda_\mathrm{b}^0)\mathrm{Br}(\Lambda_\mathrm{b}^0 \to \Lambda^0 \mathrm{X})$ can be derived from the relationship :

$$\mathrm{f}(\mathrm{b} \to \Lambda_\mathrm{b}^0)\mathrm{Br}(\Lambda_\mathrm{b}^0 \to \Lambda^0 \mathrm{X}) = \frac{\mathrm{f}(\mathrm{b} \to \Lambda_\mathrm{b}^0)\mathrm{Br}(\Lambda_\mathrm{b}^0 \to \Lambda^0 \ell^- \bar{\nu} \mathrm{X})}{\mathrm{Br}(\Lambda_\mathrm{b}^0 \to \Lambda_\mathrm{c}^+ \ell^- \bar{\nu} \mathrm{X})}. \tag{3.40}$$

The value of $\mathrm{f}(\mathrm{b} \to \Lambda_\mathrm{b}^0)\mathrm{Br}(\Lambda_\mathrm{b}^0 \to \Lambda^0 \ell^- \bar{\nu} \mathrm{X})$ comes from equation 3.27 and equation 3.33 defines $\mathrm{Br}(\Lambda_\mathrm{b}^0 \to \Lambda_\mathrm{c}^+ \ell^- \bar{\nu} \mathrm{X})$. Combining these values yields :

$$\underline{\mathrm{f}(\mathrm{b} \to \Lambda_\mathrm{b}^0)\mathrm{Br}(\Lambda_\mathrm{b}^0 \to \Lambda^0 \mathrm{X}) = (3.7 \pm 0.5)\%,} \tag{3.41}$$

which is compatible with the measurement from the DELPHI collaboration.

3.3.6 The Theory of Bottom Hadron Lifetimes

3.3.6.1 The Spectator Model

The spectator model was the first attempt to predict bottom hadron lifetimes. The dynamics of the decay are very similar to muon decay, as shown in figure 3.5. The semileptonic partial decay width for the free heavy quark ($\Gamma = 1/\tau_\mathrm{b}$) is calculable by analogy to the dynamics of muon decay as :

$$\Gamma(\mathrm{b} \to \mathrm{q}\, \ell\, \nu_\ell) = 1/\tau_\mathrm{b} = \frac{\mathrm{G_F^2\, m_b^5}}{192\, \pi^3} |\mathrm{V_{qb}}|^2\, \mathcal{P}, \tag{3.42}$$

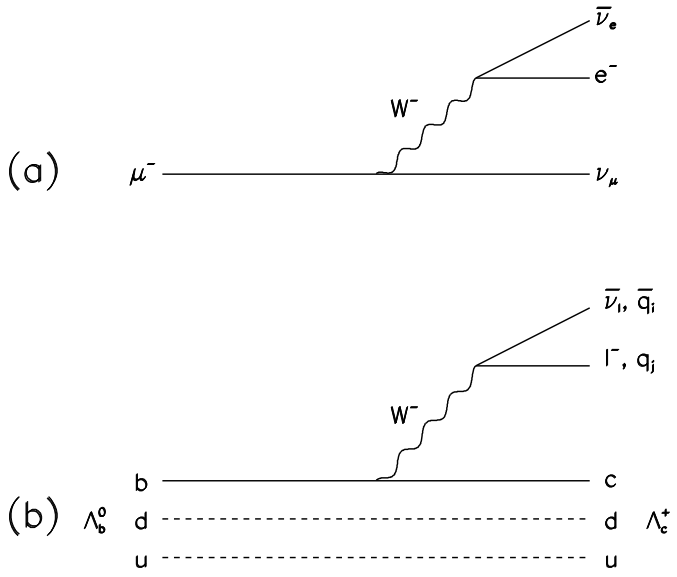

Figure 3.5: A comparison between muon decay (a) and the spectator model decay of a bottom baryon (b).

where, G_F is the Fermi constant, m_b is the b quark mass, $|V_{qb}|$ is the relevant KM matrix element and $\mathcal{P}$ is a phase space factor to account for the finite mass of the final state quark (q). For $b \to c\,\ell\,\nu_\ell$ ($\ell = \mu, e$), $\mathcal{P} \sim 0.5$.

This naive model predicted that all bottom (and charm) hadrons would have the same lifetimes. This prediction was first tested on the charm system, where it failed miserably to predict the experimentally observed pattern of lifetimes. A great deal of theoretical work was needed to fit the observed lifetime pattern,

$$\tau(D^+) > \tau(D^0) \geq \tau(D_s^+) > \tau(\Lambda_c^+), \tag{3.43}$$

into the framework of the spectator model. A more realistic picture of heavy quark decay is shown in figure 3.6. The spectator weak interaction occurs in the small inner circle with the larger outer circle denoting the QCD confinement region. It is clear that both electroweak and QCD interactions play an important role in heavy quark decays. On the short distance scale, weak interaction and QCD gluon effects can be calculated exactly, but long distance QCD effects (final state interactions, soft gluon radiation and quark confinement into hadrons) cannot be calculated perturbatively.

The inclusion of such QCD effects into the spectator model gave good agreement with data for the hadronic branching ratios of b and c hadrons. However, the lifetime

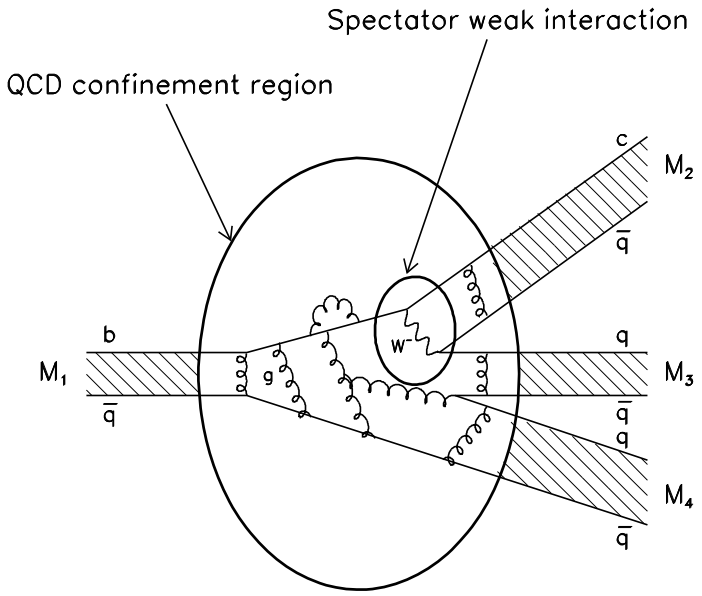

Figure 3.6: A schematic representation of a bottom meson decay. The decay involves both electroweak and QCD effects. The small inner circle contains the electroweak interaction and the larger outer circle depicts the perturbative QCD confinement region.

hierarchy was not accounted for. The heavy hadron decay must depend on more than just the heavy quark. The lifetime hierarchy was explained by introducing the decay scenarios shown in figure 3.7. Ignoring penguin decay diagrams, which are thought to be heavily suppressed due to the small KM matrix elements involved, the decay diagrams that are used to explain the bottom hadron lifetime hierarchy can be divided into three types :

Interference Interference occurs between internal and external spectator diagrams when the respective final states are identical. The interference term for bottom baryon decays can be constructive or destructive [127], depending on the exact form of the decay. However, the interference is destructive overall, and results in a small lifetime difference between B mesons and b baryons. The effect is far more important in B meson decays and is responsible for the lifetime difference between B^+ and B^0 mesons. Only charged B meson decays can produce identical final states, as shown in figure 3.8, resulting in destructive interference (after calculating the relevant QCD radiative corrections) and the prediction that : $\tau(B^+) > \tau(B^0)$. Interference effects are suppressed in other B meson decays, as $|V_{ub}| \ll |V_{cb}|$ and $|V_{us(cd)}| \ll |V_{ud(cs)}|$.

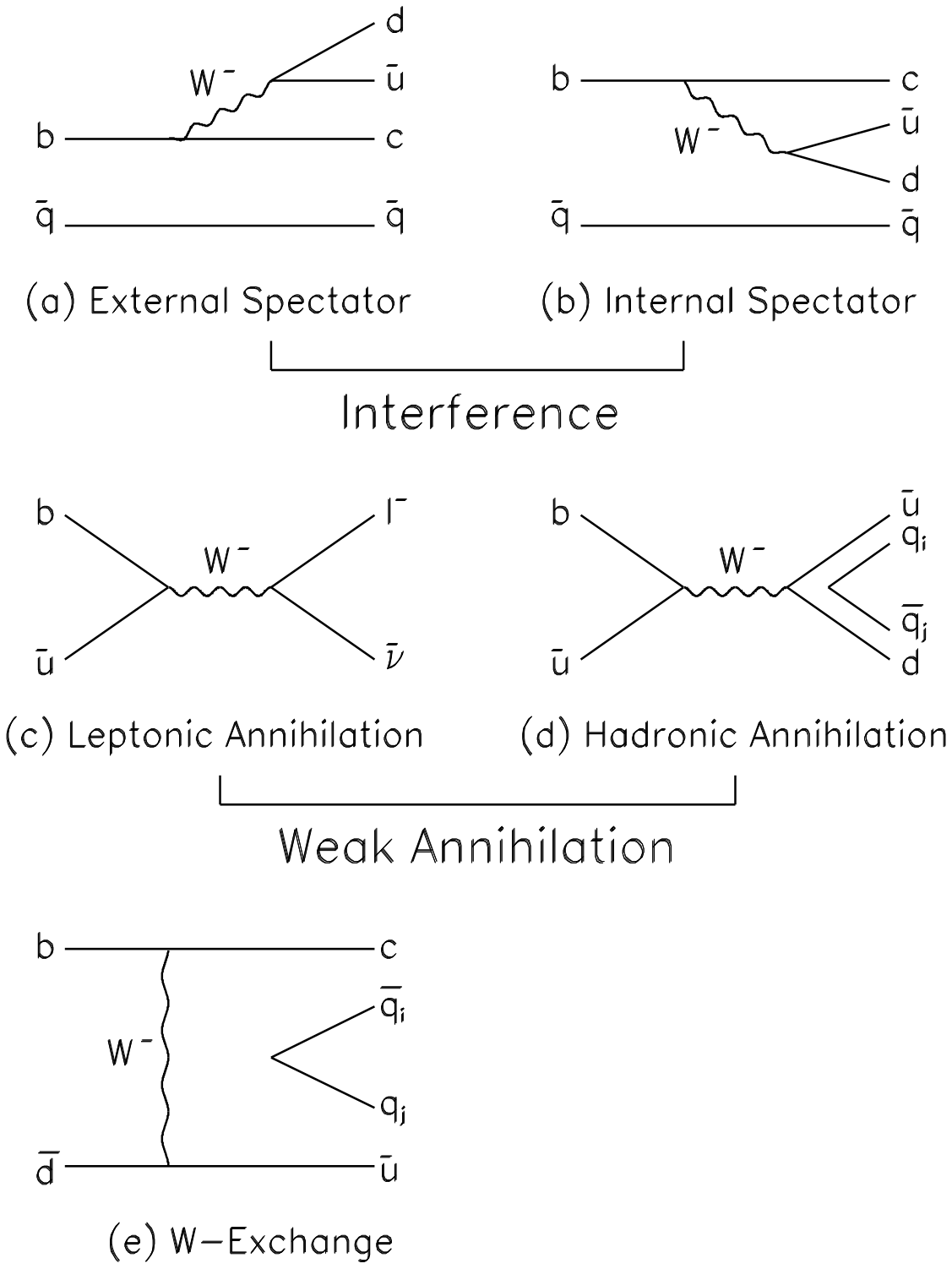

Figure 3.7: Bottom hadron decay diagrams that can be used to explain the lifetime hierarchy observed in the bottom hadron system. The interaction of the spectator decays shown in diagrams (a) and (b) give rise to interference effects. Diagrams (c) and (d) describe the weak annihilation process and diagram (e) describes the W-exchange processes.

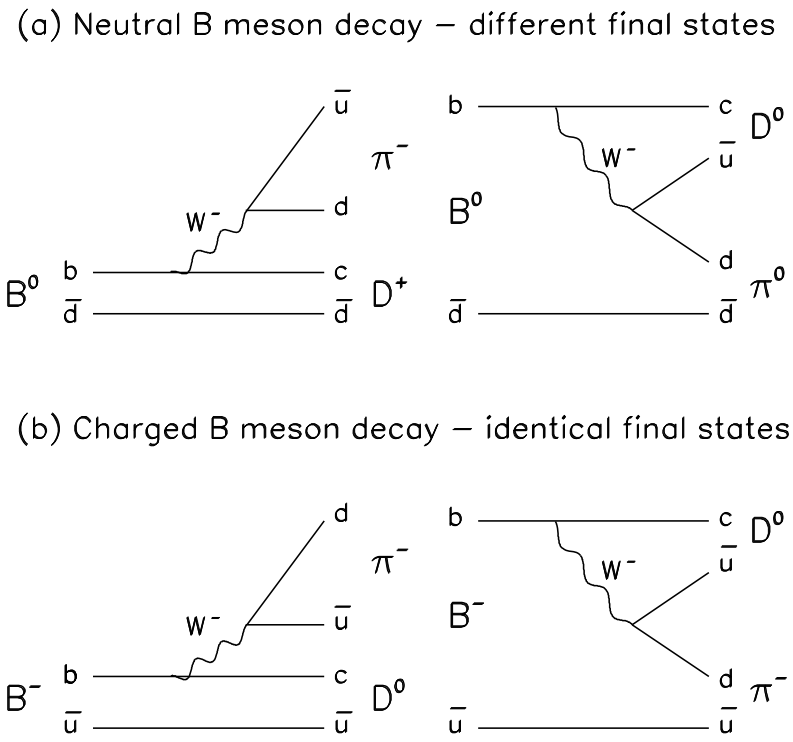

Figure 3.8: Interference effects that are responsible for the lifetime differences between charged and neutral bottom mesons.

W-Exchange The W-exchange process has the largest effect on the b baryon lifetime, where the extra spectator quarks allow the process to proceed without being helicity suppressed. The effect is much larger than interference and lowers the b baryon lifetime with respect to the B mesons. Of the mesons, only the B^0 and B_s^0 mesons experience W-exchange. The W-exchange process is heavily helicity suppressed for B mesons, in the same way that $\pi^- \to e^- \bar{\nu}_e$ is suppressed relative to $\pi^- \to \mu^- \bar{\nu}_\mu$. There have been reports [128] that the bremsstrahlung of soft spin 1 gluons act to greatly reduce the helicity suppression, but these claims are disputed [129].

Weak Annihilation Weak annihilation has a small impact on the b hadron lifetime hierarchy, but is included for completeness. A b quark can annihilate with a valence anti-quark via a W^-. This process only affects the B^- meson but is suppressed as $|V_{ub}|$ is small. Although a distinction is often made between W-exchange in the 's' (called weak annihilation here) and 't' channels (called W-exchange here), the separation is artificial as the operators describing these

processes are mixed in the QCD description that is described in the next section.

Taking all these effects into account, the following lifetime hierarchy is predicted :

$$\tau(\mathrm{B}^+) > \tau(\mathrm{B}^0) \geq \tau(\mathrm{B}_\mathrm{s}^0) > \tau(\Lambda_\mathrm{b}^0), \tag{3.44}$$

but, whereas in the charm system there is a factor of $\sim$5 difference between the D^+ and Λ_c^+ lifetimes, the corresponding lifetime difference in the bottom system is predicted to be $\leq$10% due to the larger b quark mass [127].

3.3.6.2 Predictions from QCD Expansions

There are four theoretical approaches that allow bottom hadron decays to be to be modelled : QCD sum rules, Monte Carlo simulations of lattice 'quenched' QCD, Heavy Quark Effective Theory and $1/\mathrm{m_b}$ expansions [130]. All are intrinsically based on QCD. Each technique needs to assume quark-hadron duality [131]. However, the quark level, where theorists construct their theories, is obviously different to the experimentalist's world of hadrons. At the quark level, all hadrons have the same lifetime, but big differences in lifetime for the same quark flavour are measured experimentally, ie : $\tau(\mathrm{K}^+)/\tau(\mathrm{K}_\mathrm{s}^0) \sim$140.

The only technique that will allow the treatment of inclusive b hadron decays and therefore the prediction of b hadron lifetimes is $1/\mathrm{m_b}$ expansions; which are described in this section.

The total rate for a bottom hadron ($\mathrm{H_b}$) to decay to an inclusive final state (X) can be expressed through an expansion in powers of $1/\mathrm{m_b}$ to order $1/\mathrm{m_b^3}$ as[l] :

$$\Gamma(\mathrm{H_b} \to \mathrm{X}) = \frac{\mathrm{G_F^2 m_b^5}}{192\pi^3} |\mathrm{KM}|^2 \left(\alpha \mathrm{A} + \beta \frac{\mathrm{B}}{\mathrm{m_b^2}} + \gamma \frac{\mathrm{C}}{\mathrm{m_b^3}} + \mathcal{O}\left(\frac{1}{\mathrm{m_b^4}}\right)\right), \tag{3.45}$$

where, α, β and γ are dimensionless coefficients that depend on the quark level characteristics of the final state. Phase space considerations enter through the ratio of the masses of the final state quarks to the mass of the b quark and |KM| denotes the appropriate combination of KM matrix elements for the processes under

[l]The $1/\mathrm{m_b^4}$ term cannot be evaluated at present (and is not likely to be evaluated in the immediate future).

consideration. The terms, A, B and C, account for the dependence on the decaying hadron, H_b. The usefulness of the $1/m_b$ technique relies on the ability to determine A, B and C accurately.

The first term, A, can be expressed as :

$$A = 1 - \frac{KE}{2\,m_b^2} + \frac{HS}{2\,m_b^2} + \mathcal{O}\left(\frac{1}{m_b^3}\right). \tag{3.46}$$

The leading component describes the quark level spectator result. Although expected, this is not a trivial result and it has been derived directly from the QCD formalism. The KE term describes the average kinetic energy of the b quark within the b hadron. Predictions from QCD sum rules yield KE $\sim$0.5$\pm$0.1 GeV [132] and lattice QCD predictions give an upper limit of KE $\geq$ 0.37$\pm$0.1 GeV [133]. The value of KE varies between B mesons and b baryons and experimental measurements are dominated by the large error ($\pm$30 MeV/c^2) on the mass of the b baryon. The chromomagnetic interaction [8] of the b quark with the quarks and gluons inside the b hadron is described by the HS component and can be thought of in analogy to hyperfine splitting in atomic systems. For b baryons HS=0 as the light di-quark system carries no spin. For B mesons HS is predicted to be $\sim$0.37 GeV. The second term (B) in equation 3.45 is also dependent on the chromomagnetic interaction.

The final term (C) in equation 3.45 can be expressed as : $C \propto 4\,f_b^2\,/\,3$, where f_b is the b hadron decay constant and is predicted from theory to be (180$\pm$30) MeV [127] for B mesons. At present, the decay constant for b baryon decays cannot be calculated with the required accuracy and quark model estimates are used.

Lifetime differences between b hadrons first occur at $\mathcal{O}(1/m_b^2)$ in the expansion. Although there is some $SU(3)_{flavour}$ or isospin breaking, the lifetime of B mesons are not greatly affected and the b baryon–B meson lifetime difference dominates. Differences between B meson lifetimes occur at the $\mathcal{O}(1/m_b^3)$ level and are proportional to the particular B meson decay constant. Phenomenological interference and non-spectator effects are included naturally in the $1/m_b$ expansion at this stage and the W-exchange diagrams that cause b baryon–B meson lifetime differences are also systematically included.

Although the $1/m_b$ expansion formalism is unable to predict individual b hadron lifetimes, lifetime ratios can be predicted. Figure 3.9 shows the predictions from theory compared to the most recent lifetime measurements [99]. Theoretical predictions

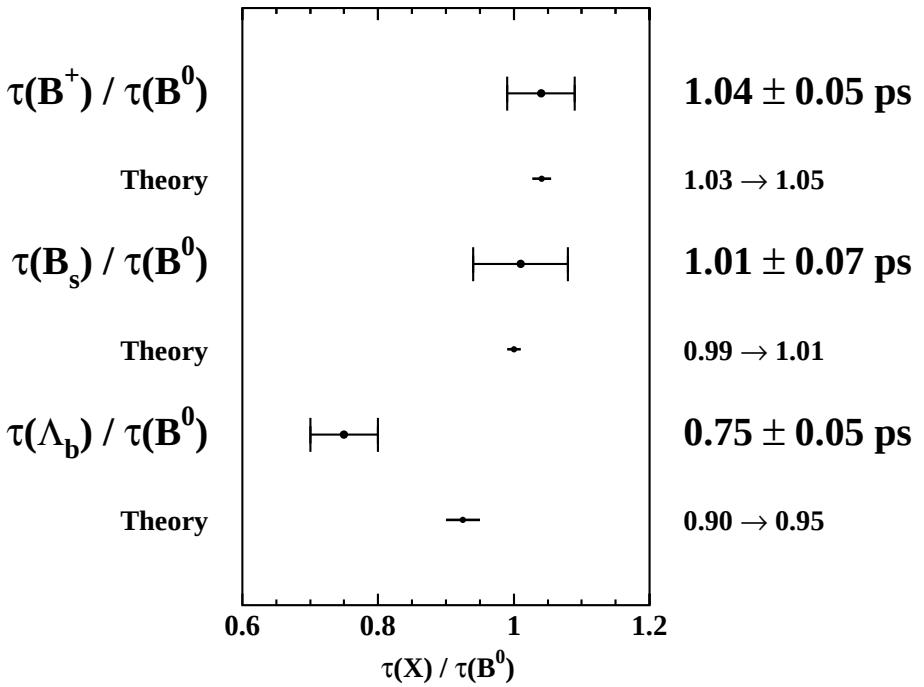

Figure 3.9: Bottom hadron lifetime ratios predicted from the QCD based theory of Bigi et al., compared to the most recent experimental results [99].

are consistent with experimental measurements for the B meson lifetime ratios. However, the b baryon lifetime prediction is 3 standard deviations from the experimental measurement. Since the baryonic matrix elements have been estimated from quark model predictions, this discrepancy could be attributed to a break down of quark-hadron duality. This is not unexpected, but, there are no qualitative distinctions between non-spectator and spectator (well described at the quark level) dynamics in the theory [131], [133].

The ratio, $\tau(\Lambda_b^0)/\tau(B^0) = 0.90 \rightarrow 0.95$, can also be predicted by scaling the observed lifetime hierarchy in the charm sector ($\tau(\Lambda_c^+)/\tau(D^0)$). The theoretical and observed lifetime hierarchies for charm mesons and baryons agree well. Therefore, if $\tau(B^0)$ is larger than $\tau(\Lambda_b^0)$ by more than 25→30%, there will be direct implications for the theory : the charm quark mass is too low a scale to allow one to go beyond qualitative predictions of charm baryon[m] lifetimes, as $\mathcal{O}(1/m_Q^4)$ contributions seem to be important; and presumably the theory-data agreement for the charm lifetime

[m] Maybe charm mesons too.

ratios is merely accidental.

3.3.7 Experimental Measurements of Bottom Hadron Lifetimes

After the discovery of the bottom quark, and before the lifetime of bottom hadrons were measured, it was thought they would be immeasurably small. The CLEO collaboration had determined that bottom quarks decay predominantly to charm quarks by measuring $|V_{ub}|/|V_{cb}| \leq 0.13$ at 90% confidence level [134] and it was assumed that $|V_{cb}| \sim 0.22$ (the same as the intra-generational coupling between the first two generations, $|V_{ud,cs}|$). This assumption, together with a b quark mass of ~ 5 GeV/c^2 yielded a b lifetime of $\mathcal{O}(10^{-14})$ s. It was therefore a big surprise when the MAC [135] and MARK-II [136] collaborations measured an average b hadron lifetime of $(1.8 \pm 0.6 \pm 0.4)$ ps and $(1.20\ ^{+0.45}_{-0.36} \pm 0.30)$ ps respectively, using an impact parameter technique. The apparent problem disappears with the current value of $|V_{cb}| \sim 0.045$. Accurate measurements of b hadron lifetimes are very important as they are truly inclusive measurements and provide sound tests for theoretical predictions.

A review of the most popular techniques for measuring the average b hadron lifetime and the b baryon lifetime are presented in the next sections. In chapters 6 and 7 systematically different techniques for measuring these lifetimes are presented along with the current world average results.

3.3.7.1 The Average Bottom Hadron Lifetime

The most popular technique for measuring τ_b, the average b hadron lifetime, uses the impact parameter distribution of high momentum leptons from semileptonic b hadron decays. A schematic representation of a B meson decay is shown in figure 3.10. Impact parameter (δ) measurements depend on a determination of the primary event vertex and error ellipse, the lepton trajectory and the b hadron direction (which is usually estimated from the jet axis). The impact parameter can be formally defined as :

$$\delta = \gamma\beta\, c\, \tau_b |\sin\theta| \sin\psi, \tag{3.47}$$

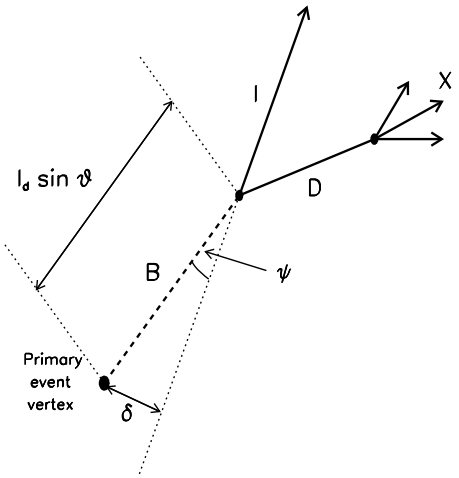

Figure 3.10: A schematic representation of the decay of a bottom meson (B) to a charmed meson (D) and a lepton (l), in the plane perpendicular to the beam direction. The impact parameter of the lepton (δ) is shown.

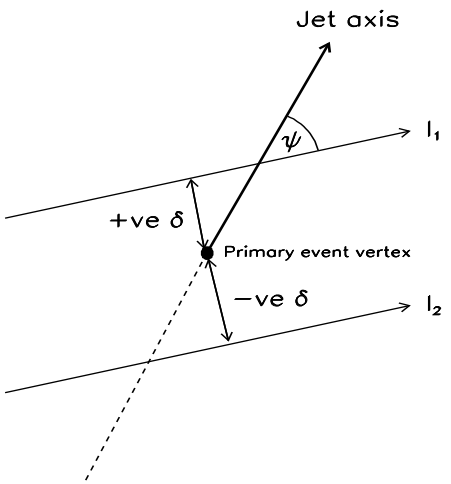

Figure 3.11: The definition of the sign of the lepton impact parameter with respect to the jet axis.

where, $\gamma\beta$ defines the relativistic boost of the b hadron, θ is the angle between the b hadron direction and the beam direction and ψ is the angle between the lepton trajectory and the b hadron direction, projected onto the plane perpendicular to the beam direction. In the relativistic limit, δ is relatively insensitive to the boost of the b hadron. This is because any increase in the decay length is compensated for by a reduction in ψ, as $\sin\psi \propto \gamma^{-1}$. To first order $\langle\delta\rangle \sim c\tau_b$. The impact parameter is a signed quantity, as shown in figure 3.11. Lepton 1 gives a positive signing as the trajectory can be extrapolated back to cross the jet axis in front of the primary event vertex. In contrast, lepton 2 gives a negative signing. Given ideal experimental circumstances, the distribution of δ would be positive for $b\bar{b}$ events, however measurement errors produce a small negative tail, which is often used to extract the experimental resolution direct from the data. Contemporary analyses use a likelihood technique pioneered by the MARK-II collaboration to extract lifetime information from the δ distribution. The δ distribution is parameterised in terms of : τ_b; signal leptons (from b$\rightarrow \ell$, b$\rightarrow$c$\rightarrow \ell$ decays); background leptons (from c$\rightarrow \ell$, K$\rightarrow \ell$, $\pi \rightarrow \ell$, misidentified leptons); and the experimental resolution for measuring δ. The impact parameter distribution of all charged tracks in $Z^0 \rightarrow b\bar{b}$ enhanced events can also be used to measure τ_b.

Another method for measuring τ_b reconstructs secondary vertices from the decay

of a b hadron. Secondary vertices are reconstructed using iterative algorithms that group well measured tracks together and require a good fit in the plane perpendicular to the beam direction (three-dimensional fitting is starting to be used too). A decay length is computed between the primary event vertex and the secondary vertex position. Backgrounds from charm and light quark events are reduced by imposing quality requirements on the secondary vertex multiplicity, the vertex mass and the impact parameters of the vertex tracks. The typical b purity is ~90%. The decay length distributions from the remaining background events are parametrised from Monte Carlo events. A likelihood fit is used to extract τ_b from the decay length distribution in data.

A summary of the latest results for the average b hadron lifetime is shown in figure 6.15.

3.3.7.2 The Bottom Baryon Lifetime

Partially reconstructed semileptonic decays of b baryons have been used by the LEP experiments to measure the b baryon lifetime ($\tau_{\Lambda_b^0}$). The $\Lambda_b^0 \rightarrow \Lambda_c^+ \ell^- \bar{\nu} X$ decay channel is used, where the Λ_c^+ is either fully reconstructed through, for example, the $pK^-\pi^+$ decay channel or the Λ^0 from the Λ_c^+ decay is reconstructed through the p,π^- decay products. As in the technique to provide evidence for b baryon production (section 3.3.5.1) $\Lambda^0\ell^-$ or $\Lambda_c^+\ell^-$ correlations are used to identify b baryons. Kinematic cuts are applied to the lepton to remove background from B meson decays such as $\overline{B} \rightarrow \Lambda_c^+ \ell^- X$. A schematic representation of semileptonic b baryon decay is shown in figure 3.12.

$\Lambda^0\ell^-$ Correlations The exact composition of b baryons in $\Lambda^0\ell^-$ events is not known and so a generic b baryon lifetime is measured. This method is statistically favourable relative to the $\Lambda_c^+\ell^-$ method but suffers from high backgrounds, especially due to Λ^0's from fragmentation processes. Two lifetime estimators are used.

In the first method the impact parameter distribution of leptons (from $\Lambda^0\ell^-$ correlations) from the b baryon decay are used. This is a relatively simple technique with little reliance on Monte Carlo to model the b baryon boost.

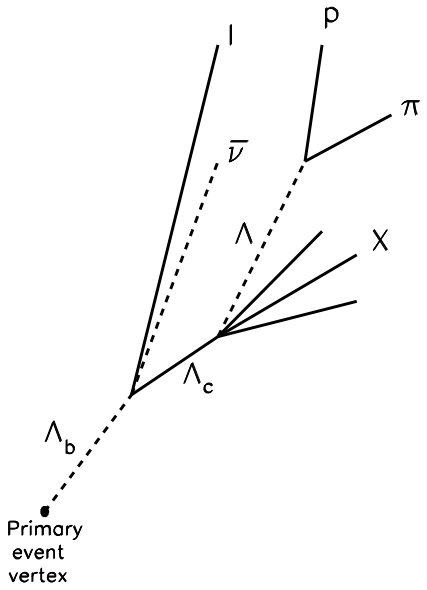

Figure 3.12: A schematic representation of a bottom baryon (Λ_b^0) decay into a charmed baryon (Λ_c^+) which subsequently decays to a Λ^0. The diagram is not to scale. The bottom baryon typically travels 3 mm before decaying, while the charmed baryon typically travels 1 mm and the Λ^0 typically travels tens of cm.

The first measurement of the b baryon lifetime was made by the ALEPH collaboration using this method [137].

The second method was pioneered by the OPAL collaboration [138]. The b baryon decay point is estimated from the $\Lambda^0\ell^-$ intersection. As shown in figure 3.12, the Λ^0 comes from the Λ_c^+ decay. The error on the location of the b baryon decay point is much larger ($\sim \times 5$) than the separation between the Λ_b^0 and Λ_c^+ vertices. The decay length is determined between the primary event vertex and the estimated b baryon decay point. The typical decay length resolution using precision vertex detectors is $\sim$450μm, the DELPHI collaboration improve this to $\sim$300μm by adding hadronic tracks (denoted X in figure 3.12) to the $\Lambda^0\ell^-$ vertex. The boost is determined by convoluting the $\Lambda^0\ell^-$ momentum spectrum in data with the momentum spectrum from b baryon decays in Monte Carlo.

$\Lambda_c^+\ell^-$ Correlations Although statistically unfavourable compared to the $\Lambda^0\ell^-$ technique due to the lower Λ_c^+ reconstruction efficiency, using $\Lambda_c^+\ell^-$ correlations provides a clean sample of Λ_b^0 baryons. All contemporary measurements reconstruct the Λ_c^+ through the p $K^-\pi^+$ decay channel with the ALEPH collabo-

ration also using the $\Lambda^0\pi^+\pi^-\pi^-$ and pK^0_s channels. The decay length between the primary event vertex and the $\Lambda^+_c\ell^-$ vertex is converted to a proper time using the momentum of the Λ^0_b, which is estimated from the momentum and invariant mass of the $\Lambda^+_c\ell^-$ pair.

The DELPHI collaboration have recently published a measurement of $\tau_{\Lambda^0_b}$ using $p\mu$ correlations [122]. The high momentum proton is assumed to come from charmed baryon decay. The main problem with this analysis is the high backgrounds from misidentified kaons and pions. The reconstructed decay time distribution, the transverse muon momentum distribution and dE/dx distribution of $p\mu$, $K\mu$, $\pi\mu$ and $X\mu$ samples are fitted simultaneously to determine the number of b baryons and the b baryon lifetime in the $p\mu$ sample.

A summary of the latest measurements of $\tau_{\Lambda^0_b}$ can be found in figure 7.14.

Chapter 4

Identifying $Z^0 \rightarrow b\bar{b}$ Events

Any multihadronic ($Z^0 \rightarrow q\bar{q}$) event recorded with the OPAL detector will leave a characteristic signature of two or more jets of particles as shown in figure 4.1. Such events are selected online using the trigger and filter (see section 2.3). A multihadronic selection [139] originally developed by the Tokyo group is used to further select events offline. A selected event is divided into jets using jet finding algorithms and each jet is searched for secondary vertices, indicating the presence of a long-lived bottom hadron. Properties of the secondary vertices are fed into a neural network algorithm which assigns a probability that the secondary vertex is the result of a bottom hadron decay. The primary event vertex is also reconstructed for each event. Each of these procedures is described in more detail in this chapter. The chapter concludes with a description of the Monte Carlo samples used in the measurements described in the following three chapters. Details relevant to bottom hadron production and decay are emphasised.

4.1 The Trigger and Filter Selection

The most important parts of the trigger used to select multihadronic events are :

The Track Trigger : At least two tracks are required to originate from the nominal event vertex, each with a transverse momentum of at least 0.45 GeV/c.

The Time-of-Flight Trigger : At least three non-adjacent scintillator counters must have registered hits.

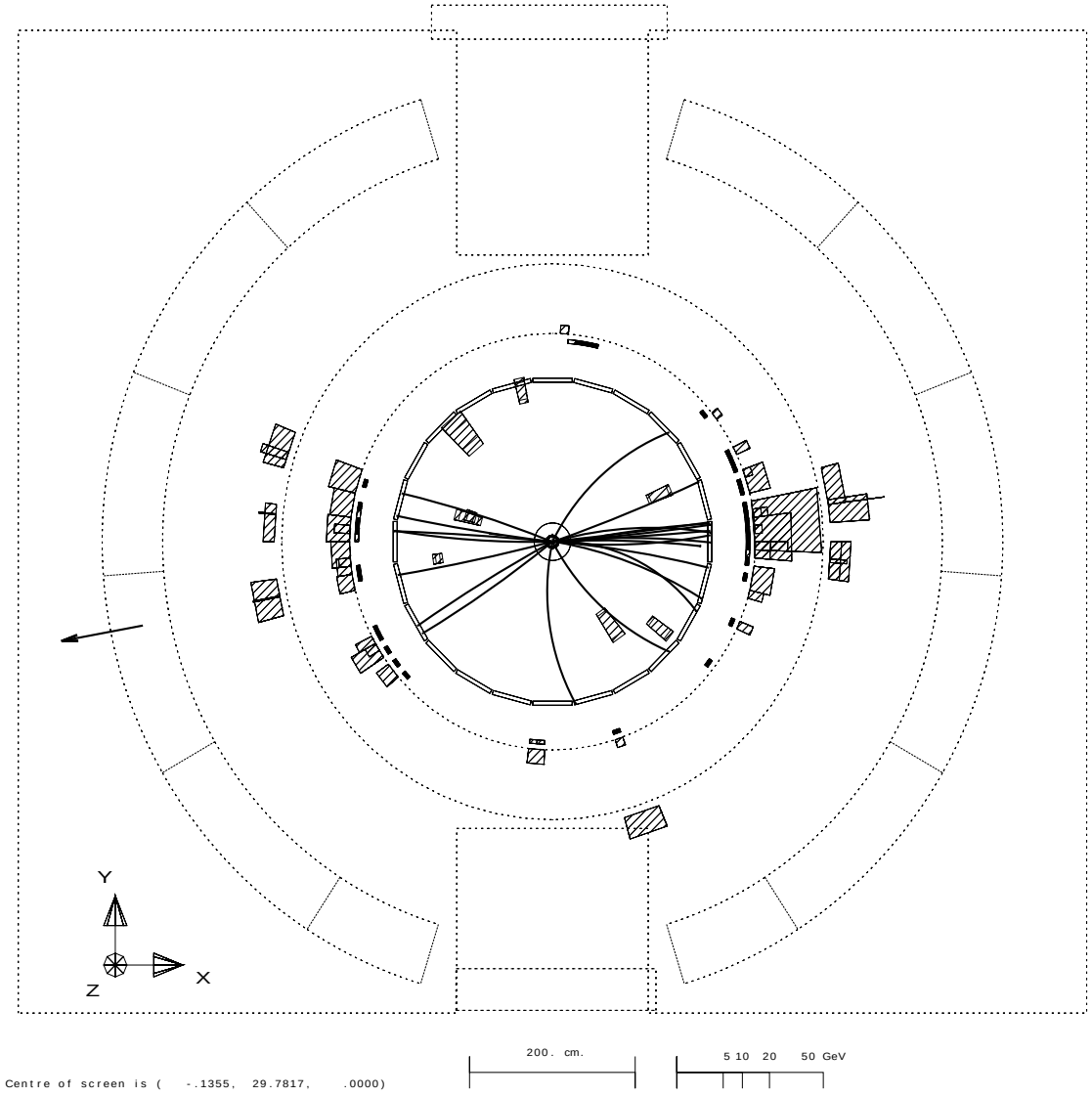

Figure 4.1: A typical $e^+e^- \rightarrow q\bar{q}$ event recorded with the OPAL detector, looking along the beam direction. Two jets of particles are clearly visible. The tracks are reconstructed in the central jet chamber, the inner (outer) layers of blocks represent energy deposited in the electromagnetic (hadronic) calorimeter. The arrow represents a muon recorded by the barrel muon detector, the outer square represents the muon endcap detector.

The Electromagnetic Trigger : The summed raw energy in either the barrel or endcaps must be at least 6 or 7 GeV respectively.

A high level of redundancy is achieved due the high multiplicities of multihadronic events. The overall efficiency is in excess of 99%.

The filter makes a preliminary event classification based on the Gold Plated Multihadron Selection [140]. This selection only uses information from the electromagnetic calorimeters and the TOF. It is loose enough to maintain a high efficiency and not exclude possible new physics processes. Events with at least five tracks form the raw data-set for the analyses presented in this thesis. Table 4.1 shows the number of raw events for each year of data taking.

Year	Number of Events
1991	407720
1992	861458
1993	831422
1994	1890461

Table 4.1: The number of raw events for each year of OPAL data-taking used in this thesis.

4.2 The Tokyo Multihadron Selection

For a charged track or electromagnetic cluster to be used in the Tokyo selection algorithm, a number of quality conditions[a] are required as shown in tables 4.2 , 4.3.

Using the good charged tracks and electromagnetic clusters two ratios, R_{vis} and R_{bal} are constructed thus :

$$R_{vis} = \frac{E_{tot}}{\sqrt{s}}, \tag{4.1}$$

$$R_{bal} = \frac{E_{bal}}{E_{tot}}, \tag{4.2}$$

[a] The track parameters are defined in section 2.3.3.1.

Good Electromagnetic Clusters		
	Barrel	Endcap
Raw energy (E_{raw})	≥ 0.1 GeV	≥ 0.2 GeV
Number of blocks in cluster	≥ 1	≥ 2

Table 4.2: Quality conditions required by the Tokyo multihadronic selection algorithm for electromagnetic clusters.

Good Charged Tracks	
Number of CJ hits	≥ 20
$\lvert d_0 \rvert$	≤ 2.0 cm
$\lvert z_0 \rvert$	≤ 40.0 cm
Radius of first hit	≤ 60.0 cm
Transverse momentum w.r.t. beam axis	≥ 0.05 GeV/c
$\lvert \cos\theta \rvert$	≤ 0.995

Table 4.3: Quality conditions required by the Tokyo multihadronic selection algorithm for charged tracks.

where, $E_{tot} = \sum E_{raw}$ and $E_{bal} = \sum E_{raw} \cos\theta$. The sums are over N_{clus} good clusters.

In order to select a multihadronic event it must satisfy all of the following requirements :

- $N_{clus} \geq 7$ good clusters,
- $N_{chgd} \geq 5$ good tracks,
- $R_{vis} \geq 0.10$,
- $R_{bal} \leq 0.65$.

The cluster and track multiplicity requirements (N_{clus}, N_{chgd}) are tuned to minimise the background from Z^0 decays to charged lepton pairs. The R_{vis} (visible energy) requirement discards two-photon events and interactions of the LEP beams with residual gas molecules. The R_{bal} (momentum imbalance) requirement rejects two-photon events, interactions of the LEP beams with residual gas molecules (and beam pipe), and cosmic rays in the endcap detectors.

The selection has been determined to be ∼98.4% efficient [139] with the reduction in detector acceptance at small θ being the major source of inefficiency. The main backgrounds are from $\tau^+\tau^-$ and two-photon events, which have been estimated to form (0.11±0.03)% and (0.5±0.02)% of the final multihadronic sample respectively [139]. Background from interactions of the LEP beams with the beam pipe or residual gas molecules, cosmic rays, $\mu^+\mu^-$ or e^+e^- events have been determined to be negligible.

4.3 Additional Quality Requirements

For the analyses presented in this thesis, further selection criteria were applied. The most important subdetector components for the selection of $Z^0 \rightarrow b\bar{b}$ events and the subsequent measurement of secondary vertices were required to be fully operational. Therefore, minimum detector status requirements were made on the following subdetectors : SI, CV, CJ, CZ, EB and EE.

Charged tracks used in the analyses were required to pass the following quality requirements :

- Minimum transverse momentum = 0.15 GeV/c,
- Maximum value of $|\tan(\lambda)| = 100$,
- Maximum value of $|z_0| = 200$ cm,
- Maximum momentum = 65 GeV/c,
- Minimum number of CJ hits = 20,
- Maximum value of $|d_0|$ with respect to the beam spot position = 5 cm,
- Maximum χ^2 from the x-y track fit = 100.

In addition electromagnetic clusters were required to satisfy :

- Minimum raw energy of cluster = 0.05 GeV,
- Minimum corrected energy of cluster in EB = 0.100 GeV,
- Minimum corrected energy of cluster in EE = 0.200 GeV.

4.4 Jet Finding

Two different algorithms are used to group charged tracks and unassociated[b] electromagnetic clusters into jet-like topologies. The two algorithms are known as the 'JADE E0 scheme' and the 'cone jet finder'. The analysis presented in chapter 5 (a measurement of Br(b hadron $\rightarrow \Lambda^0$ X)) uses the JADE jet-finder and the b hadron lifetime analyses presented in chapters 6 and 7 use the cone jet-finder. The cone jet-finder is generally believed to be better for bottom quark studies as it has superior performance for grouping particles from a b hadron decay into the same jet and therefore improving the resolution of the jet-axis direction and b tagging purities [141]. However, the cone jet-finder has only become available as standard OPAL software recently and was not available for the branching ratio study.

The thrust, T, of the event is defined as :

$$\mathrm{T} = \max\left(\frac{\sum_{\mathrm{i}} |p_{\mathrm{i}}.\hat{n}|}{\sum_{\mathrm{i}} |p_{\mathrm{i}}|}\right), \tag{4.3}$$

where, p_{i} is the momentum of a track or cluster and the sum runs over all good tracks and clusters. The axis $\hat{n}$ is chosen to maximise the expression in the parentheses and is referred to as the thrust axis of the event. It has a polar angle θ_{t}.

In the analyses presented in this thesis events are rejected if $|\cos\theta_{\mathrm{t}}| > 0.75$. This ensures that events lie within the SI acceptance and can be efficiently searched for secondary vertices.

4.4.1 The JADE Algorithm

This algorithm was first developed by the JADE collaboration [142] and is implemented at OPAL with the 'E0' recombination scheme [143]. A scaled mass :

$$\mathrm{y_{ij}} = \frac{2\mathrm{E_i E_j}\,(1-\cos\theta_{\mathrm{ij}})}{\mathrm{E^2_{vis}}} = \frac{\mathrm{M^2_{ij}}}{\mathrm{E^2_{vis}}}, \tag{4.4}$$

is used as the jet resolution parameter, where, $\mathrm{E_{vis}}$ is the total visible energy in the event and θ_{ij} is the angle between the pair of particles (i,j), of energy $\mathrm{E_i}$, $\mathrm{E_j}$, making an invariant mass, $\mathrm{M_{ij}}$, which is formed between between all possible particle pairs. The pair with the lowest invariant mass are combined to form a pseudo-particle

[b] Unassociated electromagnetic clusters are defined in section 2.3.3.2.

and if $y_{ij} < y_{cut}$ the procedure is repeated until no pairs of pseudo-particles satisfy this requirement. A low value of y_{cut} will therefore result in a large number of very collimated jets, whereas a large value will eventually result in event being divided into two hemispheres.

In bottom hadron analyses a quantity :

$$x_{min} = y_{cut}\, E^2_{vis}, \tag{4.5}$$

is often used rather than y_{cut} to ensure the minimum jet pair resolution is independent of the total visible energy in the event.

In this thesis a value of $x_{min} = 49\,(\mathrm{GeV}/c^2)^2$ is used. This gives jet masses of the same order as the b hadron mass (~ 5 GeV/c^2).

4.4.2 The Cone Algorithm

The cone jet finder was principally used at $p\bar{p}$ collider experiments [144]. The algorithm has only recently been made available for e^+e^- collider experiments [145], and has proved to be popular for bottom hadron physics due to its superior resolution of the true jet axis direction vector, which is often used to estimate the b hadron direction.

The cone algorithm simply defines a jet as a set of particles that have a total energy greater than a cutoff ε and momentum vectors that lie within a cone of half angle R. The cone axis is described by the vectorial momentum sum of the particles. In this analysis R = 0.55 radians and ε= 5.0 GeV. The value of ε is scaled by the ratio E_{vis}/E_{cm}, where, E_{vis}, E_{cm} are the total visible energy in the event and the centre of mass e^+e^- energy respectively. This reduces the sensitivity to inefficiencies in detecting all the visible energy in an event. Otherwise, events with smaller visible energies will be more sensitive to the value of ε. The full cone algorithm is described in detail in [145], including procedures to deal with overlapping cones.

4.5 Primary Vertex Determination

The primary vertex position is fit[c] on an event by event basis with two pseudo-tracks introduced into the fit to provide a constraint to the average beam spot position. The two pseudo-tracks are parallel to the x and y axes respectively and have perpendicular errors given by the beam spot spreads. The pseudo-track in the y direction essentially fixes the x position of the primary vertex, since the beam spot spread in y is so small.

For Monte Carlo data, the beam spot position and spread are initially derived from the constants file used at the time the data was generated. This can also be changed, at a later date, by the user.

For data, the beam spot position is derived by collecting events in chronological order and making a χ^2 fit to a primary vertex once there are 100 or more quality tracks. Quality tracks are defined as having p_t >0.25 GeV/c, $|d_0|$ <1 cm, and σ_{d_0} <0.1 cm. The p_t represents the track momentum in the plane orthogonal to the beam direction and d_0 is the distance of closest approach of the track to the co-ordinate origin, in the plane perpendicular to the beam direction. The track contributing the largest χ^2 is rejected if χ^2 >10 and this process continues until all tracks contribute χ^2 <10 to the vertex fit. A weighted average of 30 such contiguous vertices (corresponding to about 200 Z^0 decays) is formed. Finally, the neighbouring vertex positions are joined together and the mean and associated error recalculated as long as each new point is consistent with the running average up to that point.

The beam spot spread in data is calculated from di-muon events in the polar angle region $|\cos\theta| < 0.4$. This ensures the best possible tracking resolution. If the mean of the beam spot position is known accurately and the experimental resolutions on the d_0 and z_0 measurements for the di-muons are well understood, then the intrinsic beam spot width can be estimated from the width of the residuals at the point of closest approach to the mean beam spot position for the di-muon tracks. The beam spread values obtained using this method are in excellent agreement with the range of values expected from the LEP beam optics, assuming head-on collisions and Gaussian bunch shapes [146].

[c] The method to fit the primary vertex follows, almost exactly, that used to fit secondary vertices, as described in section 4.6.

In the following analyses the values of the beam spot size and spread shown in table 4.4 are used for Monte Carlo data. Table 4.5 summarises the intrinsic tracking

	Position			Spread		
Monte Carlo	x (cm)	y (cm)	z (cm)	σ_x (μm)	σ_y (μm)	σ_z (mm)
'Old'	0.0322	0.0552	0.4400	147	16	11.2
'New'	-0.0211	0.0434	0.4640	127	12	7.0

Table 4.4: Beam spot positions and spreads for the two generations of OPAL Monte Carlo used in this thesis. The Monte Carlo samples are described in more detail in section 4.8.2.

resolutions (d_0 and z_0) and the beam spot widths for OPAL running between 1990 and 1994 [147]. A more detailed description of the method used to obtain the beam

Year	d_0 res (μm)	z_0 res (mm)	x width (μm)	y width (μm)	z width (mm)
1991	16.8 ± 0.4	1.05 ± 0.02	148 ± 2	14 ± 2	9.6 ± 0.1
1992	16.0 ± 0.2	0.94 ± 0.01	100 ± 1	24 ± 1	7.1 ± 0.1
1993	17.1 ± 0.1	0.067 ± 0.001	153 ± 1	4 ± 3	7.1 ± 0.1
1994	19.7 ± 0.1	0.070 ± 0.001	120 ± 1	13 ± 1	7.08 ± 0.03

Table 4.5: Intrinsic tracking resolutions (d_0 and z_0) and beam spot widths in x, y and z for different years of OPAL running [147]. The changes in the intrinsic tracking resolutions reflect the commissioning of the r-ϕ and z parts of the silicon microvertex detector and the changes in beam spot widths reflect changes in the operating modes of the LEP machine.

spot position and spread can be found in [147].

4.6 Secondary Vertex Finding

A b hadron will travel a mean distance of approximately 3 mm before decaying and on decay will produce an average charged particle multiplicity of 5.72 ± 0.31 particles [148]. Displaced secondary vertices are therefore an excellent signature for b hadrons.

In this thesis two different methods are used to group tracks into secondary vertices in the plane perpendicular to the beam direction (r-ϕ). A 'tear-down' vertex finder is used to identify secondary vertices, the properties of which are used as inputs to a neural network algorithm which has been optimised to identify $b\bar{b}$ events. This $b\bar{b}$ enrichment technique is common to all analyses presented in this thesis and is described in more detail in the next section. In order to measure b hadron lifetimes, the distance between the primary and secondary vertices (the 'decay length') must be accurately measured. A 'build-up' vertex finder is used to do this. Both vertex finders are described below. More details can be found in [149].

To be considered for either secondary vertex finder, as well as passing the default quality requirements detailed in section 4.3, tracks must also satisfy the following requirements :

- Maximum $\mid d_0 \mid$ with respect to the event vertex = 1.0 cm,
- Maximum error on $\mid d_0 \mid$ (including event vertex ellipse) = 0.1 cm,
- Maximum total momentum = 65 GeV/c,
- Minimum total momentum = 0.5 GeV/c.

4.6.1 The 'Tear-down' Vertex Finder

In this algorithm all tracks within a given jet passing the quality requirements are considered in a fit to a secondary vertex in the r-ϕ plane. The fitting technique is the same as that used to reconstruct the primary event vertex. Tracks are discarded if they contribute more than 4 to the vertex χ^2 and the remaining tracks are refitted to a new secondary vertex. This process continues until there are less than two tracks remaining (in which case the vertex finding fails) or no tracks contribute more than four to the vertex χ^2.

This method will tend to resolve a displaced secondary vertex if the b hadron has travelled a significant distance before decaying and is more efficient if the charged track multiplicity from the b hadron decay is large. Figure 4.2 shows tracks measured by the silicon microvertex detector formed into two secondary vertices using this technique.

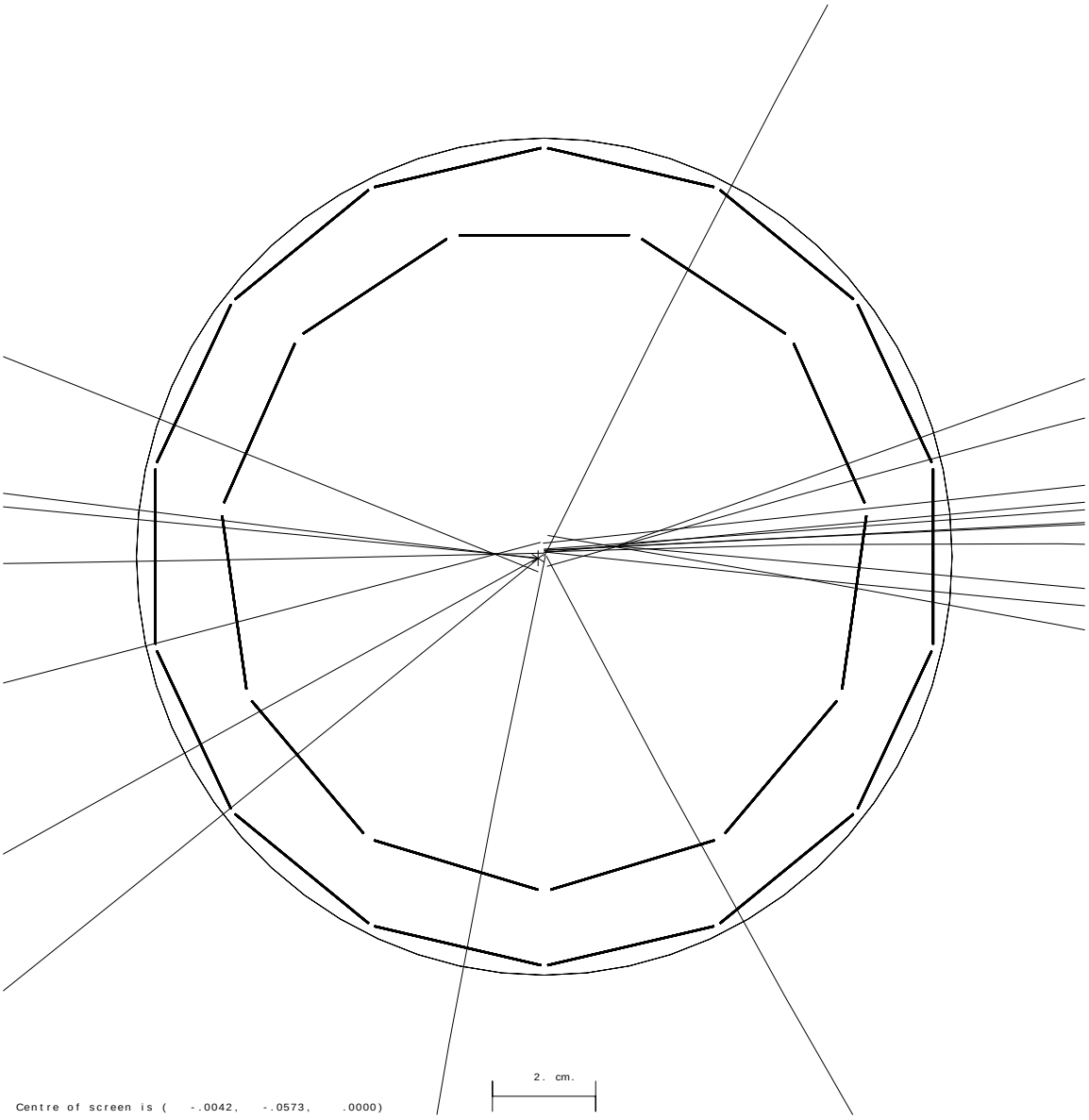

Figure 4.2: A view of the $e^+e^- \rightarrow q\bar{q}$ event shown in figure 4.1 with detail around the production vertex shown. The two concentric layers of the microvertex detector are shown. The tracks have been formed into two secondary vertices which are visible on each side of the event. The lower-most track of the secondary vertex on the left hand side is the muon candidate shown as an arrow in figure 4.1.

4.6.2 The 'Build-up' Vertex Finder

This algorithm also works in the r-ϕ plane to fit tracks to displaced secondary vertex, but with a rather different philosophy than the 'tear-down' algorithm. Two[d] precisely measured tracks (requiring at least one CV axial hit or a silicon microvertex hit) with the most significant separation from the primary event vertex are taken as seed tracks. Precisely measured tracks, at least 3 standard deviations from the primary vertex, are also taken as seeds. Separated vertex candidates are formed by looping over all possible pairs of seed tracks to form a vertex nucleus. Other tracks are added to this nucleus vertex as long as they match this vertex better than the primary vertex and the vertex probability is >1%. Once associated to a vertex, a track cannot be used again. The decay length is calculated for each vertex from a fit to the primary vertex position and the seed vertex position. The r-ϕ vector momentum sum of the seed vertex tracks is used to constrain the decay length direction. Such a constraint was also used in a measurement of the decay length in 3-prong τ decays [146]. When fitting the decay length the uncertainty from the primary vertex position is usually negligible, with the dominant error arising from uncertainties in the track parameters for the seed vertex. If there is more than one seed vertex, the best quality one is chosen using the following criteria (in order of importance) :

- The vertex with a decay length between 0 cm and 2 cm.
- The vertex with the greatest number of precisely measured tracks.
- If the number of precisely measured tracks is exactly two, then the vertex with the largest number of tracks in the seed vertex is chosen, irrespective of how well they are measured.
- The vertex with the largest decay length significance from the primary vertex.

This algorithm can reconstruct secondary vertices displaced from the primary vertex even in light quark events. The vertices arising from non-b$\bar{\text{b}}$ events are dominantly due to charm hadron decays.

[d] There must be at least two.

4.7 Tagging $Z^0 \rightarrow b\bar{b}$ Events

4.7.1 A Neural Network Algorithm for $Z^0 \rightarrow b\bar{b}$ Tagging

The neural network forms part of the standard OPAL software for b tagging [150] and is therefore treated like a 'black-box' in this application. Appendix A gives details of a similar neural network architecture that was developed to identify charged tracks from bottom hadron decays.

Seven parameters of the secondary vertices found by the 'tear-down' vertex finder were used as inputs to the neural network algorithm :

- (1) The invariant mass of the charged particles assigned to the secondary vertex, assuming pion masses.
- (2) The number of charged particles assigned to the secondary vertex.
- (3) The decay length significance of the secondary vertex relative to the primary vertex.
- (4-6) The impact parameter significance with respect to the primary vertex of the 2^{nd}, 3^{rd} and 4^{th} most separated tracks[e].
- (7) The number of tracks in the jet containing the secondary vertex which have been assigned to the primary vertex.

The output of the b tagging neural network varies between zero and one, when the output is large there is a high probability that the secondary vertex was due to a b hadron decay, as shown in figure 4.3.

4.7.2 Double Tagging Technique

To avoid unnecessary dependence on Monte Carlo modelling, the b purity was evaluated directly from the data using a double tagging technique [151].

The event is divided into two hemispheres using the thrust axis. A hemisphere is said to be tagged if a secondary vertex within the hemisphere produces a neural network output greater than a predefined tagging value. The number of singly

[e]The first most separated track was found to come predominantly from charm hadron decays.

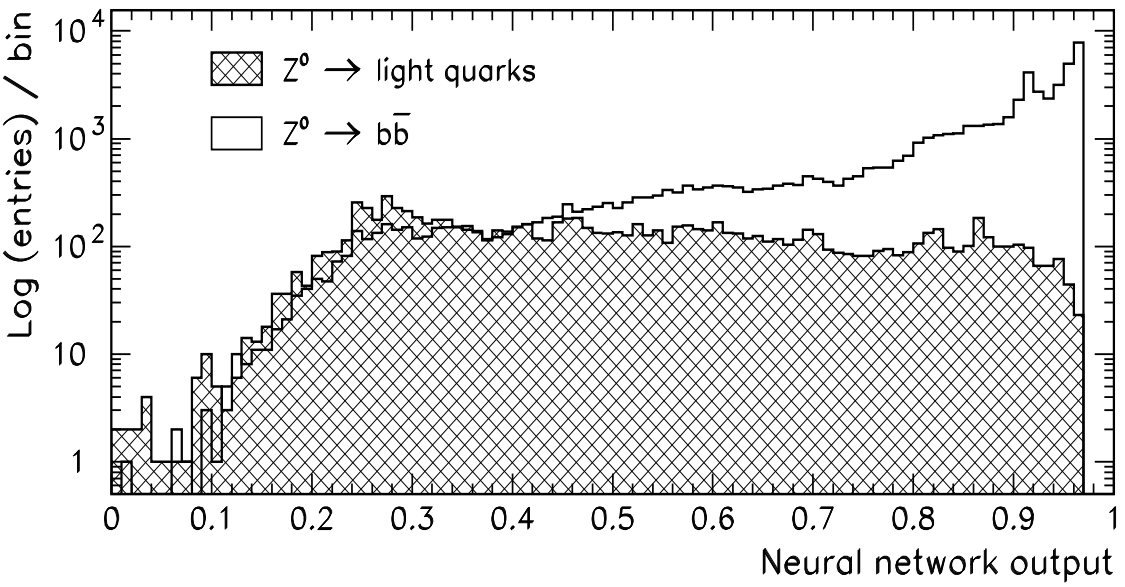

Figure 4.3: The output of the neural network used to enhance $Z^0 \rightarrow b\bar{b}$ events. The hatched area shows that the light quark background is highly suppressed when the output of the neural network is large.

tagged hemispheres (N_ν) and the number of events with two tagged hemispheres ($N_{\nu\nu}$) in a sample of N_{had} hadronic events can be expressed as :

$$N_\nu = 2\left(\varepsilon_b \frac{\Gamma_{b\bar{b}}}{\Gamma_{had}} + \varepsilon_c \frac{\Gamma_{c\bar{c}}}{\Gamma_{had}} + \varepsilon_{uds} \frac{\Gamma_{u\bar{u}} + \Gamma_{d\bar{d}} + \Gamma_{s\bar{s}}}{\Gamma_{had}}\right) N_{had}, \tag{4.6}$$

$$N_{\nu\nu} = \left(C_b \varepsilon_b^2 \frac{\Gamma_{b\bar{b}}}{\Gamma_{had}} + \varepsilon_c^2 \frac{\Gamma_{c\bar{c}}}{\Gamma_{had}} + \varepsilon_{uds}^2 \frac{\Gamma_{u\bar{u}} + \Gamma_{d\bar{d}} + \Gamma_{s\bar{s}}}{\Gamma_{had}}\right) N_{had}. \tag{4.7}$$

The quark partial widths are denoted by $\Gamma_{q\bar{q}}/\Gamma_{had}$ and Standard Model values of 0.216 and 0.171 are used for the up and down quark values respectively. The hemispheric tagging efficiencies for $b\bar{b}$, $c\bar{c}$ and lighter quark events are denoted by $\varepsilon_b, \varepsilon_c$ and ε_{uds} respectively. The values of ε_b and ε_c are extracted from the data by solving equations 4.6 and 4.7 simultaneously, while ε_{uds} is obtained from Monte Carlo. The coefficient C_b describes the efficiency correlation between hemispheres in a $b\bar{b}$ event. This is needed because the tagging probabilities for the two hemispheres are not just correlated through the flavour of the initial quark pair. This coefficient is only evaluated for $b\bar{b}$ events as the $b\bar{b}$ event fraction is dominant. The numerical value of C_b differs from unity for two reasons :

Physics Effects : Hard gluon radiation can cause both the b and $\bar{b}$ jets to fall into

one hemisphere ($\Rightarrow C_b < 1$) and also produce a small correlation between the b and $\bar{b}$ hadron's momenta ($\Rightarrow C_b > 1$).

Detector Effects : The b and $\bar{b}$ hadrons are usually produced back-to-back. Geometrical correlations will therefore be produced if the tagging efficiency is not uniform over the geometrical acceptance of the detector ($\Rightarrow C_b > 1$ or < 1). Also, the primary vertex position is common to both hemispheres ($\Rightarrow C_b < 1$). However, this is a small effect in comparison.

A non-uniform geometrical detector acceptance is expected to be the largest effect [151] and so, the relationship :

$$C_b = \frac{\varepsilon_b^{\nu\nu}}{(\varepsilon_b^{\nu})^2}, \tag{4.8}$$

can be used to evaluate C_b, where, $\varepsilon_b^{\nu\nu}$ and ε_b^{ν} are the double and single tagging efficiencies for $b\bar{b}$ events, evaluated from Monte Carlo, where detector geometries are well modelled.

Equations 4.6 and 4.7 are solved for ε_b and its error. The hemispheric b purity, P_b, can be subsequently determined through the relationship :

$$P_b = \frac{2\,N_{had}\,\Gamma_{b\bar{b}}/\Gamma_{had}}{N_{\nu}}\,\varepsilon_b. \tag{4.9}$$

4.8 The Data and Monte Carlo Samples

4.8.1 Data

Only multihadronic events recorded from towards the end of 1991 (when the silicon microvertex detector became operational) until the end of 1994 are used in this thesis to ensure comparable environments for b quark tagging[f]. Data from the 1995 physics run was not sufficiently well understood to warrant inclusion in this thesis at time of writing. The data selection is described in section 4.1.

[f] The last two periods of the 1994 data are omitted as the silicon detector was removed after an accident.

4.8.2 Monte Carlo

Two versions of the JETSET generator [76] were used to produce the Monte Carlo samples that are used in this thesis. The work presented in chapter 5, describing the measurement of Br(b hadron$\rightarrow \Lambda^0$X), use JETSET release 7.3. The b hadron lifetime measurements, described in chapters 6 and 7, use JETSET release 7.4. In both cases, OPAL uses private versions of JETSET parameters and decay tables to tune the JETSET performance and give good agreement with data.

The Monte Carlo samples used in this thesis are detailed in table 4.6. The 'new'

Thesis Name	OPAL Name	Type	N_{events}	JETSET Version
'Old'	R2218	udscb	1×10^6	7.3
'Old b$\bar{b}$'	R2277	b$\bar{b}$	200×10^3	7.3
'New'	R2790–R2793	udscb	$4\times(1\times10^6)$	7.4
'New tune b$\bar{b}$'	R2776	b$\bar{b}$	1×10^6	7.4

Table 4.6: The specification for each generation of Monte Carlo sample.

Monte Carlo samples are superior to the 'old' versions in many ways. Particle decays have been updated to follow the results of the 1994 Review of Particle Properties [28] and the tuning of JETSET parameters is detailed in [152]. In particular, the introduction of P-wave mesons has made the average charged track multiplicity from B^+ and B^0 decays agree with measurements made at the Υ(4s) more closely [153]. Also, B meson decays to baryons have been implemented. This was a major short-coming of the 'old' Monte Carlo samples. A 'new tune b$\bar{b}$' subset has a revised charm hadron decay table and updated heavy flavour fragmentation parameters[g]. Peterson parameters of $\varepsilon_b = 0.004$ and $\varepsilon_c = 0.031$ are used to predict $\langle x_E \rangle_B = 0.703$, which agrees well with the value given in equation 3.15. More details on all these changes can be found in [152] and [154]. Table 4.7 details the relative production rate and lifetime of b hadrons in each of the Monte Carlo samples compared to recent experimental results. The charged track parameters (κ_{gen}, ϕ_{gen} and $d_{0\,gen}$)[h] can be 'smeared' to

[g] In particular, the effects of B^{**} production were included.
[h] See section 2.3.3.1 for definitions.

Bottom Hadron	Relative Production Rate			Lifetime (ps)		
	Monte Carlo			Monte Carlo		
	'old'	'new'	Data[a]	'old'	'new'	Data [30]
B^+	0.40	0.40	0.40 ± 0.05	1.4	1.6	1.63 ± 0.05
B^0	0.40	0.40	0.40 ± 0.05	1.4	1.6	1.57 ± 0.05
B_s	0.12	0.12	0.13 ± 0.03	1.4	1.6	1.58 ± 0.10
Λ_b^0	0.08	0.08	0.04 ± 0.11	1.4	1.2	1.18 ± 0.07

[a] See section 3.3.5.2 for calculation details.

Table 4.7: A comparison of the bottom hadron production features for data and each generation of Monte Carlo sample.

give better agreement with data according to the following prescription :

$$\kappa_{\rm rec} \rightarrow \kappa_{\rm gen} + \alpha(\kappa_{\rm rec} - \kappa_{\rm gen}), \tag{4.10}$$

$$\phi_{\rm rec} \rightarrow \phi_{\rm gen} + \beta(\phi_{\rm rec} - \phi_{\rm gen}), \tag{4.11}$$

$$d_{0\,\rm rec} \rightarrow d_{0\,\rm gen} + \gamma(d_{0\,\rm rec} - d_{0\,\rm gen}). \tag{4.12}$$

The track parameters $\tan\lambda$ and z_0 are not smeared since the analyses in this thesis make no use of information in the z direction. The track parameter error matrix is also left unsmeared. For the 'old' Monte Carlo, values of $\alpha = 1.0$, $\beta = 1.3$ and $\gamma = 1.4$ were applied as detailed in [155]. The 'new' Monte Carlo samples required no additional smearing ($\alpha = \beta = \gamma = 1.0$) due to the much improved modelling of the central detectors [156].

Chapter 5

A Measurement of the Λ^0 Production Rate in $Z^0 \rightarrow b\bar{b}$ Events

5.1 Overview

Each multihadronic Z^0 decay passing the event selection described in section 4.3 is divided into two hemispheres using the thrust axis of the event. Properties of the secondary vertex with the largest decay length significance in each hemisphere are used as inputs to a neural network algorithm. The neural network assigns a probability that the secondary vertex was due to a b hadron decay, as described in section 4.7.1. The awayside hemispheres from these candidate b hadrons are used to provide a bias-free, b hadron enriched sample, to study Λ^0 production. The procedure used to reconstruct Λ^0's is described. Only the most energetic Λ^0 on the awayside is used. Both hemispheres can be used to calculate the branching ratio.

The Λ^0 production rate in $Z^0 \rightarrow b\bar{b}$ events can be expressed as :

$$\mathrm{Br}(\text{b hadron} \rightarrow \Lambda^0 \mathrm{X}) = \left(\frac{\mathrm{N}_{\Lambda^0}}{\mathrm{P_b}\, \mathrm{N_{hem}}\, \varepsilon_{\mathrm{pcut}}} \right), \tag{5.1}$$

where :

- $\mathrm{N}_{\Lambda^0} = \mathrm{N_{sig}} - \mathrm{N_{bkgd}}$. The number of Λ^0's from b hadron decays and background sources are denoted as $\mathrm{N_{sig}}$ and $\mathrm{N_{bkgd}}$, respectively. The Λ^0 momentum is required to exceed a minimum momentum requirement.

- P_b is the b purity of the b tagged hemispheres.

- N_{hem} is the number of hemispheres (on the awayside of a b tag) that are studied for Λ^0 production.

- ε_{pcut} is the efficiency for detecting a Λ^0 from a b hadron decay through the $p\pi^-$ decay channel. The Λ^0 momentum must exceed a minimum momentum requirement. This efficiency includes the loss due to Λ^0 decays into neutral particles ($\Lambda^0 \to n\pi^0$).

The method used to measure the purity of the b tagged sample is described in section 5.3 and the background estimation for the process b hadron $\to \Lambda^0 X$ is summarised in section 5.5. Finally, in section 5.6 the reconstructed momentum spectrum for Λ^0's from b hadron decays is extracted and used to calculate Br(b hadron $\to \Lambda^0 X$). The product branching ratio, $f(b \to B)\,Br(\Lambda_b^0 \to \Lambda^0 X)$, is also evaluated.

5.2 Event Sample and Selection

Data collected between 1991 and 1992 with the silicon microvertex detector operational were used in this analysis. The total data sample contained 1 159 952 events. The 'old' Monte Carlo data-set consisting of 993 601 events was also used. Throughout this chapter the prefix 'old' will be discarded when referring to the Monte Carlo sample. All events were required to have at least two jets, with the two most energetic jets (assumed to be the quark jets) in opposite hemispheres, as defined by the thrust axis of the event. Jets were formed using the JADE algorithm discussed in section 4.4.1. Secondary vertices were reconstructed using the 'tear-down' algorithm described in section 4.6.1. After all the selection requirements there were 649183 data and 684033 Monte Carlo events available for b tagging.

5.3 Tagging $Z^0 \to b\bar{b}$ Events

The method used to identify pure samples of $Z^0 \to b\bar{b}$ events has been outlined in the previous chapter. A double tagging technique is used to evaluate the purity of the

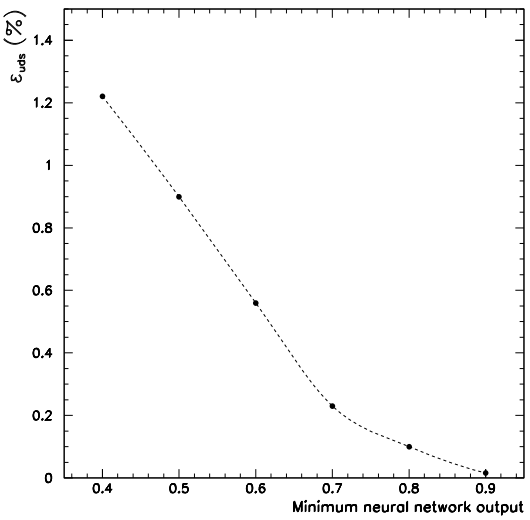

Figure 5.1: The hemispheric light quark efficiency ($\varepsilon_{\rm uds}$), derived from Monte Carlo, as a function of a minimum requirement on the output of the neural network used for b tagging.

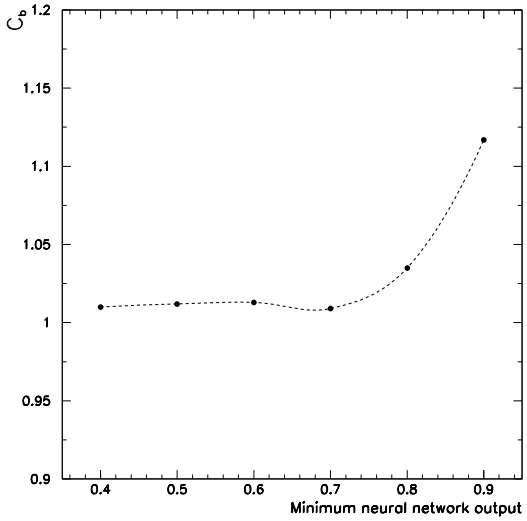

Figure 5.2: The hemispheric b efficiency correlation coefficient (C_b), derived from Monte Carlo, as a function of a minimum requirement on the output of the neural network used for b tagging.

isolated b hadron sample from the data itself, as explained in section 4.7.2. When evaluating the b purity in this way, (with reference to equations 4.6 and 4.7) the values of the light quark efficiency, $\varepsilon_{\rm uds}$, and the hemispheric efficiency correlation coefficient, C_b, need to be evaluated from Monte Carlo.

The variation in $\varepsilon_{\rm uds}$ for a range of minimum output requirements on the neural network used for b tagging is shown in figure 5.1. The efficiency falls rapidly as the minimum output requirement is increased. The neural network strongly suppresses the contribution from non–$Z^0 \to b\bar{b}$ events. Using a default minimum neural network output requirement of 0.8, the following values were derived from Monte Carlo for the purity, P_q, and the efficiency, ε_q, for different quark species on the awayside of a b tag :

$$P_b = 95.7\%,\ P_c = 3.3\%,\ P_{uds} = 1.0\%; \tag{5.2}$$

$$\varepsilon_b = 16.9\%,\ \varepsilon_c = 1.5\%,\ \varepsilon_{uds} = 0.1\%. \tag{5.3}$$

Figure 5.2 shows the variation in C_b for a range of minimum output requirements on the output of the neural network. Up to a neural network output of 0.7, C_b stays close to unity, after which it starts to increase. The rate of increase is particularly rapid for outputs exceeding 0.8.

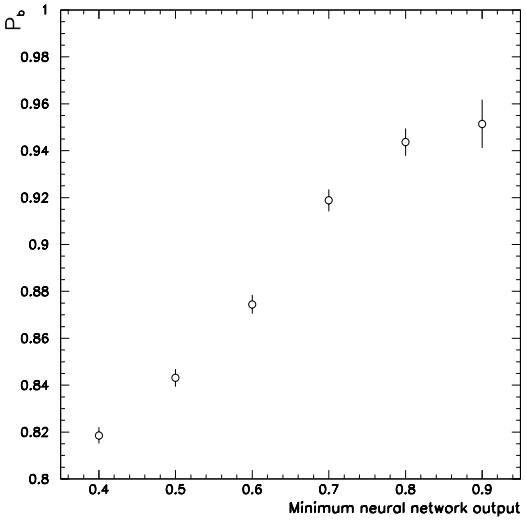

Figure 5.3: The hemispheric b purity (P_b), derived from data, as a function of a minimum requirement on the output of the neural network used for b tagging.

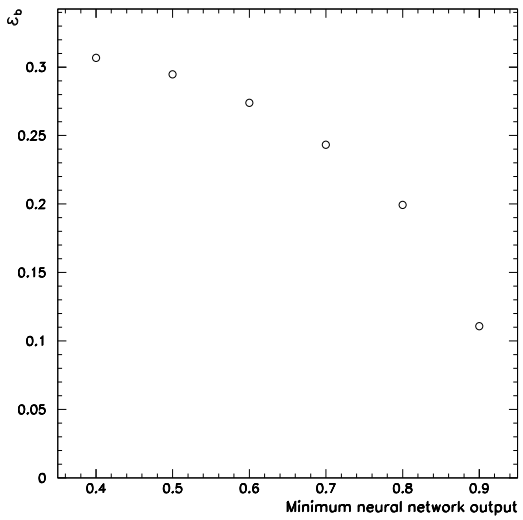

Figure 5.4: The hemispheric b efficiency (ε_b), derived from data, as a function of a minimum requirement on the output of the neural network used for b tagging.

Figure 5.3 and figure 5.4 show the hemispheric purity and efficiency measured from *data* for a range of minimum output requirements on the neural network. The purity flattens out above an output of 0.8. The efficiency drops rapidly as the requirement on the neural network output is decreased. As a consequence of this behaviour, and in light of further systematic studies presented in section 5.8, a default minimum neural network output of 0.8 is used. This yields :

$$P_b = (94.4 \pm 0.5)\%, \tag{5.4}$$

$$\varepsilon_b = (19.2 \pm 0.1)\%. \tag{5.5}$$

These results use $C_b = 1.035 \pm 0.002$ and $\varepsilon_{uds} = (0.100 \pm 0.006)\%$, derived from Monte Carlo studies.

5.4 Reconstructing Λ^0's.

When a secondary vertex in one event hemisphere yields a b tag from the neural network, the awayside hemisphere is searched for a Λ^0. The Λ^0 particle consists of a bound state of u,d and s quarks and is the lightest strange baryon with a nominal mass of 1.1157 GeV/c^2 [28]. The dominant decay modes are :

$$Br(\Lambda^0 \to p\pi^-) = (63.9 \pm 0.5)\%, \tag{5.6}$$

$$Br(\Lambda^0 \to n\pi^0) = (35.8 \pm 0.5)\%. \tag{5.7}$$

The efficient reconstruction of Λ^0 baryons on the awayside of a b tag is a common link between the analysis presented in this chapter and the measurement of the bottom baryon lifetime presented in chapter 7.

5.4.1 The Λ^0 Reconstruction Algorithm

The Λ^0 reconstruction algorithm follows the standard OPAL selection and is described in detail in [157][a]. The p,π^- decay products of the Λ^0 are used to select candidate Λ^0's using the following criteria (with reference to figure 5.5) :

- All oppositely charged pairs of tracks are considered and the higher momentum track is assumed to be a proton.
- Background is suppressed by using dE/dx information to check for consistency with track mass assignments. To avoid cross-over regions in the dE/dx curves (see [158] and figure 2.8) momentum dependent dE/dx requirements are used[b]. This requirement heavily suppresses the background from $K^0 \to \pi^+\pi^-$ decays, where the π^+ is misidentified as a proton.
- To improve the Λ^0 finding efficiency without seriously degrading the mass resolution, no CZ hits are required for the p,π^- tracks. The polar angle acceptance for Λ^0's is restricted to $|\cos\theta| < 0.9$, to ensure that tracks are well measured.
- The proton (pion) tracks are required to have an impact parameter in the plane transverse to the beam direction exceeding 0.5 (3) mm. This suppresses tracks from the primary event vertex.
- The proton and pion tracks must have an intersection between 1 cm and 130 cm on the side from the interaction point to which the Λ^0 momentum vector points.
- The angle, Φ, is defined in the plane transverse to the beam direction between the Λ^0 flight direction from the primary event vertex to the assumed Λ^0 decay point and the reconstructed Λ^0 momentum direction. The value of Φ must be smaller than 30 mrad, and also smaller than 10 mrad + 20 mrad / $p_t(\Lambda^0)$,

[a] The algorithm is referred to as 'method 2'.

[b] The dE/dx requirements are optimised for the momentum ranges : $p < 1.5\,\mathrm{GeV}/c$, $(1.5 \le p \le 2.0)\,\mathrm{GeV}/c$ and $p > 2.0\,\mathrm{GeV}/c$.

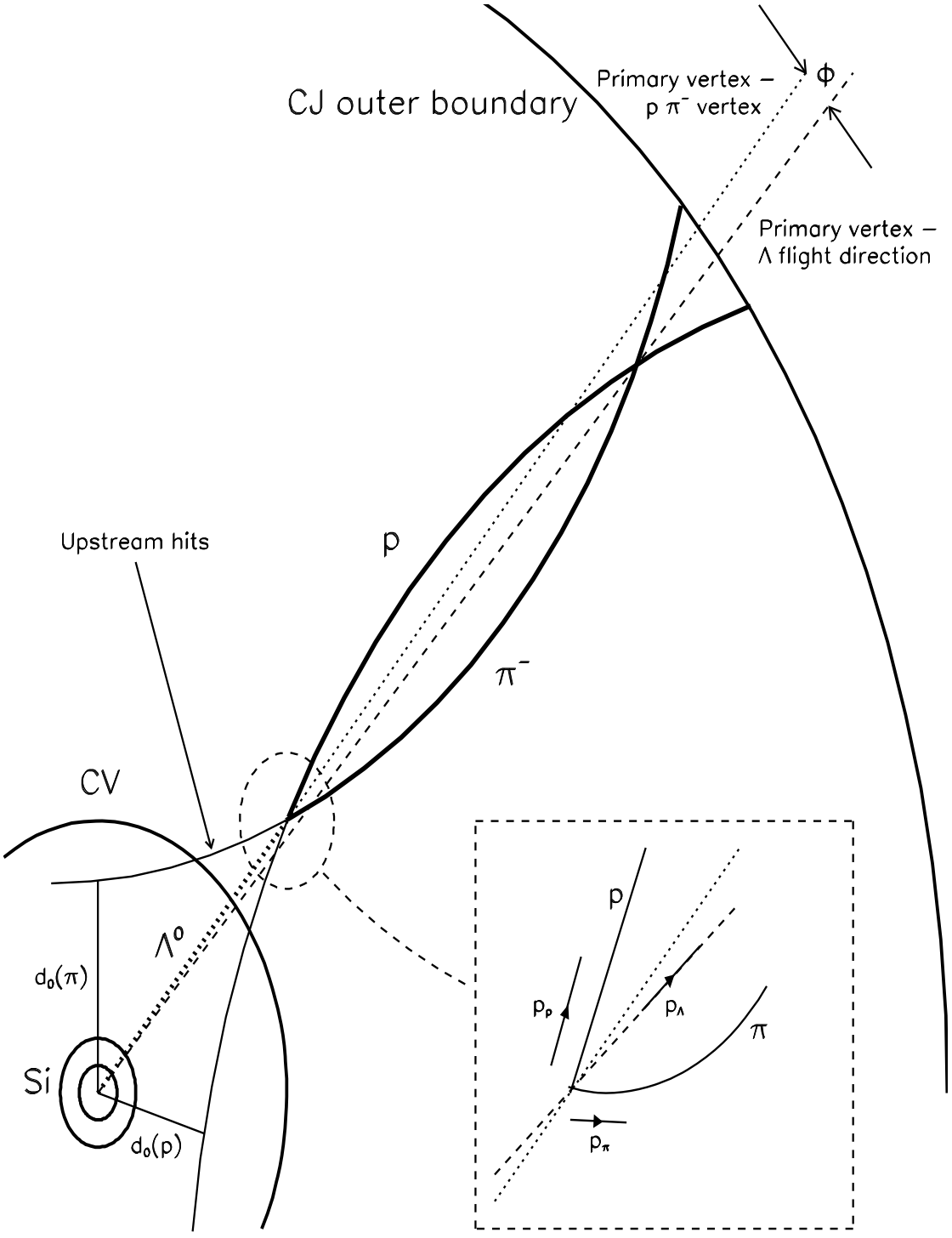

Figure 5.5: A schematic representation of the reconstruction of $\Lambda^0 \rightarrow p\pi^-$ decays using the central subdetectors of the OPAL detector (viewed in the plane perpendicular to the beam axis).

where $p_t(\Lambda^0)$ is the Λ^0 transverse momentum with respect to the beam axis in GeV/c. The latter condition accounts for multiple scattering, which is enhanced for low Λ^0 momenta.

- The probability that the Λ^0 decays before the measured radial decay distance (r), is defined as $\mathcal{P} = \exp((-m_{\Lambda^0}/p_t).(r/c\tau))$. For a Λ^0, $c\tau = 7.89$ cm [28]. The probability must be less than 95% to exclude backgrounds. For Λ^0's with small momenta ($p_t(\Lambda^0)$<1 GeV/c) the probability must be greater than 2% to exclude Λ^0's with unfeasibly short decay lengths.

- Candidate Λ^0's with hits on both tracks more than 5 cm upstream *towards* the collision point from the apparent Λ^0 decay point are removed.

- To remove γ conversions, the invariant mass of the track pair, assuming e^+e^- masses, must be greater than 40 MeV.

5.4.2 The Mass Resolution for Reconstructed Λ^0's

After the Λ^0 decay point is found the z component of the momentum of the p,π^- tracks is recalculated under the constraint that the tracks originate from the Λ^0 decay point. This improves the reconstructed Λ^0 mass resolution [159]. The reconstructed Λ^0 mass distributions from data and Monte Carlo are shown in figure 5.6. Both mass distributions are well centred around the nominal Λ^0 mass. However, the mass resolution is too narrow in the Monte Carlo. This is due to the optimistic modelling of the momentum resolution in the z direction for the central detectors[c].

For all pertinent studies presented in this thesis, the reconstructed Λ^0 mass (m_{Λ^0}) is required to fall in the range :

$$1.105\,\mathrm{GeV}/c^2 \leq m_{\Lambda^0} \leq 1.125\,\mathrm{GeV}/c^2. \tag{5.8}$$

Either side of the signal region, 5 MeV wide sidebands :

$$1.095\,\mathrm{GeV}/c^2 \leq m_{\Lambda^0} \leq 1.100\,\mathrm{GeV}/c^2 \tag{5.9}$$

[c]This defect was rectified in the 'new' Monte Carlo samples (which were not available for this analysis).

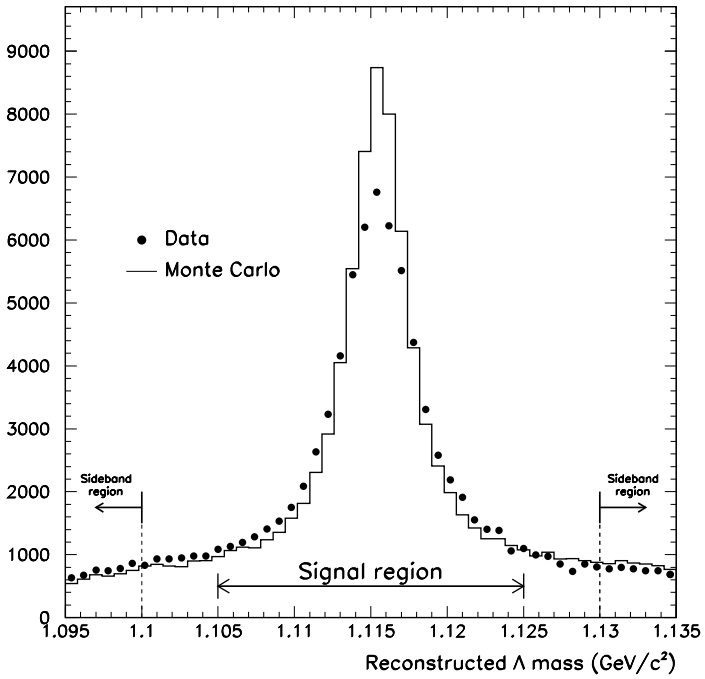

Figure 5.6: The reconstructed Λ^0 mass for data (points) and Monte Carlo (histogram), shown normalised to each other. The Monte Carlo has a better mass resolution than the data.

and :

$$1.130\,\mathrm{GeV}/c^2 \leq \mathrm{m}_{\Lambda^0} \leq 1.135\,\mathrm{GeV}/c^2, \tag{5.10}$$

are used to investigate Λ^0's from combinatorial background (fake Λ^0's). The sidebands were chosen to be far enough away from the signal region so as not to contain a significant proportion of real Λ^0's but near enough to provide an accurate representation of the background.

5.4.2.1 Smearing the Λ^0 Mass Resolution

The difference between the mass resolutions in data and Monte Carlo were substantially reduced by smearing the mass of real Λ^0's in the Monte Carlo ($\mathrm{m}_{\mathrm{mc}}^{\mathrm{old}}$) to give a new mass ($\mathrm{m}_{\mathrm{mc}}^{\mathrm{new}}$) according to the prescription :

$$\mathrm{m}_{\mathrm{mc}}^{\mathrm{new}} = \mathcal{K}(\mathrm{m}_{\mathrm{mc}}^{\mathrm{old}} - \mathrm{m}_{\Lambda^0}) + \mathrm{m}_{\Lambda^0}, \tag{5.11}$$

where, m_{Λ^0} is the nominal Λ^0 mass and the amount of smearing is defined by a factor $\mathcal{K}$.

A χ^2 test was used to gauge the agreement between data and smeared Monte Carlo in the signal and sideband region after normalising the distributions to each

other. In the signal region test, the background was subtracted using a linear fit constrained by the sidebands. Using the signal and sideband regions in the χ^2 test provided a thorough test of the smearing and helped in the estimation of systematic errors when using the smeared Λ^0 mass.

The Λ^0 mass resolution is momentum dependent, so, three Λ^0 momentum ranges ($0 \rightarrow 4\,\mathrm{GeV}/c$, $4 \rightarrow 10\,\mathrm{GeV}/c$ and $10 \rightarrow 25\,\mathrm{GeV}/c$) were investigated. A smear factor was evaluated for each range. The momentum ranges were chosen to provide adequately populated samples of Λ^0's at higher momenta, where the Λ^0 production rate is expected to have a significant contribution from b hadron decays.

The central value of $\mathcal{K}$ for each momentum range was chosen primarily to minimise the χ^2 in the signal region, but a reasonable χ^2 for the sidebands was also required. The minimum χ^2 for the sidebands was used to define the range of $\mathcal{K}$ values for the systematic error estimate. Optimal central values of $\mathcal{K} = 1.35$, 1.40 and 1.80 were found for the momentum ranges $0 \rightarrow 4$ GeV/c, $4 \rightarrow 10$ GeV/c and $4 \rightarrow 10$ GeV/c respectively. Table 5.2 summarises the ranges of $\mathcal{K}$ used to smear the Monte Carlo mass for each momentum range.

The normalised Λ^0 mass plots for data and smeared Monte Carlo for each momentum range are shown in figure 5.7. The same distribution for all Λ^0 momenta is shown in figure 5.8. These Λ^0 mass distributions show that the agreement between data and Monte Carlo is significantly improved after smearing the Monte Carlo Λ^0 mass.

5.4.3 The Λ^0 Reconstruction Efficiency

Figure 5.9 shows the efficiency for detecting all[d] Λ^0's using the decay $\Lambda^0 \rightarrow \mathrm{p}\pi^-$, as a function of the Λ^0 momentum. The percentage efficiencies are extracted from the Monte Carlo and are shown before and after smearing. The efficiency rises rapidly with Λ^0 momentum, as the π^- reconstruction efficiency increases. A maximum efficiency is reached at 4 GeV/c before it falls again at higher momenta because of the maximum Λ^0 decay length requirement, described in section 5.4.1.

On average, the smeared Λ^0 mass gives a reduction in efficiency of $\sim$1.5% compared to the unsmeared Λ^0 mass in the Λ^0 momentum range $0 \rightarrow 10\,\mathrm{GeV}/c$. The

[d] To be clear : this includes *all* possible Λ^0 decay modes.

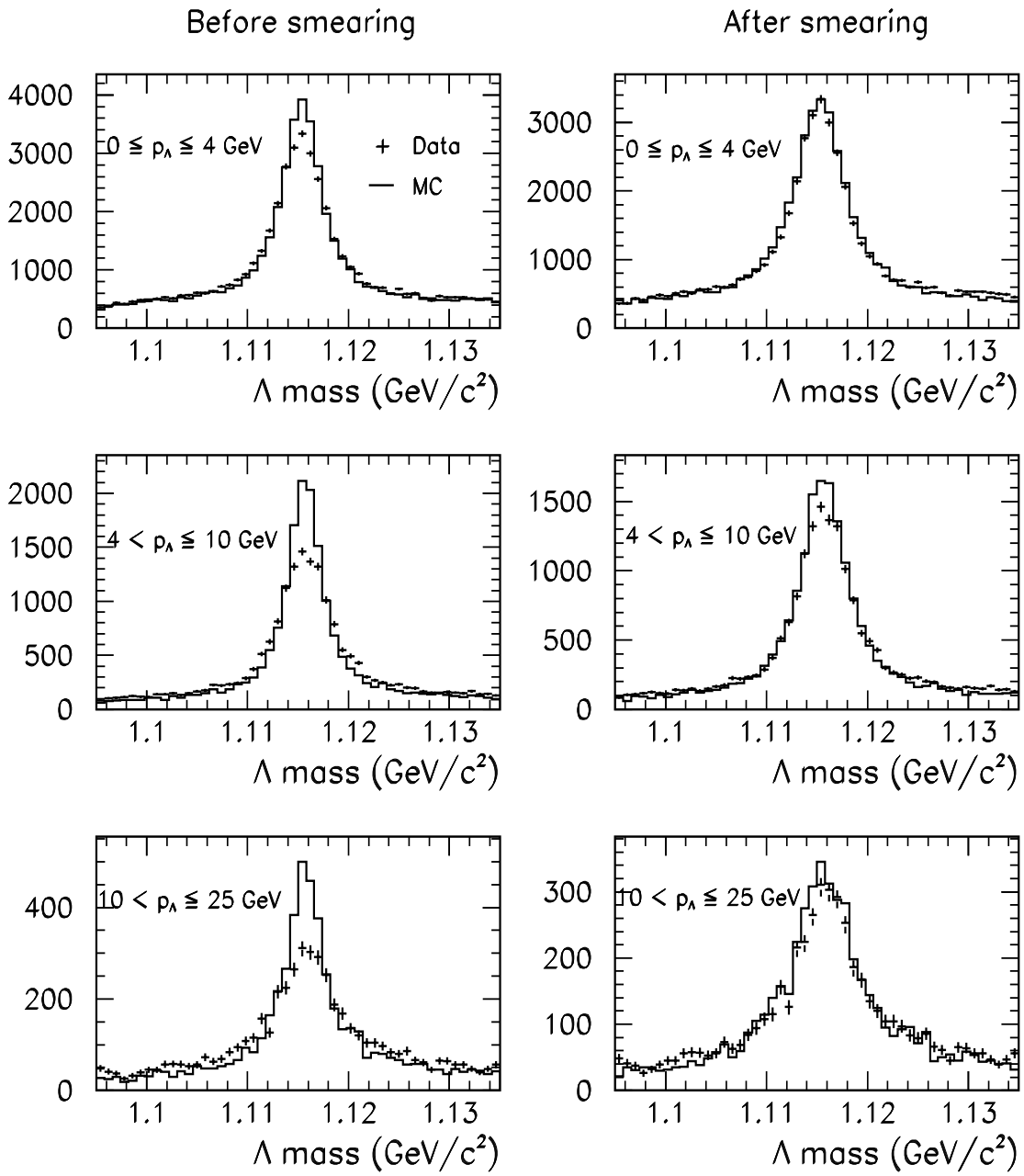

Figure 5.7: A comparison of the reconstructed Λ^0 mass for data (crosses) and Monte Carlo (histogram) for different Λ^0 momentum ranges, before and after the Monte Carlo mass is smeared. The distributions are normalised to each other.

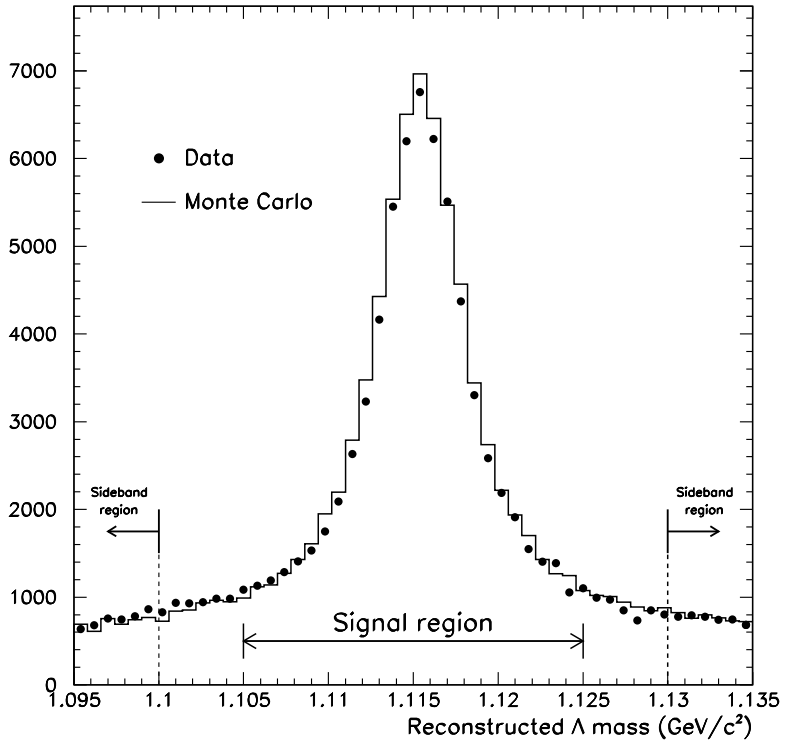

Figure 5.8: A comparison, over all Λ^0 momenta, of the reconstructed Λ^0 mass from data (points) and smeared Monte Carlo (histogram). The distributions are normalised to each other.

reduction is $\sim$2.5% in the range $10 \rightarrow 25\,\mathrm{GeV}/c$.

5.4.4 Reconstructing Λ^0's from Bottom Hadron Decays

A range of Λ^0 minimum momentum requirements were used to study the stability of the branching ratio measurement. For each minimum momentum requirement, the Λ^0 detection efficiency for Λ^0's from b hadron decays was evaluated. The generator level Monte Carlo momentum spectrum for Λ^0's from b hadron decays was weighted with the Λ^0 detection efficiency from figure 5.9. The unavoidable inefficiency due to neutral Λ^0 decays is included in this efficiency. The efficiency for detecting a Λ^0 from a b hadron decay for a range of minimum momentum requirements can therefore be evaluated.

The resulting Λ^0 reconstruction efficiency, above a range of minimum momentum requirements, is shown in figure 5.10. The efficiency is approximately constant at $\sim$22% up to a minimum momentum requirement of 3 GeV/c, before falling steadily for larger momentum requirements.

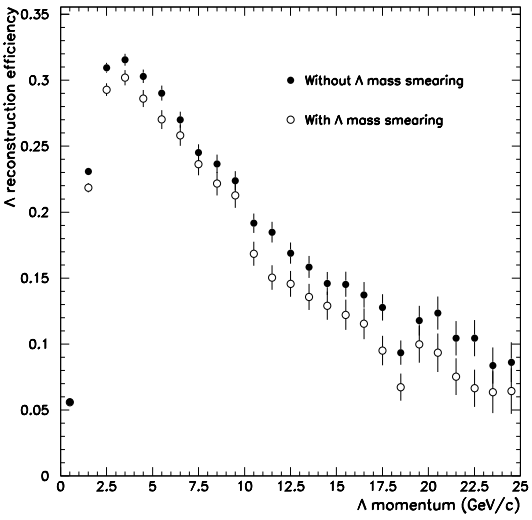

Figure 5.9: The efficiency, determined from Monte Carlo, for detecting a Λ^0 as a function of the Λ^0 momentum. The efficiency is shown before (solid points) and after (open points) smearing the Monte Carlo Λ^0 mass.

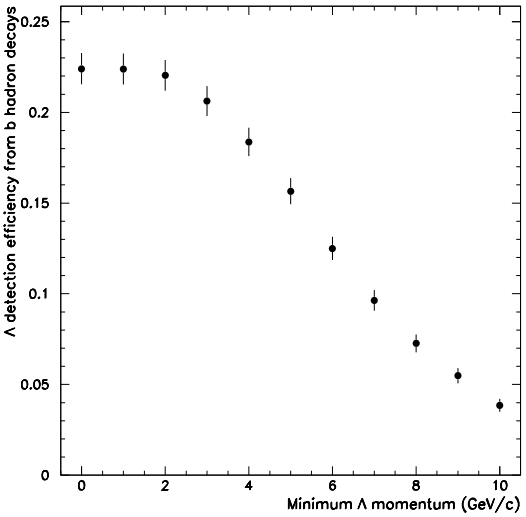

Figure 5.10: The efficiency for detecting Λ^0's from the decay of b hadrons, as a function of a minimum requirement on the Λ^0 momentum. The smeared Monte Carlo Λ^0 mass has been used.

5.5 Backgrounds to the Measurement of Br(b hadron$\rightarrow \Lambda^0$ X)

The background to the measurement of Br(b hadron$\rightarrow \Lambda^0$ X) is due to three sources of Λ^0 candidates :

- Fake Λ^0's[e]
- Λ^0's from non-$Z^0 \rightarrow b\bar{b}$ events
- Fragmentation Λ^0's from $Z^0 \rightarrow b\bar{b}$ events

In order to measure Br(b hadron$\rightarrow \Lambda^0$ X), the Λ^0 momentum spectrum for each of the background sources needs to be subtracted from the overall Λ^0 momentum spectrum on the awayside of b tagged events. The resulting Λ^0 momentum spectrum is assumed to come from b hadron decays.

In the work that follows, it is often necessary to normalise data and Monte Carlo distributions. The normalisation factor is determined by considering the total number of b tagged hemispheres in data and Monte Carlo.

[e] Fake Λ^0's arise when tracks are incorrectly identified as $p\pi^-$ combinations.

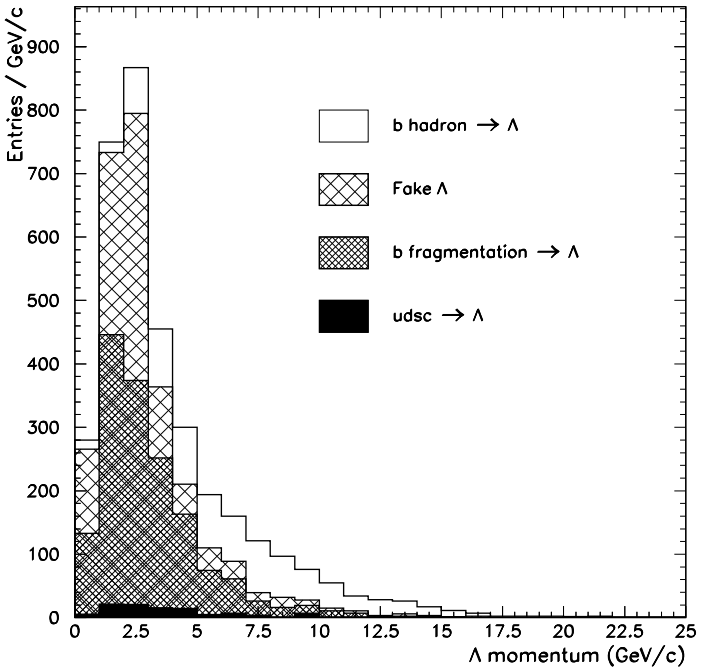

Figure 5.11: The momentum spectrum of reconstructed Λ^0's in the awayside hemispheres of b tagged events. The estimated contribution from fake Λ^0's, fragmentation Λ^0's and non-$Z^0 \rightarrow b\bar{b}$ events are indicated by the shaded areas.

5.5.1 Fake Λ^0's

Fake Λ^0's dominate the Λ^0 momentum distribution at low momentum and have a tail extending to higher momentum. The sidebands of the Λ^0 mass distribution from data were used to estimate the momentum spectrum for fake Λ^0's. Monte Carlo studies show that the fake purity in the sidebands is around 90% and weakly momentum dependent. To compensate for this, a momentum dependent scale factor derived from Monte Carlo was used to correct the sideband momentum distribution extracted from data, in 1 GeV/c bins. The extracted momentum spectrum for fake Λ^0's on the awayside from a b tagged hemisphere is shown in figure 5.11.

5.5.2 Λ^0's from non-$Z^0 \rightarrow b\bar{b}$ Events

After the neural network selection of candidate $b\bar{b}$ secondary vertices there is only a very small contribution from non-$Z^0 \rightarrow b\bar{b}$ events to the Λ^0 momentum spectrum. Monte Carlo predictions were used to model the Λ^0 momentum spectrum from this source on the awayside of b tagged events.

Figure 5.11 shows the estimated contribution from this source compared to the

overall Λ^0 momentum spectrum on the awayside of b tagged events. These events have a negligible effect in the region above 5 GeV/c where Λ^0's from b hadron decays are the dominant contribution.

5.5.3 Λ^0's from Bottom Fragmentation

The momentum distribution of Λ^0's from the fragmentation process in $Z^0 \rightarrow b\bar{b}$ events is important at low momenta and also extends well into the region dominated by Λ^0's from b hadron decays. It is therefore important to understand this contribution as well as possible.

Monte Carlo generator information was used to identify Λ^0's from this source. Figure 5.11 shows the estimated contribution. In section 5.8.3.2, further studies that checked this contribution and reduced the dependence on Monte Carlo for this important source of Λ^0's are discussed in some detail.

5.6 The Momentum Spectrum of Λ^0's from Bottom Hadron Decays

The three background sources described above are subtracted from the Λ^0 momentum spectrum on the awayside of b tagged hemispheres. The resulting Λ^0 momentum spectrum is attributed to b hadron decays and is shown in figure 5.12. The signal is compatible with the predicted shape from Monte Carlo (within statistical errors) in the range $0 \rightarrow 2\,\mathrm{GeV}/c$ giving confidence that the large subtractions in this range are realistic. The signal stays approximately constant from $3 \rightarrow 8\,\mathrm{GeV}/c$, before falling at higher momenta. As a further check of the subtraction methods, the shape of the extracted spectrum was compared to that expected from Monte Carlo predictions. These distributions are normalised to each other and shown in figure 5.12, to enable the shapes to be compared.

The data agrees well with Monte Carlo over the entire Λ^0 momentum range. This implies that the background subtractions from the overall Λ^0 momentum spectrum have been performed correctly.

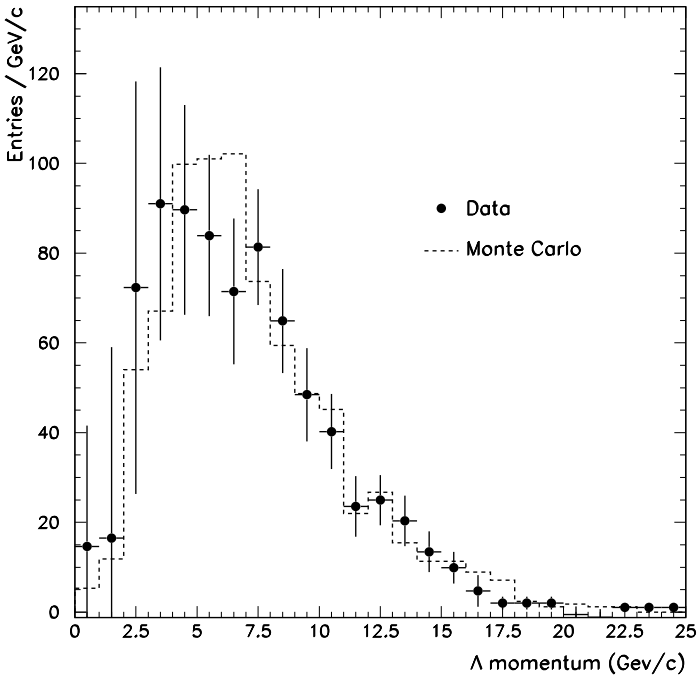

Figure 5.12: A comparison between the shape of the Λ^0 momentum spectrum from bottom hadron decays extracted from the data and that predicted by the Monte Carlo. The errors are purely statistical.

5.7 Extracting the Branching Ratio

The fractional contributions to the overall Λ^0 momentum spectrum from b fragmentation, fake Λ^0's and b hadron decays, are shown in figure 5.13 as a function of a minimum Λ^0 momentum requirement. The contribution from non-$Z^0 \rightarrow b\bar{b}$ events is negligible and almost momentum independent. Therefore, it is not shown. The contribution from b hadron decays rises with Λ^0 momentum before stabilising at 7 GeV/c, contributing approximately 60% to the overall Λ^0 rate. The Λ^0 contribution from fakes and b fragmentation remains approximately constant over the range 0$\rightarrow$3 GeV/c and 0$\rightarrow$5 GeV/c respectively, before falling at higher momenta and stabilising at 7 GeV/c with each source contributing approximately 20% to the overall Λ^0 rate. The branching ratio value at a minimum momentum requirement of 7 GeV/c is used as a central value for Br(b hadron $\rightarrow \Lambda^0$X). This maximises the Λ^0 signal from b hadron decays whilst minimising the contribution from background sources.

As a further check of the analysis method the branching ratio for a minimum momentum requirement of 7 GeV/c was extracted from Monte Carlo. A branching

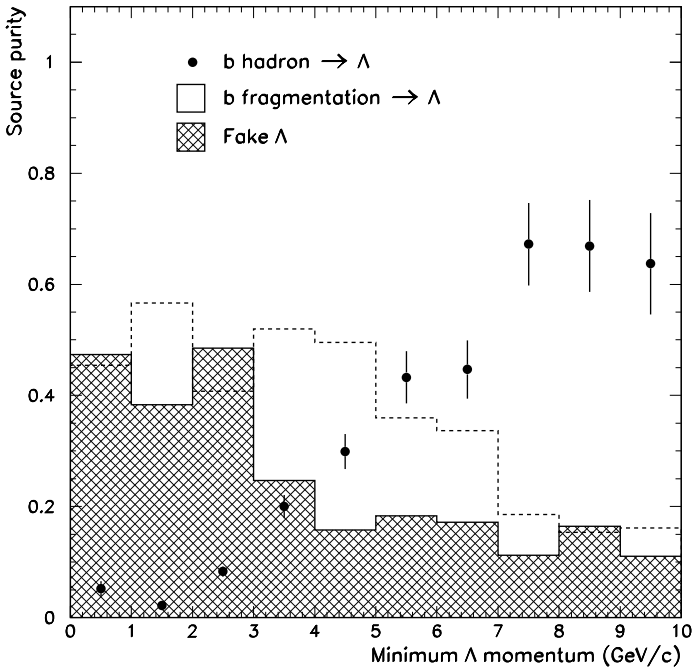

Figure 5.13: The fractional contributions of Λ^0's from b hadron decays (points), fake Λ^0's (solid histogram) and Λ^0's from b fragmentation (broken histogram) as a function of a minimum Λ^0 momentum requirement. The Λ^0's are reconstructed on the awayside from a b tag.

ratio of $(3.5 \pm 0.4)\%$ was obtained which is compatible with the generated value of 3.7%. The branching ratio extracted from Monte Carlo is independent of the minimum Λ^0 momentum requirement. Figure 5.14 shows the branching ratio and statistical errors calculated from the data for a range of Λ^0 minimum momentum requirements. The larger errors at low momenta arise from the significant subtractions made in this momentum range. At higher momentum the error increases again due to the limited number of energetic Λ^0's. The branching ratio error for each minimum Λ^0 momentum requirement is highly correlated from bin to bin. The stability of the branching ratio with varying minimum momentum requirement gives confidence in the background subtractions.

In conclusion, at a minimum Λ^0 momentum requirement of 7 GeV/c, the branching ratio is measured as :

$$\mathrm{Br}(\text{b hadron} \to \Lambda^0 \mathrm{X}) = (5.9 \pm 0.6)\%, \tag{5.12}$$

where the error is purely statistical.

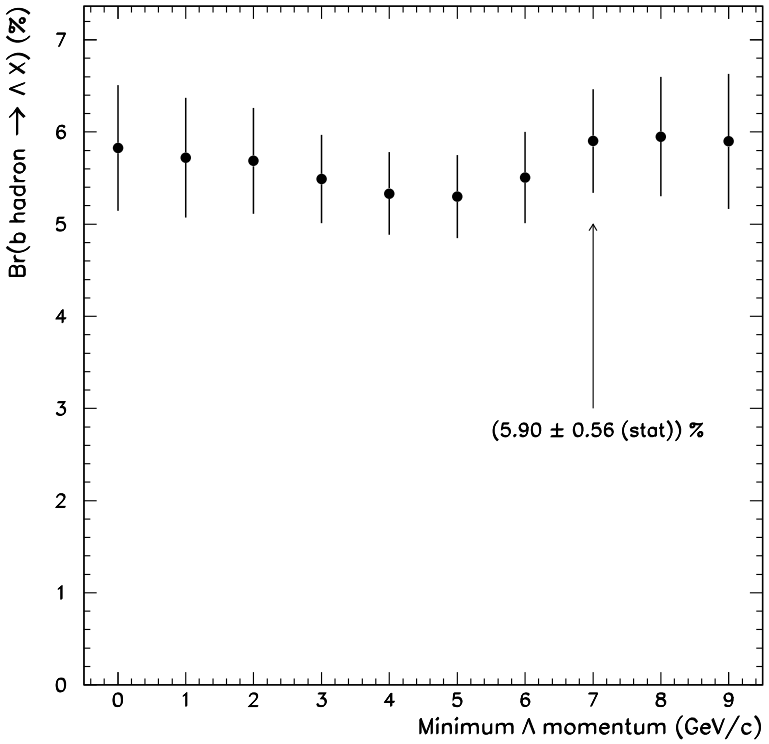

Figure 5.14: The branching ratio, Br(b hadron $\rightarrow \Lambda^0$X), derived from data as a function of a minimum momentum requirement on the Λ^0.

5.8 Systematic Error Studies

In this section, possible systematic errors on the measurement of the branching ratio arising from : the estimation of the b purity, the Λ^0 reconstruction efficiency and the identification of background sources of Λ^0's, are investigated. The final systematic errors are summarised in table 5.1.

Source of Uncertainty	Systematic Error (%)
Momentum spectrum of Λ^0's from b fragmentation	± 0.38
Monte Carlo Λ^0 mass smearing	$^{+0.24}_{-0.08}$
Momentum spectrum of fake Λ^0's	± 0.05
Total	$^{+0.45}_{-0.39}$

Table 5.1: A summary of the systematic errors on Br(b hadron $\rightarrow \Lambda^0$X).

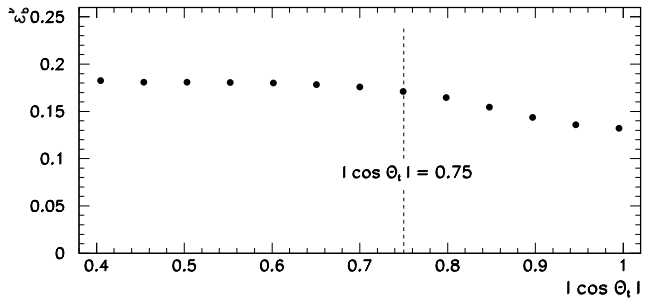

Figure 5.15: The single tagging b efficiency from Monte Carlo as a function of the polar thrust angle, θ_t. The efficiency starts to drop at the edge of the microvertex detector acceptance. The maximum polar thrust angle used in this analysis is indicated by the dashed line.

5.8.1 b Purity

The systematic error on the b purity has been evaluated by considering the dependence on Monte Carlo when evaluating the hemispheric b efficiency correlation coefficient (C_b) and the light quark efficiencies (ε_{uds}).

5.8.1.1 Hemispheric Efficiency Correlations

When extracting C_b from Monte Carlo, it is assumed that the tagging probabilities for the two hemispheres in a multihadronic event are correlated only through geometrical effects, as described in section 4.7.2.

The single tagging b efficiency from Monte Carlo (ε_b^ν) is shown as a function of the thrust angle ($|\cos\theta_t|$) in figure 5.15. The efficiency drops steadily for $|\cos\theta_t| > 0.75$, which corresponds to the acceptance edge of the microvertex detector. The behaviour of ε_b^ν reinforces the assumption that any difference in C_b from unity is primarily due to the reduction in the microvertex detector acceptance at large $|\cos\theta_t|$. In figure 5.16, C_b (for calculation details see section 4.7.2) is shown for minimum neural network output requirements of 0.7, 0.8 and 0.9, as a function of $|\cos\theta_t|$. A neural network output > 0.9 gives a substantially larger value of C_b compared to the two lower output requirements. This can be understood from figure 5.17 which shows ε_b^ν as a function of ϕ_t, the azimuthal angle of the thrust axis. The variation in amplitude of ε_b^ν increases as better secondary vertices are required through larger minimum output requirements on the neural network. The peaks in ε_b^ν at $\phi = 0,\ \pi,\ 2\pi$ arise because one of the inputs to the neural network is the

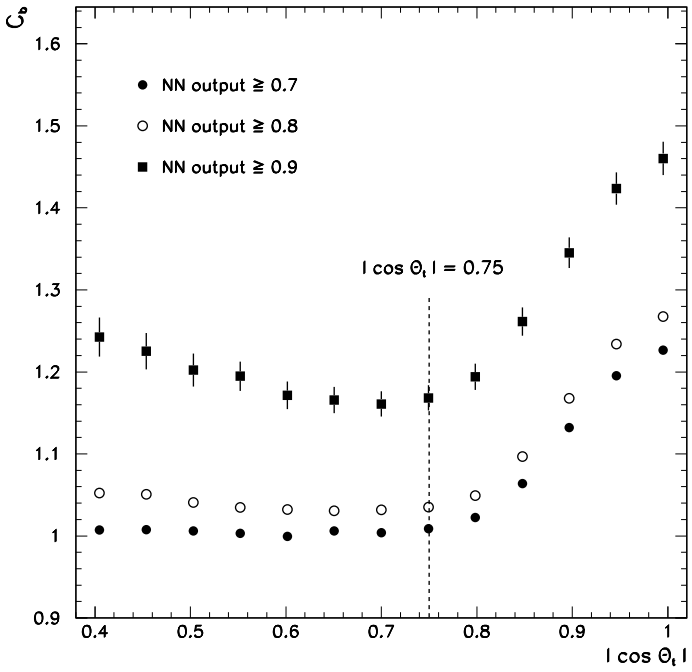

Figure 5.16: The hemispheric b efficiency correlation coefficient as a function of polar thrust angle. Three minimum requirements on the output of the neural network used for b tagging are shown. The maximum polar thrust angle used in this analysis is also shown.

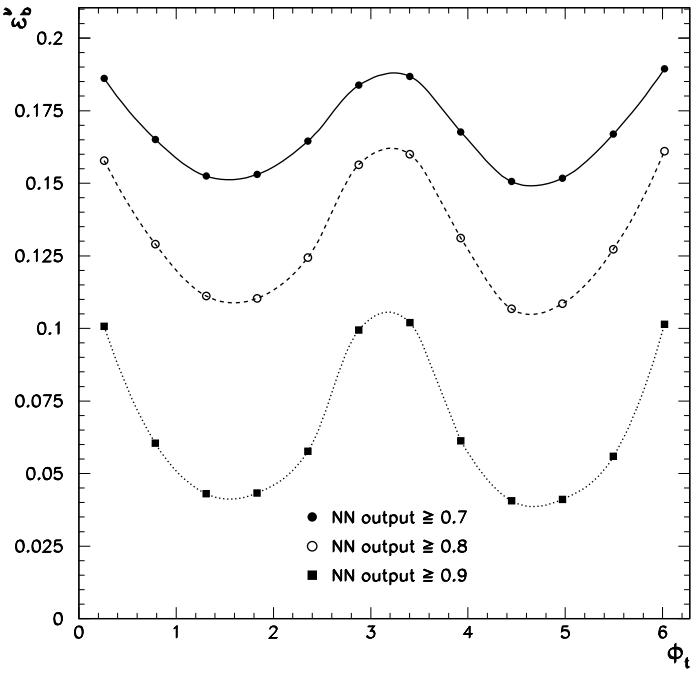

Figure 5.17: The single tagging b efficiency from Monte Carlo as a function of the azimuthal thrust angle. Three minimum requirements on the output of the neural network used for b tagging are shown.

impact parameter significance with respect to the primary vertex of the 2^{nd}, 3^{rd} and 4^{th} most separated tracks. It is easier to have significantly separated tracks when the thrust axis lies along the x-axis because the beam spot is elliptical and the major axis lies along the x-axis.

In order to reduce the dependence on C_b (and therefore Monte Carlo) it is clear that :

- The absence of the silicon detector at high $|\cos\theta_t|$, which produces undesirable efficiency correlations, can be avoided by only selecting events with $|\cos\theta_t| \leq 0.75$.
- A minimum neural network output of 0.8 (rather than 0.9) significantly reduces hemispheric efficiency correlations, as the ϕ dependence of the tagging efficiency is reduced.

To check the sensitivity of the b purity to C_b, the b purity was recalculated from data using values of C_b which were 3 standard deviations higher and lower than the central value. These gave no significant change in the calculated b purity. An error from uncertainties on C_b was therefore not assigned.

5.8.1.2 Light Quark Efficiencies

The light quark hemispheric efficiencies (ε_{uds}) are extracted from Monte Carlo generator information. It has already been shown that the contribution of $Z^0 \to u\bar{u}, d\bar{d}, s\bar{s}$ events for the default neural network output requirement is very small ($\sim$1%) and not expected to affect the calculation of the b purity significantly. The sensitivity to ε_{uds} was checked by using values of ε_{uds} equalling zero and twice the values obtained from Monte Carlo. These gave no significant change in the b purity extracted from the data. A systematic error from uncertainties on ε_{uds} is therefore unnecessary.

5.8.2 Λ^0 Reconstruction

The dominant systematic error in Λ^0 reconstruction is expected to be due to the uncertainty in the Monte Carlo Λ^0 mass smearing factor ($\mathcal{K}$) for a given momentum range. Possible biases in the Λ^0 selection procedure and potential effects from bottom baryon polarisation are also considered.

5.8.2.1 Monte Carlo Mass Smearing

The numerical value of $\mathcal{K}$ affects both the Λ^0 finding efficiency and the momentum spectra of the various background sources of Λ^0's derived from the Monte Carlo. Table 5.2 shows the range of $\mathcal{K}$ that was assigned to each Λ^0 momentum range, as described in section 5.4.2.1. The branching ratio has been recalculated at a minimum momentum requirement of 7 GeV/c for a range of $\mathcal{K}$ values[f]. The results are shown in table 5.2. An absolute change in the branching ratio of $^{+0.24}_{-0.08}$ % was observed. This is used as the systematic error due to the uncertainty on the smearing of the Monte Carlo Λ^0 mass.

$\mathcal{K}$	Λ^0 Momentum Range (GeV/c)			Br at 7 GeV/c	ΔBr
Range	$0 \leq p_\Lambda \leq 4$	$4 < p_\Lambda \leq 10$	$10 < p_\Lambda \leq 25$	(%)	(%)
Upper	1.60	1.50	1.90	6.14 ± 0.58	0.24
Central	1.35	1.40	1.80	5.90 ± 0.56	—
Lower	1.10	1.30	1.70	5.82 ± 0.55	0.08

Table 5.2: The systematic error (ΔBr) on the branching ratio due to the uncertainty on the Monte Carlo Λ^0 mass smearing factor, $\mathcal{K}$.

5.8.2.2 Selection Biases

As stated in the introduction to this chapter, only the most energetic Λ^0 from each hemisphere is used in the calculation of the branching ratio. This is not thought to introduce any significant bias to the branching ratio result. Monte Carlo studies showed that 90% of hemispheres contained only one Λ^0 with momentum > 7 GeV/c. In 95% of hemispheres with more than one Λ^0, the most energetic Λ^0 was the decay product of a b hadron.

5.8.2.3 Bottom Baryon Polarisation

As described in section 3.3.2, bottom quarks from Z^0 decays are thought to be produced with a large longitudinal polarisation. The resulting bottom baryon po-

[f] When estimating the systematic error the $\mathcal{K}$ values were varied between upper and lower limits across all Λ^0 momentum ranges.

larisation is estimated to lie in the range -$(47 \rightarrow 94)\%$ [89]. The effect of bottom baryon polarisation on the Λ^0 finding efficiency was studied in [160]. The Λ^0 momentum spectrum from polarised bottom baryons was found to be slightly softer than from unpolarised bottom baryons. The effect on the Λ^0 reconstruction efficiency was minimal. A systematic error from bottom baryon polarisation is not included in this analysis.

5.8.3 Background Sources to the Λ^0 Momentum Spectrum

In this section, the systematic errors that may arise in the evaluation of background sources of Λ^0's are considered. The backgrounds are subtracted from the overall Λ^0 momentum spectrum on the awayside of b tagged events.

5.8.3.1 Fake Λ^0's

The fake Λ^0 momentum spectrum is derived from the sidebands of the Λ^0 mass distribution in the data. Monte Carlo only provides a small correction factor to account for the fake purity of the sideband. The normalisation of the fake Λ^0 momentum spectrum from data was checked. The normalisation was varied whilst keeping all other background levels fixed and the momentum spectrum for Λ^0's from b hadron decays was extracted. A χ^2 test was used to compare the shape of the extracted Λ^0 momentum spectrum to the Monte Carlo prediction.

A normalisation factor of 1.05 minimised the χ^2 and gave a branching ratio at 7 GeV/c of $(5.85 \pm 0.56)\%$. This is an absolute difference of 0.05% compared to the result given in section 5.7. This difference was adopted as the systematic error due to the uncertainty on the normalisation of the fake Λ^0 spectrum.

The shape of the Λ^0 momentum spectrum from this source and from b fragmentation are very similar, as shown in figure 5.11. It is not possible to assign a normalisation factor to the fake and b fragmentation Λ^0's separately. However, the shape of the fake Λ^0 momentum spectrum is essentially fixed from data. This method for estimating a systematic error is therefore thought to be more suited to fake Λ^0's. An independent study of the systematic error associated with Λ^0's from b fragmentation is presented in the next section.

5.8.3.2 Λ^0's from b Fragmentation

There is a non-negligible tail in the momentum spectrum from this process and so uncertainties in this rate will affect the extracted branching ratio. The branching ratio is shown as a function of minimum momentum requirement in figure 5.14. Although the result is fairly stable there is a small drop in the branching ratio in the range 3→5 GeV/c. This is the region where the contribution from b fragmentation to the overall Λ^0 momentum spectrum changes rapidly, as shown in figure 5.13. Therefore, the rate of this process may not be properly modelled in the Monte Carlo.

There is no independent way of verifying either the normalisation or shape of the Λ^0 momentum spectrum predicted by Monte Carlo. The difference in measured branching ratios at 5 and 7 GeV/c is therefore used to estimate the systematic error. Adopting the entire difference as the systematic error seemed too conservative. The b fragmentation contribution to the overall Λ^0 momentum spectrum falls rapidly between 5→7 GeV/c and so the systematic error would be expected to fall also. The difference was therefore scaled by the ratio of the relative contributions from b fragmentation Λ^0's at minimum momentum requirements of 5 and 7 GeV/c. From this study, a systematic error of ± 0.38% was assigned to the branching ratio result at 7 GeV/c.

5.9 Results

After including all the systematic errors the final result becomes :

$$\mathrm{Br}(\text{b hadron} \to \Lambda^0\mathrm{X}) = (5.9 \pm 0.6\,(\mathrm{stat})^{+0.5}_{-0.4}\,(\mathrm{syst}))\%, \tag{5.13}$$

where the dominant error comes from the uncertainties on the Λ^0 momentum spectrum from b fragmentation.

This result compares well to that published by the DELPHI collaboration [126], $\mathrm{Br}(\text{b hadron} \to \Lambda^0\mathrm{X}) = (5.9 \pm 0.7\,(\mathrm{stat}) \pm 0.9\,(\mathrm{syst}))\%$[g]. Their independent method is outlined in section 3.3.5.3.

[g] Strictly speaking, the DELPHI collaboration measure the average number of Λ^0's produced per b hadron decay, n(b hadron→ Λ^0X). This is equivalent to Br(b hadron→ Λ^0X) under the assumption that only one Λ^0 is produced per b hadron decay, this is not unreasonable, as shown in equation 3.19.

5.10 An Estimation of $f(b \rightarrow \Lambda_b^0)Br(\Lambda_b^0 \rightarrow \Lambda^0 X)$

The branching ratio, Br(b hadron $\rightarrow \Lambda^0$ X), can be expressed as :

$$\mathrm{Br(b\ hadron} \rightarrow \Lambda^0 \mathrm{X}) = \mathrm{f}(\mathrm{b} \rightarrow \Lambda_\mathrm{b}^0)\,\mathrm{Br}(\Lambda_\mathrm{b}^0 \rightarrow \Lambda^0 \mathrm{X}) + (1 - \mathrm{f}(\mathrm{b} \rightarrow \Lambda_\mathrm{b}^0))\,\mathrm{Br}(\mathrm{B} \rightarrow \Lambda^0 \mathrm{X}). \tag{5.14}$$

The product branching ratio, $f(b \rightarrow \Lambda_b^0)Br(\Lambda_b^0 \rightarrow \Lambda^0 X)$, can be derived using the following measurements :

- Br(b hadron$\rightarrow \Lambda^0$ X) is the measured value of $(5.9^{+0.8}_{-0.7})\%$ (statistical and systematic errors combined).
- Br(B$\rightarrow \Lambda^0$ X) = (3.8$\pm$0.7)% [28]. This result comes from Υ(4s) experiments. At LEP energies, B_s^0 mesons are also produced. The decay, $B_s^0 \rightarrow \Lambda^0$ X, is assumed to have the same branching ratio as the mix of B mesons produced from Υ(4s) decays.
- $f(b \rightarrow \Lambda_b^0) = 0.09 \pm 0.03$, as shown in equation 3.38.

Combining these measurements yields :

$$\mathrm{f}(\mathrm{b} \rightarrow \Lambda_\mathrm{b}^0)\,\mathrm{Br}(\Lambda_\mathrm{b}^0 \rightarrow \Lambda^0 \mathrm{X}) = (2.3^{+0.9}_{-0.8})\%. \tag{5.15}$$

The uncertainty on Br(b hadron$\rightarrow \Lambda^0$ X) is the largest contribution to the error.

This result compares well to the value of $(2.2 \pm 1.5)\%$ derived by the DELPHI collaboration and an independent estimate of $(3.7 \pm 0.5)\%$. Both these methods are described in section 3.3.5.3.

5.11 Summary

In this chapter, a study of Λ^0 production in awayside hemispheres from a b tag is presented. A neural network algorithm using the properties of the secondary vertex with the largest decay length significance in the tagged hemisphere, is used to enhance $Z^0 \rightarrow b\bar{b}$ events. The Λ^0 momentum spectrum was measured and background contributions from fakes, b fragmentation and non-$Z^0 \rightarrow b\bar{b}$ events were subtracted, leaving the Λ^0 momentum spectrum from b hadron decays.

The shape of the extracted momentum spectrum was consistent with Monte Carlo predictions and the observed rate of Λ^0 production was used to measure the inclusive branching ratio , Br(b hadron $\rightarrow \Lambda^0$X) = $(5.9 \pm 0.6\,(\mathrm{stat})^{+0.5}_{-0.4}\,(\mathrm{syst}))\%$.

The dominant systematic errors come from :

- The dependence on Monte Carlo for the Λ^0 momentum spectrum from b fragmentation. It may be possible to extract information on this momentum spectrum through studies of b tagged events with two Λ^0's[h] or a D*[i] on the away-side. Such investigations were statistically limited using the 1991 and 1992 data-sets only.

- Uncertainties on the smearing of the Monte Carlo Λ^0 mass needed to give good agreement with data. This error could be reduced with a more complete investigation into the fundamental causes of the data–Monte Carlo mass resolution discrepancy. The 'new' Monte Carlo samples address this deficiency, as shown in figure 7.1.

This measured value of Br(b hadron$\rightarrow \Lambda^0$ X), the measurement of Br(B$\rightarrow \Lambda^0$X) from Υ(4s) experiments and an estimate of f(b $\rightarrow \Lambda^0_{\mathrm{b}}$), described in section 3.3.5.2, were used to extract f(b $\rightarrow \Lambda^0_{\mathrm{b}}$) Br($\Lambda^0_{\mathrm{b}} \rightarrow \Lambda^0$X) = $(2.3^{+0.9}_{-0.8})\%$. This value is consistent with predictions from other estimates, as described in section 3.3.5.3.

[h] One of the Λ^0's must come from fragmentation (predominantly the less energetic one).

[i] The D* is assumed to come from b hadron decay, therefore a Λ^0 on the same side must come from fragmentation.

Chapter 6

A Measurement of the Average Bottom Hadron Lifetime

6.1 Overview

Events were resolved into jets using the cone algorithm described in section 4.4.2. Only events with exactly two jets were used in this analysis. The event is divided into two hemispheres using the thrust axis of the event. Hemispheres are b tagged using the neural network algorithm described in section 4.7.1 and the awayside hemispheres were searched for secondary vertices using the 'build-up' algorithm described in section 4.6.2.

The decay length between the primary event vertex and the secondary vertex is converted into a decay time using an estimate of the b hadron momentum. A novel technique based around a neural network algorithm is used to estimate the b hadron momentum. The neural network allows charged tracks from the decay of the b hadron and b fragmentation to be statistically separated. The average b hadron lifetime is extracted from the distribution of reconstructed decay times using a binned maximum likelihood fit.

6.2 Event Sample

Data collected between 1991 and 1994 with the silicon microvertex detector operational were used in this analysis. The 'new' Monte Carlo data-sets were also used.

The prefix 'new' will be discarded when referring to these Monte Carlo samples. The 'new tune $b\bar{b}$' Monte Carlo was used to evaluate some of the systematic errors.

6.3 The Decay Length Measurement

6.3.1 Method

The decay length is calculated under the assumption that all tracks in a jet originate from either the primary event vertex or from the secondary vertex formed when the b hadron decays. Tracks that come from the decay of a charm hadron are not accounted for. This is not an unreasonable approach, since the distance travelled by the charm hadron is usually shorter than that travelled by the b hadron. The measurement of the primary and secondary vertex positions leading to a direction constrained decay length measurement has been discussed in section 4.6.2.

Two track secondary vertices were not used in this analysis, as they behaved in a systematically different manner to other secondary vertex multiplicities, as shown in figure 6.1[a]. Two track vertices formed 9% (11%) of the Monte Carlo (data) sample.

A set of quality requirements are imposed on the secondary vertices used to form the decay length measurement. Following the prescription described in [161], the following selection criteria were tuned (for this analysis) using $b\bar{b}$ Monte Carlo.

- The transverse miss distance significance was required to be less than 3. The transverse miss distance is defined as the distance between the primary and secondary vertices projected onto an axis orthogonal to the summed momentum vector of tracks associated to the secondary vertex. This condition helps to remove secondary vertices formed from random track combinations.

[a] The following quality requirements for two track vertices were optimised in light of Monte Carlo studies :

- The invariant mass of the secondary vertex tracks (using pion masses) was required to be greater than 0.7 GeV/c^2,
- For negative decay lengths, the secondary vertex was rejected if it was more than 1 standard deviation from the primary vertex.

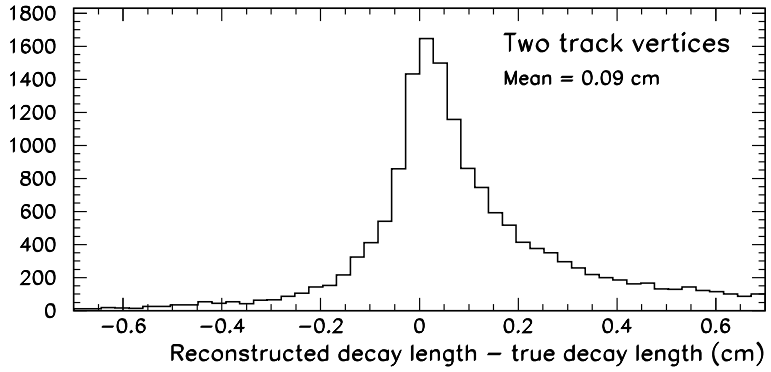

Figure 6.1: The reconstructed decay length resolution for two track secondary vertices, derived from Monte Carlo. The distribution is biased to positive values. This is because there is an enhanced probability of faking a two track vertex near the primary event vertex because of the large number of candidate tracks. Since the vertex quality requirements are tuned to remove such fake vertices, small decay lengths are suppressed. Two track vertices are not used in this analysis.

- The decay length error (calculated from the parameters of the tracks making up the secondary vertex) was required to be less than 0.06 cm.

- The invariant mass of the secondary vertex tracks (under the assumption of pion masses) was required to be greater than 0.8 GeV/c^2, to suppress badly reconstructed vertices.

- For negative decay lengths, the secondary vertex was rejected if it was more than 2 standard deviations from the primary vertex.

Table 6.1 shows the effect of each quality requirement on the efficiency for reconstructing a good secondary vertex from a b hadron decay.

To convert the two-dimensional decay length ($\ell_{\rm d}$) into the three-dimensional quantity (L) needed for the estimation of the decay time, the polar angle of the jet axis ($\theta_{\rm jet}$) was used :

$$\mathrm{L} = \frac{\ell_{\rm d}}{\sin\theta_{\rm jet}}. \tag{6.1}$$

The jet axis is assumed to model the b hadron flight direction well. The uncertainty on $\sin\theta_{\rm jet}$ leads to a negligible error on the calculation of three-dimensional decay length.

Quality Requirement	Efficiency Loss
Trans. miss distance sig. < 3	7%
Decay length error < 0.06 cm	6%
Vertex mass > 0.8 GeV/c^2	4%
Decay length sig. > -2	2%
All of the above	17%
≥ 3 vertex tracks	9%
Total	26%

Table 6.1: The effect of each quality requirement on the efficiency for identifying secondary vertices from bottom hadron decays in Monte Carlo.

6.3.2 Performance

The performance of the decay length estimator was investigated using $b\bar{b}$ Monte Carlo samples. Approximately 83% of the vertices with more than two tracks passed the selection criteria described above. The quality requirements remove a number of the secondary vertices giving little correlation between true and reconstructed decay time, as shown in figure 6.2. The overall efficiency for reconstructing a good secondary vertex from b hadron decay that passed all the selection criteria was measured from Monte Carlo to be $\sim$74%. Figure 6.3 shows the distribution of the difference between the reconstructed and true decay lengths, after all the quality requirements. The distribution is well centred with a mean of 0.02 cm and the full width at half maximum[b] is $\sim$0.13 cm.

6.4 The Boost Estimate

The technique used to calculate the boost needed to convert the decay length measurement into a decay time is similar to that used in studies of B meson oscillations [161] and B** production [162] by the OPAL collaboration. The event is treated as a two body decay of the Z^0. This allows the total energy in the awayside

[b] This will be referred to as the central width.

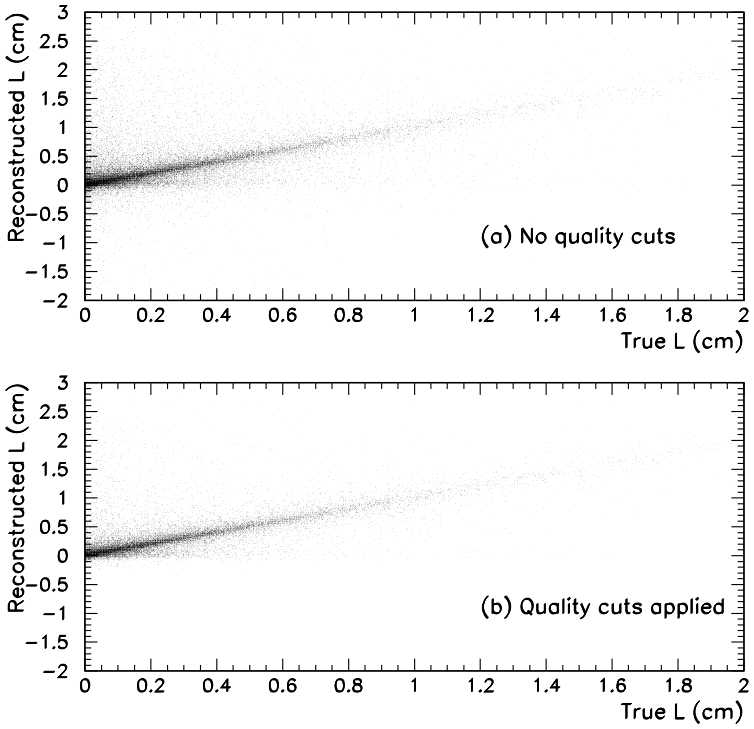

Figure 6.2: The upper plot shows the correlation between the reconstructed three-dimensional decay length and the true three-dimensional decay length before any quality requirements are made on the secondary vertices. The lower plot shows the correlation after the quality requirements are applied. Both plots are for Monte Carlo data.

jet, $E_{b\ jet}$, (the b jet)[c] to be estimated from the energy flow of charged tracks and unassociated electromagnetic clusters in the event. Within the b jet charged tracks are classified as coming from b decay or b fragmentation by a neural network algorithm and unassociated electromagnetic clusters are similarly classified using angular information. The total fragmentation energy in the b jet is denoted by $E_{b\ frag}$. The energy of the b hadron (E_b) can therefore be calculated as :

$$E_b = E_{b\ jet} - E_{b\ frag}. \tag{6.2}$$

6.4.1 Method

The event is treated as a two body decay of an object of mass $\mathcal{M}$, where $\mathcal{M}$ is the mass of the Z^0 boson, 91.2 GeV/c^2 [28]. The two bodies are the b jet, of mass $m_{b\ jet}$ and momentum p, and the rest of the event, of mass m_{rest} and momentum -p.

[c]Reminder : The decay length measurement is performed in the awayside jet, which is opposite to the b tagged jet.

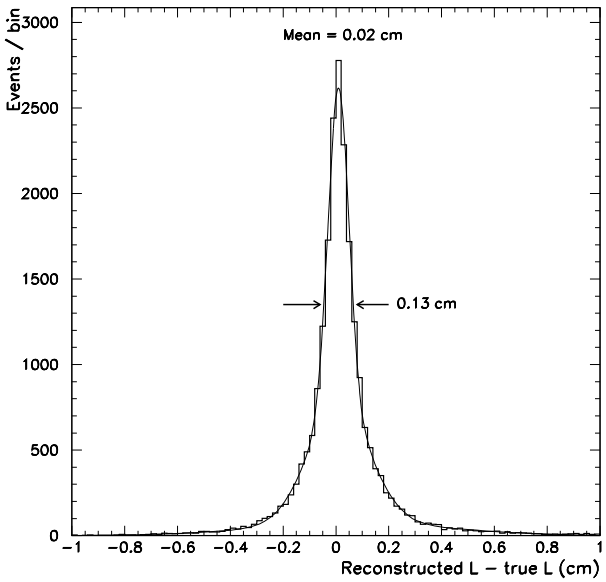

Figure 6.3: The resolution of the three-dimensional decay length estimator derived from Monte Carlo. All the quality requirements have been applied to the secondary vertices. The distribution has been parameterised with three Gaussians and the full width at half maximum and mean are shown.

The following relationships due to energy conservation can be used to estimate the energy of the b jet :

$$\mathcal{M} = \sqrt{\mathrm{p}^2 + \mathrm{m}^2_{\mathrm{b\ jet}}} + \sqrt{\mathrm{p}^2 + \mathrm{m}^2_{\mathrm{rest}}}\,, \tag{6.3}$$

solving for p^2 :

$$\Rightarrow \mathrm{p}^2 = \left(\frac{\mathrm{m}^2_{\mathrm{b\ jet}} + \mathcal{M}^2 - \mathrm{m}^2_{\mathrm{rest}}}{2\mathcal{M}}\right)^2 - \mathrm{m}^2_{\mathrm{b\ jet}}. \tag{6.4}$$

Using :

$$\mathrm{E}_{\mathrm{b\ jet}} = \sqrt{\mathrm{p}^2 + \mathrm{m}^2_{\mathrm{b\ jet}}} \tag{6.5}$$

$$\Rightarrow \mathrm{E}_{\mathrm{b\ jet}} = \frac{\mathcal{M}^2 + \mathrm{m}^2_{\mathrm{bjet}} - \mathrm{m}^2_{\mathrm{rest}}}{2\mathcal{M}}. \tag{6.6}$$

The mass of the b jet is assumed to be the mass of the $\mathrm{B}^{\pm}$, B^0 meson, 5.28 GeV/c^2 [28]. The mass of the rest of the event is calculated from the energy and momentum of charged tracks (using pion masses, 139.6 MeV/c^2 [28]) and unassociated electromagnetic clusters (zero mass) not assigned to the b jet.

6.4.2 Estimating the Bottom Fragmentation Energy

The fragmentation energy in the b jet is divided into charged and neutral components. These components are treated separately for the calculation of the total fragmentation energy in the b jet.

6.4.2.1 Estimating the Charged Fragmentation Energy

An artificial neural network was used to classify tracks as coming from b hadron decay or b fragmentation. Full details are given in appendix A. Four characteristics were used to classify each track presented to the neural network :

- The d_0 significance (d_0/σ_{d_0}) with respect to the primary vertex, where σ_{d_0} denotes the error on d_0,
- The d_0 significance with respect to the secondary vertex,
- The track momentum,
- $\cos\theta_{tb}$, where θ_{tb} is the angle between the track and the jet axis.

A neural network output near one indicates there is a high probability that the track originates from b hadron decay, rather than b fragmentation.

The distribution of the difference between true and reconstructed charged b fragmentation energies was used to tune the estimation of the charged fragmentation energy using the neural network. The best performance was found when a neural network output >0.5 was used to denote a track originating from b hadron decay. The charged fragmentation energy resolution is shown in figure 6.4. The distribution has a mean of 0.02 cm and the width of the central Gaussian is 9 GeV.

6.4.2.2 Estimating the Neutral Fragmentation Energy

The neutral fragmentation energy is much harder to identify as there is no tracking information to associate an unassociated electromagnetic cluster to either the primary or secondary vertex. Only the angle of the unassociated electromagnetic cluster relative to the jet axis ($\cos\theta_{cj}$) is used.

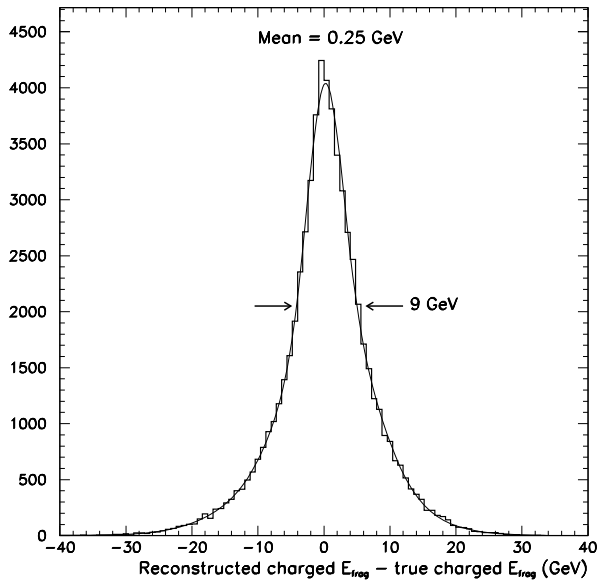

Figure 6.4: The charged fragmentation energy resolution determined from Monte Carlo. A neural network is used to determine whether charged tracks originate from b hadron decay or b fragmentation. The distribution has been parameterised with three Gaussians. The central width and mean are shown.

To optimise the cluster information, the distribution of the difference between total true and reconstructed b hadron energies was used after the charged fragmentation energy had been tuned[d]. The best performance was found with the following rules[e] :

$$\cos\theta_{\rm cj} \leq 0.850 \Longrightarrow \text{b fragmentation}, \tag{6.7}$$

$$\cos\theta_{\rm cj} \geq 0.965 \Longrightarrow \text{b hadron decay}, \tag{6.8}$$

$$0.965 < \cos\theta_{\rm cj} < 0.850 \Longrightarrow \text{weighted}. \tag{6.9}$$

6.4.3 Performance

Using the estimates of the b jet and b fragmentation energies, the b hadron energy was determined and compared to the true value from Monte Carlo. To make the calculation of the boost less sensitive to events where the visible energy is lower (due to the presence of neutrinos for example) the mass of the rest of the event ($m_{\rm rest}$)

[d] The OPAL Monte Carlo software does not allow an electromagnetic cluster to be simply associated with a particular neutral particle.

[e] 'Weighted' means that the cluster energy is shared between the b fragmentation (55%) and b hadron (45%) energy sums.

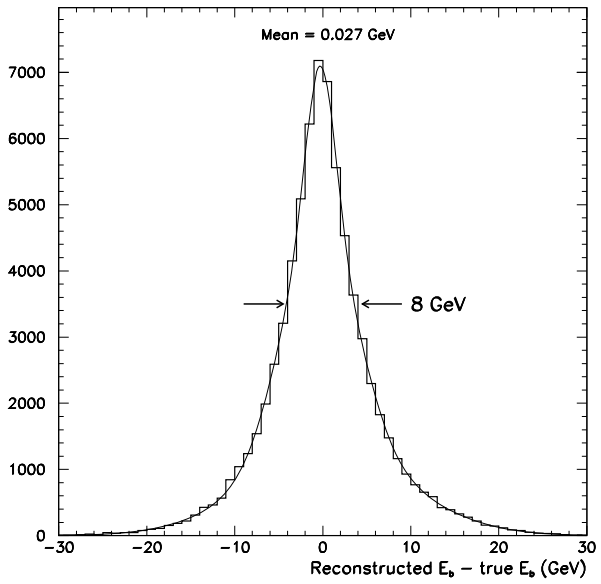

Figure 6.5: The resolution of the bottom hadron energy estimator, derived from Monte Carlo. The distribution has been parameterised with three Gaussians and the central width and mean are shown.

is scaled by a factor 87 GeV / E_{vis}, where E_{vis} is the total visible energy in the event. Figure 6.5 shows the distribution of the difference between reconstructed and true b hadron energies. The distribution has a central width of ∼8 GeV and is well centred, with a mean of ∼0.03 GeV.

6.5 The Performance of the Decay Time Estimator

The reconstructed decay time (t) of a b hadron is evaluated by combining the three-dimensional decay length (L) and the b hadron energy estimate (E_b) with the B meson mass (m_b) :

$$t = \frac{m_b L}{\sqrt{E_b^2 - m_b^2}}. \tag{6.10}$$

Figure 6.6a shows the correlation between true and reconstructed decay times. The decay time resolution shown in figure 6.6b has a central width of ∼0.85 ps and is well centred about zero.

In the next section the technique used to extract the b hadron lifetime from the reconstructed decay time distribution is discussed.

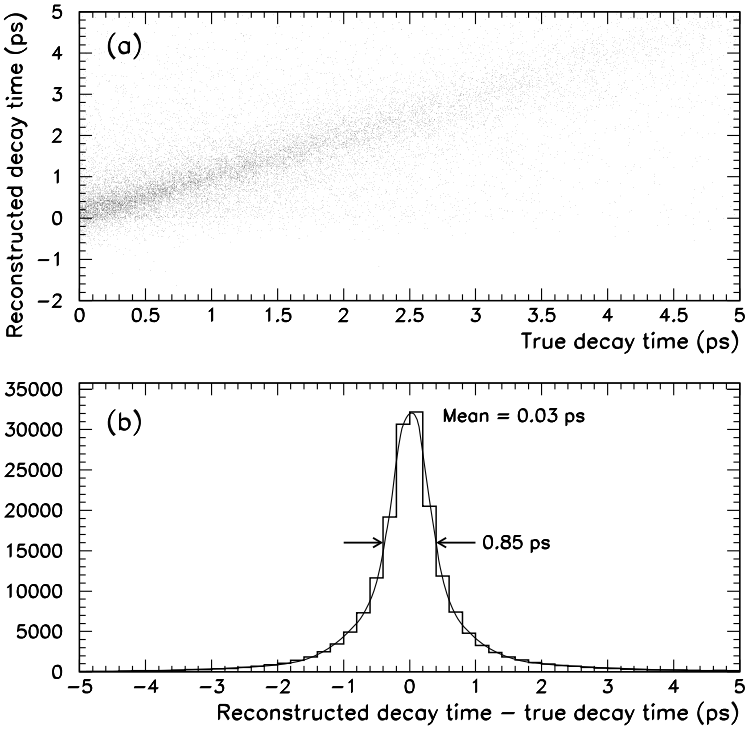

Figure 6.6: Plot (a) shows the correlation between reconstructed and true b hadron decay times. Plot (b) shows the decay time resolution parameterised with three Gaussians. Both plots are from Monte Carlo events.

6.6 Determining the Average Bottom Hadron Lifetime

6.6.1 Overview

A binned[f] maximum likelihood fitting technique [163] was used to extract the average b hadron lifetime from the distribution of reconstructed decay times. The fit was implemented using the CERN computer library routine `MINUIT` [164].

6.6.2 The Maximum Likelihood Technique

The distribution of reconstructed decay times can be parameterised into three components :

- A **physics function** which contains the average b hadron lifetime information.

[f] The binning greatly increases the speed of the fitting procedure without affecting the accuracy of the final result, as shown in section 6.9.3.

- A **signal resolution function** which describes the distribution of reconstructed decay times, from real b hadron decays, for a given true decay time.

- A **background resolution function** which describes the reconstructed decay time distribution of non-$b\bar{b}$ events on the awayside of the neural network b tag. Monte Carlo studies have shown that this background is very small, forming approximately 3.5% of the total awayside sample. There is also a small background (0.5% of the total awayside sample) from events where both the b quarks are in the same (b tagged) hemisphere due to the emission of an energetic gluon. This background is suppressed by rejecting events with more than two jets. In both these cases the reconstructed decay time distribution is expected to contain very little lifetime information.

A generalised likelihood function ($\mathcal{L}$) can be defined, for N reconstructed times, as :

$$\mathcal{L}(\mathrm{t_i};\tau_\mathrm{b},\vec{\mathrm{a}}) = \prod_{\mathrm{i}=1}^{\mathrm{N}} \mathbb{P}(\mathrm{t_i};\tau_\mathrm{b},\vec{\mathrm{a}}), \tag{6.11}$$

where :

$$\vec{\mathrm{a}} = \vec{\mathrm{a_p}} + \vec{\mathrm{a_s}} + \vec{\mathrm{a_b}}. \tag{6.12}$$

The normalised probability density function, $\mathbb{P}$, is a function of : the average b hadron lifetime, denoted by τ_b; the reconstructed decay time, denoted by $\mathrm{t_i}$; and the parameters needed to describe the physics, signal resolution and background resolution functions, denoted by vectors $\vec{\mathrm{a_p}}, \vec{\mathrm{a_s}}$ and $\vec{\mathrm{a_b}}$ respectively (the parameters are derived in a separate study, described below). The estimate of τ_b that makes the data most likely is given by a maximum value of $\mathcal{L}$. In practice a log-likelihood function :

$$-\log\mathcal{L}(\mathrm{t_i};\tau_\mathrm{b},\vec{\mathrm{a}}) = -\sum_{\mathrm{i}=1}^{\mathrm{N}} \log\mathbb{P}(\mathrm{t_i};\tau_\mathrm{b},\vec{\mathrm{a}}), \tag{6.13}$$

is minimised.

The precise form of $\mathbb{P}$ is :

$$\mathbb{P}(\mathrm{t_i};\tau_\mathrm{b},\vec{\mathrm{a}}) = \mathrm{z}\int_0^\infty \mathcal{P}(\mathrm{t}',\tau_\mathrm{b},\vec{\mathrm{a_p}})\mathcal{R}_\mathrm{sig}(\mathrm{t_i},\mathrm{t}',\vec{\mathrm{a_s}})\,\mathrm{dt}' + (1-\mathrm{z})\mathcal{R}_\mathrm{bkgd}(\mathrm{t_i},\vec{\mathrm{a_b}}). \tag{6.14}$$

The physics function is denoted by $\mathcal{P}$ and the signal and background resolution functions by $\mathcal{R}_{\rm sig}$ and $\mathcal{R}_{\rm bkgd}$ respectively. All the functions are individually normalised to unity. The integration is performed numerically using the CERN computer library routine `DADAPT` [165], which employs the technique of adaptive Gaussian quadrature [166]. The parameter z describes the amount of signal in the fitted sample and is derived using a double tagging technique, as described in section 4.7.2.

In the following sections the exact form of each of the constituent parts of the likelihood function are described in more detail.

6.6.3 The Physics Function

The physics function which describes the distribution of true decay times as a function of the average b hadron lifetime is given by :

$$\mathcal{P}(\mathrm{t}^{'},\tau_{\rm b},\vec{\mathrm{a}_{\rm p}}) = \frac{1}{\tau_{\rm b}}\exp(-\mathrm{t}^{'}/\tau_{\rm b})\frac{1}{\mathcal{F}(\mathrm{t}^{'},\vec{\mathrm{a}_{\rm p}})\mathcal{N}(\mathrm{t}^{'},\vec{\mathrm{a}_{\rm p}})}, \tag{6.15}$$

where :

$$\mathcal{F}(\mathrm{t}^{'},\vec{\mathrm{a}_{\rm p}}) = \exp(\mathrm{a}+\mathrm{bt}^{'})+\mathrm{c}, \tag{6.16}$$

$$\vec{\mathrm{a}_{\rm p}} = \{\mathrm{a},\mathrm{b},\mathrm{c}\} \tag{6.17}$$

and :

$$\mathcal{N}(\mathrm{t}^{'},\vec{\mathrm{a}_{\rm p}}) = \int_0^\infty \frac{1}{\tau_{\rm b}}\exp(-\mathrm{t}^{'}/\tau_{\rm b})\,\frac{1}{\mathcal{F}(\mathrm{t}^{'},\vec{\mathrm{a}_{\rm p}})}\,\mathrm{dt}^{'}. \tag{6.18}$$

As well as a lifetime exponential, the physics function contains a correction function, $\mathcal{F}$, which is used to account for biases in the true decay time distribution at small decay times. The bias corrected physics function is normalised by the function $\mathcal{N}$[g].

The bias arises from two independent sources :

Secondary Vertex Quality Requirements : This effect dominates and shifts the mean of the true decay time distribution by +0.05 ps. The efficiency for detecting a good secondary vertex that passes all the quality requirements decreases

[g] This integral is also performed using `DADAPT`.

as the true decay time tends towards zero. This is because it becomes harder to form a good secondary vertex separated from the primary vertex when the decay length is small.

The Neural Network b Tag : This effect shifts the mean of the true decay time distribution by –0.02 ps. The b tagged hemisphere is on the awayside from the one containing the secondary vertex used to calculate τ_{b}. The primary vertex is common to quantities (such as decay lengths) calculated in either hemisphere. Two pieces of information are needed to explain the source of this bias :

1. The tagging probability is enhanced when the error on the primary vertex position is small, giving significantly displaced secondary vertices. Hence, tagged events tend to have a smaller than average primary vertex error.
2. The primary vertex error will be reduced when there are more tracks available for the primary vertex fit. This is more likely when the mean decay length, and hence the true decay time, is small.

Combining these two points implies that the awayside b tag produces a bias towards small decay times.

The bias effect is shown as a function of true decay time in figure 6.7. The bias correction function, $\mathcal{F}$, is derived from the ratio between the true decay time distribution after b tagging and secondary vertex quality requirements with the distribution before these selection criteria. The distribution of $\mathcal{F}$ is well parameterised using the parameter values shown in figure 6.7. The bias mainly affects the region $\mathrm{t}^{'} < 1.5$ ps.

6.6.4 The Signal Resolution Function

The reconstructed decay time deviates from the true decay time due to imperfect secondary vertex reconstruction and b hadron energy estimation. Some vertices are reconstructed near to the primary vertex, even though the true decay length may be quite large. The relationship between the reconstructed and true decay time is not trivial, and depends on the value of the true decay time. A $\mathrm{b\bar{b}}$ Monte Carlo sample is

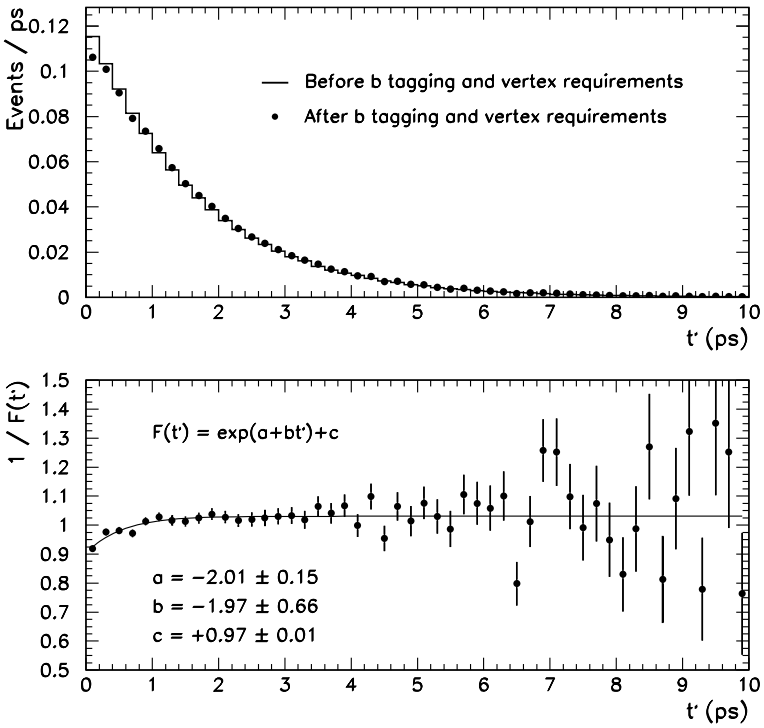

Figure 6.7: The upper plot shows the effect of the neural network b tagging and secondary vertex quality requirements on the true decay time ($t^{'}$) in Monte Carlo. The mean true decay time is increased. The lower plot shows the bias correction function, $1/\mathcal{F}$, as a function of true decay time.

used to parameterise the function which describes the distribution of reconstructed decay times for a given true decay time.

The shape of the reconstructed decay time distribution predicted by the resolution function varies with true decay time, as shown in figure 6.8 for five slices of true decay time : $t_i \leq 1\,ps$, $1\,ps < t_i \leq 2\,ps$, $2\,ps < t_i \leq 4\,ps$, $4\,ps < t_i \leq 8\,ps$ and $t_i > 8\,ps$. The enhanced number of events around zero in reconstructed decay time for large true decay times are due to events where the secondary vertex is reconstructed near the primary vertex even though the true decay length is large. The form of the resolution function is therefore rather complicated as it must account for the peaks in the reconstructed decay time distribution around both zero and the true decay time.

The precise form of the resolution function is :

$$\mathcal{R}_{sig}(t_i, t^{'}, \vec{a_s}) = (1-n)\Big(a\,\mathcal{G}_1 + (1-a)\,\mathcal{G}_2\Big) + n\Big(b\,\mathcal{G}_3 + (1-b)\,\mathcal{G}_4\Big), \tag{6.19}$$

where, $\mathcal{G}_{\rm n}$ represents a normalised Gaussian and the parameters a, b, n are used to ensure the resolution function as a whole remains normalised ($0 < \{\rm a,\ b,\ n\} < 1$). The Gaussians are described by :

$$\underset{\rm n=1,2}{\mathcal{G}_{\rm n}} = \frac{1}{\sqrt{2\pi}\,\sigma_{\rm n}}\ \exp\left(-\frac{1}{2}\left(\frac{\rm t_i - t_i^{'} - k_n}{\sigma_{\rm n}}\right)^2\right) \tag{6.20}$$

$$\underset{\rm n=1,2}{\sigma_{\rm n}} = \alpha_{\rm n} + \beta_{\rm n} {\rm t_i^{'}} \tag{6.21}$$

and :

$$\underset{\rm n=1,2}{\mathcal{G}_{\rm n+2}} = \frac{1}{\sqrt{2\pi}\frac{\rm x_n+y_n}{2}} \exp\left(-\frac{1}{2}\left(\frac{\rm t_i - \varphi_n}{\sigma_{\rm n+2}}\right)^2\right) \tag{6.22}$$

$$\underset{\rm n=1,2}{\sigma_{\rm n+2}} = \begin{cases} \rm x_n & \text{if } t_i\text{-}\varphi_n\ > 0 \\ \rm y_n & \text{if } t_i\text{-}\varphi_n\ < 0 \end{cases} \tag{6.23}$$

where :

$$\vec{\rm a_s} = \{\rm a, b, n, k_{1,2}, \alpha_{1,2}, \beta_{1,2}, \varphi_{1,2}, x_{1,2}, y_{1,2}\}. \tag{6.24}$$

Two of the Gaussians ($\mathcal{G}_{1,2}$) parameterise a non-zero difference between the reconstructed and true decay times and include widths that vary linearly with true decay time. The other two Gaussians ($\mathcal{G}_{3,4}$) are independent of true decay time and have asymmetric widths to account for the difference in tails to negative and positive reconstructed decay times.

The parameterisation of the reconstructed decay time distributions was implemented using a maximum likelihood fitting technique. The true and reconstructed decay times were calculated for each event and used as an input to the fit, which was implemented with the `MINUIT` [164] package.

Figure 6.8 shows the reconstructed decay time in slices of true decay time and the parameterisations from the resolution function are overlaid. At large true decay times ($\rm t^{'} > 4$ ps)[h] the parameterisation of the reconstructed decay time distribution is less accurate. This effect is investigated in section 6.9.1. Table 6.2 shows the numerical value for each of the parameters used in the resolution function.

[h] Approximately 15% of the total sample.

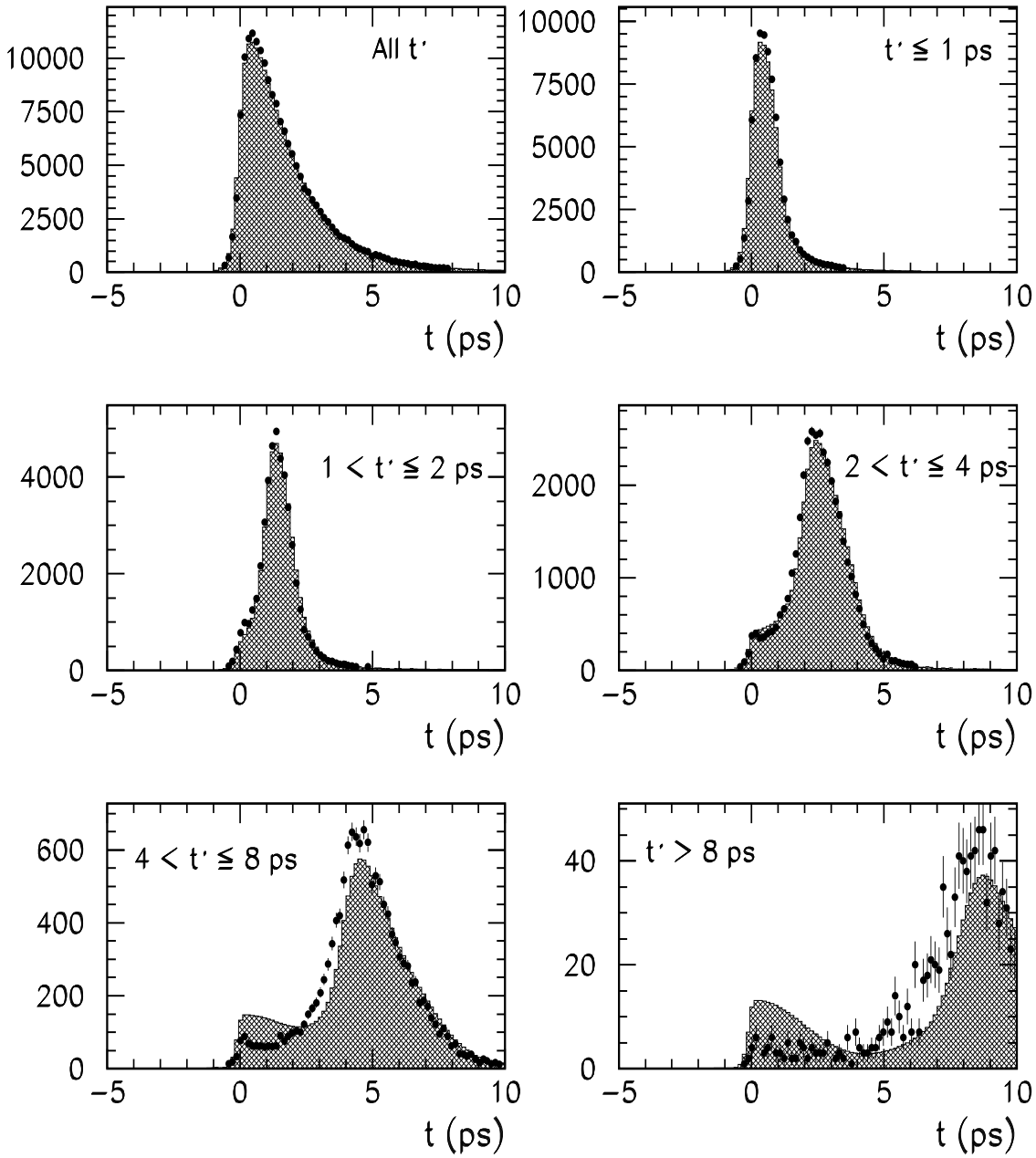

Figure 6.8: Distributions of the reconstructed decay time shown for different slices of true decay time for signal events. The points represent Monte Carlo data and the shaded histogram is the fit from the signal resolution function.

Normalisation		$\mathcal{G}_1$		$\mathcal{G}_2$		$\mathcal{G}_3$		$\mathcal{G}_4$	
a	0.476 ± 0.009	k_1	0.130 ± 0.005	k_2	-0.003 ± 0.001	φ_1	2.661 ± 0.051	φ_2	0.112 ± 0.011
b	0.242 ± 0.004	α_1	0.182 ± 0.002	α_2	0.400 ± 0.004	x_1	5.946 ± 0.057	x_2	1.903 ± 0.018
n	0.235 ± 0.002	β_1	0.064 ± 0.001	β_2	0.207 ± 0.004	y_1	1.742 ± 0.030	y_2	0.207 ± 0.007

Table 6.2: The parameters for the signal resolution function.

Normalisation		$\mathcal{G}_1$		$\mathcal{G}_2$		$\mathcal{G}_3$		$\mathcal{G}_4$	
q	0.377 ± 0.030	x_1	7.654 ± 0.451	x_2	0.051 ± 0.009	x_3	0.449 ± 0.059	x_4	1.852 ± 0.147
r	0.150 ± 0.017	σ_1	4.817 ± 0.236	σ_2	0.195 ± 0.011	σ_3	0.502 ± 0.032	σ_4	1.089 ± 0.078
s	0.778 ± 0.035								

Table 6.3: The parameters for the background resolution function.

6.6.5 The Background Resolution Function

The distribution of reconstructed decay times from background sources (predominantly u,d,s or c quarks on the awayside of a b tag) is shown in figure 6.9. A background resolution function, $\mathcal{R}_{\rm bkgd}$, consisting of 4 normalised Gaussians each centred around a unique reconstructed decay time, accurately described the distribution of reconstructed decay times from background sources :

$$\mathcal{R}_{\rm bkgd}(t_i, \vec{a_b}) = q\Big(r\,\mathcal{G}_1 + (1-r)\,\mathcal{G}_3\Big) + (1-q)\Big(s\,\mathcal{G}_2 + (1-s)\,\mathcal{G}_4\Big), \tag{6.25}$$

where :

$$\underset{n=1,4}{\mathcal{G}_n} = \frac{1}{\sqrt{2\pi}\,\sigma_n}\,\exp\left(-\frac{1}{2}\left(\frac{t_i - x_n}{\sigma_n}\right)^2\right), \tag{6.26}$$

and :

$$\vec{a_b} = \{q, r, s, \sigma_{1,4}, x_{1,4}\}. \tag{6.27}$$

Figure 6.9 shows the parameterisation of the background using the parameter values shown in table 6.3. The parameterisation agrees well with the data points. The reconstructed time distribution has very little lifetime dependence, since charm hadrons are heavily suppressed by the awayside neural network b tag.

6.7 Proof of Principle

The technique to extract the average b hadron lifetime, τ_b, was first tested with Monte Carlo samples. To provide a test environment as close to data as possible, all five quark flavours were used and neural network tagging was used to enhance $Z^0 \to b\bar{b}$ events.

The sample used for the lifetime fit contained 70 248 reconstructed decay times. The distribution of reconstructed decay times was divided into 200 bins between -5→25 ps. There were no reconstructed decay times <-5 ps and 68 reconstructed decay times >25 ps (0.1% of the total). The numerical integration over true decay time was performed over the range 0→20 ps. The proportion of signal events was determined from Monte Carlo 'cheat' information to be :

$$z_{\rm mc} = 96.59\%. \tag{6.28}$$

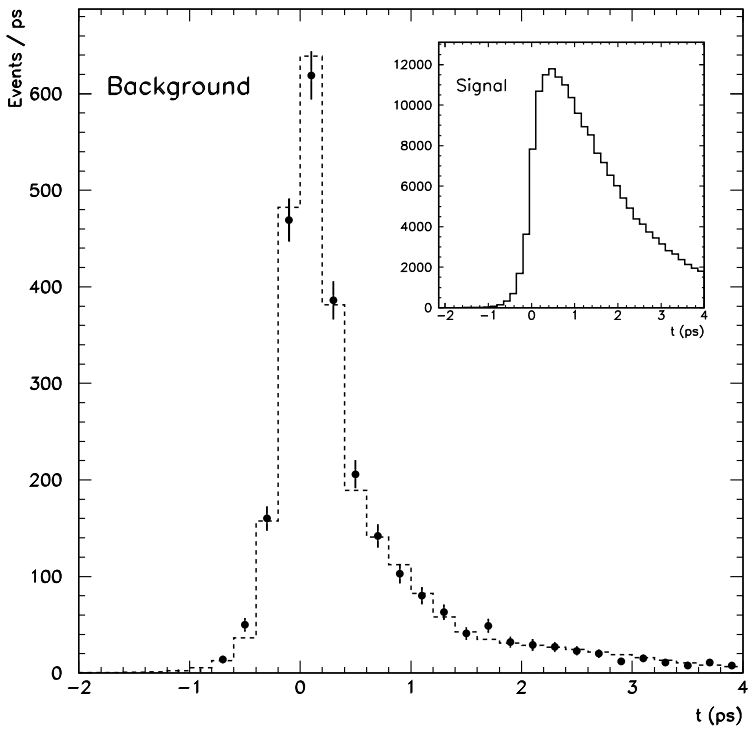

Figure 6.9: The reconstruction decay time distribution for background events. The points represent Monte Carlo data and the dashed line is the fit from the background resolution function. The distribution of reconstructed decay times for signal events is also shown for comparison. The background forms approximately 4% of the total sample.

The lifetime fit yielded :

$$\tau_{\mathrm{b}} = (1.575 \pm 0.009)\,\mathrm{ps}, \tag{6.29}$$

where the error is purely statistical. This fitted lifetime agrees very well with the actual average b hadron lifetime in the Monte Carlo sample of 1.571 ps. The reconstructed decay time distribution is parameterised as shown in figure 6.10. The bottom hadron composition of the fitted sample was compared to the default mix in the Monte Carlo, to check for biases towards a particular b hadron species. The results given in table 6.4 show there is no evidence of any bias in the fitted sample.

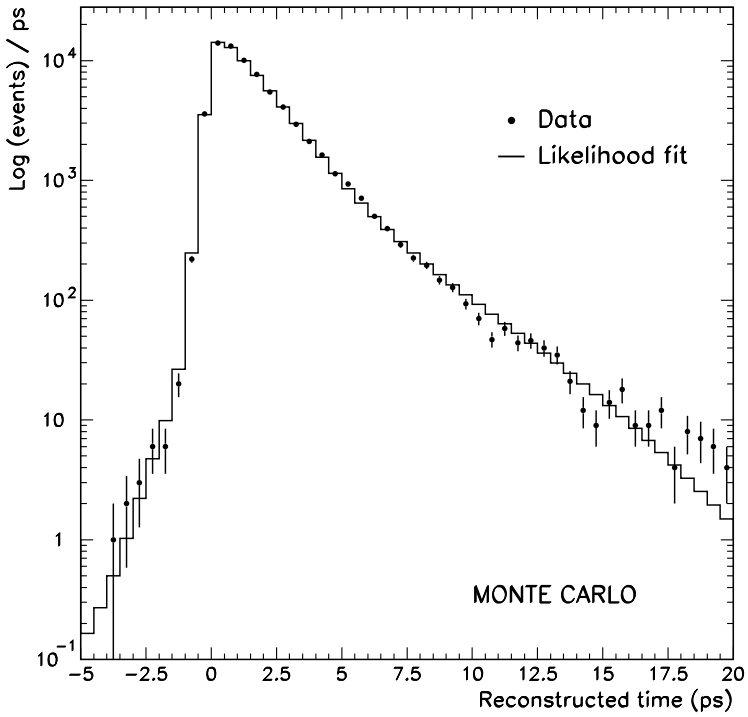

Figure 6.10: The reconstructed decay time distribution for Monte Carlo data, including all backgrounds. The solid line is the result of the lifetime fit.

6.8 Results

6.8.1 The Signal Proportion

The signal proportion, z, was evaluated using the double tagging technique described in section 4.7.2. As in the previous analysis, the output of the b tagging neural network was required to exceed 0.8. However, the value of z was evaluated with new values of C_b, the hemispheric efficiency correlation coefficient, and ε_{uds}, the light quark hemispheric tagging efficiency, as different jet finder and secondary vertex finding algorithms are used in this analysis.

The values of C_b and ε_{uds} were evaluated using Monte Carlo samples :

$$C_b = (1.013 \pm 0.002), \tag{6.30}$$

$$\varepsilon_{uds} = (0.095 \pm 0.006)\%. \tag{6.31}$$

The double tagging technique was first tested with Monte Carlo samples. The true value of z_{mc} is given in equation 6.28 as $z_{mc} = 96.59\%$. The double tagging result

Bottom Hadron	Default Sample	Fitted Sample
B meson	93.2%	93.2%
B^0	43.0%	43.4%
$B^{\pm}$	44.5%	44.2%
B_s^0	12.5%	12.4%
b baryon	6.8%	6.8%
Λ_b^0	88.5%	90.4%
Ξ_b^-	7.7%	6.7%
Ξ_b^0	3.8%	2.9%

Table 6.4: The composition of the bottom hadron sample in Monte Carlo. The generated and fitted sample composition are shown.

was $z'_{mc} = (96.33 \pm 0.50)\%$. A small correction factor, $c = +(0.26 \pm 0.50)\%$[i], was applied to the double tagging result to account for a possible bias from secondary vertex quality requirements enhancing the b purity in the sample used for the lifetime fit.

In data, the double tagging result was $z'_{data} = (94.58 \pm 0.41)\%$. All of the 1991–4 data and the values of C_b and ε_{uds} from Monte Carlo were used to obtain this result. The final result, after correcting by the Monte Carlo correction factor, c, is :

$$z_{data} = (94.84 \pm 0.64)\%. \tag{6.32}$$

6.8.2 The Average Bottom Hadron Lifetime

The binning and integration ranges used in the Monte Carlo proof of principle study were retained when evaluating τ_b for the 95 620 reconstructed decay times in the 1991–4 data-set. There was 1 reconstructed decay time < -5 ps and 76 reconstructed decay times > 25 ps (0.1% of the total).

Using the central value of z given in equation 6.32, the result of the lifetime fit is :

$$\tau_b = (1.652 \pm 0.008)\,\text{ps}, \tag{6.33}$$

[i]The error comes from the uncertainty on the double tagging result.

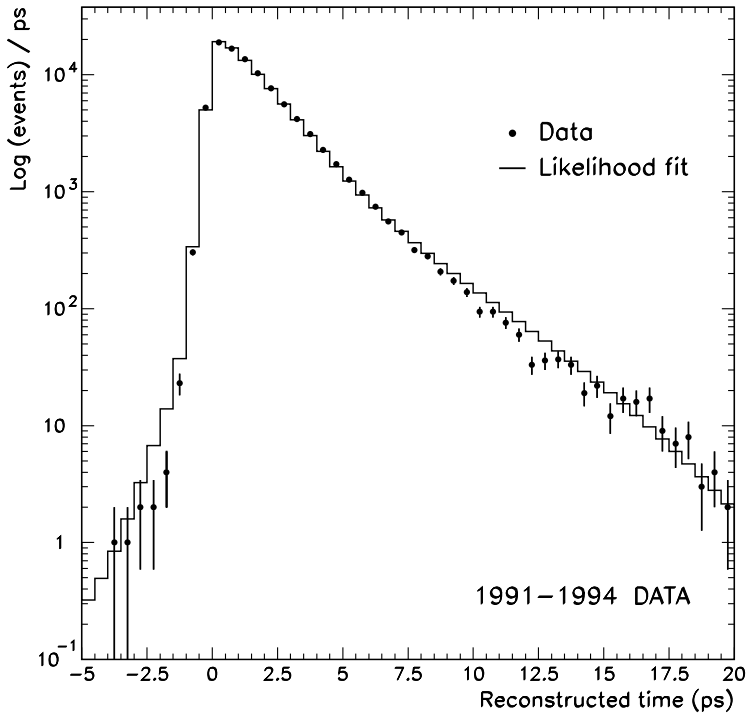

Figure 6.11: The reconstructed decay time distribution in data. The solid line is the result of the lifetime fit. The difference between the likelihood prediction and the data-points above 8.5 ps is investigated in section 6.9.1.

where the error is purely statistical. The reconstructed decay time distribution is shown in figure 6.11. There is a systematic difference between the likelihood prediction and the data-points above 8.5 ps which is investigated in section 6.9.1.

6.9 Studies of Possible Systematic Errors

In this section the systematic error on τ_b is evaluated. A summary is given in table 6.7.

The effect of reparameterising the resolution functions using Monte Carlo with different bottom fragmentation parameters and smeared track parameters (predominantly affecting the boost and decay length estimates, respectively) is described. Uncertainties from the bias correction function, the signal proportion (z), the boost estimate and the binning of the maximum likelihood fit are also discussed.

6.9.1 Resolution Functions

Firstly, uncertainties in the Monte Carlo bottom fragmentation modelling were studied. Such uncertainties predominantly affect the boost estimate and therefore the parameterisation of the resolution function. The 'new tune $b\bar{b}$' Monte Carlo sample was used to reparameterise the resolution functions for this study. This Monte Carlo sample is described in section 4.8.2 and provides superior modelling of $\langle x_E \rangle$ for bottom hadrons when compared to experimental measurements. The fitted lifetime result using the new resolution function was $\tau_b = (1.637 \pm 0.008)\,\mathrm{ps}$. Since this result uses superior bottom fragmentation modelling, it was adopted as a new central value.

A systematic error of ± 0.015 ps was assigned to account for the difference between this new central value and that presented in section 6.8.2. Unless stated, all further systematic checks use the standard Monte Carlo samples which give better statistical precision.

A χ^2 test was used to provide a cross-check of the fitted value of τ_b from Monte Carlo and data. A series of likelihood predictions for reconstructed decay time distributions were computed for both Monte Carlo and data. The average b hadron lifetime was varied between 1.4 ps and 1.8 ps. Default parameters were used for z, the resolution functions and the bias correction function. The reconstructed decay time distribution from Monte Carlo (data) was compared to the likelihood function prediction from Monte Carlo (data) after normalising above a low reconstructed decay time cut-off. A cut-off of > 2 ps was used, to remove the known bias effects shown in figure 6.7. Finally, a χ^2 value was computed between the normalised reconstructed decay time and likelihood distributions over the range 2 ps to 15 ps.

The results from Monte Carlo and data are shown in table 6.5 and figures 6.12a,b respectively. In both cases the χ^2 minimum is compatible with the fitted lifetime, which is denoted by the dotted line in the figure. However, the χ^2 per degree of freedom at the minima is approximately 1.6 in both cases indicating poor agreement between the reconstructed decay time and likelihood distributions. The most likely source of this is an imperfect parameterisation of the signal resolution function[j].

[j] The low reconstructed decay time cut-off of 2 ps excludes the contributions from the background resolution function or the bias correction function.

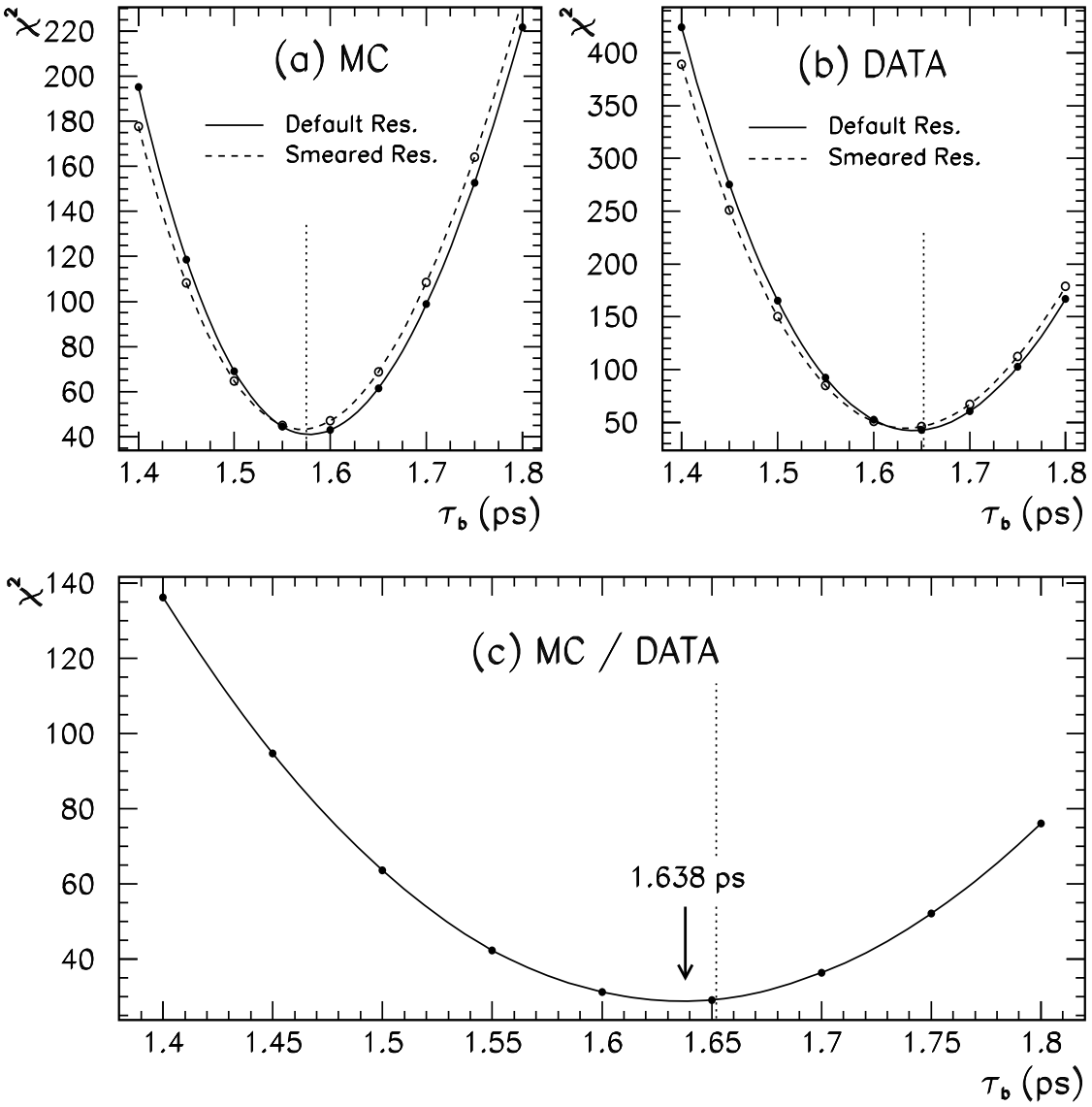

Figure 6.12: Plots (a, b) show the χ^2 between the reconstructed decay time and likelihood distributions in Monte Carlo and data respectively. The χ^2 minima correspond well to the fitted value of τ_b, shown by the dotted line. The dashed lines show the effect of using smeared Monte Carlo to reparameterise the resolution functions. In both cases the χ^2 magnitude at the minima indicates poor agreement between the distributions. Plot (c) shows that better agreement can be obtained when the effects of the resolution function parameterisation are suppressed. The difference between the χ^2 minimum and fitted value is used as an systematic error due to uncertainties on the parameterisation of the resolution function not covered by uncertainties in the track parameters. The numerical results are given in table 6.5.

Monte Carlo	$\chi^2_{\rm min}$	$\chi^2_{\rm min}$/dof	$\tau_{\rm b}$ at $\chi^2_{\rm min}$
Default Res.	41.32	1.59	1.587±0.016
Smeared Res.	44.33	1.71	1.577±0.016
Fitted $\tau_{\rm b}$	—	—	1.575±0.009
Data	$\chi^2_{\rm min}$	$\chi^2_{\rm min}$/dof	$\tau_{\rm b}$ at $\chi^2_{\rm min}$
Default Res.	40.78	1.57	1.649±0.013
Smeared Res.	43.16	1.66	1.641±0.013
Fitted $\tau_{\rm b}$	—	—	1.652±0.008
MC Res. / Data Res.	28.10	1.08	1.638±0.023

Table 6.5: The χ^2 results shown in figure 6.12. There are 26 degrees of freedom (dof). The error on the value of $\tau_{\rm b}$ at the χ^2 minimum ($\sigma(\tau_{\rm b})$) is derived from $\Delta\chi^2_{\rm min} = 1$.

To test this hypothesis the signal resolution function was reparameterised from a smeared $b\bar{b}$ Monte Carlo sample. This accounts for systematic uncertainties in the charged track parameters. Section 4.8.2 details the smearing procedure. For this study a (default [167]) 10% smear ($\alpha = \beta = 1.1$) was used. The χ^2 test was repeated for the smeared Monte Carlo reconstructed decay time sample, and the results are shown in figure 6.12. Table 6.5 shows that the position of the χ^2 minimum in both data and Monte Carlo have moved significantly ($> \sigma(\tau_{\rm b})/2$), and the χ^2 value itself indicates a worse fit.

To reduce sensitivity to the signal resolution function the χ^2 test was repeated between the quantities $\mathbb{S}$ and $\mathbb{L}$:

$$\mathbb{S} = \frac{\mathcal{S}_{\rm data}}{\mathcal{S}_{\rm mc}}, \tag{6.34}$$

$$\mathbb{L} = \frac{\mathcal{L}_{\rm data}(\tau = 1.4\,{\rm ps} \rightarrow 1.8\,{\rm ps})}{\mathcal{L}_{\rm mc}(\tau = 1.57\,{\rm ps})}; \tag{6.35}$$

where, $\mathcal{S}_{\rm mc(data)}$ and $\mathcal{L}_{\rm mc(data)}$ denote the reconstructed decay time distributions and likelihood predictions from Monte Carlo (data). Systematic effects from parameterisation imperfections in the signal resolution function will largely cancel. The χ^2 result is shown in figure 6.12c and table 6.5. The χ^2 per degree of freedom at the minimum is ∼1.1, indicating reasonable agreement between $\mathbb{S}$ and $\mathbb{L}$. The difference between the fitted data lifetime and this χ^2 minimum is 0.014 ps, and this is

assigned as a systematic error to account for uncertainties in the parameterisation of the signal resolution function, even though the difference is compatible with zero within the independent statistical error.

This error is independent of that due to uncertainties on the charged track parameters. The signal resolution function was reparameterised using smeared $b\bar{b}$ Monte Carlo samples and a systematic error of ± 0.022 ps was assigned to account for the different fitted lifetime result.

Finally, in section 6.6.4 it was noted that the parameterisation of the signal resolution function was less accurate for large true decay times ($t' > 4$ ps). To check this had no effect on the fitted lifetime, the form of the likelihood function for the signal resolution function was slightly modified with the aim of improving the large true decay time behaviour. The modification (with reference to equation 6.19) is :

$$n \rightarrow n \exp(-w\, t'), \tag{6.36}$$

where, a new parameter, w, has been introduced. The new parameter allows the contribution from $\mathcal{G}_{3,4}$ in equation 6.25 to be reduced as the true decay time increases. When the true decay time is large, there will be many tracks with significant impact parameters and so it is unlikely that a secondary vertex will be reconstructed near the primary vertex. The new parameterisation is shown in figure 6.13, and the agreement with the data is significantly improved compared to figure 6.8 for large true decay times. However, tests of this parameterisation with Monte Carlo samples indicated that the mean of the likelihood prediction for the reconstructed decay time distribution was biased and gave a biased lifetime result of $\tau_b = (1.448 \pm 0.009)$ ps. This is a shift of -0.127 ps from the default fitted lifetime value. In data, a lifetime shift of -0.129 ps was observed[k]. The default resolution function was therefore adopted as it introduced less bias in the Monte Carlo lifetime fit.

6.9.2 Bias Correction Function

Systematic errors due to the parameterisation of the bias correction function were evaluated in two ways. Firstly, the statistically independent 'new tune $b\bar{b}$' Monte

[k] Therefore, the bias corrected result using the modified resolution function for the data is consistent with the default result.

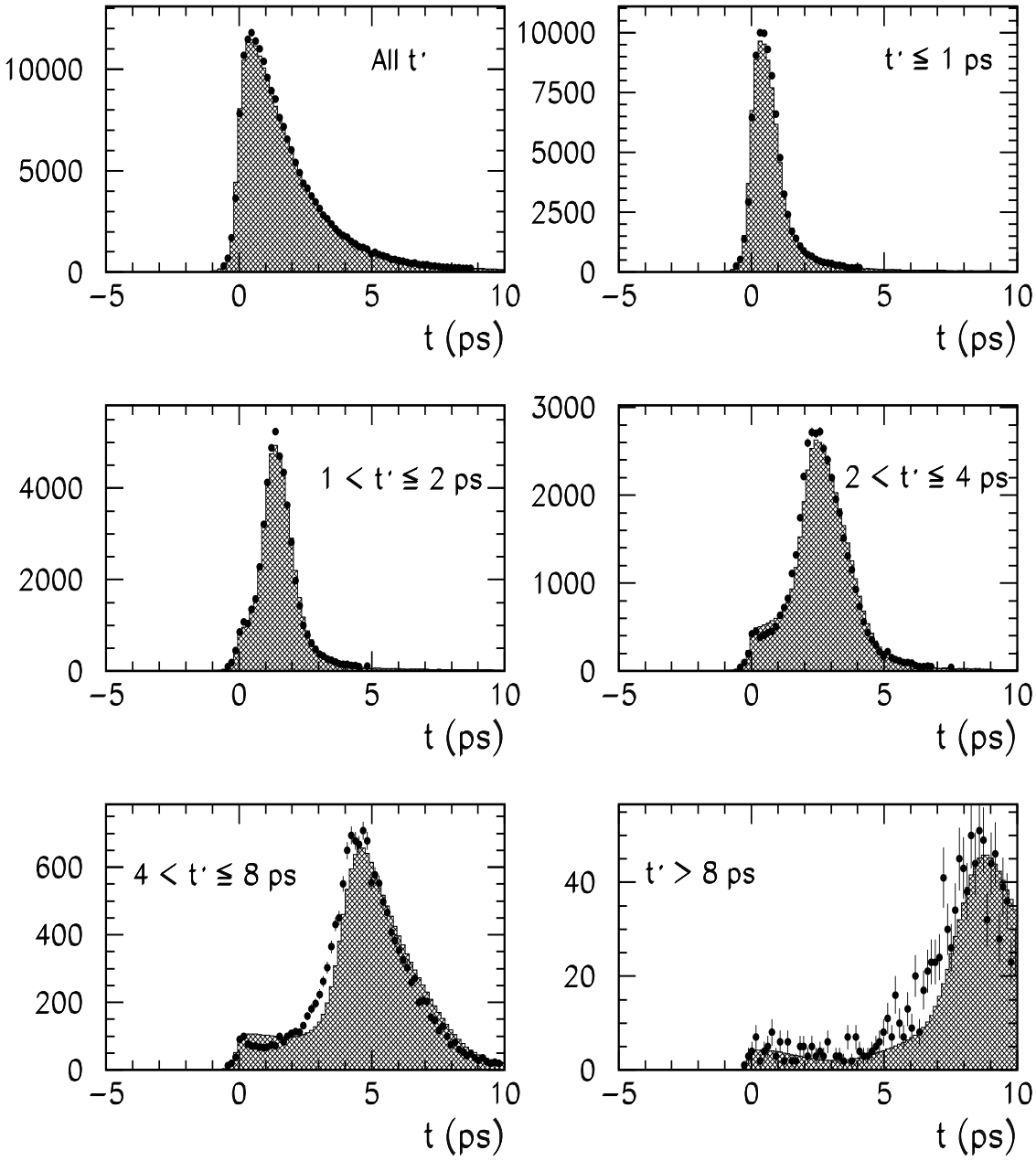

Figure 6.13: An alternate parameterisation of the signal resolution function designed to improve the description of the reconstructed decay time distribution for $t' > 4$ ps. The points represent Monte Carlo data and the shaded histogram is the fit from the resolution function. This figure should be compared to figure 6.8.

Year	Signal Proportion, z (%)	τ_b (ps)
1991	93.82 ± 1.38	1.602 ± 0.029
1992	94.51 ± 0.84	1.648 ± 0.015
1993	95.17 ± 0.88	1.636 ± 0.017
1994	95.00 ± 0.76	1.671 ± 0.016
1991–4 (w.a.)	94.80 ± 0.45	1.648 ± 0.009
1991–4 (full)	94.84 ± 0.64	1.652 ± 0.008

Table 6.6: The value of the signal proportion, z, evaluated for each year of data-taking using a double tagging technique. The resulting fitted value of τ_b is also shown. The z and τ_b results for 1991–4 are from an error weighted average of each individual year (w.a.) and a fit to all four years together (full).

Carlo sample was used to re-parameterise the bias correction function. A systematic error of ±0.007 ps was assigned to account for the difference in the fitted lifetime.

The smeared $b\bar{b}$ Monte Carlo sample was also used to re-evaluate the fit parameters. The effect on the fitted lifetime using this new bias correction function was small. A systematic error of ±0.002 ps was assigned to cover the change in the fitted lifetime. This is a conservative estimate as the systematic error assigned from the χ^2 study, described in section 6.9.1, also addresses this source of error.

6.9.3 Miscellaneous Studies

A lifetime error of $^{+0.010}_{-0.009}$ ps was assigned due to the uncertainty on the proportion of signal events, z. This was estimated using one standard deviation errors on the value of z derived from double tagging ($z_{data} = (94.84 \pm 0.64)\%$).

The data-set was divided into four independent years (1991–94) and each year was fitted separately. Data from 1991 to 1994 made up approximately 8%, 26%, 21% and 45% of the total data-set. The value of z derived for each year, from the double tagging technique and associated Monte Carlo correction, is shown in table 6.6 with the corresponding fitted lifetime. The lifetime fit results are shown in figure 6.14. The fit result from each individual year is compatible with the lifetime fitted from the combined sample. The χ^2 per degree of freedom between the individual results and the combined result is ∼1.8, which corresponds to a probability of ∼15%. Also

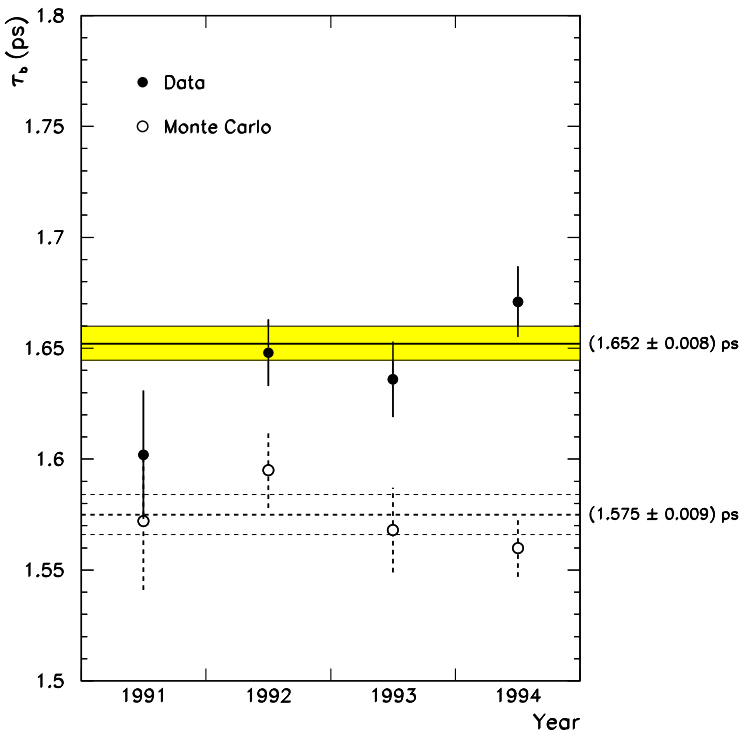

Figure 6.14: The fitted values of τ_b for each year of data-taking are shown by the solid points. The value of z has been evaluated separately for each year, using a double tagging technique. The solid filled area indicates the lifetime result (and statistical error) from the full 1991–4 data-set, using a value of z evaluated from this full data-set. The dashed detail is the equivalent result for Monte Carlo samples of comparable size to the individual data samples. Note that the fitted lifetime from data is derived using the default resolution functions (see section 6.9.1).

shown on figure 6.14 is the result of a similar analysis of Monte Carlo data using comparable statistics to the data sub-samples. The results in table 6.6 also show that the error weighted average of individual lifetime results from each year are consistent with the default central lifetime result shown in figure 6.14.

When reconstructing the decay time of the b hadron, the $B^{\pm}$, B^0 meson mass, 5.28 GeV/c^2, is used. The sensitivity of τ_b to this assumption was investigated. Assuming a production ratio of $B^{\pm}$:B^0:B_s^0:Λ_b^0 = (40:40:13:7)% and using the bottom hadron masses detailed in section 3.3.4, a higher b jet mass of 5.32 GeV/c^2 was derived. The reconstructed decay time distribution was calculated and the resolution and bias correction functions were reparameterised, to reduce sensitivity to these sources. A systematic error of ±0.001 ps was assigned to account for the fitted value of τ_b from data using the new b jet mass.

Finally, the extracted lifetime from the binned lifetime fit was checked against an

Systematic Effect	Correction (ps)
Bottom Hadron Fragmentation	-0.015
Source of Uncertainty	**Systematic Error (ps)**
Bottom hadron fragmentation in resolution function	± 0.015
Parameterisation uncertainties in resolution function	± 0.014
Track parameter uncertainties in resolution function	± 0.022
Parameterisation uncertainties in bias correction function	± 0.007
Track parameter uncertainties in bias correction function	± 0.002
Uncertainty on signal proportion	$^{+0.010}_{-0.009}$
Mass of bottom quark jet	± 0.001
Total	± 0.034

Table 6.7: A summary of the systematic corrections and errors for τ_b.

unbinned fit. The unbinned fit yielded $\tau_b = (1.6517 \pm 0.0078)$ ps, which is compatible with the binned result of (1.6523 ± 0.0078) ps. The binned fit was adopted for all fits presented in this analysis as it took approximately 500 times less computer processor time.

The systematic errors are summarised in table 6.7. The largest contribution ($\sim$90% of the total systematic error) comes from uncertainties on the signal resolution function. The uncertainties arise from the description of the charged track parameters, the Monte Carlo b fragmentation scheme and parameterisation uncertainties derived from a χ^2 study.

6.10 Summary and Discussion

The average bottom hadron lifetime is measured to be :

$$\tau_b = (1.637 \pm 0.008\,(\text{stat}) \pm 0.034\,(\text{syst}))\,\text{ps}. \tag{6.37}$$

This result is shown in figure 6.15 compared to the most recent measurements from Z^0 experiments [169]. The world average result published at the HEP95 confer-

ence [99] is also shown. This weighted average is derived from the measurements[l] shown on the figure with common systematic errors accounted for [170]. For example, the impact parameter measurements have a common reliance on models describing heavy quark semileptonic decays. The secondary vertex methods have systematic errors largely uncorrelated to the other measurements and, so, provide a very useful cross-check of $\tau_{\rm b}$.

The result from this analysis is $\sim$1.7 standard deviations from the world average result. This has a probability of $\sim$9%. However, the mix of bottom hadrons in the leptonic impact parameter analyses will differ from that in the secondary vertex analyses. The error weighted average[m] of the $\tau_{\rm b}$ measurements that use secondary vertex techniques are compatible with the result from this analysis within $\sim$1.1 standard deviations, which corresponds to a probability of $\sim$27%.

It is interesting to speculate over the apparent difference in measured lifetime between the leptonic impact parameter and secondary vertex methods. A naive analysis, taking no account of common systematic errors, indicates that there is a $\sim$2.5 standard deviation difference between the error weighted average of the two lifetime measuring techniques[n]. It has already been stated that the LEP leptonic impact parameter methods have a common reliance on b decay models. Model imperfections could, in principle, cause all these $\tau_{\rm b}$ measurements to be systematically reduced.

However, this aside, if the partial semileptonic widths for B mesons and b baryons are equal then[o] :

$$\frac{{\rm Br_{sl}(B)}}{{\rm Br_{sl}}(\Lambda_{\rm b}^0)} = \frac{{\rm Br(B} \to \ell\nu{\rm X)}}{{\rm Br}(\Lambda_{\rm b}^0 \to \ell\nu{\rm X})} = \frac{\Gamma_{\rm sl}({\rm B})}{\Gamma_{\rm tot}({\rm B})}\,\frac{\Gamma_{\rm tot}(\Lambda_{\rm b}^0)}{\Gamma_{\rm sl}(\Lambda_{\rm b}^0)} = \frac{\tau({\rm B})}{\tau(\Lambda_{\rm b}^0)}, \qquad (6.38)$$

where, $\rm Br_{sl}$ indicates a semileptonic branching ratio and $\Gamma_{\rm sl}(\Gamma_{\rm tot})$ indicate semileptonic (total) partial widths. Current measurements indicate that $\tau(\Lambda_{\rm b}^0) < \tau({\rm B})$, as shown in figure 3.9, and therefore ${\rm Br_{sl}}(\Lambda_{\rm b}^0) < {\rm Br_{sl}(B)}$ is predicted. This means that event samples used in leptonic impact parameter measurements of $\tau_{\rm b}$ will contain an enhanced number of B mesons compared to b baryons, and so the average lifetime should be greater than that seen in a truly generic b hadron sample. Clearly,

[l] Excluding this analysis.
[m] No attempt is made to account for common systematic errors.
[n] The lifetime result from this analysis is used in this study.
[o] This idea is used in section 3.3.5.2.

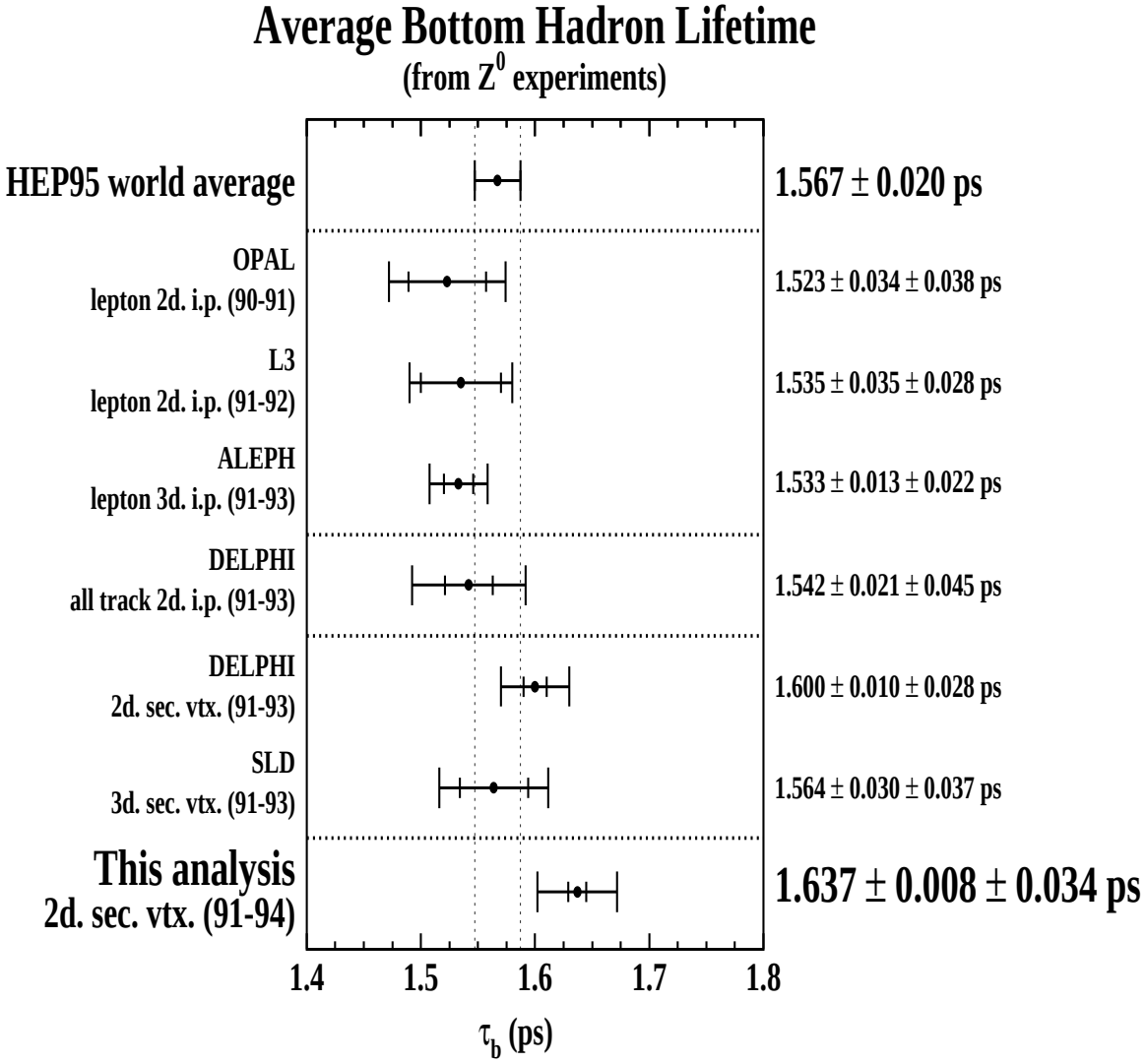

Figure 6.15: A summary of average bottom hadron lifetimes from Z^0 experiments. There are two types of measurement, leptonic (charged track) impact parameters and secondary vertex methods using the estimated bottom hadron decay length. Both of these methods are described in section 3.3.7.1. The result from the analysis described in this chapter is also shown along with the current world average result. The DELPHI collaboration have recently updated their secondary vertex measurement to $\tau_b = (1.582 \pm 0.011\,(\text{stat}) \pm 0.027\,(\text{syst}))$ ps [171]. The CDF collaboration have measured $\tau_b = (1.46 \pm 0.06\,(\text{stat}) \pm 0.06\,(\text{syst}))$ ps using data from $p\bar{p}$ collisions at a centre of mass energy of 1.8 TeV. They use the decay vertices from b hadron $\rightarrow J/\psi$, $J/\psi \rightarrow \mu^+\mu^-$ to extract τ_b [168].

this prediction is contrary to the observations recorded in figure 6.15. One possible interpretation of this result is that it indicates an anomalously high b baryon semileptonic branching ratio. Recent (preliminary) semileptonic bottom branching ratios from the $\Upsilon(4s)$ and LEP collaborations are [28][p] :

$$\mathrm{Br}(\mathrm{b} \to \mathrm{c}\,\ell\,\nu\,\mathrm{X}) = (10.2 \pm 0.4)\% \quad (\Upsilon(4s)) \tag{6.39}$$

$$= (11.2 \pm 0.4)\% \quad (\mathrm{LEP}). \tag{6.40}$$

These results are compatible within 1.8 standard deviations. The $\Upsilon(4s)$ measurement contains no Λ_b^0 (or B_s^0) decays, unlike the result from the LEP collaborations. These results could also be consistent with a higher semileptonic bottom baryon branching ratio, however, more work and data is needed to clarify this possible discrepancy and to reduce dependence on b decay models.

[p] These are the most recent preliminary results from the 1995 Particle Data Group off-year partial update and include an error to account for b decay modelling in the LEP results. The value of $\mathrm{Br}(\mathrm{b} \to \mathrm{c}\,\ell\,\nu\,\mathrm{X})$ used in section 3.3.5.2 comes from the 1994 Particle Data Group review, which is solely derived from $\Upsilon(4s)$ measurements.

Chapter 7

A Measurement of the Bottom Baryon Lifetime

7.1 Overview

The procedure used to measure the bottom baryon lifetime has many aspects in common with the analysis techniques used to measure the average bottom hadron lifetime. The cone algorithm (described in section 4.4.2) was used to resolve jets and events were divided into two hemispheres using the thrust axis. The hemispheres were b tagged using the neural network technique described in section 4.7.1. If there was only one jet[a] in the awayside hemisphere from a b tag it was searched for secondary vertices using the 'build-up' algorithm described in section 4.6.2. The subsequent decay length measurement was converted into a decay time using an estimate of the bottom hadron momentum, following the technique described in the previous chapter.

In the measurement of the average bottom hadron lifetime, the reconstructed decay time distribution is dominated by bottom mesons (in section 3.3.5.2 it was estimated that $f(b \rightarrow \Lambda_b^0) = 0.09 \pm 0.03$). To enhance the contribution from bottom baryons, a Λ^0 originating from bottom hadron decay is required in the hemisphere used for the decay time measurement. This results in the decay time distribution containing an almost equal contribution from bottom mesons and baryons. A binned

[a] The jet-axis was used to associate a jet to a particular hemisphere.

maximum likelihood fit was used to extract the bottom baryon enhanced lifetime from the overall reconstructed decay time distribution. Finally, an estimate of the bottom meson component of the reconstructed decay time distribution was used to extract the bottom baryon lifetime.

7.2 Enhancing the Bottom Baryon Component

In a generic sample of bottom hadron decays, the average bottom hadron lifetime, τ_{b}, can be decomposed into bottom meson and bottom baryon lifetimes, denoted τ_{B} and $\tau_{\Lambda^0_{\mathrm{b}}}$ respectively :

$$\tau_{\mathrm{b}} = \mathrm{f}\tau_{\mathrm{B}} + (1-\mathrm{f})\tau_{\Lambda^0_{\mathrm{b}}}, \tag{7.1}$$

where :

$$\mathrm{f} = \mathrm{f}(\mathrm{b} \to \mathrm{B}) = 0.91 \pm 0.03. \tag{7.2}$$

This value of $\mathrm{f}(\mathrm{b} \to \mathrm{B})$ is derived from the estimate of $\mathrm{f}(\mathrm{b} \to \Lambda^0_{\mathrm{b}})$ described in equation 3.38.

The bottom baryon component is enhanced by requiring a Λ^0 originating from b hadron decay in the awayside hemisphere from a b tag. The resulting bottom baryon enhanced lifetime, $\tau_{\mathrm{b}\Lambda^0}$, can be expressed as :

$$\tau_{\mathrm{b}\Lambda^0} = \mathrm{g}\tau_{\mathrm{B}} + (1-\mathrm{g})\tau_{\Lambda^0_{\mathrm{b}}}, \tag{7.3}$$

where :

$$\mathrm{g} = \frac{\mathrm{f}(\mathrm{b} \to \mathrm{B})\,\mathrm{Br}(\mathrm{B} \to \Lambda^0\mathrm{X})}{\mathrm{Br}(\mathrm{b\ hadron} \to \Lambda^0\mathrm{X})} = 0.61 \pm 0.11. \tag{7.4}$$

The values of $\mathrm{Br}(\mathrm{B} \to \Lambda^0\mathrm{X})$ and $\mathrm{Br}(\mathrm{b\ hadron} \to \Lambda^0\mathrm{X})$ are detailed in equations 3.21 and 5.13, respectively.

Using equations 7.1 and 7.3, the bottom baryon enhanced lifetime can be parameterised in terms of the average bottom hadron lifetime and the bottom baryon lifetime as :

$$\tau_{\mathrm{b}\Lambda^0} = \frac{\mathrm{g}}{\mathrm{f}}\tau_{\mathrm{b}} + \left(1 - \frac{\mathrm{g}}{\mathrm{f}}\right)\tau_{\Lambda^0_{\mathrm{b}}}, \tag{7.5}$$

where, the ratio g/f is derived from equations 7.4 and 7.2 as[b] :

$$\underline{\frac{g}{f} = 0.68 \pm 0.13.} \tag{7.6}$$

As a cross-check, the value of value of g/f was recalculated, with the derivation of Br(b hadron$\rightarrow \Lambda^0$X) decomposed into bottom baryon and meson components :

$$\frac{g}{f} = \frac{Br(B \rightarrow \Lambda^0 X)}{f(b \rightarrow B)\, Br(B \rightarrow \Lambda^0 X) + f(b \rightarrow \Lambda_b^0)\, Br(\Lambda_b^0 \rightarrow \Lambda^0 X)} \tag{7.7}$$

$$\Rightarrow \underline{\frac{g}{f} = 0.54 \pm 0.12.} \tag{7.8}$$

In this derivation of g/f, the independent estimate of $f(b \rightarrow \Lambda_b^0)\, Br(\Lambda_b^0 \rightarrow \Lambda^0 X)$, defined in equation 3.41, is used. It should be noted that this estimate is derived under the assumption that the bottom baryon semileptonic branching ratio can be obtained from the B meson semileptonic branching ratio scaled by the lifetime ratio $\tau(\Lambda_b^0)/\tau(B)$, as described in section 6.10.

The fractional error on both derivations of g/f is $\sim$20%. The two values of g/f are correlated through Br(B$\rightarrow \Lambda^0$X), so a simple error weighted average is not appropriate[c]. A constrained χ^2 technique was therefore used to derive an 'optimised' value for g/f, where :

$$\chi^2 = \frac{(A-a)^2}{\Delta A^2} + \frac{(B-b)^2}{\Delta B^2} + \frac{(C-c)^2}{\Delta C^2} + \frac{(D-d)^2}{\Delta D^2} \tag{7.9}$$

The upper case letters denote measured values[d] :

$$A = Br(b \text{ hadron} \rightarrow \Lambda^0 X) = (5.9 \pm 0.8)\%, \tag{7.10}$$

$$B = f(b \rightarrow B) = 0.91 \pm 0.03, \tag{7.11}$$

$$C = f(b \rightarrow \Lambda_b^0) Br(\Lambda_b^0 \rightarrow \Lambda^0 X) = (3.72 \pm 0.48)\%, \tag{7.12}$$

$$D = Br(B \rightarrow \Lambda^0 X) = (4.0 \pm 0.5)\%, \tag{7.13}$$

where, the sources of the numerical values have been referenced earlier in this section. The lower case letters in the χ^2 expression denote the parameters which are free to move in the fit. The descriptions of b and c are the same as the upper

[b] Note that the $f(b \rightarrow B)$ terms cancel when forming the ratio.
[c] For reference, an error weighted average yields g/f = 0.60$\pm$0.09.
[d] In this nomenclature, ΔA refers to the total error on A.

case equivalents. The parameters d and a are introduced to exploit the following relationships :

$$\mathrm{d} = \frac{\frac{\mathrm{g}}{\mathrm{f}}\,\mathrm{c}}{1 - \frac{\mathrm{g}}{\mathrm{f}}\,\mathrm{b}}, \tag{7.14}$$

$$\mathrm{a} = \mathrm{b}\,\mathrm{d} + \mathrm{c}. \tag{7.15}$$

The result of the fit is :

$$\mathrm{b} = \mathrm{f}(\mathrm{b} \to \mathrm{B}) = 0.91 \pm 0.03, \tag{7.16}$$

$$\mathrm{c} = \mathrm{f}(\mathrm{b} \to \Lambda_{\mathrm{b}}^{0})\mathrm{Br}(\Lambda_{\mathrm{b}}^{0} \to \Lambda^{0}\mathrm{X}) = (3.41 \pm 0.43)\%, \tag{7.17}$$

$$\boxed{\frac{\mathrm{g}}{\mathrm{f}} = 0.55 \pm 0.05,} \tag{7.18}$$

with $\chi^2 = 1.96$ for 1 degree of freedom.

7.3 Event Sample and Selection

Data collected between 1991 and 1994 with the silicon microvertex detector operational were used in this analysis. The 'new' and 'new tune $\mathrm{b\bar{b}}$' Monte Carlo samples were combined (where appropriate) to increase the overall size of the Monte Carlo data-set. As usual, the prefix 'new (tune)' is discarded henceforth.

All events were required to have at least two jets, with the two most energetic jets lying in opposite thrust hemispheres. Events with more than one jet on the awayside from a b tag were rejected, to suppress Λ^0's which do not originate from a b jet.

The procedure detailed in section 5.4 was used to reconstruct Λ^0's from the p,π^- decay products. The Monte Carlo samples accurately model the reconstructed Λ^0 mass distribution seen in the data, as shown in figure 7.1. This figure should be compared to figure 5.6, which shows the equivalent reconstructed mass distribution for the 'old' Monte Carlo samples. The agreement between data and 'new' Monte Carlo is much improved. The mean of the Monte Carlo mass peak is slightly higher than in data. This is a known artefact of the Monte Carlo sample due to a systematic effect [172]. To enhance Λ^0's that originate from b hadron decay, the Λ^0 momentum was required to exceed 5 GeV/c. To reduce the contribution from fake Λ^0's, the reconstructed Λ^0 mass had to fall within the signal region shown on figure 7.1.

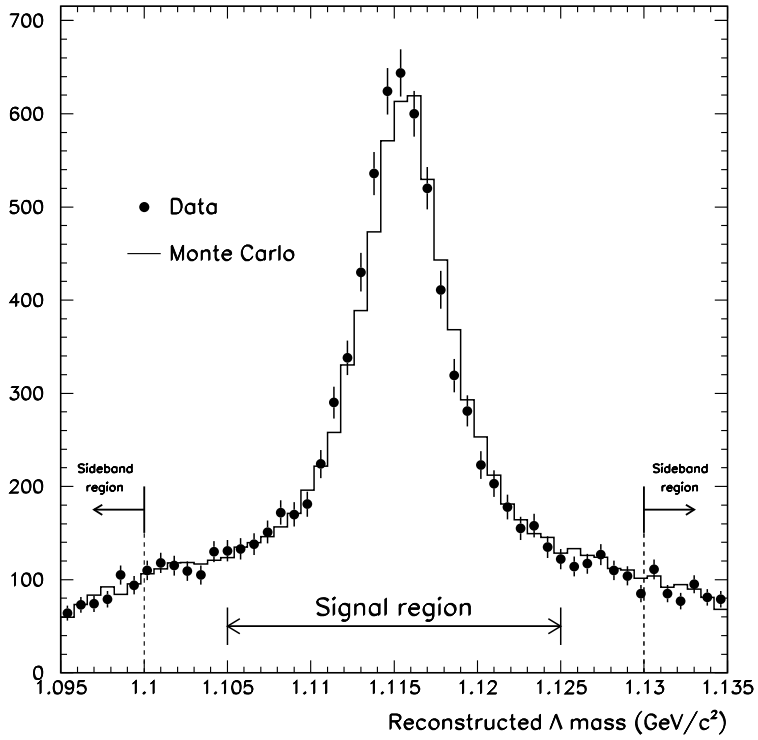

Figure 7.1: The reconstructed Λ^0 mass for Monte Carlo (histogram) compared to data (points). The distributions are normalised to each other. The shift in the mean reconstructed mass between data and Monte Carlo is discussed in the text.

7.4 Sources of Λ^0's

The reconstructed decay times on the awayside from a b tag can be divided into three groups, as shown in figure 7.2. Monte Carlo samples were used to investigate each of these groups.

Signal decay times are produced in $Z^0 \rightarrow b\bar{b}$ events when a real Λ^0, associated with the jet containing the secondary vertex used in the decay time estimation, originates from a b hadron decay. Signal decay times account for approximately 60% of the total number of reconstructed decay times. The Λ^0's in signal events originate from an approximately equal mix of bottom meson and baryon decays, as shown by the estimate of g in equation 7.4.

The time dependent background arises from two sources : (i) secondary vertices in $Z^0 \rightarrow b\bar{b}$ events with an associated fake Λ^0; and (ii) the associated Λ^0 is real and from b fragmentation. In both these cases, $Z^0 \rightarrow b\bar{b}$ events are involved, and therefore, the reconstructed time distribution contains generic lifetime (τ_b) information.

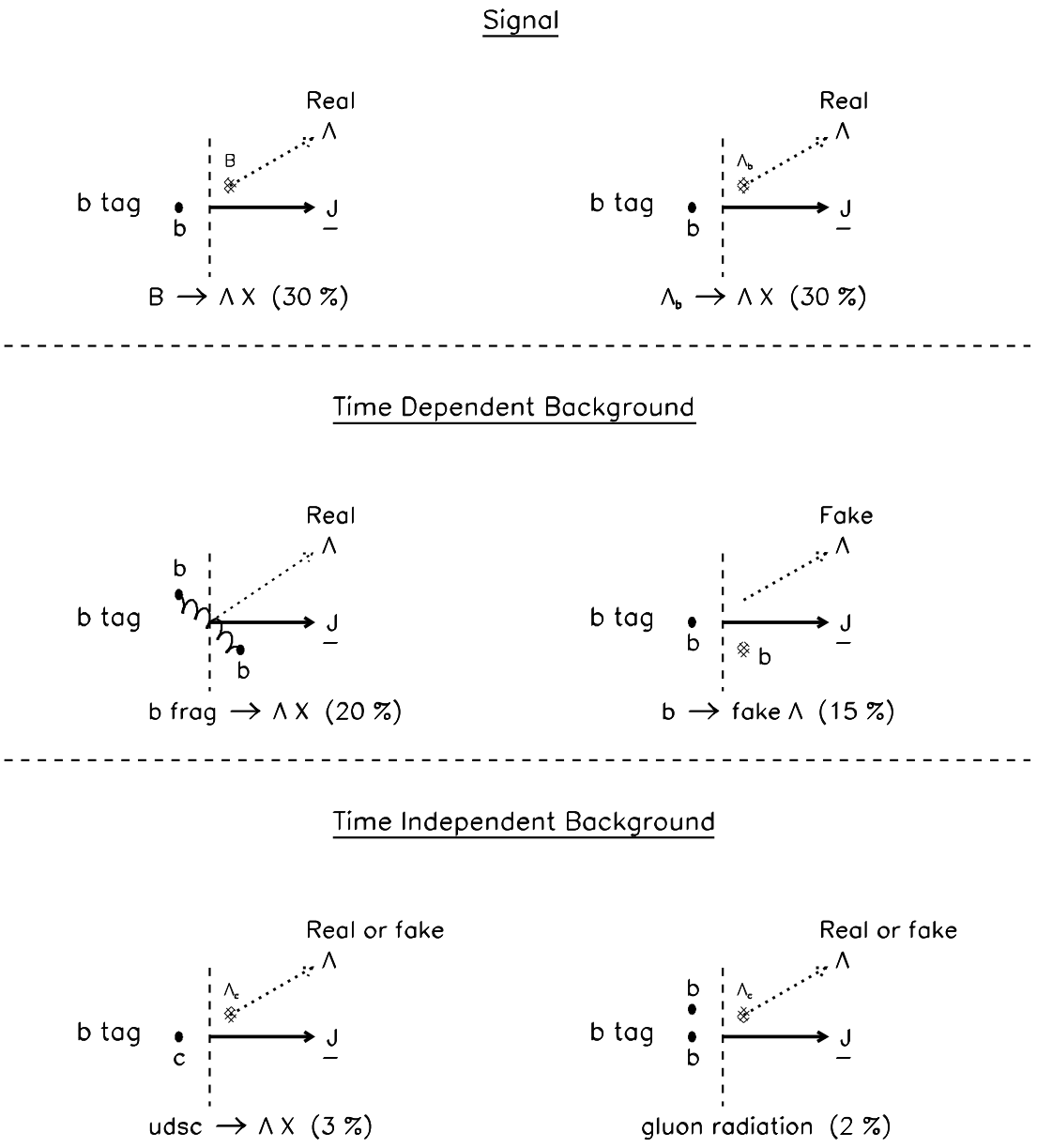

Figure 7.2: Sources of Λ^0's in b tagged events. The vertical dashed line in each subfigure represents the boundary between hemispheres and J indicates the jet-axis of the awayside jet. The numbers in brackets represent the fraction of the total sample due to the source in question, derived from Monte Carlo studies.

When a primary bottom baryon is produced, a companion anti-baryon must also be created. The companion baryon could be a Λ^0 originating from b fragmentation. This would enhance the bottom baryon component in the time dependent background and is discussed further in section 7.8.3. The time dependent background accounts for approximately 35% of the total number of reconstructed decay times. Fragmentation Λ^0's form approximately 60% of this background.

A time independent background arises in non-$Z^0 \rightarrow b\bar{b}$ events. Such events can occur if a light quark event is b tagged or if both bottom hadrons in a $Z^0 \rightarrow b\bar{b}$ event are in the b tagged hemisphere, due to hard gluon radiation. The reconstructed decay time contains little lifetime information. The time independent background is heavily suppressed compared to the time dependent background and comprises only 5% of the total number of reconstructed decay times. Light hadron events account for approximately 60% of this background.

7.5 Determining the Bottom Hadron Decay Time

Each jet on the awayside from a b tag containing a Λ^0 of momentum $> 5\,\mathrm{GeV}/c$ was searched for secondary vertices. The overall method for determining the bottom hadron decay time follows that used in the previous chapter. The quality requirements for selecting secondary vertices were re-evaluated using awayside secondary vertices in $Z^0 \rightarrow b\bar{b}$ events with associated real Λ^0's originating from bottom hadron decay. The secondary vertex finding was modified to allow Λ^0's to be vertexed as pseudo-tracks. This did not worsen the decay length resolution.

7.5.1 The Decay Length Measurement

The overall method for reconstructing secondary vertices follows that described in the previous chapter. Two track secondary vertices formed 12% (7%) of the total data (Monte Carlo) sample and were not considered in this analysis.

A modified 'build-up' vertexing algorithm that allowed Λ^0's to be vertexed was used to reconstruct secondary vertices. Since the Λ^0 is neutral, a pseudo-track representing the Λ^0 was constructed from the p,π^- decay products of the Λ^0 [173]. The pseudo-track was treated as a standard charged track by the vertexing algorithm.

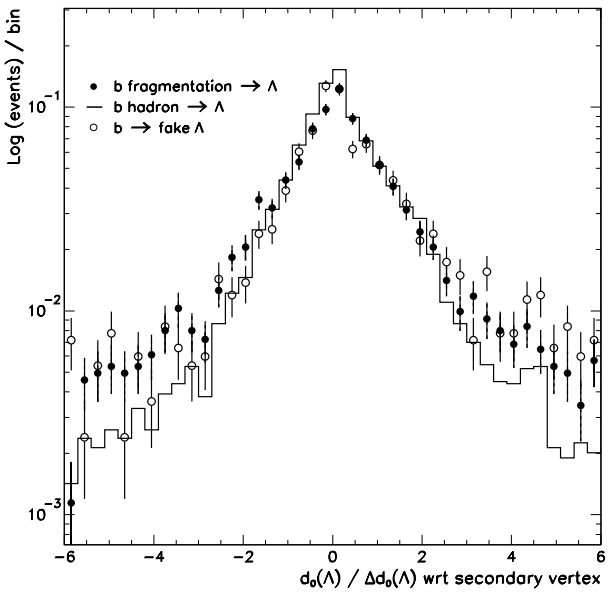

Figure 7.3: The distribution of the Λ^0 pseudo-track d_0 significance from Monte Carlo. The d_0 measurement is defined with respect to the reconstructed secondary vertex. The d_0 significance distribution for Λ^0 pseudo-tracks originating from bottom hadron decay has the smallest width. This indicates that the Λ^0 pseudo-track can provide useful vertexing information.

The Λ^0 pseudo-track can provide useful vertexing information. The distribution of the d_0 significance (with respect to the reconstructed secondary vertex position) for Λ^0 pseudo-tracks from various sources is shown in figure 7.3. Pseudo-tracks reconstructed from Λ^0's that originate from b hadron decays yield a d_0 significance distribution with a smaller width compared to Λ^0's originating from b fragmentation or fake Λ^0's.

Monte Carlo samples were used to determine how often the Λ^0 pseudo-track formed part of the secondary vertex for each of the Λ^0 sources described previously. The results are shown in table 7.1. Pseudo-tracks reconstructed from Λ^0's that originate from b hadron decay are vertexed most often. This is explained by the form of d_0 significance distribution shown in figure 7.3.

The secondary vertex quality requirements are the same as those described in section 6.3.1. The requirements were re-tuned using Monte Carlo samples, but no significant improvements were found by altering the cut values. Similar efficiencies for reconstructing secondary vertices in signal Λ^0 events were observed as described in section 6.3.1, for generic signal events. Figure 7.4 shows the decay length resolution[e]

[e] The reconstructed two-dimensional decay length is converted to a three-dimensional quantity

Source of Λ^0's	Secondary Vertex Inclusion Rate (%)
Signal	59 ± 1
Fragmentation	40 ± 1
Fake	42 ± 1
Light Hadron	53 ± 7

Table 7.1: The secondary vertex inclusion rate for Λ^0's, derived from Monte Carlo studies.

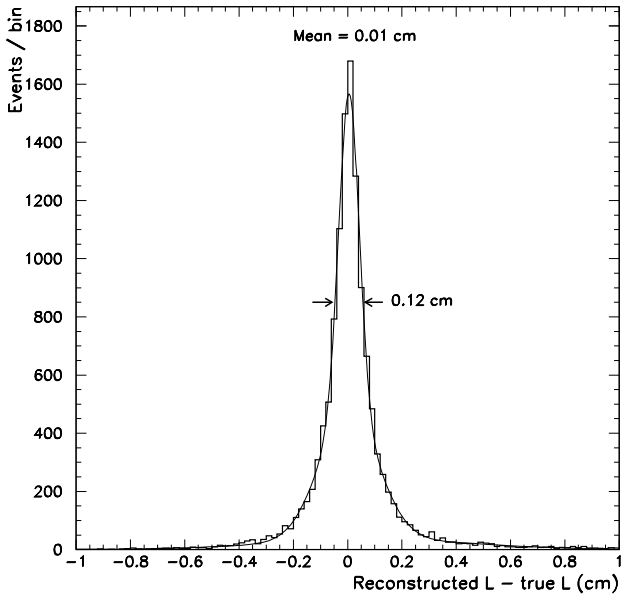

Figure 7.4: The resolution of three-dimensional decay length estimator, derived from Monte Carlo. All the quality requirements have been applied to the secondary vertices. The distribution has been parameterised with three Gaussians and the full width at half maximum and mean are shown.

for $b\bar{b}$ Monte Carlo signal events, after all the quality requirements have been applied. The distribution is well centred with a central width of 0.12 cm.

7.5.2 The Performance of the Boost Estimator

The boost was determined exactly as described in the previous chapter. Figure 7.5 shows the distribution of the difference between the true and reconstructed bottom hadron energies in Monte Carlo. With reference to equation 6.6, a factor of 85 GeV/E_{vis} was determined to give the best performance when scaling m_{rest} to make

using the jet axis, as shown in equation 6.1.

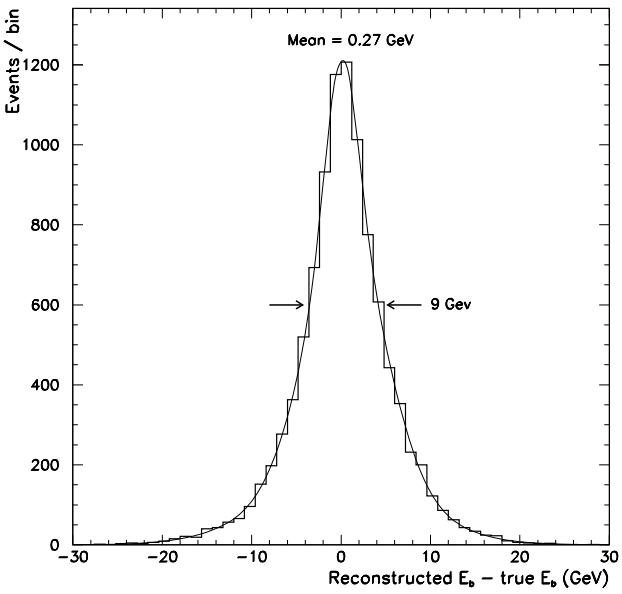

Figure 7.5: The resolution of the bottom hadron energy estimator, derived from Monte Carlo. The distribution has been parameterised with three Gaussians and the central width and mean are shown.

the calculation of the boost less sensitive to the visible energy in the event (E_{vis}). The distribution is well centred and has a central width of ∼9 GeV.

7.5.3 The Performance of the Decay Time Estimator

When converting the decay length measurement into a decay time using the boost estimate, a bottom hadron mass of 5.47 GeV/c^2 was used. This was derived from the bottom hadron masses detailed in section 3.3.4 and the assumption that bottom mesons and baryons populate the overall reconstructed decay time sample equally.

The decay time resolution is shown in figure 7.6. The distribution has a central width of ∼0.8 ps and is well centred.

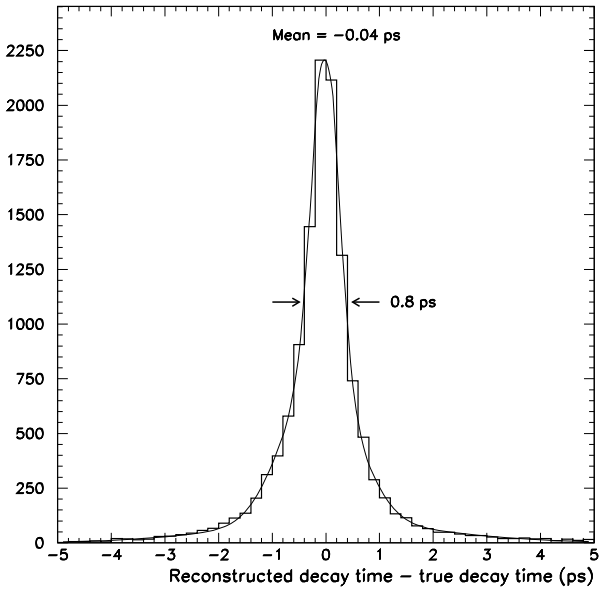

Figure 7.6: The reconstructed decay time resolution, derived from Monte Carlo. The distribution is parameterised with three Gaussians.

7.6 Determining the Bottom Baryon Enhanced Lifetime

7.6.1 Overview

A binned maximum likelihood fitting technique [163] was used to extract the bottom baryon enhanced lifetime, $\tau_{b\Lambda^0}$, from the distribution of reconstructed decay times on the awayside from a b tag. The fit was implemented using the CERN computer library routine `MINUIT` [164].

The bottom baryon lifetime, $\tau_{\Lambda_b^0}$, was subsequently estimated using the relationship :

$$\tau_{\Lambda_b^0} = \frac{\tau_{b\Lambda^0} - g/f\,\tau_b}{1 - g/f}, \tag{7.19}$$

where, the value of g/f comes from equation 7.18 and the value of τ_b was presented in the previous chapter.

The likelihood function used to determine $\tau_{b\Lambda^0}$ is much more complex than the one used for the measurement of the average bottom hadron lifetime. The main differences arise from the extra backgrounds that must be accounted for. As described in section 7.4, the background makes up approximately 40% of the total event sam-

ple and, moreover, approximately 90% of the background results in a reconstructed decay time distribution with lifetime dependence.

The likelihood function used to describe the distribution of N reconstructed times (t) on the awayside from a b tag can be expressed in terms of a normalised probability density function ($\mathbb{P}$) as :

$$-\log\mathcal{L} = -\sum_{i=1}^{N}\log\mathbb{P}(t_i;\tau_{b\Lambda^0},s,p,\vec{a}), \tag{7.20}$$

where :

$$\vec{a} = \vec{a_p} + \vec{a_s} + \vec{a_{b_1}} + \vec{a_{b_2}}. \tag{7.21}$$

The precise form of $\mathbb{P}$ is :

$$\begin{aligned}\mathbb{P}(t_i;\tau_{b\Lambda^0},s,p,\vec{a}) = s&\int_0^\infty \mathcal{P}_1(t',\tau_{b\Lambda^0},\vec{a_p})\,\mathcal{R}_{sig}(t_i,t',\vec{a_s})\,dt'\\ +\quad &(1-s)p\int_0^\infty \mathcal{P}_2(t',\tau_b,\vec{a_p})\,\mathcal{R}^{tdep}_{bkgd}(t_i,t',\vec{a_{b_1}})\,dt'\\ +\quad &(1-s)(1-p)\,\mathcal{R}^{tindep}_{bkgd}(t_i,\vec{a_{b_2}}).\end{aligned} \tag{7.22}$$

Physics function $\mathcal{P}_1$ describes the distribution of true decay times (t') as a function of $\tau_{b\Lambda^0}$, which is derived in this analysis. Physics function $\mathcal{P}_2$ describes the distribution of true decay times, for time dependent background events, as a function of the average bottom hadron lifetime, τ_b. The parameters s and p describe the composition of the overall sample as follows :

$$s = \frac{N_{sig}}{N_{total}}, \tag{7.23}$$

$$p = \frac{N^{bkgd}_{tdep}}{N^{bkgd}_{total}}; \tag{7.24}$$

where, N_{total}, N_{sig}, N^{bkgd}_{total} and N^{bkgd}_{tdep} denote the number of all, signal, background and time dependent background reconstructed decay times, respectively. The signal and time dependent (independent) background resolution functions are denoted as $\mathcal{R}_{sig}$ and $\mathcal{R}^{tdep}_{bkgd}$ ($\mathcal{R}^{tindep}_{bkgd}$), respectively. Finally, the parameters needed to describe the physics functions and signal, time dependent (time independent) background resolution functions are denoted by $\vec{a_p}$, $\vec{a_s}$ and $\vec{a_{b_1}}$($\vec{a_{b_2}}$) respectively. All the functions

are individually normalised to unity and the integration over true decay time is performed numerically, as described in section 6.6.2.

In the following sections the exact form of each of the constituent parts of the likelihood function are described in more detail.

7.6.2 The Physics Functions

The signal physics function has the following form :

$$\mathcal{P}_1(\mathrm{t}^{'}, \tau_{\mathrm{b}\Lambda^0}, \vec{\mathrm{a}_\mathrm{p}}) = \frac{1}{\mathcal{F}(\mathrm{t}^{'}, \vec{\mathrm{a}_\mathrm{p}})\,\mathcal{N}_\mathrm{p}(\mathrm{t}^{'}, \vec{\mathrm{a}_\mathrm{p}})}\,\frac{1}{\tau_{\mathrm{b}\Lambda^0}}\,\exp(-\mathrm{t}^{'}/\tau_{\mathrm{b}\Lambda^0}). \tag{7.25}$$

The physics function for time dependent background events can similarly be described as :

$$\mathcal{P}_2(\mathrm{t}^{'}, \tau_\mathrm{b}, \vec{\mathrm{a}_\mathrm{p}}) = \frac{1}{\mathcal{F}(\mathrm{t}^{'}, \vec{\mathrm{a}_\mathrm{p}})\,\mathcal{N}_\mathrm{b}(\mathrm{t}^{'}, \vec{\mathrm{a}_\mathrm{p}})}\,\frac{1}{\tau_\mathrm{b}}\,\exp(-\mathrm{t}^{'}/\tau_\mathrm{b}). \tag{7.26}$$

Both physics functions include the bias, described in section 6.6.3, through the function :

$$\mathcal{F}(\mathrm{t}^{'}, \vec{\mathrm{a}_\mathrm{p}}) = \exp(\mathrm{a} + \mathrm{b}\mathrm{t}^{'}) + \mathrm{c}, \tag{7.27}$$

where :

$$\vec{\mathrm{a}_\mathrm{p}} = \{\mathrm{a}, \mathrm{b}, \mathrm{c}\}. \tag{7.28}$$

The bias corrected signal and time dependent background physics functions are normalised by $\mathcal{N}_\mathrm{p}$ and $\mathcal{N}_\mathrm{b}$ respectively, where :

$$\mathcal{N}_\mathrm{p}(\mathrm{t}^{'}, \vec{\mathrm{a}_\mathrm{p}}) = \int_0^\infty \frac{1}{\tau_{\mathrm{b}\Lambda^0}}\exp(-\mathrm{t}^{'}/\tau_{\mathrm{b}\Lambda^0})\,\frac{1}{\mathcal{F}(\mathrm{t}^{'}, \vec{\mathrm{a}_\mathrm{p}})}\,\mathrm{d}\mathrm{t}^{'}, \tag{7.29}$$

$$\mathcal{N}_\mathrm{b}(\mathrm{t}^{'}, \vec{\mathrm{a}_\mathrm{p}}) = \int_0^\infty \frac{1}{\tau_\mathrm{b}}\exp(-\mathrm{t}^{'}/\tau_\mathrm{b})\,\frac{1}{\mathcal{F}(\mathrm{t}^{'}, \vec{\mathrm{a}_\mathrm{p}})}\,\mathrm{d}\mathrm{t}^{'}. \tag{7.30}$$

The parameterised bias correction function is shown in figure 7.7. The bias mainly affects the region $\mathrm{t}^{'} < 1.5$ ps.

7.6.3 The Signal Resolution Function

This resolution function describes the distribution of reconstructed decay times (for a given true decay time) in $\mathrm{Z}^0 \rightarrow \mathrm{b}\bar{\mathrm{b}}$ events with an associated Λ^0 that originates

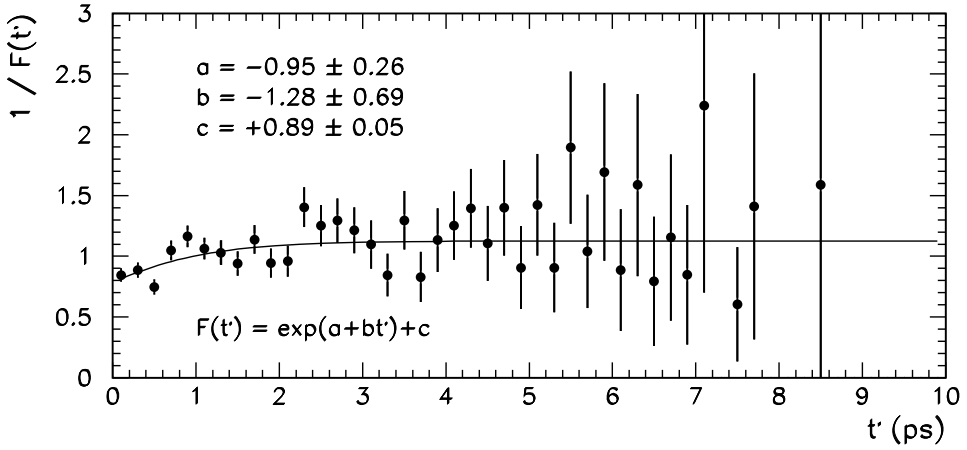

Figure 7.7: The parameterised bias correction function, $1/\mathcal{F}$, as a function of true decay time.

from b hadron decay. The form of this resolution function follows that used for the signal in the average bottom hadron lifetime analysis, described in section 6.6.4. The parameter values :

$$\vec{a_s} = \{a, b, n, k_{1,2}, \alpha_{1,2}, \beta_{1,2}, \varphi_{1,2}, x_{1,2}, y_{1,2}\}, \tag{7.31}$$

used to describe the resolution function are re-evaluated for this analysis and are shown in table 7.2. Figure 7.8 shows the shape of the reconstructed decay time distribution in slices of true decay time, with the resolution function parameterisations overlaid.

7.6.4 The Time Dependent Background Resolution Function

This resolution function describes the distribution of reconstructed decay times (for a given true decay time) in $Z^0 \rightarrow b\bar{b}$ events with an associated fragmentation or fake Λ^0. The form of this resolution function is exactly the same as the signal resolution function. The parameter values :

$$\vec{a_{b_1}} = \{a', b', n', k'_{1,2}, \alpha'_{1,2}, \beta'_{1,2}, \varphi'_{1,2}, x'_{1,2}, y'_{1,2}\}, \tag{7.32}$$

used to describe the resolution function are shown in table 7.3. Figure 7.9 shows the parameterised reconstructed decay time distributions in slices of true decay time.

Normalisation		$\mathcal{G}_1$		$\mathcal{G}_2$		$\mathcal{G}_3$		$\mathcal{G}_4$	
a	0.468 ± 0.044	k_1	0.024 ± 0.017	k_2	-0.015 ± 0.007	φ_1	-0.352 ± 0.115	φ_2	0.036 ± 0.051
b	0.274 ± 0.028	α_1	0.161 ± 0.011	α_2	0.386 ± 0.018	x_1	6.562 ± 0.037	x_2	1.592 ± 0.095
n	0.176 ± 0.008	β_1	0.076 ± 0.006	β_2	0.174 ± 0.016	y_1	0.210 ± 0.078	y_2	0.109 ± 0.040

Table 7.2: The parameters for the signal resolution function.

Normalisation		$\mathcal{G}_1$		$\mathcal{G}_2$		$\mathcal{G}_3$		$\mathcal{G}_4$	
a'	0.573 ± 0.081	k'_1	0.015 ± 0.031	k'_2	-0.063 ± 0.013	φ'_1	0.652 ± 0.360	φ'_2	0.099 ± 0.036
b'	0.244 ± 0.023	α'_1	0.138 ± 0.022	α'_2	0.374 ± 0.026	x'_1	6.909 ± 0.191	x'_2	1.509 ± 0.075
n'	0.321 ± 0.014	β'_1	0.127 ± 0.013	β'_2	0.222 ± 0.028	y'_1	1.010 ± 0.180	y'_2	0.164 ± 0.025

Table 7.3: The parameters for the time dependent background resolution function.

Normalisation		$\mathcal{G}_1$		$\mathcal{G}_2$		$\mathcal{G}_3$		$\mathcal{G}_4$	
q	0.338 ± 1.292	x_1	8.868 ± 2.620	x_2	0.089 ± 0.411	x_3	0.077 ± 0.649	x_4	0.920 ± 0.449
r	0.137 ± 0.521	σ_1	4.371 ± 1.655	σ_2	0.284 ± 0.256	σ_3	0.318 ± 0.542	σ_4	1.056 ± 0.182
s	0.587 ± 0.906								

Table 7.4: The parameters for the time independent background resolution function.

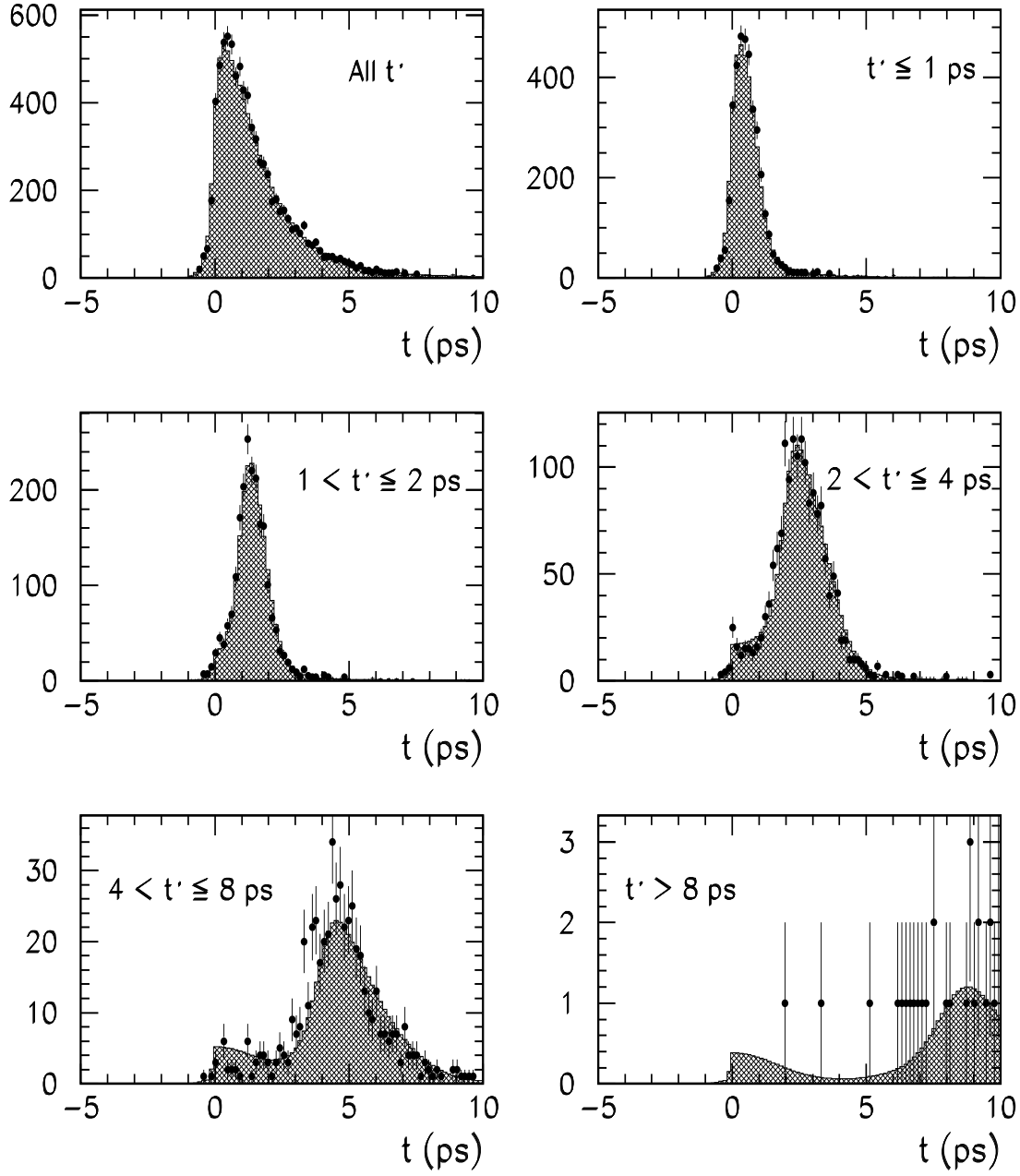

Figure 7.8: Distributions of the reconstructed decay time shown for different slices of true decay time for signal events. The points represent Monte Carlo data and the shaded histogram is the fit from the resolution function.

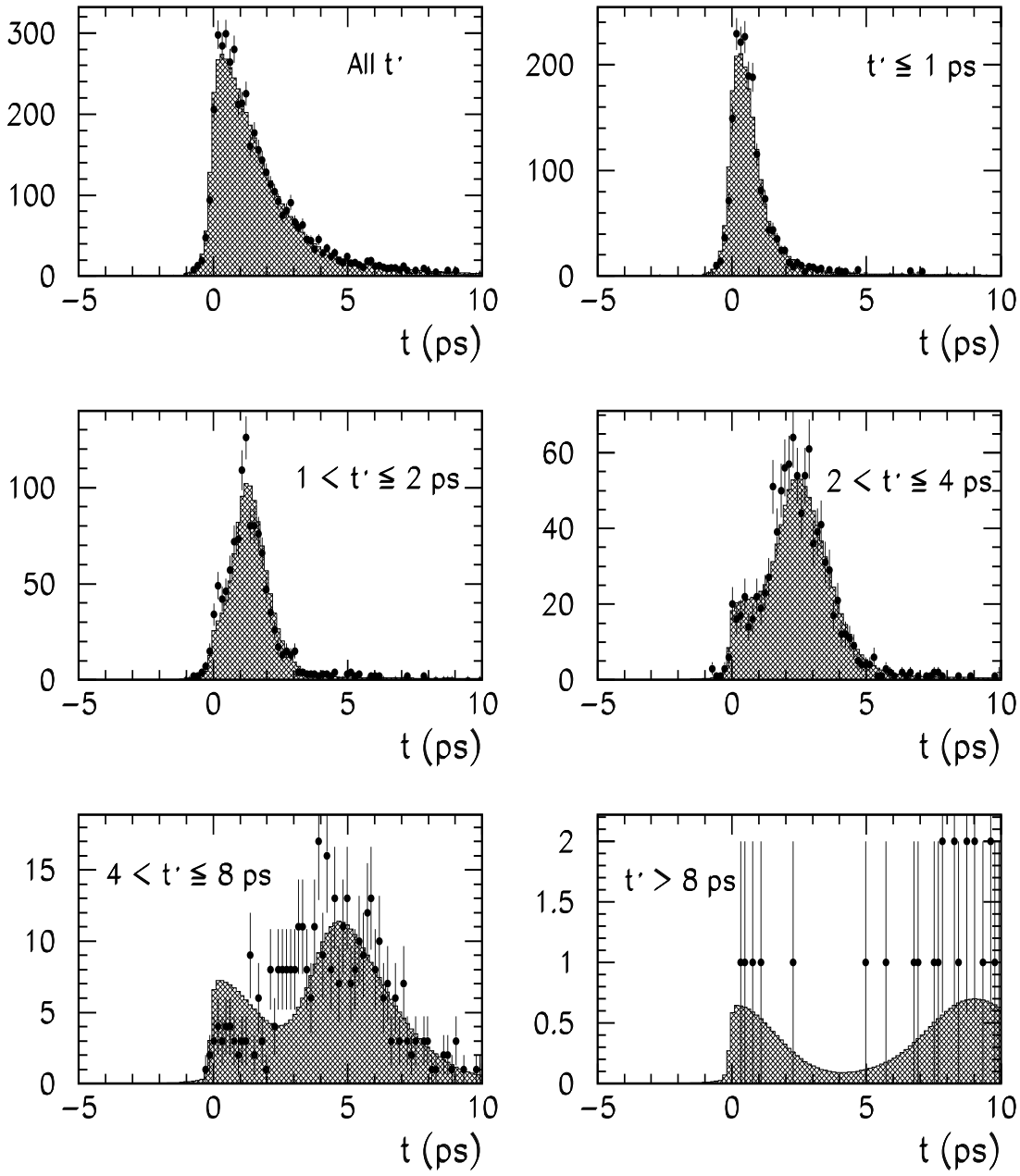

Figure 7.9: Distributions of the reconstructed decay time shown for different slices of true decay time for time dependent background events. The points represent Monte Carlo data and the shaded histogram is the fit from the resolution function.

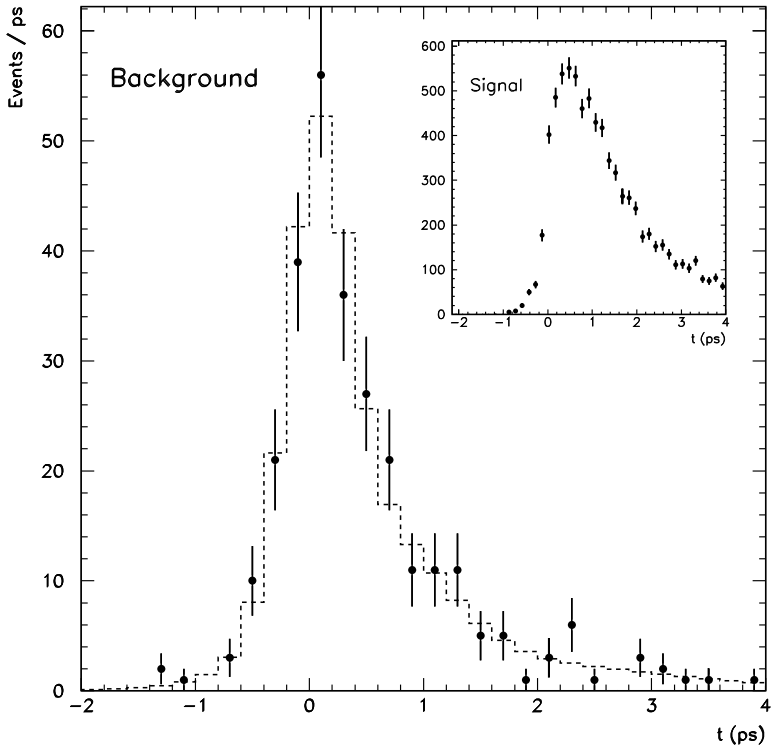

Figure 7.10: The reconstructed decay time distribution for time independent background events. The points represent Monte Carlo data and the dashed line is the fit from the resolution function. The distribution of reconstructed decay times for signal events is also shown, as an inset, for comparison.

7.6.5 The Time Independent Background Resolution Function

As in the average bottom hadron lifetime analysis, the time independent background is very small. The awayside b tag heavily suppresses secondary vertices from u, d, s or c quarks, which form the majority of this background. The form of the resolution function follows that described in section 6.6.5. The parameter values :

$$\vec{a_b} = \{q, r, s, \sigma_{1,4}, x_{1,4}\}, \tag{7.33}$$

used to describe the resolution function are shown in table 7.4. The parameterised reconstructed decay time distribution for the time independent background is shown in figure 7.10.

7.7 Proof of Principle

The technique used to extract the bottom baryon enhanced lifetime, $\tau_{b\Lambda^0}$, was firstly tested with Monte Carlo data. All five quark flavours were used and neural network tagging was used to enhance $Z^0 \rightarrow b\bar{b}$ events. The Monte Carlo fitting sample contained 3225 reconstructed decay times. The reconstructed decay time distribution was divided into 200 bins between -5$\rightarrow$25 ps. There were no reconstructed decay times <-5 ps and 7 reconstructed decay times >25 ps (0.22% of the total). The numerical integration over true decay time was performed over the range 0$\rightarrow$20 ps.

Monte Carlo 'cheat' information was used to determine that :

$$\tau_{\Lambda_b^0} = 1.20\,\text{ps}, \tag{7.34}$$

$$\tau_b = 1.57\,\text{ps}, \tag{7.35}$$

$$g/f = 0.51, \tag{7.36}$$

$$s = 0.62, \tag{7.37}$$

and :

$$p = 0.91. \tag{7.38}$$

The single exponential lifetime fit yielded :

$$\tau_{b\Lambda^0} = (1.38 \pm 0.06)\,\text{ps}, \tag{7.39}$$

where the error is purely statistical. This is consistent with the value of 1.39 ps derived from the Monte 'cheat' information. The parameterised reconstructed decay time distribution is shown in figure 7.11.

7.8 Results

In this section, values of s and p are derived[f] for the data and the value of $\tau_{b\Lambda^0}$ extracted from the lifetime fit in data is presented. The systematic errors on $\tau_{b\Lambda^0}$ are evaluated and the ratio $\tau_{b\Lambda^0}/\tau_b$ is derived to investigate the significance of the bottom baryon component in the reconstructed decay time distribution. Finally,

[f] See equations 7.23 and 7.24 for definitions.

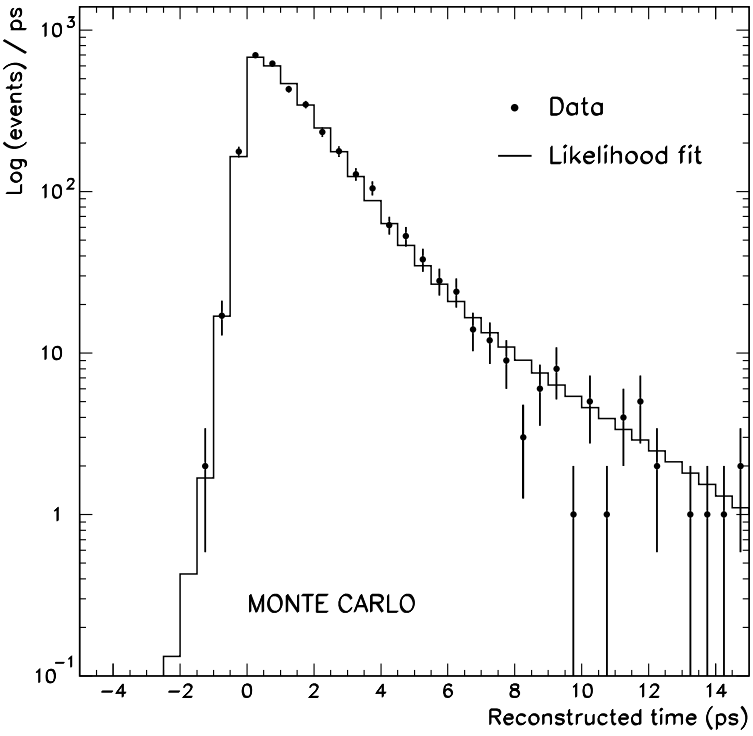

Figure 7.11: The reconstructed decay time distribution for Monte Carlo data, including all backgrounds. The solid line is the result of the lifetime fit.

equation 7.19 is used with the estimate of g/f presented in equation 7.18 to measure $\tau_{\Lambda_b^0}$.

7.8.1 The Bottom Baryon Enhanced Sample Composition

The composition of the bottom baryon enhanced reconstructed decay time distribution is described by the values of s and p. The overall bottom baryon enhanced reconstructed decay time distribution is denoted by $\mathcal{T}$. If $\mathcal{T}_{\rm sig}$ and $\mathcal{T}_{\rm tdep}$ ($\mathcal{T}_{\rm tindep}$) represent the reconstructed decay time distributions from signal and time dependent (independent) background sources, then $\mathcal{T}$ can be expressed (with reference to equation 7.22) as :

$$\mathcal{T} = {\rm s}\,\mathcal{T}_{\rm sig} + \overbrace{(1-{\rm s}){\rm p}}^{\mathcal{M}}\,\mathcal{T}_{\rm tdep} + (1-{\rm s})(1-{\rm p})\,\mathcal{T}_{\rm tindep}. \qquad (7.40)$$

However, s and p are correlated. The composition of the sample can be re-expressed in terms of two uncorrelated parameters, z and k, which are described below. The systematic error on $\tau_{{\rm b}\Lambda^0}$, due to uncertainties in the composition of the

overall reconstructed decay time distribution, is derived from the uncertainties on z and k.

An alternate formulation for $\mathcal{T}$, in terms of the b purity, z, is :

$$\mathcal{T} = \mathrm{z}\,\mathcal{T}_{\mathrm{b\bar{b}}} + (1-\mathrm{z})\,\mathcal{T}_{\mathrm{light}}, \tag{7.41}$$

where, $\mathcal{T}_{\mathrm{b\bar{b}}}$ and $\mathcal{T}_{\mathrm{light}}$ denote the reconstructed decay time distributions in $\mathrm{Z^0} \to \mathrm{b\bar{b}}$ and light quark events, respectively. The fraction of $\mathrm{Z^0} \to \mathrm{b\bar{b}}$ events where the Λ^0 originates from b fragmentation or is fake, can therefore be expressed as :

$$\mathrm{k} = \mathcal{M}/\mathrm{z}. \tag{7.42}$$

Using these definitions, p and s can be defined, in terms of z and k, as :

$$\mathrm{p} = \frac{\mathrm{z\,k}}{1-\mathrm{z}+\mathrm{z\,k}}, \tag{7.43}$$

$$\mathrm{s} = 1 - \frac{\mathrm{z\,k}}{\mathrm{p}}. \tag{7.44}$$

The value for z is taken from data using the double tagging technique described in section 6.8.1. A correction factor, $(+0.13 \pm 0.50)\%$[g], is derived from Monte Carlo studies and the final value of z is :

$$\mathrm{z} = (94.97 \pm 0.81)\%. \tag{7.45}$$

The value of k is derived from Monte Carlo studies. A conservative estimate of the uncertainty on k is taken from studies of Br(b hadron $\to$ Λ^0 X), presented in section 5.8.3. The final value for k is :

$$\mathrm{k} = 0.36 \pm 0.02. \tag{7.46}$$

The error is dominated by the uncertainty on the rate of Λ^0's from b fragmentation.

Using these values of z and k, the following values of s and p are derived :

$$\begin{aligned} \mathrm{s} &= 0.608 \pm 0.005 \pm 0.019, \\ \mathrm{p} &= 0.872 \pm 0.019 \pm 0.007, \end{aligned} \tag{7.47}$$

where, the first (second) error comes from the uncertainty on z (k).

[g] The error comes from the double tagging result.

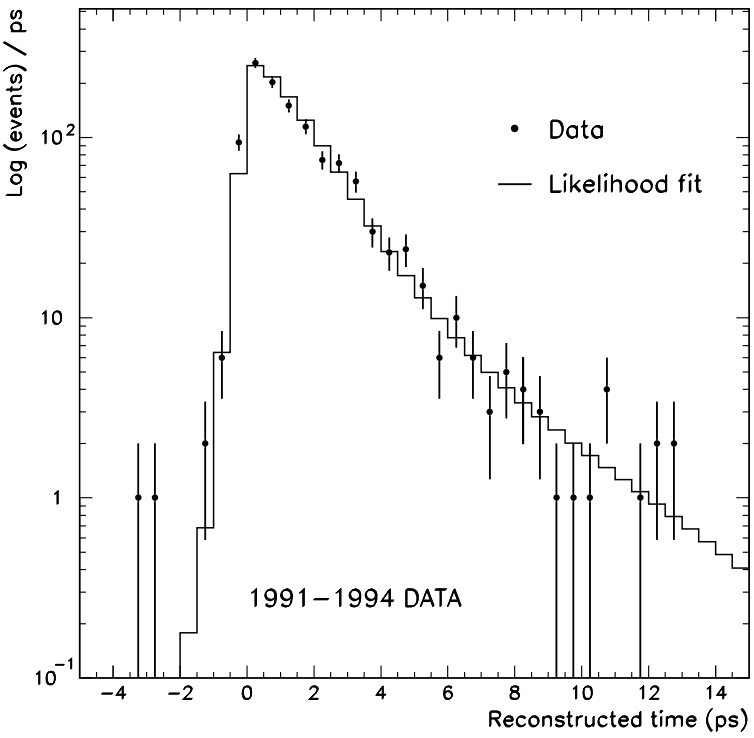

Figure 7.12: The reconstructed decay time distribution in data. The solid line is the result of the lifetime fit.

7.8.2 Measuring the Bottom Baryon Enhanced Lifetime

The binning and integration ranges used in the Monte Carlo proof of principle were retained for the following studies using 1379 reconstructed decay times from 1991–4 data. There were no reconstructed times <-5 ps and 2 reconstructed times >25 ps (0.15% of the total).

Using the values of s and p derived above and $\tau_{\rm b} = 1.637$ ps, as measured in the previous chapter, the result of the lifetime fit was :

$$\tau_{\rm b\Lambda^0} = (1.38 \pm 0.09)\,{\rm ps}, \tag{7.48}$$

where the error is purely statistical. The parameterised reconstructed decay time distribution is shown in figure 7.12.

7.8.3 Studies of Possible Systematic Errors

In this section, possible systematic errors on the measurement of $\tau_{\rm b\Lambda^0}$ are investigated and these results are summarised in table 7.5. The statistical error on $\tau_{\rm b\Lambda^0}$ is larger

Source of Uncertainty	Systematic Error (ps)
Track parameter uncertainties in resolution function	± 0.047
Track parameter uncertainties in bias correction function	± 0.019
Companion baryon effects on τ_b	± 0.013
Uncorrelated systematic errors on τ_b	± 0.010
Δz	± 0.016
Δk	± 0.007
Total	± 0.056

Table 7.5: A summary of the systematic errors for $\tau_{b\Lambda^0}$.

than the total systematic error from all of these effects.

Firstly, the effect of charged track parameter uncertainties on the resolution and bias correction functions is described. Uncertainties on τ_b, affecting the background physics function, are also evaluated. Finally, the effect of uncertainties on the composition of the overall reconstructed decay time distribution (described by k and z) and the sensitivity to the Λ^0 minimum momentum requirement are investigated.

The error due to uncertainties on the charged track parameters was evaluated using smeared Monte Carlo samples to re-evaluate the parameters in the resolution functions, as described in section 6.9.1. A systematic error of ± 0.047 ps was assigned to account for the change in fitted lifetime.

The bias correction function was also reparameterised using the results from a smeared $b\bar{b}$ Monte Carlo sample. A systematic error of ± 0.019 ps was assigned to account for the change in fitted lifetime.

A Λ^0 originating from b fragmentation can be the companion anti-baryon during primary bottom baryon production. Monte Carlo studies indicated that the bottom hadron composition for a b fragmentation event sample was 80% B meson/20% b baryon, compared to 93% B meson/7% b baryon for $Z^0 \rightarrow b\bar{b}$ events with fake Λ^0's. The average b hadron lifetime for these two Λ^0 sources (that form the time dependent background) is 1.54 ps compared to 1.57 ps for a truly generic sample. The lifetime is lowered due to b baryon enhancement in b fragmentation events. A ratio, 1.54 ps/1.57 ps = 0.98, was used to scale τ_b in the $\tau_{b\Lambda^0}$ fit, to check

Minimum Λ^0 Momentum (GeV/c)	s	p
4	0.53±0.02	0.89±0.02
5	0.61±0.02	0.87±0.02
6	0.64±0.03	0.82±0.03

Table 7.6: Values of s and p for different minimum Λ^0 momentum requirements. The default requirement is 5 GeV/c.

the sensitivity to possible b baryon enhancement. Uncertainties on τ_b will affect the background physics function, as shown in equation 7.26. The systematic error assigned to cover the shift in the fitted lifetime was ±0.013 ps.

An additional systematic error was assigned to account for the uncorrelated systematic errors on τ_b, ie : uncertainties in the Monte Carlo bottom fragmentation modelling, parameterisation uncertainties in the signal resolution function and parameterisation uncertainties in the bias correction function. The values of these systematic errors are shown in table 6.7. A systematic error of ±0.010 ps was assigned to $\tau_{b\Lambda^0}$ to cover the change in fitted lifetime when the central value of τ_b in the time dependent background resolution function was moved by the uncorrelated systematic errors detailed above.

The composition of the overall reconstructed decay time distribution is defined in terms of s and p. Since s and p are correlated, the systematic error due to the sample composition uncertainty is evaluated using the uncertainties on z and k, which are uncorrelated. Systematic errors of ±0.016 ps and ±0.007 ps were assigned to account for differences in the fitted value of $\tau_{b\Lambda^0}$ due to the uncertainties on z and k, shown in equations 7.46 and 7.45.

Finally, as a cross-check of the overall method, $\tau_{b\Lambda^0}$ was evaluated for minimum Λ^0 momentum requirements of 4 GeV/c and 6 GeV/c. The values of s and p were re-evaluated for this study and the new values are shown in table 7.6. The resolution and bias correction functions were also reparameterised. The fitted lifetime results were (1.40±0.08) ps for the 4 GeV/c momentum requirement and (1.41±0.12) ps for the 6 GeV/c momentum requirement. Both of these results are consistent with the default result, using a 5 GeV/c momentum requirement, of (1.38±0.09) ps.

7.8.4 Deriving the Bottom Baryon Lifetime

The final value for $\tau_{b\Lambda^0}$, including all systematic errors is :

$$\tau_{b\Lambda^0} = (1.38 \pm 0.09\,(\text{stat}) \pm 0.06\,(\text{syst}))\,\text{ps}. \tag{7.49}$$

A ratio, $\tau_{b\Lambda^0}/\tau_b$, can be formed using the τ_b measurement from the previous chapter :

$$\tau_b = (1.637 \pm 0.008\,(\text{stat}) \pm 0.034\,(\text{syst}))\,\text{ps}. \tag{7.50}$$

All the systematic errors on the measurement of $\tau_{b\Lambda^0}$ (apart from Δk) are correlated with the τ_b measurement and are treated accordingly to estimate :

$$\tau_{b\Lambda^0}/\tau_b = 0.84 \pm 0.06, \tag{7.51}$$

which differs from unity by 2.7 standard deviations. This is consistent with a bottom baryon lifetime significantly smaller than the average bottom hadron lifetime.

An estimate of $\tau_{\Lambda_b^0}$ is made using equation 7.19. The strong dependence of $\tau_{\Lambda_b^0}$ on g/f is shown in figure 7.13. The thicker central curve indicates the central value of $\tau_{\Lambda_b^0}$ and the thinner outer lines represent the total error, due to uncertainties on $\tau_{b\Lambda^0}$ and τ_b. The vertical band indicates the 'optimised' value of g/f, presented in equation 7.18. The final result is :

$$\tau_{\Lambda_b^0} = (1.10 \pm 0.19\,(\text{stat}) \pm 0.13\,(\text{syst}) \pm 0.05\,(\text{syst}))\,\text{ps}. \tag{7.52}$$

The first error is due to the statistical uncertainty on $\tau_{b\Lambda^0}$, the second error is due to the systematic error on $\tau_{b\Lambda^0}$ and τ_b and the final error is due to the uncertainty on g/f.

Figure 7.14 shows this result compared to the most recent results from Z^0 experiments [174], presented at the HEP95 conference [99]. This result is consistent with the current world average[h], which is derived taking correlated errors into account [170]. The $\tau_{\Lambda_b^0}$ measurement presented in this chapter is the first not to use baryon-lepton ($\Lambda_c^+\ell$, $\Lambda^0\ell$ or pμ) correlations. It therefore provides a systematically independent cross-check.

In section 3.3.6.2, a theoretical prediction for bottom hadron lifetime ratios was described. The predictions are shown graphically in figure 3.9. The ratio prediction,

[h] The result from this analysis is not used to form the average.

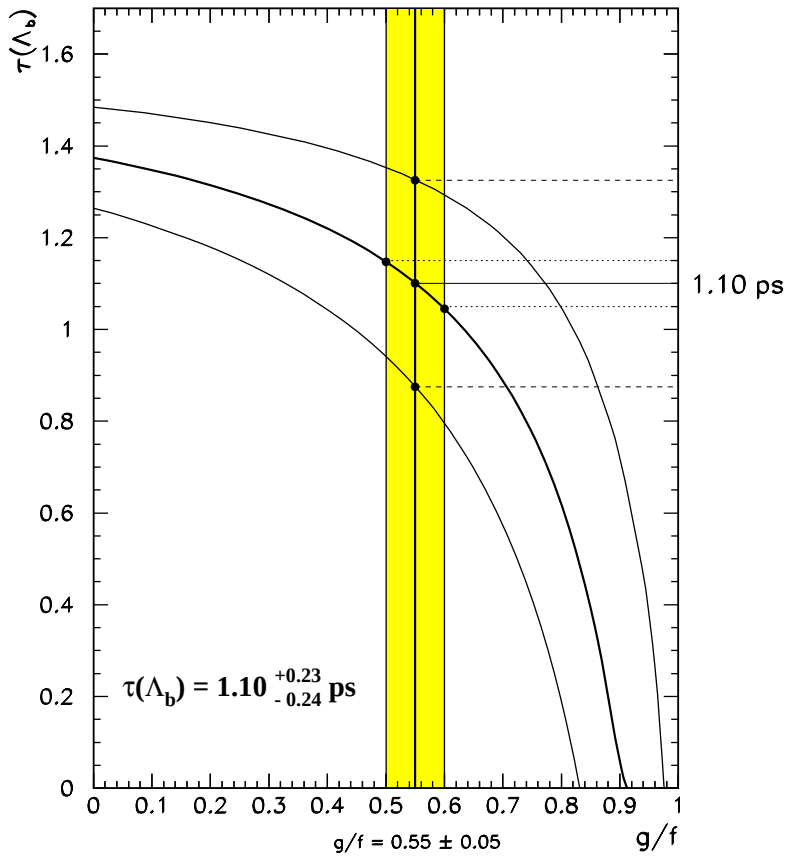

Figure 7.13: The estimate of $\tau_{\Lambda^0_b}$ plotted as a function of g/f. The thick central curve indicates the central value of $\tau_{\Lambda^0_b}$ and the thinner outer lines indicate the total error. The 'optimised' value of g/f from equation 7.18 (shown as the shaded band) and the resulting value of $\tau_{\Lambda^0_b}$ are indicated on the figure. The composition of the error on $\tau_{\Lambda^0_b}$ is described in the text.

$\tau(\Lambda^0_b)/\tau(B^0) = 0.90 \rightarrow 0.95$, is pertinent to the results from this analysis, under the assumption that $\tau_b \cong \tau(B^0)$. Current lifetime measurements, presented at the HEP95 conference, indicate that $\tau(\Lambda^0_b)/\tau(B^0) = 0.75 \pm 0.05$. The $\tau_{\Lambda^0_b}$ result from this analysis can be combined with the τ_b result from the previous chapter to estimate :

$$\tau_{\Lambda^0_b}/\tau_b = 0.67 \pm 0.12. \tag{7.53}$$

The correlation between systematic errors common to $\tau_{b\Lambda^0}$ and τ_b is accounted for when forming the ratio. This result is consistent with the HEP95 results within 0.6 standard deviations, but, lies 1.8 standard deviations outside the predicted theoretical range.

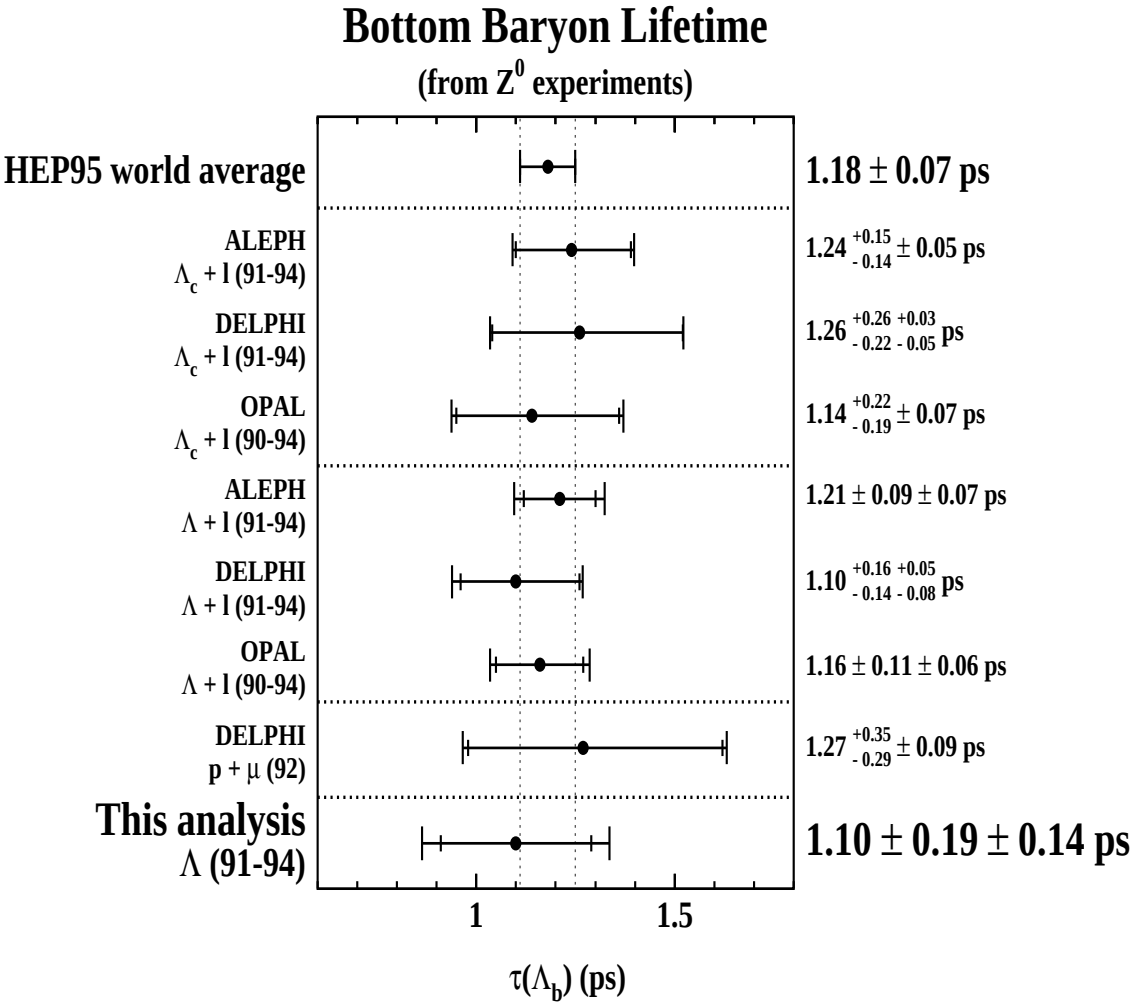

Figure 7.14: A summary of bottom baryon lifetime measurements. There are three types of measurement : $\Lambda_c^+\ell$ correlations, $\Lambda^0\ell$ correlations and pμ correlations. Each measurement technique is described in section 3.3.7.2. The result from the analysis described in this chapter is also shown, along with the current world average result. The DELPHI collaboration have recently updated their $\Lambda_c^+\ell$ result to $(1.19^{+0.21}_{-0.18}\ ^{+0.07}_{-0.08})$ ps and their $\Lambda^0\ell$ result to $(1.10^{+0.19}_{-0.17} \pm 0.09)$ ps. They also describe a new result using $\Lambda^0\ell\pi$ correlations, which yields : $\tau_{\Lambda_b^0} = (1.46^{+0.22}_{-0.21}\ ^{+0.07}_{-0.09})$ ps [175].

7.9 Summary

In this analysis, estimates of the bottom hadron decay length and momentum were combined to estimate the bottom hadron decay time. The bottom baryon component of the decay time distribution was enhanced by requiring a high momentum Λ^0 to be associated with the jet in which the decay length measurement was made.

A binned maximum likelihood fit was used to estimate the bottom baryon enhanced lifetime, $\tau_{b\Lambda^0}$. The bottom baryon lifetime was to be observed to be significantly smaller than the average bottom hadron lifetime from the measurement of the ratio :

$$\tau_{b\Lambda^0}/\tau_b = 0.84 \pm 0.06,$$

where, τ_b represents the average bottom hadron lifetime, presented in the previous chapter. This ratio differs from unity by 2.7 standard deviations.

The bottom baryon lifetime :

$$\tau_{\Lambda_b^0} = (1.10 \pm 0.19\,(\text{stat}) \pm 0.13\,(\text{syst}) \pm 0.05\,(\text{syst}))\,\text{ps},$$

was derived from the measurement of $\tau_{b\Lambda^0}$ using an estimate of the proportion of the bottom baryon enhanced decay time distribution due to an average bottom hadron lifetime component (g/f = 0.55±0.05). The first error is due to the statistical uncertainty on $\tau_{b\Lambda^0}$, the second error is due to the systematic error on $\tau_{b\Lambda^0}$ and τ_b (dominated by track parameter uncertainties in the resolution functions used in the $\tau_{b\Lambda^0}$ measurement). The final error is due to the uncertainty on g/f.

This measurement of the bottom baryon lifetime is the first not to use baryon-lepton correlations ($\Lambda_c^+\ell$, $\Lambda^0\ell$ or pμ) and so provides a very useful cross-check of the contemporary measurements shown in figure 7.14.

Finally, the ratio :

$$\tau_{\Lambda_b^0}/\tau_b = 0.67 \pm 0.12,$$

is derived. This is consistent with the prediction using lifetime results presented at the HEP95 conference. It is not consistent with the range of QCD-based theoretical predictions described in section 3.3.6.2.

Appendix A

Artificial Neural Networks

A.1 Introduction

When analysing experimental data, selection requirements are often applied to variables in order to enhance a particular feature of the data. For example, the decay length significance (the decay length divided by its error) is often used in the study of bottom hadrons to produce an enriched sample of $Z^0 \to b\bar{b}$ events. It is often desirable to use several selection variables to highlight a particular feature of the data. Making optimal use of the selection variables is not a trivial matter. Sophisticated algorithms, designed for multi-dimensional discrimination, are often used [176]. Neural networks currently seem to be the most powerful and automated of such algorithms [177].

In this analysis, a neural network is used to determine whether a charged track comes from bottom hadron decay or fragmentation. This information is vital for an estimation of the charged fragmentation energy, which is needed for the decay time estimation described in chapter 6.

A.2 Implementation

The neural network used in this study is implemented with the `JETNET` package [178]. The neural network structure can be visualised as shown in figure A.1. Only one

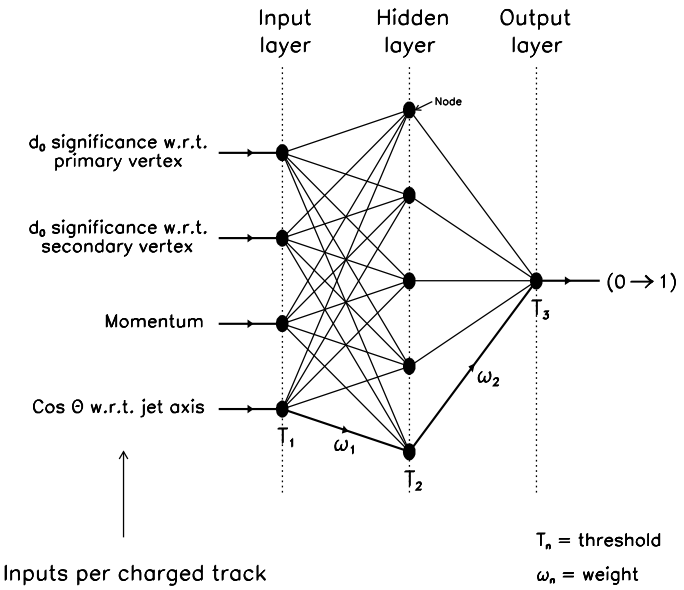

Figure A.1: A schematic representation of the neural network architecture used in this application. The topology is referred to as 'forward-feed'.

hidden layer is shown but any number are, in principle, possible[a].

In this example of a 'forward-feed' architecture, each neuron in the input layer is connected to each neuron in the hidden layer, and each node in the hidden layer is connected to the output node. Each node has an associated threshold (T) and each input node is weighted (ω), as shown in the figure. The 'processing' consists of adding, with suitably adjusted weights, all the incoming information at a node and (ideally) responding 0 or 1 depending if a given threshold is exceeded. In reality (ie: in computer code simulations) the response of the neuron is a smooth sigmoid function that varies between 0 and 1. In this implementation, the sigmoid response function is of the form :

$$\mathrm{g(x)} = \frac{1}{1 + \exp(-2\mathrm{x})}. \tag{A.1}$$

During the learning phase, the combination of weights and thresholds are optimised as follows :

- The desired properties of a track known to come from either bottom hadron decay or b fragmentation are fed into the inputs of the neural network.

[a] Any task can be solved with a structure involving two hidden layers, but many nodes may be required.

- The response of the neural network to this input pattern is calculated.

- This response is compared to the desired response. In this case, the response is 1 for tracks from bottom hadron decay and 0 for tracks from b fragmentation. The weights and thresholds are updated internally, as a result of this comparison. A back-propagation algorithm that minimises the summed squared errors over all input tracks between the desired and actual neural network outputs is used to do this.

This process is repeated a number of times to allow the learning process to converge. It is important not to 'over-train' the neural network. Otherwise, statistical properties of the training sample may reduce the performance of the neural network as measured by an independent testing sample [179]. In the `JETNET` implementation, the temperature (β), learning rate (η) and momentum (α) of the neural network may be altered. The temperature is used to set the gain of the sigmoid response function, the learning rate affects the rate of gradient descent when minimising the error in the back propagation algorithm and the momentum can make learning more efficient and less oscillatory by reducing sensitivity to local minima. Default values of β=1.0, η=0.01 and α=0.5 were used.

In order to avoid biases, the neural network was presented with signal (bottom hadron decay) and background (b fragmentation) tracks alternately. The total training sample consisted of 10 000 tracks of each type from the 'old $b\bar{b}$' Monte Carlo data set[b]. All tracks had to satisfy the quality requirements described in section 4.3. After training, the neural network was tested on a sample of 10 000 signal and 10 000 background tracks from a statistically independent Monte Carlo subsample.

To test the performance of the neural network during training and testing, a 'figure of merit' ($\mathcal{F}$) parameter was defined [179]. The figure of merit provides a measure of the separation between the distributions $\mathcal{S}$ and $\mathcal{B}$ which describe the binned neural network output for signal and background tracks respectively. The value of $\mathcal{F}$ is defined as :

$$\mathcal{F} = \frac{1}{\mathrm{N_{trks}}} \sum_{\mathrm{i}=1}^{\mathrm{N_{bins}}} \frac{(\mathcal{S}_\mathrm{i} - \mathcal{B}_\mathrm{i})^2}{(\mathcal{S}_\mathrm{i} + \mathcal{B}_\mathrm{i})}, \tag{A.2}$$

[b]The 'new' Monte Carlo data sets were not available for this study.

where, N_{bins} are the number of binning channels for $\mathcal{S}$, $\mathcal{B}$, and N_{trks} is the number of tracks presented to the neural network (20 000). The parameter, $\mathcal{F}$, can be thought of as an inverted overlap integral. Therefore, if $\mathcal{F}$=0 then the $\mathcal{S}$ and $\mathcal{B}$ distributions are identical and the neural network has not distinguished between the track classes. If $\mathcal{F}$=1 the track classes have been completely distinguished between.

A.3 Results

The best performance was achieved with a neural network architecture of 4 input nodes, 8 nodes in the hidden layer and 1 output node, as shown in figure A.1. The four inputs used were :

- The d_0 significance (d_0/σ_{d_0}) with respect to the primary vertex, where σ_{d_0} represents the error on d_0,
- The d_0 significance with respect to the secondary vertex,
- The track momentum,
- $\cos\theta_{tb}$, where θ_{tb} is the angle between the track and the jet axis.

Figure A.2 shows these quantities for secondary vertices consisting of more than two charged tracks. Clear differences can be seen between tracks from bottom hadron decay and fragmentation. Adding more nodes to the hidden layer or adding more hidden layers did not improve the performance of the neural network (evaluated with $\mathcal{F}$). Figure A.3 shows the behaviour of $\mathcal{F}$ as a function of the number of training or testing cycles. A peak value of $\mathcal{F}$=29.5% is achieved during training, which drops to 28.0% for the testing sample. This behaviour is expected as the neural network inevitably picks up statistical features of the training sample. At 200 training cycles the training (testing) process is stopped, as $\mathcal{F}$ is not changing significantly. Figure A.4 shows the output of the neural network for tracks identified in the Monte Carlo as coming from bottom hadron decay or fragmentation. The neural network output peaks towards 1 for tracks coming from bottom hadron decay and towards 0 for tracks from b fragmentation. The relationship between the purity and efficiency for identifying tracks from bottom hadron decay, by requiring a minimum output from the neural network, is shown in figure A.5.

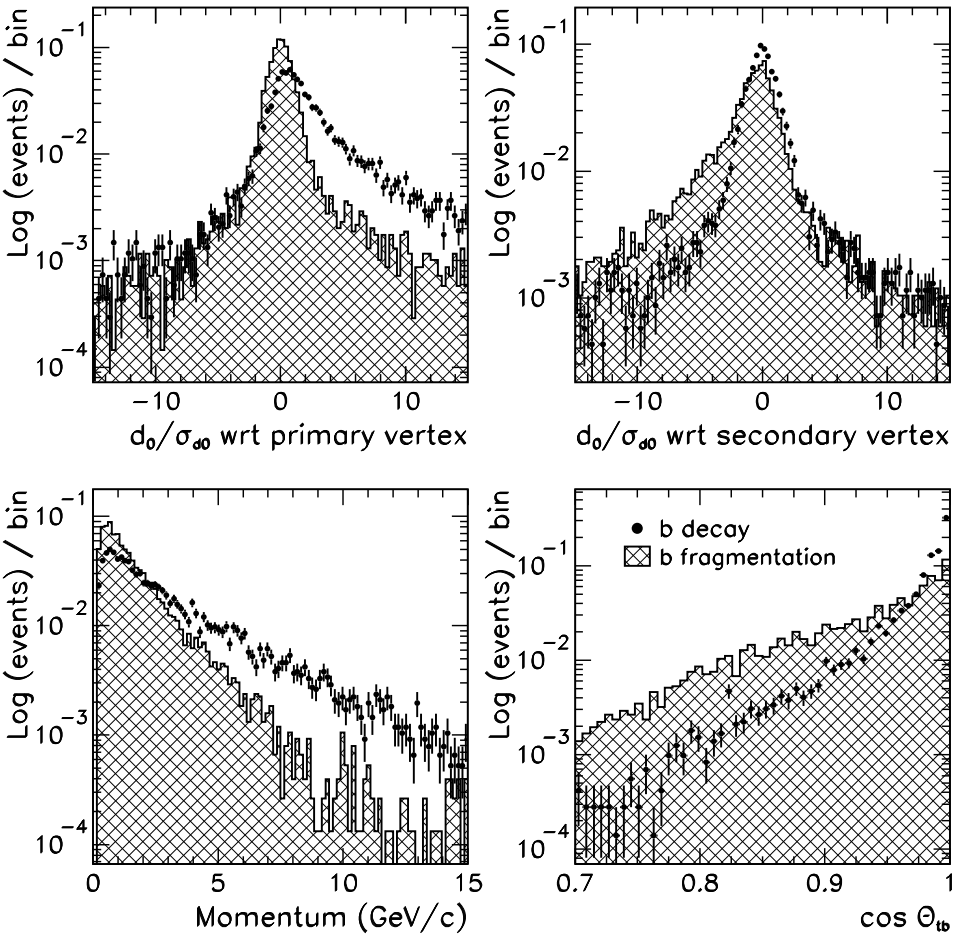

Figure A.2: Neural network inputs for secondary vertices consisting of greater than two charged tracks. The points represent tracks from bottom hadron decay and the hatched area represents tracks from fragmentation in $Z^0 \to b\bar{b}$ events. All distributions are normalised to unit area.

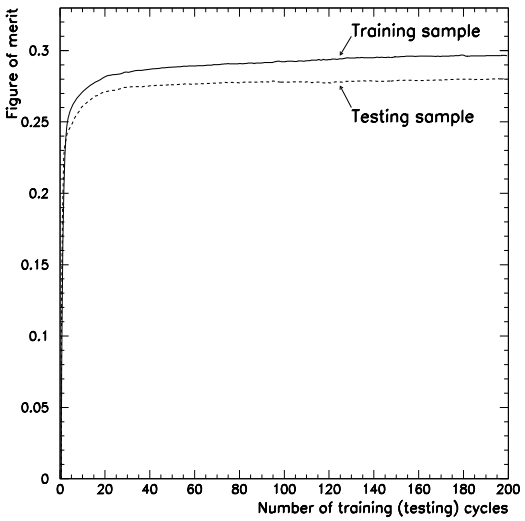

Figure A.3: The evolution of the figure of merit during the training and testing of the neural network.

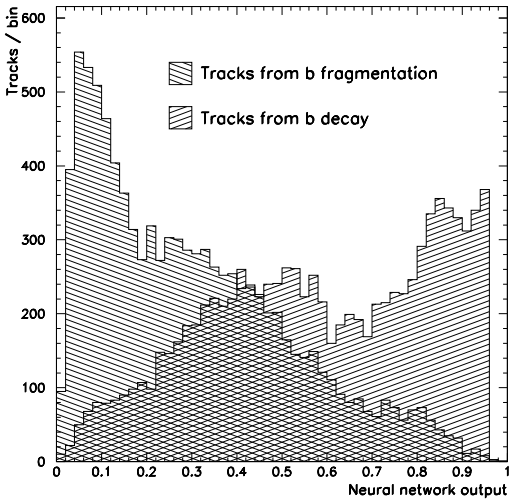

Figure A.4: The output of the neural network, after training, for tracks from bottom hadron decay (signal) and tracks from b fragmentation (background).

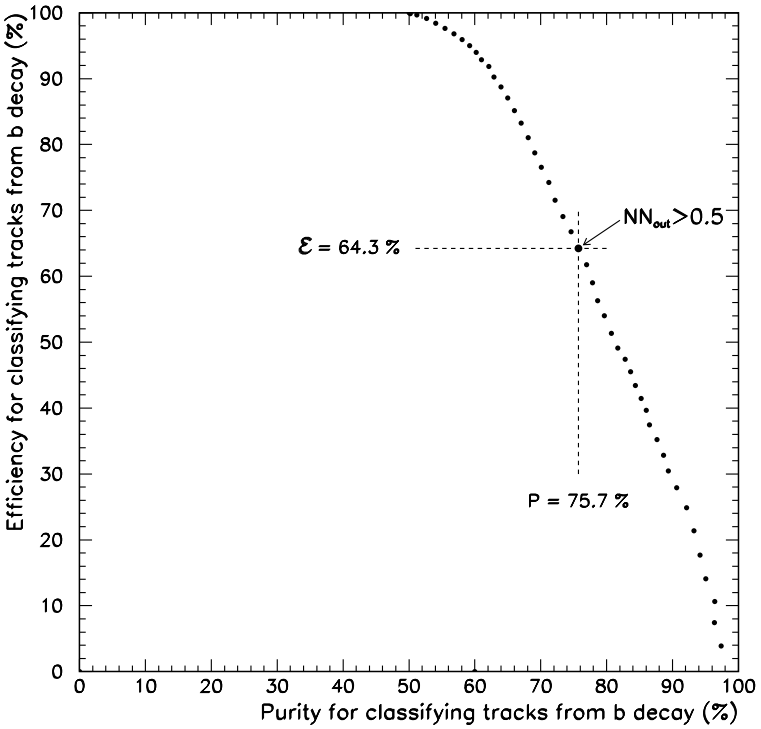

Figure A.5: The efficiency for identifying tracks from bottom hadron decay plotted against the purity of such tracks. The purity and efficiency values for a neural network output >0.5 are shown.

The sensitivity of the neural network output to each of the inputs was investigated by removing each of the inputs in turn and retraining and testing the neural network. A variable $\mathcal{S}$ was evaluated :

$$\mathcal{S} = \frac{\mathcal{F}_{\rm o} - \mathcal{F}_{\rm i}}{\mathcal{F}_{\rm o}}, \tag{A.3}$$

where, $\mathcal{F}_{\rm i}$ and $\mathcal{F}_{\rm o}$ are the figures of merit with input 'i' removed and all the inputs used, respectively. The sensitivity to each input is shown in table A.3.

Input Variable	Sensitivity
d_0/σ_{d_0} w.r.t. primary	0.31
$\cos\theta_{\rm tb}$	0.14
d_0/σ_{d_0} w.r.t. secondary	0.10
Track momentum	0.10

Table A.1: The relative sensitivity of the neural network output to each of the inputs.

Appendix B

The OPAL Collaboration

The members of the OPAL collaboration[a] are :

G. Alexander[23], J. Allison[16], N. Altekamp[5], K. Ametewee[25], K.J. Anderson[9], S. Anderson[12], S. Arcelli[2], S. Asai[24], D. Axen[29], G. Azuelos[18,a], A.H. Ball[17], E. Barberio[26], R.J. Barlow[16], R. Bartoldus[3], J.R. Batley[5], G. Beaudoin[18], J. Bechtluft[14], C. Beeston[16], T. Behnke[8], A.N. Bell[1], K.W. Bell[20], G. Bella[23], S. Bentvelsen[8], P. Berlich[10], S. Bethke[14], O. Biebel[14], V. Blobel[8], I.J. Bloodworth[1], J.E. Bloomer[1], P. Bock[11], H.M. Bosch[11], M. Boutemeur[18], B.T. Bouwens[12], S. Braibant[12], P. Bright-Thomas[25,f], R.M. Brown[20], H.J. Burckhart[8], C. Burgard[27], R. Bürgin[10], P. Capiluppi[2], R.K. Carnegie[6], A.A. Carter[13], J.R. Carter[5], C.Y. Chang[17], C. Charlesworth[6], D.G. Charlton[1,b], D. Chrisman[4], S.L. Chu[4], P.E.L. Clarke[15], I. Cohen[23], J.E. Conboy[15], O.C. Cooke[16], M. Cuffiani[2], S. Dado[22], C. Dallapiccola[17], G.M. Dallavalle[2], C. Darling[31], S. De Jong[12], L.A. del Pozo[8], M.S. Dixit[7], E. do Couto e Silva[12], M. Doucet[18], E. Duchovni[26], G. Duckeck[8], I.P. Duerdoth[16], J.E.G. Edwards[16], P.G. Estabrooks[6], H.G. Evans[9], M. Evans[13], F. Fabbri[2], P. Fath[11], F. Fiedler[12], M. Fierro[2], H.M. Fischer[3], R. Folman[26], D.G. Fong[17],

[a] At the time this thesis was completed.

M. Foucher[17], H. Fukui[24], A. Fürtjes[8], P. Gagnon[7], A. Gaidot[21], J.W. Gary[4], J. Gascon[18], S.M. Gascon-Shotkin[17], N.I. Geddes[20], C. Geich-Gimbel[3], S.W. Gensler[9], F.X. Gentit[21], T. Geralis[20], G. Giacomelli[2], P. Giacomelli[4], R. Giacomelli[2], V. Gibson[5], W.R. Gibson[13], D.M. Gingrich[30,a], J. Goldberg[22], M.J. Goodrick[5], W. Gorn[4], C. Grandi[2], E. Gross[26], M. Gruwé[8], C. Hajdu[32], G.G. Hanson[12], M. Hansroul[8], M. Hapke[13], C.K. Hargrove[7], P.A. Hart[9], C. Hartmann[3], M. Hauschild[8], C.M. Hawkes[5], R. Hawkings[8], R.J. Hemingway[6], G. Herten[10], R.D. Heuer[8], M.D. Hildreth[8], J.C. Hill[5], S.J. Hillier[1], T. Hilse[10], P.R. Hobson[25], R.J. Homer[1], A.K. Honma[28,a], D. Horváth[32,c], R. Howard[29], R.E. Hughes-Jones[16], D.E. Hutchcroft[5], P. Igo-Kemenes[11], D.C. Imrie[25], M.R. Ingram[16], A. Jawahery[17], P.W. Jeffreys[20], H. Jeremie[18], M. Jimack[1], A. Joly[18], G. Jones[16], M. Jones[6], R.W.L. Jones[8], U. Jost[11], P. Jovanovic[1], J. Kanzaki[24], D. Karlen[6], T. Kawamoto[24], R.K. Keeler[28], R.G. Kellogg[17], B.W. Kennedy[20], J. King[13], J. Kirk[29], S. Kluth[8], T. Kobayashi[24], M. Kobel[10], D.S. Koetke[6], T.P. Kokott[3], S. Komamiya[24], R. Kowalewski[8], T. Kress[11], P. Krieger[6], J. von Krogh[11], P. Kyberd[13], G.D. Lafferty[16], H. Lafoux[21], R. Lahmann[17], W.P. Lai[19], D. Lanske[14], J. Lauber[15], J.G. Layter[4], A.M. Lee[31], E. Lefebvre[18], D. Lellouch[26], J. Letts[2], L. Levinson[26], C. Lewis[15], S.L. Lloyd[13], F.K. Loebinger[16], G.D. Long[17], B. Lorazo[18], M.J. Losty[7], J. Ludwig[10], A. Luig[10], A. Malik[21], M. Mannelli[8], S. Marcellini[2], C. Markus[3], A.J. Martin[13], J.P. Martin[18], G. Martinez[17], T. Mashimo[24], W. Matthews[25], P. Mättig[3], W.J. McDonald[30], J. McKenna[29], E.A. Mckigney[15], T.J. McMahon[1], A.I. McNab[13], F. Meijers[8], S. Menke[3], F.S. Merritt[9], H. Mes[7], J. Meyer[27], A. Michelini[8], G. Mikenberg[26], D.J. Miller[15], R. Mir[26], W. Mohr[10], A. Montanari[2], T. Mori[24], M. Morii[24], U. Müller[3], B. Nellen[3], B. Nijjhar[16], R. Nisius[8], S.W. O'Neale[1], F.G. Oakham[7], F. Odorici[2], H.O. Ogren[12], T. Omori[24], M.J. Oreglia[9], S. Orito[24], M. Palazzo[2], J. Pálinkás[33,d], J.P. Pansart[21], G. Pásztor[32], J.R. Pater[16], G.N. Patrick[20], M. Pearce[1], S. Petzold[27], J.E. Pilcher[9], J. Pinfold[30], D.E. Plane[8], P. Poffenberger[28], B. Poli[2], A. Posthaus[3], H. Przysiezniak[30], D.L. Rees[1], D. Rigby[1], M.G. Rison[5], S.A. Robins[13], N. Rodning[30], J.M. Roney[28], A. Rooke[15], E. Ros[8], A.M. Rossi[2], M. Rosvick[28], P. Routenburg[30], Y. Rozen[8], K. Runge[10], O. Runolfsson[8], D.R. Rust[12], R. Rylko[25], E.K.G. Sarkisyan[23], M. Sasaki[24], C. Sbarra[2], A.D. Schaile[8,e], O. Schaile[10], F. Scharf[3], P. Scharff-Hansen[8], P. Schenk[4], B. Schmitt[3], M. Schröder[8], H.C. Schultz-Coulon[10], M. Schulz[8], P. Schütz[3], J. Schwiening[3], W.G. Scott[20], T.G. Shears[16], B.C. Shen[4], C.H. Shepherd-Themistocleous[27], P. Sherwood[15], G.P. Siroli[2], A. Sittler[27], A. Skillman[15], A. Skuja[17], A.M. Smith[8], T.J. Smith[28], G.A. Snow[17], R. Sobie[28], S. Söldner-Rembold[10], R.W. Springer[30], M. Sproston[20], A. Stahl[3], M. Starks[12],

K. Stephens[16], J. Steuerer[27], B. Stockhausen[3], D. Strom[19], F. Strumia[8], P. Szymanski[20], R. Tafirout[18], H. Takeda[24], P. Taras[18], S. Tarem[22], M. Tecchio[8], N. Tesch[3], M. Thiergen[10], M.A. Thomson[8], E. von Törne[3], S. Towers[6], M. Tscheulin[10], E. Tsur[23], A.S. Turcot[9], M.F. Turner-Watson[8], P. Utzat[11], R. Van Kooten[12], G. Vasseur[21], M. Verzocchi[10], P. Vikas[18], M. Vincter[28], E.H. Vokurka[16], F. Wäckerle[10], A. Wagner[27], C.P. Ward[5], D.R. Ward[5], J.J. Ward[15], P.M. Watkins[1], A.T. Watson[1], N.K. Watson[7], P. Weber[6], P.S. Wells[8], N. Wermes[3], J.S. White[28], B. Wilkens[10], G.W. Wilson[27], J.A. Wilson[1], T. Wlodek[26], G. Wolf[26], S. Wotton[11], T.R. Wyatt[16], S. Xella[2], S. Yamashita[24], G. Yekutieli[26], K. Yoshimura[24], V. Zacek[18],

[1]School of Physics and Space Research, University of Birmingham, Birmingham B15 2TT, UK

[2]Dipartimento di Fisica dell' Università di Bologna and INFN, I-40126 Bologna, Italy

[3]Physikalisches Institut, Universität Bonn, D-53115 Bonn, Germany

[4]Department of Physics, University of California, Riverside CA 92521, USA

[5]Cavendish Laboratory, Cambridge CB3 0HE, UK

[6] Ottawa-Carleton Institute for Physics, Department of Physics, Carleton University, Ottawa, Ontario K1S 5B6, Canada

[7]Centre for Research in Particle Physics, Carleton University, Ottawa, Ontario K1S 5B6, Canada

[8]CERN, European Organisation for Particle Physics, CH-1211 Geneva 23, Switzerland

[9]Enrico Fermi Institute and Department of Physics, University of Chicago, Chicago IL 60637, USA

[10]Fakultät für Physik, Albert Ludwigs Universität, D-79104 Freiburg, Germany

[11]Physikalisches Institut, Universität Heidelberg, D-69120 Heidelberg, Germany

[12]Indiana University, Department of Physics, Swain Hall West 117, Bloomington IN 47405, USA

[13]Queen Mary and Westfield College, University of London, London E1 4NS, UK

[14]Technische Hochschule Aachen, III Physikalisches Institut, Sommerfeldstrasse 26-28, D-52056 Aachen, Germany

[15]University College London, London WC1E 6BT, UK

[16]Department of Physics, Schuster Laboratory, The University, Manchester M13 9PL, UK

[17]Department of Physics, University of Maryland, College Park, MD 20742, USA

[18]Laboratoire de Physique Nucléaire, Université de Montréal, Montréal, Quebec H3C 3J7,

Canada

[19]University of Oregon, Department of Physics, Eugene OR 97403, USA

[20]Rutherford Appleton Laboratory, Chilton, Didcot, Oxfordshire OX11 0QX, UK

[21]CEA, DAPNIA/SPP, CE-Saclay, F-91191 Gif-sur-Yvette, France

[22]Department of Physics, Technion-Israel Institute of Technology, Haifa 32000, Israel

[23]Department of Physics and Astronomy, Tel Aviv University, Tel Aviv 69978, Israel

[24]International Centre for Elementary Particle Physics and Department of Physics, University of Tokyo, Tokyo 113, and Kobe University, Kobe 657, Japan

[25]Brunel University, Uxbridge, Middlesex UB8 3PH, UK

[26]Particle Physics Department, Weizmann Institute of Science, Rehovot 76100, Israel

[27]Universität Hamburg/DESY, II Institut für Experimental Physik, Notkestrasse 85, D-22607 Hamburg, Germany

[28]University of Victoria, Department of Physics, P O Box 3055, Victoria BC V8W 3P6, Canada

[29]University of British Columbia, Department of Physics, Vancouver BC V6T 1Z1, Canada

[30]University of Alberta, Department of Physics, Edmonton AB T6G 2J1, Canada

[31]Duke University, Dept of Physics, Durham, NC 27708-0305, USA

[32]Research Institute for Particle and Nuclear Physics, H-1525 Budapest, P O Box 49, Hungary

[33]Institute of Nuclear Research, H-4001 Debrecen, P O Box 51, Hungary

[a] and at TRIUMF, Vancouver, Canada V6T 2A3

[b] and Royal Society University Research Fellow

[c] and Institute of Nuclear Research, Debrecen, Hungary

[d] and Depart of Experimental Physics, Lajos Kossuth University, Debrecen, Hungary

[e] and Ludwig-Maximilians-Universität, München, Germany

[f] Nobby has subsequently passed to the other side (ALEPH)

References

[1] CDF Collaboration, F. Abe et al., Phys. Rev. Lett. **74** (1995), 2626.
D0 Collaboration, S. Abachi et al., Phys. Rev. Lett. **74** (1995), 2632.
The original 'discovery' papers are referenced in these papers, which describe the latest results.

[2] R.P. Feynman, 'The Feynman Lectures on Physics, Volume 2', Addison Wesley (1966).

[3] F. Halzen and A.D. Martin, 'Quarks and Leptons : An Introductory Course in Modern Particle Physics', John Wiley & Sons (1984).

[4] I.J.R. Aitchison and A.J.G. Hey, 'Gauge Theories in Particle Physics, Second Edition', Adam Hilger (1989).

[5] G.D. Coughlan and J.E. Dodd, 'The Ideas of Particle Physics, Second Edition', Cambridge University Press (1991).

[6] G.'t Hooft, Nucl. Phys. **B33** (1971), 173; Nucl. Phys. **B35** (1971), 167; Utrecht preprint THU-92/25 (1992).

[7] R.P. Feynman, 'Quantum Electrodynamics', Benjamin (1961).

[8] D.H. Perkins, 'Introduction to High Energy Physics, Third Edition', Addison Wesley (1987).

[9] S.A. Bludman, Il Nuovo Cimento **9** (1958), 443.

[10] J.J. Aubert et al., Phys. Rev. Lett. **33** (1974), 1404.
J.E. Augustin et al., Phys. Rev. Lett. **33** (1974), 1406.

[11] Gargamelle Collaboration, H.J. Hasert et al., Phys. Lett. **46B** (1973), 121; Phys. Lett. **46B** (1973), 138.

[12] UA1 Collaboration, G. Arnison et al., Phys. Lett. **122B** (1983), 103; Phys. Lett. **126B** (1983), 398.
UA2 Collaboration, G. Banner et al., Phys. Lett. **122B** (1983), 476; Phys. Lett. **129B** (1983), 130.

[13] S.L. Glashow, Nucl. Phys. **22** (1961), 579.
A. Salam, in : 'Elementary Particle Theory', ed. N. Svartholm, Almqvist and Wikel (1968), 361.
S. Weinberg, Phys. Rev. Lett. **19** (1967), 1264.

[14] T.D. Lee and C.N. Yang, Phys. Rev. **98** (1955), 1501.
C.S. Wu et al., Phys. Rev. **105** (1957), 1413.

[15] P.W. Higgs, Phys. Lett. **12** (1964), 132; Phys. Rev. Lett. **13** (1964), 508; Phys. Rev. **145** (1966), 1156.

[16] J.F. Grivaz, LAL preprint LAL-95-83. Rapporteur talk presented at the International Europhysics Conference on High Energy Physics, Brussels (July 1995). To be published.

[17] ATLAS Collaboration, Letter of Intent CERN-LHCC/92-4 (1992); Technical Proposal CERN-LHCC/94-43 (1994).

[18] CMS Collaboration, Letter of Intent CERN-LHCC/92-3 (1992); Technical Proposal CERN-LHCC/94-38 (1994).

[19] LEP Electroweak Working Group, P. Antilogus et al., LEPEWWG/95-02 (1995); OPAL Technical Note TN-312 (unpublished).

[20] H. Fritsch, M. Gell-Mann and H. Leutwyler, Phys. Lett. **B47** (1973), 365.

[21] A. Kirk, 'Gluonium 95', proceedings of the Hadron 95 Conference, Manchester (July 1995).

[22] S.L. Lloyd, in : 'Electron-Positron Annihilation Physics', ed. B. Foster, Adam Hilger (1990), 52.

[23] N. Cabibbo, Phys. Rev. Lett. **10** (1963), 531.

[24] S.L. Glashow, J. Iilopoulos and L. Maiani, Phys. Rev. **D2** (1970), 1285.

[25] M. Kobayashi and T. Maskawa, Prog. Theor. Phys. **49** (1973), 652.

[26] J.H. Christenson, J. Cronin, V. Fitch and R. Turlay, Phys. Rev. Lett. **13** (1964), 138.

[27] M.L. Perl et al., Phys. Rev. Lett. **35** (1975), 1489.

[28] L. Montanet et al., Physical Review **D50** (1994), 1173.
A 1995 off-year partial update for the 1996 edition is available on the Particle Data Group WWW pages (`http://pdg.lbl.gov/`).

[29] L. Wolfenstein, Phys. Rev. Lett. **51** (1984), 1945.

[30] Proceedings of the International Europhysics Conference on High Energy Physics, Brussels (July 1995). To be published.

[31] Proceedings of the 17$^{\text{th}}$ International Symposium on Lepton-Photon Interactions, Beijing (August 1995). To be published.

[32] H. Georgi and S. Glashow, Phys. Rev. Lett. **32** (1974), 438.
D.V. Nanopoulos, Nucl. Part. Phys. **15** (1986), 161.

[33] H. Henke and I. Wilson, 'The LEP Main Ring Accelerator Accelerating Structure', CERN 89-09 (1989).

[34] G. Altarelli et al., 'Interim Report on the Physics Motivations for an Energy Upgrade of LEP2', CERN-TH/95-151 (1995); CERN-PPE/95-78 (1995).

[35] OPAL Collaboration, K. Ahmet et al., Nucl. Instr. and Meth. **A305** (1991), 275.

[36] ALEPH Collaboration, Nucl. Instr. and Meth. **A294** (1990), 121.

[37] DELPHI Collaboration, Nucl. Instr. and Meth. **A303** (1991), 233.

[38] L3 Collaboration, Nucl. Instr. and Meth. **A289** (1990), 35.

[39] 'Experiments at CERN in 1994', ed. G.G. Harigel, ISSN 0259-093X (1994).

[40] S. Myers, 'The LEP Collider - from Design to Approval and Commissioning', Sixth John Adams Memorial Lecture, CERN 91-08 (1991).

[41] L. Arnaudon et al., CERN-PPE/92-125 (1992).

[42] A.A. Sokolov and I.M. Ternov, Sov. Phys. **JETP 4** (1957), 396.

[43] V.N. Baier, Sov. Phys. Usp. **14** (1972), 695.
L. Arnaudon et al., Phys. Lett. **B284** (1992), 431.
A.C. Melissinos, University of Rochester preprint UR-1331 (1993).

[44] L. Arnaudon et al., CERN-SL/94-07 (1994).

[45] P.P. Allport et al., Nucl. Instr. and Meth. **A324** (1993), 34.

[46] P.P. Allport et al., Nucl. Instr. and Meth. **A346** (1994), 476.

[47] J.R. Carter et al., Nucl. Instr. and Meth. **A286** (1990), 99.
J.M. Roney et al., Nucl. Instr. and Meth. **A279** (1989), 236.

[48] R.D. Heuer and A. Wagner, Nucl. Instr. and Meth., **A265** (1988), 11.
H.M. Fischer et al., Nucl. Instr. and Meth., **A252** (1986), 492.

[49] H. Mes et al., Nucl. Instr. and Meth., **A265** (1988), 445.

[50] A.H. Ball, 'Calorimetry in the OPAL Experiment at LEP', proceedings of the Beijing Calorimetry Symposium (October 1994). OPAL Conference Report CR-199 (unpublished).
P. Mättig, 'Photon Energy Resolution in the Lead Glass Calorimeters', OPAL technical note TN-324 (1995) (unpublished).

[51] A. Ji-Gang et al., Nucl. Instr. and Meth., **A267** (1988), 386.

[52] C. Beard et al., Nucl. Instr. and Meth., **A286** (1990), 117.

[53] R.M. Brown et al., IEEE Trans. Nucl. Sci. **30** (1983), 479.
M. Akrawy et al., Nucl. Instr. and Meth., **A290** (1990), 76.

[54] A.H. Ball et al., IEEE Trans. Nucl. Sci. **37** (1990).
G. Artusi et al., Nucl. Instr. and Meth., **A279** (1989), 523.

[55] G. Bella et al., Nucl. Instr. and Meth., **A252** (1986), 503.
G. Mikenberg et al., Nucl. Instr. and Meth., **A265** (1988), 223.

[56] J. Allison et al., Nucl. Instr. and Meth., **A236** (1985), 284.

[57] G.T.J. Arnison et al., Nucl. Instr. and Meth., **A294** (1990), 431.

[58] D.C. Imrie et al., Nucl. Instr. and Meth., **A238** (1989), 515.

[59] B.E. Anderson et al., IEEE Trans. Nucl. Sci. **41** (1994), 845.

[60] OPAL Collaboration, R. Akers et al., OPAL Physics Note PN-142 (1994).

[61] M. Arginon et al., Nucl. Instr. and Meth., **A313** (1992), 103; CERN-PPE/91-32 (1991).

[62] M. Arginon et al., Nucl. Instr. and Meth., **A333** (1993), 330; CERN-PPE/93-48 (1993).

[63] J. Baines et al., Nucl. Instr. and Meth., **A325** (1993), 271; CERN-ECP/92-08.

[64] D. Charlton et al., Nucl. Instr. and Meth., **A325** (1993), 129; CERN-PPE/92-136.

[65] G. Hanson et al., 'OPAL User Guide for the SHIFT Project', OPAL Offline Note OFFL-0478 (1992).

[66] C. Hawkes et al., 'ROPE User Guide (version 4.09)', OPAL Offline Note OFFL-0487 (1995).

[67] R. Cranfield et al., 'OPALCAL 506 User Guide', OPAL Offline Note OFFL-0036 (1992).

[68] CERN computer library long write up.
Documents are available from : `http://wwwcn.cern.ch/pl/index.html`

[69] D. Ward and J. Banks, 'A GROPE Primer (latest revisions for GR202)', OPAL Offline Note (1995).

[70] 'The CJ Processor for ROPE (version 7.21)', OPAL Offline Note (1991).
'The CT Processor for ROPE (version 3.03)', OPAL Offline Note (1991).

[71] W.J. Murray, 'Bhabha Physics at the Z^0 Pole', Ph.D. Thesis, Cambridge University (1990).

[72] P. Billoir, Nucl. Instr. and Meth., **225** (1984), 352.

[73] 'The Control System of the OPAL Detector at LEP', presented at the International Conference on Accelerator and Large Experimental Physics Control Systems, Vancouver (1989).

[74] J. Allison et al., Nucl. Instr. and Meth., **A317** (1992), 47.

[75] R. Brun et al., 'GEANT User Guide (version 3.0)', CERN-DD/EE/84-1.

[76] T. Sjöstrand, Comp. Comm. **82** (1994), 74; Comp. Phys. Comm. **39** (1986), 347; CERN-TH/92-6488 (1992); CERN-TH/93-7112 (1993).
M. Bengtsson and T. Sjöstrand, Comp. Phys. Comm. **43** (1987), 367; Nucl. Phys. **B289** (1987), 810.

[77] CFS Collaboration, S.W. Herb et al., Phys. Rev. Lett. **39** (1977), 252.

[78] CFS Collaboration, W.R. Innes et al., Phys. Rev. Lett. **39** (1977), 1240.

[79] CFS Collaboration, K. Ueno et al., Phys. Rev. Lett. **42** (1979), 486.

[80] PLUTO Collaboration, C. Berger et al., Phys. Lett. **B76** (1978), 243.
DASP II Colaboration, C.W. Darden et al., Phys. Lett. **B76** (1978), 246.
DESY-Heidelberg Collaboration, J.K. Bienleim et al., Phys. Lett. **B78** (1978), 360.
DASP II Colaboration, C.W. Darden et al., Phys. Lett. **B78** (1978), 364.

[81] CLEO Collaboration, D. Andrews et al., Phys. Rev. Lett. **44** (1980), 1108.
CUSB Collaboration, T. Böhringer et al., Phys. Rev. Lett. **44** (1980), 1111.

[82] CLEO Collaboration, D. Andrews et al., Phys. Rev. Lett. **45** (1980), 219.
CUSB Collaboration, G. Finocchiaro et al., Phys. Rev. Lett. **45** (1980), 222.

[83] C. Quigg and J.L. Rosner, Phys. Lett. **B72** (1978), 462.

[84] M. Battle et al., Phys. Rev. Lett. **71** (1993), 3922.

[85] G.J. Barker, 'A Measurement of the Mean b Hadron Lifetime Using the Central Drift Chambers of the OPAL Experiment at LEP', Ph.D. Thesis, University of London (1993).

[86] J.A. Mckenna, 'Heavy Flavour Physics', invited talk at the Lake Louise Institute on Collider Physics (1993); OPAL Conference Report CR-118 (unpublished).

[87] R. Marshall, in : 'Electron-Positron Annihilation Physics', ed. B. Foster, Adam Hilger (1990), 1.

[88] J.H. Kühn and P.M. Zerwas, in : 'Z^0 Physics at LEP 1, Volume 1', CERN 89-08 (1989).

[89] G. Bonvicini et al., Phys. Rev. Lett. **73** (1994), 392.

[90] ALEPH Collaboration, 'Measurement of the Λ_b^0 Polarisation in Z^0 Decays', contribution EPS-400 to the International Europhysics Conference on High Energy Physics, Brussels (1995).

[91] B. Anderson et al., Phys. Rep. **97** (1983), 33; Z. Phys. **C1** (1979), 105.

[92] X. Artu and G. Mennessier, Nucl. Phys. **B70** (1974), 93.

[93] B. Anderson, G. Gustafson and B. Sjöstrand, Phys. Scrip. **32** (1985), 574.

[94] OPAL Collaboration, R. Akers et al., Phys. Lett. **B353** (1995), 595.

[95] JADE Collaboration, W. Bartel et al., Phys. Lett. **101B** (1981), 129.

[96] OPAL Collaboration, R. Akers et al., Z. Phys. **C68** (1995), 531.

[97] C. Peterson et al., Phys. Rev. **D27** (1983), 105.

[98] ALEPH Collaboration, D. Buskulic et al., Phys. Lett. **B357** (1995), 699.

[99] S. Komamiya, 'b and c Physics', invited talk given at the International Europhysics Conference on High Energy Physics, Brussels (July 1995); University of Tokyo preprint UT-ICEPP 92-12 (1995).

[100] DELPHI Collaboration, P. Abreu et al., Phys. Lett. **B345** (1995), 598.

[101] L3 Collaboration, M. Acciarri et al., Phys. Lett. **B345** (1995), 589.
DELPHI Collaboration, P. Abreu et al., Z. Phys. **C68** (1995), 353.

[102] OPAL Collaboration, R. Akers et al., Z. Phys. **C66** (1995), 19.

[103] CLEO Collaboration, G. Crawford et al., Phys. Rev. **D45** (1992), 572.

[104] ARGUS Collaboration, H. Albrecht et al., Z. Phys. **C42** (1989), 519.

[105] W. Kwong and J.L. Rosner, Phys. Rev. **D44** (1991), 212.

[106] S. Capstick and N. Isgur, Phys Rev. **D34** (1986), 2809.

[107] M. Basile et al., Lettere al Nuovo Cimento **31** (1981), 97.

[108] D. Drijard et al., Phys. Lett. **B108** (1982), 361.

[109] M. Basile et al., Il Nuovo Cimento **A68** (1982), 289.

[110] G. Bari et al., Il Nuovo Cimento **A104** (1991), 1787.

[111] UA1 Collaboration, C. Albajar et al., Phys. Lett. **B273** (1991), 540.

[112] CDF Collaboration, F. Abe et al., Phys. Rev. **D47** (1993), 2639.

[113] OPAL Collaboration, R. Akers et al., 'Search for Exclusive Λ_b^0 Decays with the OPAL Detector at LEP', contribution EPS-262 to the International Europhysics Conference on High Energy Physics, Brussels (1995).

[114] ALEPH Collaboration, D. Buskulic et al., 'Search for Λ_b^0 Baryon Exclusive Hadronic Decays', contribution EPS-401 to the International Europhysics Conference on High Energy Physics, Brussels (1995).

[115] Q.P. Xu and A.N. Kamal, Alberta preprint THY-23-92.
T. Mannel and W. Roberts, CEBAF preprint CEBAF-TH-92-14.
S. Rudaz and M.B. Voloshin, Phys. Lett. **252B** (1990), 443.

[116] DELPHI Collaboration, P. Abreu et al., 'Search for Exclusive Decays of the Λ_b^0 Baryon and Measurement of its Mass', CERN-PPE/96-16. To be submitted to Phys. Lett. **B**.

[117] N. Isgur and M.B. Wise, Nucl. Phys. **B348** (1991), 276.

[118] ALEPH Collaboration, P. Abreu et al., Phys. Lett. **B278** (1992), 209.

[119] ALEPH Collaboration, D. Buskulic et al., Phys. Lett. **B357** (1995), 685.

[120] DELPHI Collaboration, P. Abreu et al., 'Beauty Baryon Production Properties and Lifetimes', contribution EPS-564 to the International Europhysics Conference on High Energy Physics, Brussels (1995).

[121] OPAL Collaboration, R. Akers et al., Z. Phys. **C69** (1996), 195.

[122] DELPHI Collaboration, P. Abreu et al., Z. Phys. **C68** (1995), 375.

[123] OPAL Collaboration, R. Akers et al., Z. Phys. **C67** (1995), 57.

[124] OPAL Collaboration. R. Akers et al., Z. Phys. **C66** (1995), 555.

[125] OPAL Collaboration, R. Akers et al., Phys. Lett. **B353** (1995), 402.

[126] DELPHI Collaboration, P. Abreu et al., Phys. Lett. **B347** (1995), 447.

[127] I.I. Bigi, 'The QCD Perspective on Lifetimes of Heavy Flavour Hadrons', Notre Dame du Lac preprint UND-HEP-95-BIG02 (1995); hep-ph/9508408.

[128] G. Altarelli et al., Phys Lett. **B261** (1991), 303.

[129] I.I. Bigi et al., Phys. Lett. **B280** (1992), 271.

[130] M. Shiffman, 'Recent Progress in the Heavy Quark Theory', invited talk at the V International Symposium on Particles, Strings and Cosmology (PACOS), Baltimore (1995); Minnesota preprint UMN-TH-1345-95; hep-ph/9505289.
I.I. Bigi, 'Quo Vadis, Fascinum ?', invited talk at Workshop on the Tau/Charm

Factory, Argonne National Laboratory (1995); Notre Dame du Lac preprint UND-HEP-95-BIG08'; hep-ph/9508294.
I.I. Bigi, 'Lifetimes of Heavy-Flavour Hadrons - Whence and Whither ?', invited talk at the 6th International Symposium on Heavy Flavour Physics, Pisa (1995); Notre Dame du Lac preprint UND-HEP-95-BIG06; hep-ph/9507364.

[131] B. Blok and T. Mannel, 'Parton Hadron Duality in Non-leptonic b Hadron Decays', Technion preprint TTP 95-22 (1995); hep-ph/9505288.

[132] P. Ball and V. Braun, Phys. Rev. **D49** (1994), 2472.

[133] I.I. Bigi, M. Shiffman, N.G. Uraltsev and A. Vainshtein, Phys. Rev. **D52** (1995), 196.

[134] V. Barger et al., J. Phys. **G5** (1985), 147.

[135] MAC Collaboration, E. Fernandez et al., Phys. Rev. Lett. **51** (1983), 1022.

[136] MARK-II Collaboration, N.S. Lockyer et al., Phys. Rev. Lett. **51** (1983), 1316.

[137] ALEPH Collaboration, D. Buskulic et al., Phys. Lett. **B297** (1992), 449.

[138] OPAL Collaboration, P.D. Acton et al., Phys. Lett. **B295** (1992), 357.

[139] OPAL Collaboration, G. Alexander et al., Z. Phys. **C52** (1991), 175.
T. Mori, 'Multihadronic Cross Section in 1990', OPAL Technical Note TN-025 (1990) (unpublished).
G. Duckeck, 'Large Acceptance Multihadron Selection', OPAL Technical Note TN-086 (1992) (unpublished).

[140] S.L. Lloyd, 'The OPAL Primer (version 3.0)', OPAL Internal Note (1995).

[141] R.V. Kowalewski, 'A Study of Jet Finding for b Physics in OPAL', OPAL Technical Note TN-180 (1993) (unpublished).

[142] JADE Collaboration, S. Bethke et al., Phys. Lett. **B213** (1988), 235.

[143] OPAL Collaboration, M. Akrawy et al., Z. Phys. **C49** (1991), 375.

[144] UA1 Collaboration, G. Arnison et al., Phys. Lett. **B132** (1983), 214.
UA1 Collaboration, G. Arnison et al., Phys. Lett. **B123** (1983), 115.
UA2 Collaboration, J. Alitti et al., Phys. Lett. **B257** (1991), 232.
CDF Collaboration, F. Abe et al., Phys. Rev. **D45** (1992), 1448.

[145] OPAL Collaboration, R. Akers et al., Z. Phys. **C68** (1995), 179.
L.A. del Pozo, 'Tests of QCD from Jet and Hadron Production at LEP', Ph.D. Thesis, Cambridge University (1993).

[146] OPAL Collaboration, P.D. Acton et al., Phys. Lett. **B273** (1991), 355.

[147] R. Hawkings and S. de Jong, 'The Beam Spot Location in OPAL in 1994 Data', OPAL Technical Note TN-321 (1995) (unpublished).
S. de Jong, 'Determination of the LEP Beam Spot Location in OPAL. An Update of TN041', OPAL Technical Note TN-251 (1994) (unpublished).
S. de Jong, 'Determination of the LEP Beam Spot Location in OPAL with Pass 3 Data', OPAL Technical Note TN-041 (1991) (unpublished).

[148] OPAL Collaboration, R. Akers et al., Z. Phys. **C61** (1993), 209.

[149] R.V. Kowalewski, 'A Study of Lifetime Tagging of b Hadrons in OPAL', OPAL Technical Note TN-181 (1993) (unpublished).

[150] R.V. Kowalewski and P.S. Wells, 'BTagging Software (version 108/29)', OPAL Internal Note (1993).

[151] OPAL Collaboration, R. Akers et al., Z. Phys. **C65** (1995), 17.
R.J. Batley, 'A measurement of $\Gamma(Z^0 \to b\bar{b})/\Gamma(Z^0 \to \text{hadrons})$ using Double Lifetime Tagging', OPAL Technical Note TN-140 (1993) (unpublished).

[152] R.J. Hemingway, 'An OPAL Tune of JETSET 7.4 using Z^0 Data', OPAL Technical Note TN-279 (1995) (unpublished).

[153] T.E. Browder et al., 'A Review of Hadronic and Rare B Decays', in : 'B Decays, Second Edition', ed. S. Stone, World Scientific (1994), 158.

[154] C. Darling et al., 'OPAL Updates to JETSET 7.4 Decay Tables', OPAL Technical Note TN-322 (1995) (unpublished).

[155] S.L. Lloyd and M.P. Singh, 'A Study of the Charged Particle Multiplicity in Events Containing a Tagged b Quark Jet', OPAL Technical Note TN-117 (1992) (unpublished).
OPAL Collaboration, P.D. Acton et al., Z. Phys. **C53** (1992), 539.

[156] P. Ward, Cambridge University and member of the OPAL Collaboration, *private communication*, November 1995.

[157] OPAL Collaboration, P.D. Acton et al., Phys. Lett. **B291** (1992), 503.

[158] O. Biebel et al., Nucl. Instr. and Meth. **A323** (1992), 169.
M. Hauschild et al., Nucl. Instr. and Meth. **A314** (1992), 74.

[159] M. Pearce, 'An Improved Measurement of the Λ^0 Production Rate in b Tagged Events', OPAL technical Note TN-268 (1994) (unpublished).

[160] OPAL Collaboration, R. Akers et al., OPAL Physics Note PN-145 (1994).
J. Steuerer, The University of Victoria and member of the OPAL Collaboration, *private communication*, November 1994.

[161] OPAL Collaboration, R. Akers et al., Z. Phys. **C66** (1995), 555.
M. Jimack, 'Determining the Proper Time of b Hadrons using Vertexing of Leptons and Other Tracks', OPAL Technical Note TN-206 (1994) (unpublished).

[162] OPAL Collaboration, R. Akers et al., Z. Phys. **C66** (1995), 19.

[163] R. Barlow, 'Statistics', John Wiley & Sons (1989).

[164] F. James, 'MINUIT : Function Minimisation and Error Analysis (version 94.1)', CERN program library long write-up D506 (1994).

[165] F. James, CERN program library short write-up D102 (1994).

[166] G. Arfken, 'Mathematical Methods for Physicists, Third Edition', Academic Press Inc. (1985).

[167] R. Batley, Cambridge University and member of the OPAL Collaboration, *private communication*, July 1995.

[168] CDF Collaboration, F. Abe et al., Phys. Rev. Lett. **71** (1993), 3421.

[169] OPAL Collaboration, P.D. Acton et al., Z. Phys. **C60** (1993), 217.
L3 Collaboration, O. Adriani et al., Phys. Lett. **B317** (1993), 474.
ALEPH Collaboration, D. Buskulic et al., Phys. Lett. **B369** (1996), 151.
DELPHI Collaboration, P. Abreu et al., Z. Phys. **C63** (1994), 3.
DELPHI Collaboration, P. Abreu et al., 'Updated Precision Measurement of the Average Lifetime of B hadrons', contribution EPS-751 to the International Europhysics Conference on High Energy Physics, Brussels (1995).
SLD Collaboration, K. Abe et al., Phys. Rev. Lett. **75** (1995), 3624.

[170] LEP B Lifetimes Working Group, D. Bloch et al., OPAL Technical Note TN-276 (unpublished).

[171] DELPHI Collaboration, P. Abreu et al., 'Updated Precision Measurement of the Average Lifetime of B Hadrons', CERN-PPE/96-13. To be submitted to Phys. Lett. **B**.

[172] M. Hauschild, member of the OPAL Collaboration, *private communication*, February 1996.

[173] M. Hansroul and R. Kowalewski, 'The OU Processor for ROPE (version 2.12)', OPAL Internal Note (1993). The routine `OUATRK` was used.

[174] ALEPH Collaboration, D. Buskulic et al., 'Updated Measurement of the b Baryon Lifetime', contribution EPS-753 to the International Europhysics Conference on High Energy Physics, Brussels (1995).
Also, see [120], [122], [121] and [125].

[175] DELPHI Collaboration, P. Abreu et al., 'Determination of the Average Lifetime of b Baryons', CERN-PPE/96-21. To be submitted to Z. Phys. **C**.

[176] A. De Angelis, invited talk at the XXIV Symposium on Multiparticle Dynamics, Vietri Sul Mare (1994); CERN-PPE/94-174 (1994).

[177] C. Bortolotto, A. De Angleis, N. De Groot and J. Seixas, Int. J. Mod. Phys. **C3** (1992), 733.

[178] C. Peterson and T. Rögnvaldsson, 'JETNET 3.0 - A Versatile Artificial Neural Network Package', Lund preprint LU-TP 93-29 (1993), CERN-TH/7135-94 (1994), Comp. Phys. Comm. **81** (1994), 185.

[179] G. Bahan and R. Barlow, Comp. Phys. Comm. **74** (1993), 199.